

Rab18 and a Rab18 GEF complex are required for normal ER structure

Andreas Gerondopoulos,¹ Ricardo Nunes Bastos,¹ Shin-ichiro Yoshimura,² Rachel Anderson,¹ Sarah Carpanini,³ Irene Aligianis,⁴ Mark T. Handley,⁴ and Francis A. Barr¹

¹Department of Biochemistry, University of Oxford, Oxford OX1 3QU, England, UK

²Department of Cell Biology, Graduate School of Medicine, Osaka University, Suita, Osaka 565-0871, Japan

³Division of Neurobiology, The Roslin Institute and Royal (Dick) School of Veterinary Studies, University of Edinburgh, Edinburgh EH25 9RG, Scotland, UK

⁴MRC Human Genetics Unit, Institute of Genetics and Molecular Medicine, University of Edinburgh, Edinburgh EH4 2XU, Scotland, UK

The ancestral Rab GTPase Rab18 and both subunits of the Rab3GAP complex are mutated in the human neurological and developmental disorder Warburg Micro syndrome. Here, we demonstrate that the Rab3GAP complex is a specific Rab18 guanine nucleotide exchange factor (GEF). The Rab3GAP complex localizes to the endoplasmic reticulum (ER) and is necessary for ER targeting of Rab18. It is also sufficient to promote membrane recruitment of Rab18. Disease-associated point mutations of conserved residues in either the Rab3GAP1 (T18P and

E24V) or Rab3GAP2 (R426C) subunits result in loss of the Rab18 GEF and membrane-targeting activities. Supporting the view that Rab18 activity is important for ER structure, in the absence of either Rab3GAP subunit or Rab18 function, ER tubular networks marked by reticulon 4 were disrupted, and ER sheets defined by CLIMP-63 spread out into the cell periphery. Micro syndrome is therefore a disease characterized by direct loss of Rab18 function or loss of Rab18 activation at the ER by its GEF Rab3GAP.

Introduction

Rab18 is one of the most highly conserved Rab GTPase regulators of membrane traffic being present in the last eukaryotic common ancestor of both the plant and animal kingdoms (Elias et al., 2012; Klöpper et al., 2012). A defined biological function has remained elusive, partly because it was lost in the budding yeast lineage used for the genetic screens for regulators of membrane traffic. Rab18 has been linked to lipid droplet formation (Martin et al., 2005; Ozeki et al., 2005), ER–Golgi trafficking (Dejgaard et al., 2008), and the regulation of secretory granules (Vazquez-Martinez et al., 2007) and peroxisomes (Gronemeyer et al., 2013), and may be exploited during hepatitis C infection (Salloum et al., 2013). However, no clear molecular function or site of action has been defined for Rab18, despite the fact that loss-of-function mutations are found in the autosomal-recessive human neurological and developmental disorder Warburg Micro syndrome (Bem et al., 2011). These children suffer from multiple specific developmental abnormalities in brain and eye development, profound global developmental delay, and neurodegeneration (Bem et al., 2011). However, the pattern of Rab18

conservation in both plants and animals indicates that the essential cellular function is unlikely to be specific to neuronal cells (Lütcke et al., 1994; Klöpper et al., 2012).

In addition to Rab18, a known Rab regulatory complex is mutated in Warburg Micro syndrome (Aligianis et al., 2005, 2006; Handley and Aligianis, 2012; Handley et al., 2013). This is the Rab3 GTPase-activating protein (GAP) complex originally identified using biochemical purification from brain tissue as a cellular factor promoting GTP hydrolysis by Rab3 (Fukui et al., 1997; Nagano et al., 1998). Like Rab18, the Rab3GAP complex is both more widely conserved and more broadly expressed than Rab3 and is ubiquitously expressed in human tissues (Nagano et al., 1998), raising the possibility that regulation of Rab3 is not its only function.

Simple logic suggests that the Rab3GAP complex and Rab18 act in the same pathway because mutations result in the same disease phenotype. We therefore set out to identify the cellular site of action of Rab18 and its functional relationship with Rab3GAP. Two simple alternatives present themselves, either

Correspondence to Francis A. Barr: francis.barr@bioch.ox.ac.uk; or Mark T. Handley: mark.handley@igmm.ed.ac.uk

Abbreviations used in this paper: GAP, GTPase-activating protein; GEF, guanine nucleotide exchange factor; Rtn4, reticulon 4.

© 2014 Gerondopoulos et al. This article is distributed under the terms of an Attribution-Noncommercial-Share Alike-No Mirror Sites license for the first six months after the publication date (see <http://www.rupress.org/terms>). After six months it is available under a Creative Commons License (Attribution-Noncommercial-Share Alike 3.0 Unported license, as described at <http://creativecommons.org/licenses/by-nc-sa/3.0/>).

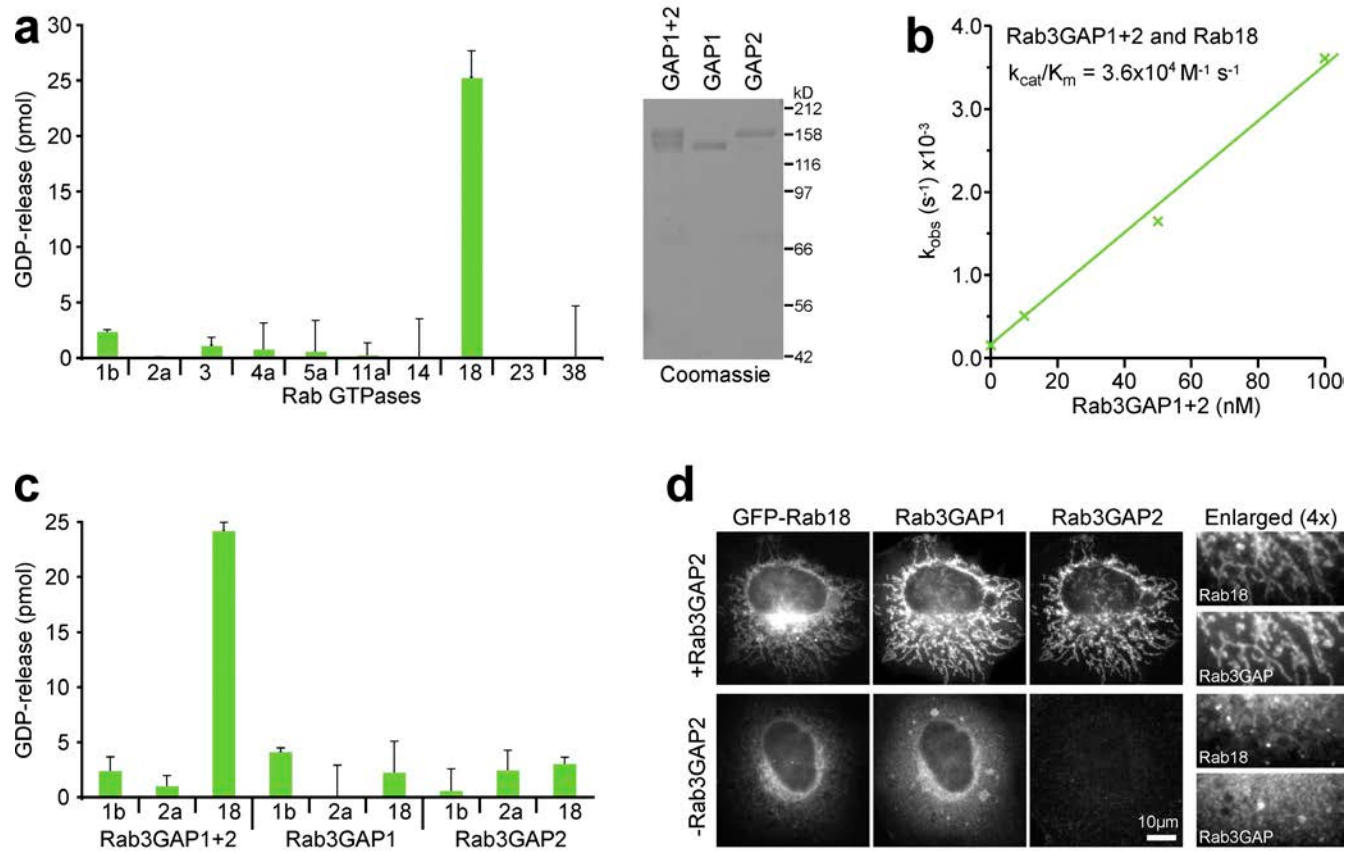


Figure 1. Rab3GAP is a Rab18 GEF. (a) Rab3GAP complexes were used for GEF assays toward a representative group of Rab GTPases. Error bars indicate the standard deviation of the mean ($n = 3$). Rab3GAP complexes and individual subunits (GAP1 and GAP2) were analyzed on protein gels stained with colloidal Coomassie brilliant blue stain. (b) Mant-GDP kinetic GEF assays were performed using the Rab3GAP complex and Rab18 as a substrate to derive catalytic efficiency (k_{cat}/K_m). Initial rates of nucleotide exchange were derived from three independent experiments and are plotted as a function of Rab3GAP concentration. (c) Rab3GAP complexes and individual subunits were used for GEF assays toward Rab1b, Rab2a, and Rab18. Error bars indicate the standard deviation of the mean ($n = 3$). (d) HeLa cells were cotransfected for 20 h with GFP-Rabs and Myc-tagged Rab3GAP1 in the presence and absence of the Tom70-FLAG-Rab3GAP2 mitochondrial-targeting fusion. The cells were fixed and then stained with FLAG and Myc antibodies; Rabs were visualized using GFP fluorescence. Bars are marked in the figure.

Rab3GAP acts downstream of Rab18 as an effector complex for the active GTP form of Rab18, or Rab3GAP acts upstream of Rab18 as a potential guanine nucleotide exchange factor (GEF) regulator promoting Rab18 activation. The evidence presented here provides strong support for the hypothesis that the Rab3GAP complex is the cellular GEF activating Rab18, and this activity is required for Rab18 localization to the ER where it acts in a pathway maintaining normal ER morphology.

Results

Rab3GAP is a Rab18 GEF

Most disease-causing mutations in Rab3GAP1 are frameshift and nonsense mutations likely to affect protein expression (Handley and Aligianis, 2012; Handley et al., 2013). However, several missense loss-of-function mutations cluster in a highly conserved N-terminal domain of Rab3GAP1, suggesting this is an important function determinant of Rab3GAP activity discrete from the C-terminal Rab3 GAP domain (Handley and Aligianis, 2012; Handley et al., 2013). Rab3GAP is a binary complex formed from two different subunits and mutations in either subunit cause Micro syndrome (Handley and Aligianis,

2012; Handley et al., 2013). Thus, if Rab3GAP functions as a Rab GEF, both of its subunits could be required for full nucleotide exchange activity. We therefore tested the *in vitro* nucleotide exchange activity of a purified Rab3GAP complex in addition to that of the individual Rab3GAP1/2 subunits (Fig. 1 a, see inset showing Coomassie brilliant blue-stained gel). Screening against a panel of Rabs revealed a specific GDP release activity directed toward Rab18, whereas no activity was seen toward Rab3, the other Rab implicated in Micro syndrome (Fig. 1 a). Kinetic analysis showed that catalytic efficiency (k_{cat}/K_m) toward Rab18 is $3.6 \times 10^4 \text{ M}^{-1} \text{ s}^{-1}$ (Fig. 1 b). By comparison, the catalytic efficiencies of Rabex5 and DENND1 GEFs for Rab5 and Rab35 are $\sim 2.5 \times 10^4 \text{ M}^{-1} \text{ s}^{-1}$ (Delprato et al., 2004; Delprato and Lambright, 2007; Wu et al., 2011). Both subunits were required for this Rab18 GEF activity, and neither subunit alone stimulated GDP release above the basal level seen with other nontarget Rabs (Fig. 1 c).

Rab GEFs form part of the minimal machinery needed for Rab targeting (Barr, 2013; Blümer et al., 2013). The ability of the Rab3GAP complex to promote Rab18 recruitment to a heterologous membrane *in vivo* was therefore tested (Gerondopoulos et al., 2012). When Rab3GAP2 was ectopically targeted to mitochondria,

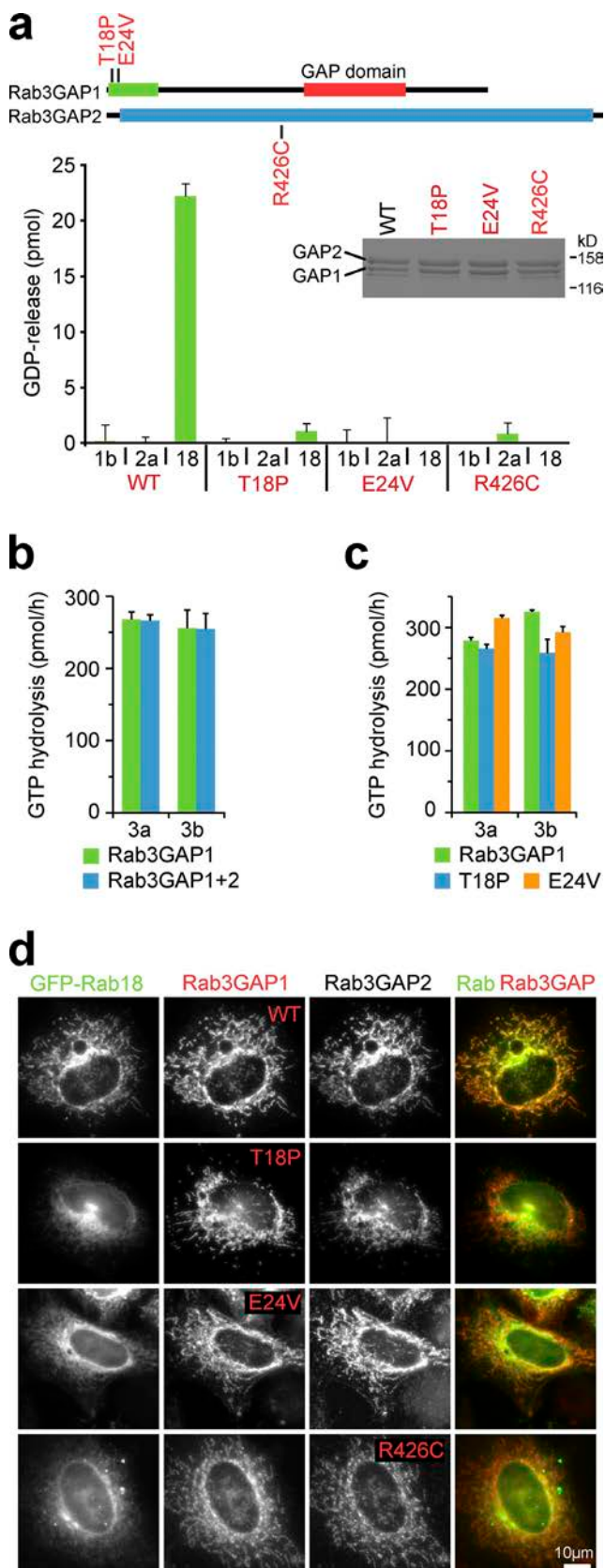


Figure 2. Disease-associated mutations in Rab3GAP1 and Rab3GAP2 result in loss of Rab18 GEF activity. (a) A schematic of the Rab3GAP complex showing the Rab3 GAP domain and the conserved N-terminal region of Rab3GAP1. Pathological missense mutations in Rab3GAP1 and Rab3GAP2 are marked. Wild-type and disease mutant Rab3GAP complexes were used

its expression triggered recruitment of both coexpressed Rab3GAP1 and Rab18 to this compartment (Fig. 1 d). Omission of Rab3GAP2 resulted in loss of this Rab18 recruitment activity (Fig. 1 d). Rab3GAP therefore fulfils the requirements expected of a specific and highly active Rab18 GEF by promoting membrane association of Rab18.

Effect of disease-associated mutations on Rab18 GEF activity

The effects of known disease-causing point mutations in Rab3GAP1 and Rab3GAP2 were then tested. First, recombinant Rab3GAP complexes were made using Rab3GAP1 T18P or E24V and wild-type Rab3GAP2, or wild-type Rab3GAP1 and Rab3GAP2 R426C (Fig. 2 a). Of these complexes, only the form with both wild-type subunits showed activity toward Rab18 (Fig. 2 a). Complexes carrying either a mutant Rab3GAP1 or Rab3GAP2 subunit showed no activity toward Rab18 above the basal level seen with related non-target Rabs (Fig. 2 a). Analysis of the GAP activity of the complex toward Rab3a and Rab3b showed that this is due to the Rab3GAP1 subunit of the complex and does not require the Rab3GAP2 subunit (Fig. 2 b). Furthermore, screening of Rab3GAP1 against a panel of human Rabs confirmed that it showed greatest activity toward Rab3a, Rab3b, and Rab3c, as expected (Fukui et al., 1997; Nagano et al., 1998), but also has some activity toward a subset of other Rabs, although not Rab18 (Fig. S1 a). However, disease-associated point mutants in Rab3GAP1 had no effect on the GAP activity toward the Rab3 family, or the other potential targets Rab5a and Rab43 (Fig. 2 c; and Fig. S1 a, inset bar graph). No GAP activity of either wild-type or mutant Rab3GAP1 toward Rab18 was detected.

In agreement with the biochemical data defining a specific Rab18 GEF activity, the ability of the resulting mutant complexes to drive mitochondrial recruitment of Rab18 was abolished in the heterologous membrane-targeting assay (Fig. 2 d). These same mutations did not affect the capacity of Rab3GAP2 to recruit Rab3GAP1. The Rab3GAP complex is therefore a Rab18 GEF that forms part of the membrane-targeting machinery for Rab18, and Rab3GAP mutations associated with Micro syndrome disrupt this activity. These same mutations do not alter the GAP activity of this complex toward Rab3, making it unlikely that reduced GTP hydrolysis by Rab3 is the major change leading to Warburg Micro syndrome.

for GEF assays toward Rab1b, Rab2a, and Rab18. Error bars indicate the standard deviation of the mean ($n = 3$). (b) Wild-type Rab3GAP1, Rab3GAP1 and Rab3GAP2, or (c) wild-type and disease mutant Rab3GAP1 were used for GTPase assays with Rab3a or Rab3b. Error bars indicate the range ($n = 2$). This is a subset of the full screening data presented in the inset bar graph panel of Fig. S1 a. (d) HeLa cells were cotransfected for 20 h with GFP-Rabs, wild-type and disease mutant Myc-tagged Rab3GAP1, and the Tom70-FLAG-Rab3GAP2 mitochondrial-targeting fusion as indicated in the figure. The cells were fixed and then stained with FLAG and Myc antibodies; Rabs were visualized using GFP fluorescence. Bars are marked in the figure.

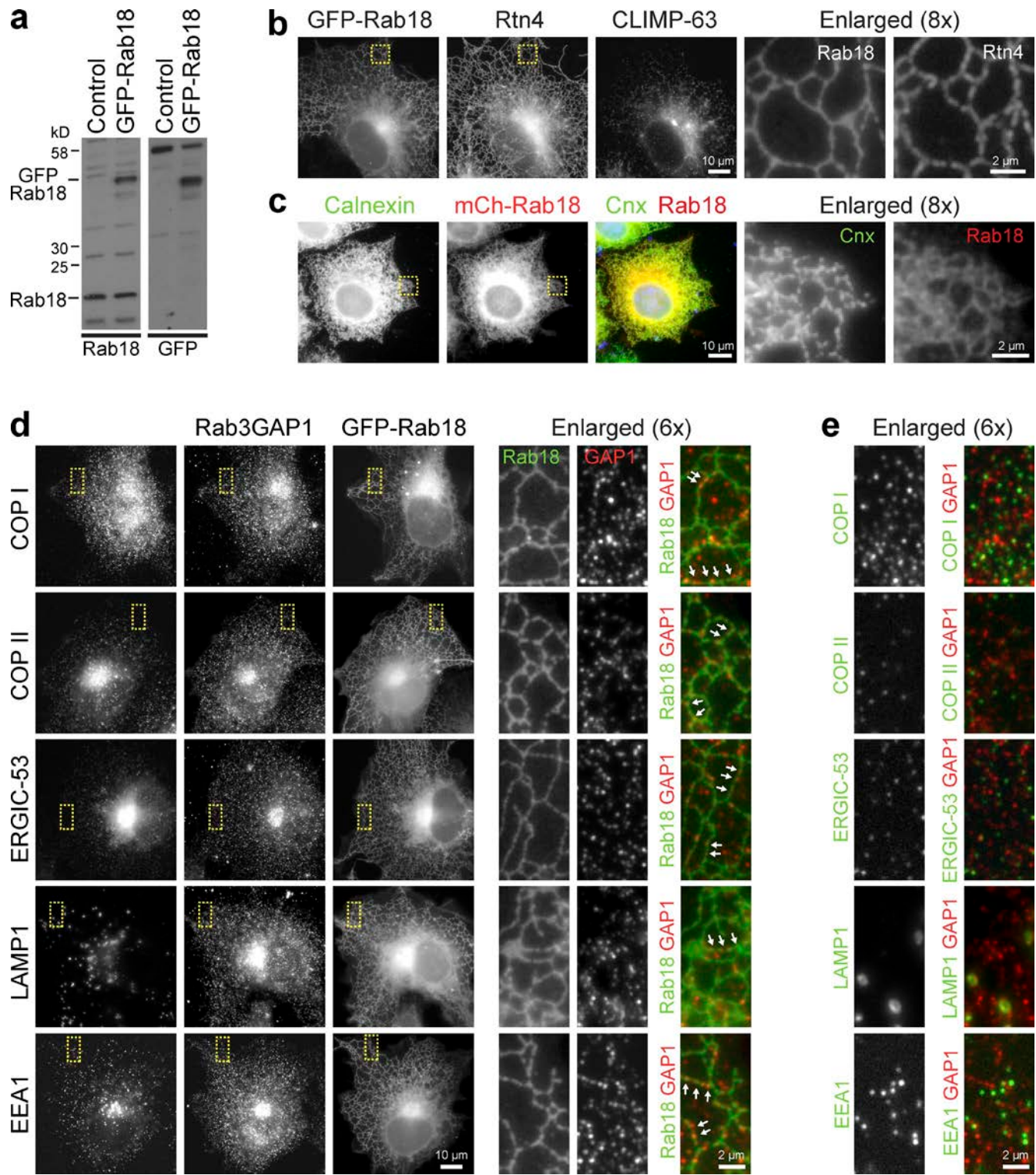


Figure 3. Analysis of Rab18 and Rab3GAP1 localization to the ER. (a) Western blot of COS7 control cells and COS7 cells expressing GFP-Rab18 with antibodies to endogenous Rab18 and GFP. (b) GFP-Rab18, reticulon 4 (Rtn4), and CLIMP-63 staining is shown in COS7 cells. (c) Calnexin staining and mCherry (mCh)-tagged Rab18 are shown in HeLa cells. (d) COS7 cells expressing GFP-Rab18 were stained for Rab3GAP1 and markers for COP I (β -COP), COP II (Sec31), ERGIC-53, and LAMP1. Arrowheads in the enlarged region show details of Rab3GAP1 localization to ER tubules marked by GFP-Rab18. (e) The enlarged region corresponding to the yellow boxed area in d shows details of the Rab3GAP1 and different compartment markers. Bars are marked in the figure.

Localization of Rab18 and Rab3GAP to the ER

Because of differing reports that Rab18 is present on lipid droplets, Golgi, and other organelles of the secretory pathway, the localization of Rab18 was investigated. Because antibodies capable of specifically detecting Rab18 on Western blots (Fig. S1 b) failed to detect any specific signal in immunofluorescence using a variety of different fixation protocols, cells expressing GFP-Rab18 were used. Western blotting showed that GFP-Rab18 was expressed at a similar level to the endogenous protein in COS7 cells (Fig. 3 a). These cells were then stained with the ER tubule and sheet markers reticulon 4 (Rtn4) and CLIMP-63, respectively. At this level of expression, Rab18 was present on ER tubules marked by Rtn4 (Fig. 3 b), a region lacking the ER sheet marker CLIMP-63. In HeLa cells, mCherry-tagged Rab18 was found to be present in both the perinuclear region and the cell periphery and to overlap with the ER marker calnexin (Fig. 3 c).

The localization of the Rab3GAP complex was then investigated using an antibody to the Rab3GAP1 subunit. Rab3GAP1 was detected in punctate structures spread throughout the volume of the cell (Fig. 3 d). Many of these punctate structures overlapped with Rab18-positive ER tubules in the cell periphery (Fig. 3 d, marked by arrows in the enlarged region). However, they did not show any overlap with markers for either COP I or COP II vesicles, the ER–Golgi recycling compartment marker ERGIC-53, or the endosome and lysosome markers EEA1 and LAMP1 (Fig. 3 d, and the enlarged region in Fig. 3 e). These observations are consistent with the idea that the Rab3GAP complex could activate Rab18 at the ER. However, the pattern of localization suggests that the Rab3GAP complex is restricted to a subdomain of the ER.

Rab3GAP complex regulates ER localization of Rab18

The requirement for Rab3GAP in Rab18 localization to the ER was then tested. Western blotting confirmed that Rab3GAP subunits, Rab18, and the negative control Rab7 were all efficiently depleted (Fig. S1 b). Furthermore, depletion of either subunit by siRNA affects levels of the other (Fig. S1 b), consistent with a report that deletion of Rab3GAP1 in mice results in loss of Rab3GAP2 protein (Sakane et al., 2006). Depletion of either subunit of the Rab3GAP complex resulted in loss of Rab18 from ER tubules and accumulation in a diffuse pattern most probably reflecting cytoplasmic localization in over 80% of cells (Fig. 4, a and b). Biochemical fractionation showed that in control cells Rab18 was found only in the membrane fraction, and in the absence of the Rab3GAP complex it was partially redistributed to the cytosol fraction (Fig. 4 c).

The role of Rab18 activation in the dynamics of the ER was then followed using live-cell imaging of mCherry-tagged Rab18 and a GFP-tagged ER marker. Dynamic tubular networks undergoing rapid branch migration and the formation of new connections by tubule fusion characterized the ER in control cells (Fig. 4 d and Video 1), as expected. These features were lost in the absence of the Rab18 GEF. Depletion of either Rab3GAP1 or Rab3GAP2 alone or in combination resulted in the loss of Rab18 from defined ER tubules and redistribution to a diffuse

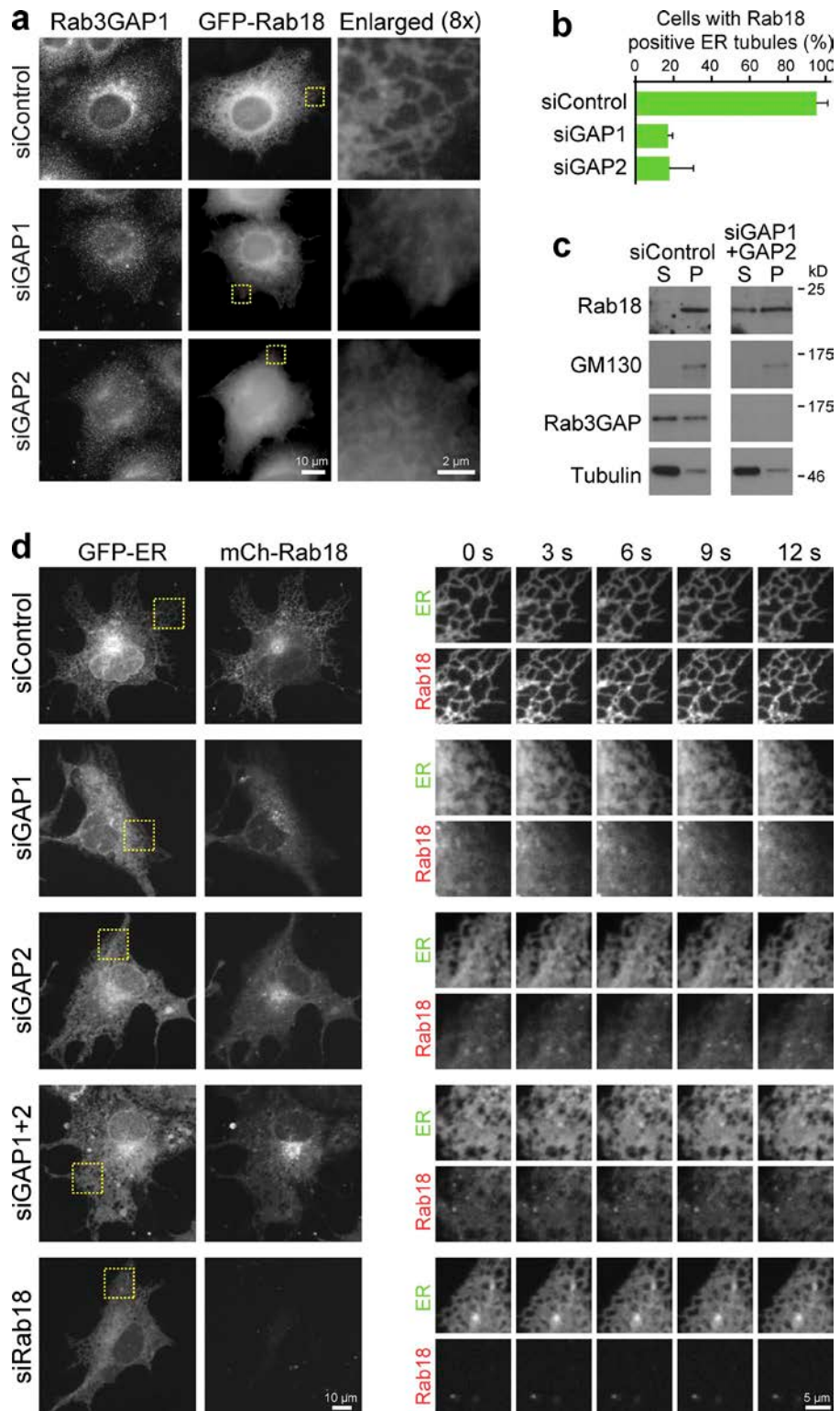
cytoplasmic pattern (Fig. 4 d). In addition to the loss of Rab18-positive tubular networks, ER sheets with dynamic edges extended into the cell periphery (Fig. 4 d and Videos 2–5). These results support the idea that Rab18 membrane association and localization to the ER requires the activity of its cognate GEF in the form of the Rab3GAP complex. They also suggest that the Rab18 pathway is important for maintaining the structure of the ER.

Altered ER morphology in the absence of Rab18 or the Rab3GAP complex

The ER can be divided into a perinuclear region defined by the marker CLIMP-63, whereas the peripheral ER tubular network lacks CLIMP-63 but is positive for Rtn4 (Voeltz and Prinz, 2007; Friedman and Voeltz, 2011). A role for Rab3GAP and Rab18 function in supporting this organization was tested in two different cell lines. When COS7 cells were depleted of Rab3GAP subunits or Rab18, CLIMP-63 spread away from the perinuclear region into the cell periphery, suggesting that ER sheets are expanded under these conditions (Fig. 5 a). This spread in CLIMP-63 was highly penetrant and observed in ~80% of cells depleted of Rab3GAP subunits or Rab18 (Fig. 5 b, green bars). Measurements of the area occupied by CLIMP-63 indicated that ER sheet volumes increased from 30% of the cell area to 60–80% in cells depleted of Rab3GAP subunits or Rab18 (Fig. 5 b, blue bars). In addition to the redistribution of Rab18 from the ER to the cytoplasm, HeLa cells depleted of Rab3GAP also showed a loss of calnexin staining in peripheral ER tubular networks (Fig. S1 c). Quantitation again confirmed that this was a highly penetrant effect, and fewer than 20% of Rab18- or Rab3GAP complex-depleted cells showed calnexin in peripheral ER tubular networks, compared with greater than 90% of control cells (Fig. S1, d and e). No alterations in the ER–Golgi Sec31 COP II vesicle coat protein or TGN46 trans-Golgi markers were observed in HeLa cells (Fig. S2 a). Similarly, the ERGIC-53 ER–Golgi recycling compartment marker and the TGN46 trans-Golgi marker were not obviously altered when Rab18 or the Rab3GAP complex was depleted in COS7 cells (Fig. S2 b). Western blots did not reveal major changes in the ER chaperones BIP, ERp72, or calnexin (Fig. S3 a), suggesting that the observed changes in ER morphology are not the result of a stress response and instead reflect a specific function for Rab18 at the ER.

To eliminate the possibility that indirect or off-target effects of the RNA interference procedure caused altered ER structure, rescue experiments were performed for Rab18. Cells were treated with two different Rab18 siRNA duplexes directed to the 3'UTR of the mRNA, then transfected with empty vector or GFP-tagged Rab18. Depletion of Rab18 using the Rab18.8 3'UTR duplex resulted in the spread of CLIMP-63 into the peripheral region, and this was reversed by expression of GFP-Rab18 resistant to the siRNA (Fig. 6 a). Western blotting showed that the level of GFP-Rab18 was similar to that of the endogenous Rab18, and that depletion of Rab18 was efficient under these conditions (Fig. 6 b). Measurements of the area occupied by CLIMP-63 indicated that ER sheet volumes increased from 30% of the cell area to 60–80% in cells depleted of Rab18 with either of the Rab18 3'UTR

Figure 4. Rab3GAP is required for ER localization of Rab18. (a) HeLa cells expressing GFP-Rab18 were depleted of Rab3GAP subunits (siGAP1 and siGAP2) for 72 h and then stained with a Rab3GAP1 antibody. The enlarged region from the yellow boxed area shows details of Rab18 localization. (b) The presence of GFP-Rab18 on ER tubules was scored for all conditions and plotted in the bar graph. Error bars indicate the standard deviation of the mean ($n = 3$ independent experiments). (c) HeLa cells were depleted of Rab3GAP subunits (GAP1 and GAP2) for 72 h. Western blots show the distribution of endogenous Rab18 to the membrane pellet (P) and soluble (S) cytosol fractions marked by the Golgi membrane protein GM130 and tubulin, respectively. Rab3GAP1 depletion was confirmed by Western blotting. (d) COS7 cells expressing a GFP-tagged ER marker and mCherry-tagged Rab18 were depleted of Rab3GAP subunits alone or in combination or Rab18 for 72 h then imaged at 1.5-s intervals using a spinning-disk confocal microscope. The entire cell is shown for $t = 0$, and a time series from the yellow boxed area is depicted in the enlarged regions. Bars are marked in the figure.



duplexes tested (Fig. 6 c, green bars). In both cases this effect was rescued by expression of GFP-Rab18 (Fig. 6 c, blue bars). Live-cell imaging of cells depleted of endogenous Rab18 using the Rab18.7 3'UTR duplex resulted in the loss of dynamic ER tubular networks and the expansion of less dynamic sheet areas, and this was reversed by expression of mCherry-Rab18 resistant to the siRNA (Fig. 6 d and Videos 6–8).

Rab10 has previously been implicated in the regulation of ER structure (English and Voeltz, 2013), and its relationship to Rab18 was therefore investigated. Rab10 was depleted efficiently (Fig. S3 a), but this resulted in only a partial spread of ER sheets to the cell periphery (Fig. 5, a and b). The localization of Rab10 and Rab18 was then compared in HeLa and COS7 cells. Whereas Rab18 targeted to ER tubular networks in both

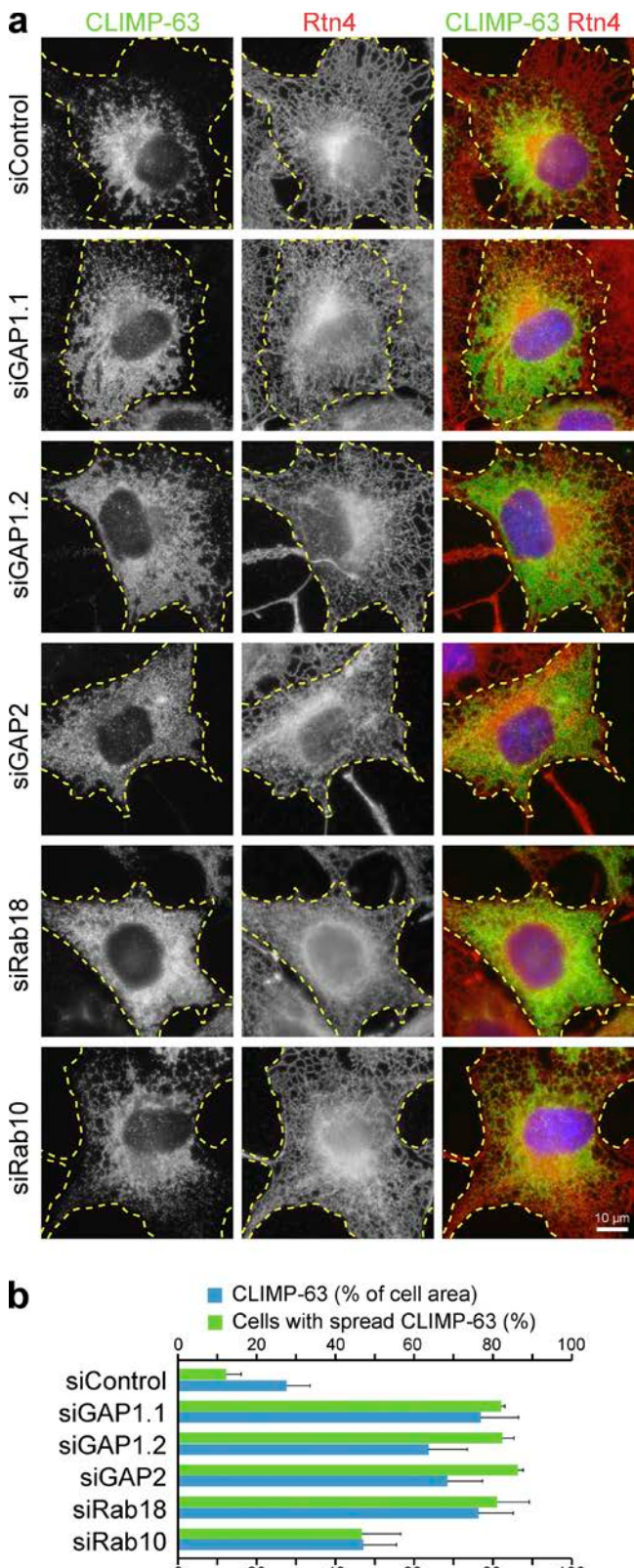


Figure 5. ER sheets spread into the cell periphery when Rab18 or its GEF complex is depleted. (a) COS7 cells were depleted of Rab3GAP subunits (GAP1 and GAP2), Rab18, or Rab10 for 72 h. Two different siRNA duplexes to Rab3GAP1 (GAP1.1 and GAP1.2) were used. The cells were fixed and then stained with antibodies to CLIMP-63 and reticulon 4 (Rtn4). DNA was stained with DAPI (blue in the merged panel). Dotted yellow lines mark the cell boundaries. The bar is marked in the figure. (b) The area

of CLIMP-63 as a function of total cell area was measured using ImageJ (National Institutes of Health) for 50–70 cells per experiment, for three independent experiments (blue bars). Additionally, the percentage of cells showing spread CLIMP-63 was also counted (green bars). In both cases the mean values are plotted in the bar graph, with error bars indicating the standard deviation of the mean.

Warburg Micro syndrome and ER shaping

To confirm that the ER defects observed in cell lines depleted of Rab18 and Rab3GAP complex subunits are relevant for the human disease, the localization of CLIMP-63 and Rtn4 was investigated in two patient cell lines. These cell lines carried either the Rab18 L24Q nucleotide-binding site mutation, or the Rab3GAP1 (c.649-2A>G) splicing mutation (Aligianis et al., 2005; Bem et al., 2011). In comparison to control fibroblasts, CLIMP-63 spread away from the perinuclear region into the cell periphery and clearly defined Rtn4-positive tubules were lost in both the Rab18 L24Q and Rab3GAP1 (c.649-2A>G) patient cell lines (Fig. 7 a). Measurements of the area occupied by CLIMP-63 indicated that ER sheet volumes increased from 20% of the cell area to 60–70% in cells with mutant Rab18 or Rab3GAP1 (Fig. 7 b). Spread of ER sheets and a loss of fragmentation of ER tubules were therefore observed in patient fibroblasts.

After the initial discovery of Rab3GAP and Rab18 mutations it was found that the ER transmembrane protein TBC1D20 is mutated in Warburg Micro syndrome and the blind sterile mouse (Liegel et al., 2013). TBC1D20 is a GAP for Rab1 and Rab2 with some limited activity toward Rab18 in vitro (Haas et al., 2007). TBC1D20 interacts with the reticulon family of ER-shaping proteins (Haas et al., 2007), and has been implicated in secretion (Wendler et al., 2010). The relationship between Rab3GAP complex and TBC1D20 in ER shaping was therefore investigated. As already shown, depletion of the Rab3GAP1 and Rab3GAP2 subunits resulted in the redistribution of Rab18 to the cytoplasm, the spread of the ER sheet marker CLIMP-63, and fragmentation of the peripheral ER tubular network defined by Rtn4 (Fig. 7 c). By contrast, depletion of TBC1D20 resulted in a slight spread of the ER sheets marked by CLIMP-63 (Fig. 7 c). In addition, alterations in the distribution of Rab18 to the peripheral ER reticular network were observed. Instead of precisely following the Rtn4-positive ER tubules as in the control samples, Rab18 spread across the fenestrations in the reticular network (Fig. 7 c). This created a hybrid webbed network in which fingers of Rtn4 are linked by sheets containing Rab18. Therefore, although loss of TBC1D20 function results in altered ER structure, the differences in the phenotype suggest it plays a different role to the Rab3GAP complex and Rab18.

of CLIMP-63 as a function of total cell area was measured using ImageJ (National Institutes of Health) for 50–70 cells per experiment, for three independent experiments (blue bars). Additionally, the percentage of cells showing spread CLIMP-63 was also counted (green bars). In both cases the mean values are plotted in the bar graph, with error bars indicating the standard deviation of the mean.

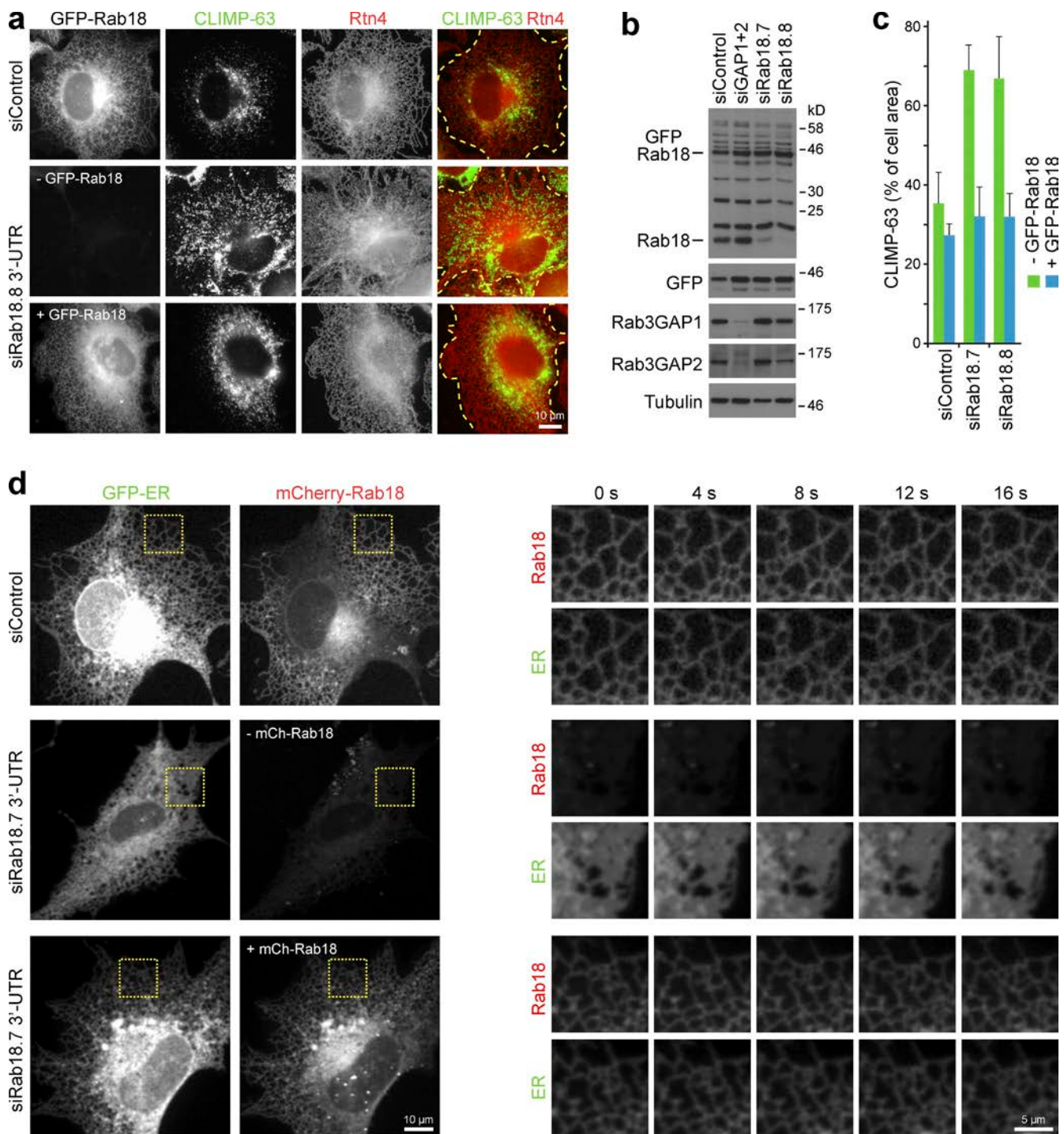


Figure 6. Loss of dynamic ER tubules in Rab18-depleted cells. (a) COS7 cells were treated with control or Rab18.8 3'-UTR siRNA for 52 h, then transfected with empty vector or GFP-Rab18 for 20 h. Cells were fixed and then stained with antibodies to CLIMP-63 and Rtn4. Dotted yellow lines mark the cell boundaries. (b) COS7 cells were treated with control, Rab3GAP (siGAP1+2), Rab18.7, or Rab18.8 3'-UTR siRNA for 52 h, then transfected with empty vector or GFP-Rab18 for 20 h. Cell lysates were Western blotted with antibodies to Rab18, GFP, Rab3GAP subunits, and tubulin as a loading control. Rab18 antibodies see multiple nonspecific bands; lines in the figure indicate endogenous Rab18 and GFP-Rab18. (c) The area of CLIMP-63 as a function of total cell area was measured using ImageJ for 40–60 cells per experiment, for three independent experiments. This was performed for cells expressing (blue bars) or not expressing (green bars) GFP-Rab18. Mean values are plotted in the bar graph, with error bars indicating the standard deviation of the mean. (d) COS7 cells expressing a GFP-ER marker were treated with control or Rab18.7 3'-UTR siRNA for 52 h, then transfected with empty vector or mCherry-Rab18 for 20 h. The cells were then imaged at 2-s intervals using a spinning-disk confocal microscope. The entire cell is shown for t = 0, and a time series showing images every 4 s from the yellow boxed area is depicted in the enlarged regions. Bars are marked in the figure.

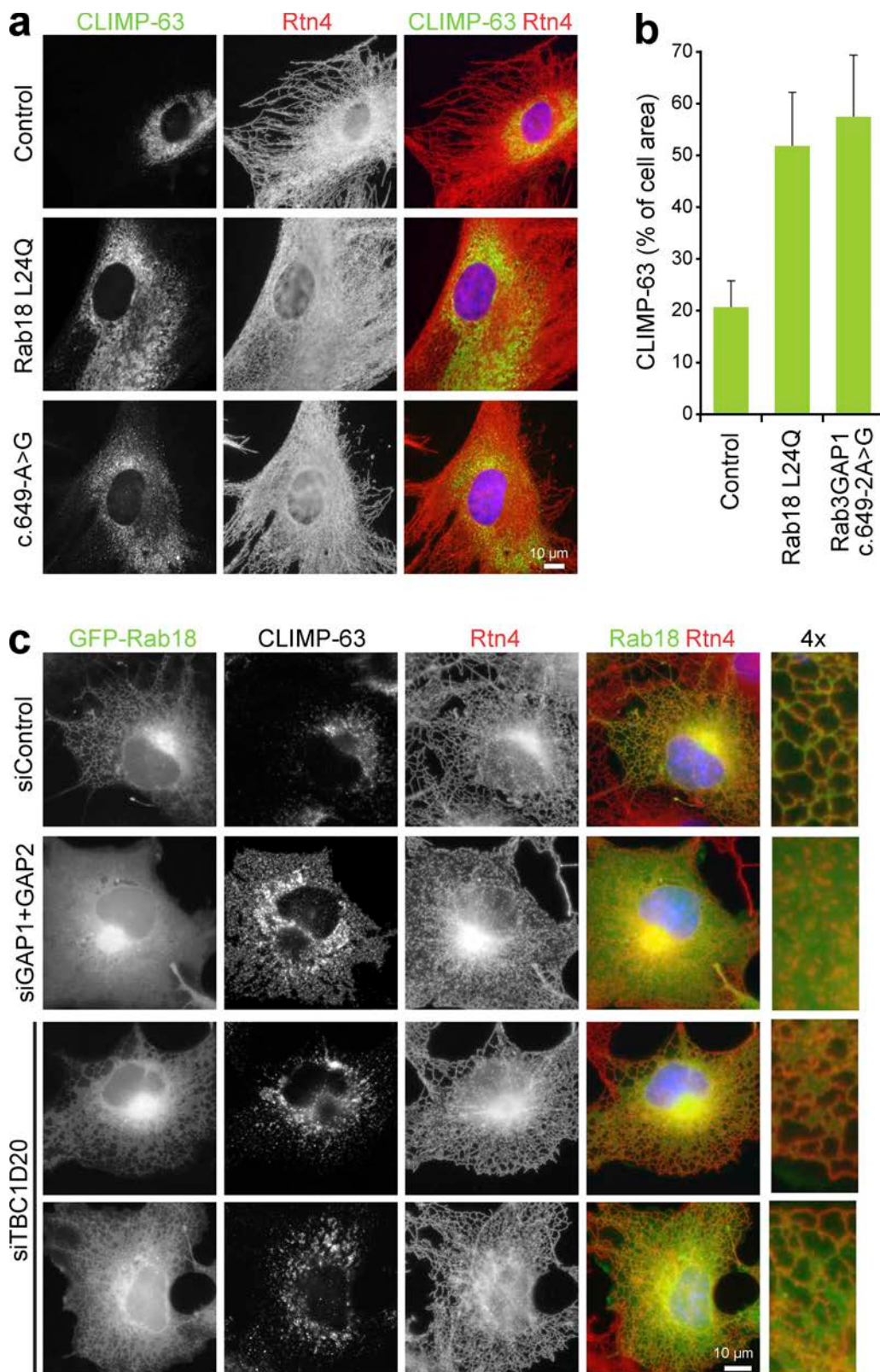


Figure 7. Warburg Micro syndrome patient cell lines show altered ER morphology. (a) Control and patient fibroblasts were fixed and then stained with antibodies to CLIMP-63 and reticulon 4 (Rtn4). DNA was stained with DAPI (blue in the merged panel). (b) The area of CLIMP-63 as a function of total cell area was measured using ImageJ for 50–70 cells per experiment, for three independent experiments. The mean values are plotted in the bar graph, with error bars indicating the standard deviation of the mean. (c) COS7 cells expressing GFP-Rab18 were treated with control, Rab3GAP (siGAP1+GAP2), or TBC1D20 siRNA duplexes for 72 h. The cells were fixed and then stained with antibodies to CLIMP-63 and Rtn4. DNA was stained with DAPI (blue in the merged panel). The merged panel shows a comparison of GFP-Rab18 and Rtn4 localization to ER tubular networks. Bars are marked in the figure.

Intriguingly, both TBC1D20 and Rab18 have been linked to ER-associated lipid droplet structures (Martin et al., 2005; Ozeki et al., 2005; Liegel et al., 2013; Salloum et al., 2013). To test if Rab3GAP, Rab18, and TBC1D20 play a general role in lipid droplet formation and turnover, cells were fed oleate–BSA complexes for 18 h to induce lipid droplet formation. These cells were then stained for ER markers CLIMP-63 and Rtn4, and lipid droplets were detected with BODIPY (Fig. S4 a). Western blotting confirmed efficient depletion of target proteins (Fig. S4 b). Compared with the control cells, BODIPY stained larger more intense structures clustered against the nucleus after depletion of Rab18 pathway components or TBC1D20 (Fig. S4 a), suggesting more lipid was stored. A time-course analysis of lipid storage and turnover revealed that after 18 h, cells depleted of Rab3GAP complex subunits, Rab18, or TBC1D20 showed twofold higher staining with BODIPY than control cells (Fig. S4 c). In all cases, after removal of oleate by transfer to fresh growth medium this signal declined at the same rate over the following 36 h (Fig. S4 d). Rab18, Rab3GAP, and TBC1D20 are therefore not essential for lipid droplet formation or turnover under these conditions. Furthermore, neither mCherry-tagged Rab18 nor the ER tubular network marker Rtn4 showed any obvious enrichment on lipid droplet structures (Fig. S5 a). Live-cell imaging showed that lipid droplets often lie adjacent to the ER tubular networks in control cells (Fig. S5 b) and move together with Rab18-positive ER tubular networks (Video 9). However, in cells depleted of Rab18 or the Rab3GAP complex, lipid droplets showed an increased rather than decreased association with ER sheets (Fig. S5 b). This change could potentially facilitate lipid storage without requiring a direct role for Rab18 or the Rab3GAP complex in lipid droplet biogenesis.

Discussion

Rab3GAP is a Rab18 GEF

Rab3GAP1 and Rab3GAP2 were originally isolated from bovine brain as subunits of a complex promoting GTP hydrolysis by Rab3 (Fukui et al., 1997; Nagano et al., 1998). This has led to the suggestion that a defect in neurotransmission resulting from altered Rab3 function contributes to Warburg Micro syndrome (Aligianis et al., 2005, 2006). As we show here, the Rab3GAP complex also has specific and potent Rab18 GEF activity. Supporting the view that Rab18 is the physiological target of Rab3GAP, the catalytic efficiency of $3.6 \times 10^4 \text{ M}^{-1}\text{s}^{-1}$ is equivalent to Rab GEFs with known targets (Langemeyer et al., 2014). In agreement with this idea, disease-associated mutations in Rab3GAP abolish this Rab18 GEF activity and cause a loss of Rab18 from the ER in fibroblast cell lines. The presence of Rab18 (Elias et al., 2012; Klöpper et al., 2012) and the Rab3GAP complex in a wide variety of eukaryotes lacking Rab3, including plants, also supports the view that the essential cellular function of this pathway is not the regulation of neurotransmission. Neurological dysfunction may therefore be caused by more fundamental cellular defects linked to perturbed ER function.

ER regulation by Rab GTPase pathways

The ER is organized into two morphologically discrete domains, the perinuclear ER sheets and peripheral tubular networks (Voeltz

and Prinz, 2007; Friedman and Voeltz, 2011). These domains are further specialized into functional regions, including the so-called ER exit sites where biosynthetic cargo transport occurs, sites where lipid droplets form, and contact sites with other cellular organelles such as mitochondria, endosomes, and the plasma membrane (Friedman and Voeltz, 2011; Rowland and Voeltz, 2012). However, in most cases an essential requirement for normal ER morphology in these processes remains unclear. A series of factors required for ER tubular network formation have been identified, and these can be divided into factors promoting ER tubule formation such as the reticulon, DP1 and REEP integral membrane protein family (Voeltz et al., 2006; Shibata et al., 2008; Park et al., 2010), and transmembrane GTPases of the atlastin family promoting ER tubule fusion to generate networks (Hu et al., 2009; Orso et al., 2009). Less is known about the mechanism of sheet formation, but the transmembrane protein CLIMP-63 is thought to localize to and stabilize ER sheets by acting as a luminal spacer (Klopfenstein et al., 2001; Shibata et al., 2010).

Rab GTPases can now be added to this emerging picture. In contrast to the factors already discussed, which are integral membrane proteins, Rabs are peripheral membrane proteins recruited from the cytosol thought to act as regulators of membrane fusion and organelle identity (Barr, 2013; Pfeffer, 2013). Rab10 is associated with ER networks and promotes ER tubule dynamics (English and Voeltz, 2013). In polarized cells, Rab10 and its cognate GEF DENND4/CRAG are required together with a transmembrane sorting receptor TANGO1 for the basolateral transport of collagen (Yoshimura et al., 2010; Lerner et al., 2013). This raises the intriguing possibility that polarized transport is already specified at the level of the ER. However, how Rab10 is activated at the ER and what its downstream effector proteins are remains unclear.

In this work we show that the Rab3GAP complex activates Rab18, and this is required for Rab18 recruitment to the ER. Further studies will be needed to define the downstream effector pathways coupling to Rab18, and it would be premature to specify what precise events Rab18 regulates. It may directly act in the pathway of lipid droplet biogenesis; however, details of effectors are crucial. The altered ER structure reported here suggests that Rab18 effectors may regulate ER tubule tethering and fusion, or perhaps act as inhibitors of ER sheet extension. Understanding the interplay between Rab18, Rab10, and tubular network-promoting factors of the reticulon and atlastin families will therefore be an important goal for future work.

Previous studies have implicated Rab18 in lipid droplet formation, and have reported that Rab18 is highly enriched on lipid droplets (Martin et al., 2005; Ozeki et al., 2005). However, these studies relied on high-level expression of Rab18 to induce alterations in lipid droplet apposition to ER membranes and Rab18 localization to lipid droplets (Martin et al., 2005; Ozeki et al., 2005). Under the conditions used here, where tagged Rab18 was expressed at levels similar to the endogenous protein, Rab18 was found on tubular networks forming the ER and was not enriched on lipid droplets. Lipid storage was increased twofold after 18 h in cells depleted of Rab18 or its GEF, suggesting there is a link between Rab18 function and lipid droplets.

However, there was also increased association of ER sheets with lipid droplets in Rab18- or Rab18 GEF-depleted cells. One possibility is that this could facilitate lipid storage without requiring a direct role for Rab18 or its GEF complex.

Relationship of ER-shaping factors and human disease

A sobering feature of the proteins associated with ER network formation is their mutation in a spectrum of human neurological disorders (Blackstone, 2012). Atlastins, spastin, reticulon 2, REEP1, and REEP2 are all mutated in hereditary spastic paraplegia (Hazan et al., 1999; Park et al., 2010; Montenegro et al., 2012; Fink, 2013; Esteves et al., 2014), whereas Rab18 and the Rab3GAP1 and Rab3GAP2 subunits are mutated in Warburg Micro syndrome (Aligianis et al., 2005, 2006; Bem et al., 2011; Handley and Aligianis, 2012; Handley et al., 2013). In each case, these diseases are associated with progressive ascending spasticity. Other evidence supports the idea that Warburg Micro syndrome and hereditary spastic paraplegias (HSPs) should be considered as related disorders. A combination of mouse and human genetics has shown that the ER transmembrane protein TBC1D20 is mutated in Warburg Micro syndrome and the blind sterile mouse (Liegel et al., 2013). This is notable because TBC1D20 is a GAP for Rab1 and Rab2, and interacts with the reticulon family of proteins in the ER (Haas et al., 2007). TBC1D20 therefore provides a link between Warburg Micro syndrome and the reticulon family of ER-shaping proteins mutated in some hereditary spastic paraplegias. Other evidence linking HSPs and Warburg Micro syndrome is provided by the identification of Rab3GAP2 mutations in corticospinal motor neuron disease (Novarino et al., 2014), an autosomal-recessive HSP. This correlation between altered ER structure and neurological disorders is intriguing, and provides further support for the view that ER form and function are closely linked. As already mentioned, diverse cellular processes are associated with the ER, and explaining the dependencies on structural organization will be a complex task requiring the generation of specific experimental models to look at ER structure–function relationships in neuronal cells and during development.

Materials and methods

Reagents and antibodies

General laboratory chemicals were obtained from Sigma-Aldrich and Thermo Fisher Scientific. Duplexes for Rab18, Rab3GAP1, and Rab3GAP2 siRNA were obtained from Thermo Fisher Scientific and the sequences are listed in Table S1. A luciferase duplex was used as a control in all siRNA experiments. Commercially available antibodies were used to α -tubulin (mouse DM1A; Sigma-Aldrich), Myc-epitope (mouse clone 9E10; Sigma-Aldrich), FLAG-epitope (mouse monoclonal M2; Sigma-Aldrich), Rab7 (rabbit clone D95F2; Cell Signaling Technology), Rab10 (rabbit D36C4; Cell Signaling Technology), Rab18 (mouse 60057 and rabbit polyclonal; ProteinTech), Rab3GAP1 (rabbit 21663; ProteinTech), Rab3GAP2 (rabbit NBP1-84199; Novus Biologicals), GM130 (mouse clone 35; BD), β -COP (mouse G6160; Sigma-Aldrich), Sec31 (mouse clone 32; BD), TGN46 (sheep; AbD Serotec), LMAN1/ERGIC-53 (mouse 1A8; Novus Biologicals), calnexin (rabbit 10427; ProteinTech), ERp72 (rabbit clone D70D12; Cell Signaling Technology), PDI (rabbit clone C81H6; Cell Signaling Technology), GPR78/BiP (rabbit ab21685; Abcam), EEA1 (mouse clone 14; BD), LAMP1 (mouse clone H4A3; BD), NOGOA/Rtn4 (rabbit; AbD Serotec), and CLIMP-63 (mouse; Enzo Life Sciences). Affinity-purified sheep

anti-GFP polyclonal was made previously by us. Secondary antibodies raised in donkey to mouse, rabbit, sheep/goat, and human conjugated to HRP, Alexa 488, -555, -568, and -647 were obtained from Molecular Probes and Jackson ImmunoResearch Laboratories, Inc.

Molecular biology and Rab protein expression

Human Rab GTPases were amplified using PCR from human testis, fetus, and liver cDNA and cloned into pFAT2 for bacterial expression or pGFP-C2 for eukaryotic expression of GFP-tagged Rabs (Fuchs et al., 2007; Yoshimura et al., 2010). Human Rab3GAP1 and Rab3GAP2 were amplified by PCR from human testis cDNA. Point mutations were introduced using the QuikChange method. Mammalian expression constructs were made using pcDNA4/TO and pcDNA5/FRT/TO vectors (Invitrogen). Mitochondrial targeted Rab3GAP was created in pcDNA5 by fusing the mitochondrial outer membrane targeting sequence of yeast Tom70p and three copies of the FLAG epitope sequence to the 5-prime end of the Rab3GAP1 or Rab3GAP2 cDNA. Rab proteins in pFAT2 were expressed in BL21 (DE3) pRIL at 18°C for 12–14 h. Cell pellets were disrupted in 20 ml IMAC20 (20 mM Tris-HCl, pH 8.0, 300 mM NaCl, 20 mM imidazole, and protease inhibitor cocktail; Roche) using an Emulsiflex C-5 system (Avestin, Inc.). lysates were clarified by centrifugation at 16,000 rpm in a rotor (model JA-17; Beckman Coulter) for 30 min. To purify the tagged protein, 0.5 ml of nickel-charged NTA-agarose (QIAGEN) was added to the clarified lysate and rotated for 2 h. The agarose was washed three times with IMAC20 and the bound proteins eluted in IMAC200 (IMAC20 with 200 mM imidazole) collecting 1.5-ml fractions. All manipulations were performed on ice or in an 8°C cold room. Purified proteins were dialyzed against TBS (50 mM Tris-HCl, pH 7.4, and 150 mM NaCl) and then snap-frozen in liquid nitrogen for storage at –80°C. Protein concentration was measured using the Bradford assay.

Cell culture

Patient cell lines, HeLa, HEK293, and COS7 cells were cultured in DMEM containing 10% bovine calf serum (Invitrogen) at 37°C and 5% CO₂. For plasmid and siRNA transfection Mirus LT1 (Mirus Bio LLC) and Oligofectamine (Invitrogen), respectively, were used according to the manufacturer's instructions. For RNA interference experiments HeLa cells were plated at 18,000 cells per well and COS7 cells at 8,000 cells per well of a 6-well plate, respectively.

Purification of GEF complexes

FLAG- and Myc-tagged forms of Rab3GAP1 and Rab3GAP2 were transiently expressed in 8 × 15-cm dishes of 70% confluent HEK293T cells. For this purpose 800 μ l OptiMEM (Invitrogen) was mixed with 24 μ l Mirus LT1, and after 5 min 6 μ g of each plasmid DNA was added. After 25 min this transfection mix was added to the cells. After 40 h of growth the cell pellet was lysed for 20 min on ice in 5 ml cell lysis buffer (50 mM Tris-HCl, pH 7.4, 1 mM EDTA, 150 mM NaCl, 0.5% [vol/vol] Triton-X 100, and protease inhibitor cocktail). Cell extracts were split into 1-ml aliquots and clarified by centrifugation at 20,000 g in a microfuge (model 5417R; Eppendorf) for 20 min. The FLAG-tagged proteins were isolated from the clarified cell lysate using 100 μ l anti-FLAG M2 affinity gel (Sigma-Aldrich) for 4 h at 4°C. The beads were washed ten times with 1 ml of cell lysis buffer, high salt buffer (50 mM Tris-HCl, pH 7.4, and 500 mM NaCl), and TBS, and then the proteins were eluted with 100 μ l (200 μ g/ml) FLAG-peptide in TBS containing 2 mM dithiothreitol. Eluted proteins were analyzed on 7.5–10% SDS-PAGE gels stained with Coomassie brilliant blue, and concentrations estimated by comparison to a series of bovine serum albumin standards in the range of 0.1 mg to 1 mg. The peak fractions were snap-frozen in liquid nitrogen for storage at –80°C without dialysis.

Nucleotide binding and Rab GEF screening

GEF assays were performed as described previously (Yoshimura et al., 2010). Nucleotide loading was performed as follows: 10 μ g GST-tagged Rab was incubated in 50 mM Hepes-NaOH, pH 6.8, 0.1 mg/ml BSA, 125 μ M EDTA, 10 μ M Mg-GDP, and 5 μ Ci [³H]-GDP (10 mCi/ml; 5,000 Ci/mmol) in a total volume of 200 μ l for 20 min at 4°C. For standard GDP-releasing GEF assays, 100 μ l of the loading reaction was mixed with 10 μ l (10 mM) Mg-GTP, 10–100 nM GEF, or a buffer control, and adjusted with assay buffer to a final volume of 120 μ l. The GEF reaction occurred for 20 min at 30°C. After this, 2.5 μ l were taken for a specific activity measurement, and the remainder was split into two tubes, then incubated with 500 μ l ice-cold assay buffer containing 1 mM MgCl₂ and 20 μ l packed glutathione-Sepharose for 60 min at 4°C. After three washes with 500 μ l ice-cold assay buffer the Sepharose was transferred to a vial containing

4 ml scintillation fluid and counted. The amount of nucleotide exchange was calculated in pmoles GDP-released. For GTP-binding assays the following modifications were made: only unlabeled GDP was used in the loading reaction; in the GEF reaction 0.5 μ l (10 mM) GTP and 1 μ Ci [³⁵S]-GTPyS (10 mCi/ml; 5,000 Ci/mmol) were used. The amount of nucleotide exchange was calculated in pmoles GTP-bound.

Kinetic analysis of GEF activity

First, 10 nmol of hexahistidine-GST-Rab was loaded with 2'-(3')-bis-O-(N-methylanthranoyl)-GDP (Mant-GDP; Jena Bioscience) in 20 mM Hepes, pH 6.8, 1 mg/ml BSA, 20 mM EDTA, pH 8.0, and 40 mM Mant-GDP at 30°C for 30 min. After loading, 25 mmol MgCl₂ was added and the sample was exchanged into reaction buffer (20 mM Hepes, pH 6.8, 1 mg/ml BSA, 150 mM NaCl, and 1 mM MgCl₂) using Zeba spin columns (Thermo Fisher Scientific). Nucleotide exchange was measured using 1 nmol of the loaded Rab and the amount of GEF was specified in the figure legends in a final volume of 100 μ l reaction buffer by monitoring the quenching of fluorescence after release of Mant-GDP using a Tristar LB 941 plate reader (Berthold Technologies) under control of MikroWin software. Samples were excited at 350 nm and emission monitored at 440 nm. GTP was added to a final concentration of 0.1 mM to start the exchange reaction at 30°C. Curve fitting and extraction of pseudo first-order rate constants (k_{obs}) was performed as described previously (Delprato et al., 2004; Delprato and Lambright, 2007). Because $k_{obs} = (k_{cat}/K_m) [GEF] + k_{basal}$, where k_{basal} is the rate constant measured in the absence of GEF, catalytic efficiency (k_{cat}/K_m) can be obtained.

Rab GAP assays

For Rab-loading reactions, 10 μ l of assay buffer, 73 μ l H₂O, 10 μ l (10 mM) EDTA, pH 8.0, 5 μ l of 1 mM GTP, 2 μ l γ -[³²P]GTP (10 mCi/ml; 5,000 Ci/mmol; ICN), and 100 pmol Rab protein were mixed on ice. GAP reactions were started by the addition of 0.5 pmol Rab3GAP1 mixed with 5.0 pmol Rab3GAP2 or buffer as specified in the figures. A 2.5- μ l aliquot of the assay mix was scintillation counted to measure the specific activity in cpm/pmol GTP. Reactions were then incubated at 30°C for 60 min. The 5- μ l aliquots were immediately added to 795 μ l of ice-cold 5% (wt/vol) activated charcoal slurry in 50 mM NaH₂PO₄, left for 1 h on ice, and centrifuged at 16,100 g in a benchtop microfuge (model 5417R; Eppendorf) to pellet the charcoal. A 400- μ l aliquot of the supernatant was scintillation counted, and the amount of GTP hydrolyzed was calculated from the specific activity of the reaction mixture.

MitoGEF assays

For MitoGEF assays, HeLa cells were seeded on no. 1.5 glass coverslips (Menzel-Gläser; Thermo Fisher Scientific) at a density of 30,000 cells per well on a 12-well plate, and then left for 30 h to adhere. The cells were transfected with 0.25 μ g of mitochondrial-targeted Tom70-3xFLAG-Rab3GAP2, Myc-Rab3GAP1, and GFP-tagged Rab GTPases in combination using 1.5 μ l Mirus LT1 in 50 μ l OptiMEM. After 20 h the cells were processed for microscopy.

Membrane fractionations

For membrane fractionation the cells were washed from the dish in PBS containing 1 mM EDTA, then homogenized using 20 passes through an 18-gauge needle in 50 mM Hepes-NaOH, pH 7.4, and 200 mM sucrose. Unbroken cells were removed by centrifugation at 1,000 g for 10 min in a microfuge. A membrane pellet and cytosol were prepared from this post-nuclear supernatant by centrifugation at 100,000 g for 60 min in a rotor (model TLA-100; Beckman Coulter). Equivalent proportions of the membrane pellet and cytosol were analyzed by Western blotting.

Fixed-cell and live-cell microscopy

For fixed-cell imaging, cells were grown on no. 1.5 glass coverslips, washed twice with 2 ml of PBS, and fixed for 2 h in 2 ml PLP (2% [wt/vol] paraformaldehyde in 87.5 mM lysine, 87.5 mM sodium phosphate, pH 7.4, and 10 mM sodium periodate). Coverslips were washed three times in 2 ml (100 mM) sodium phosphate, pH 7.4, before permeabilization in 1 mg/ml BSA, 0.12 mg/ml saponin, and 100 mM sodium phosphate, pH 7.4, for 30 min. In all cases primary and secondary antibody staining was performed in PBS for 60 min at room temperature. Affinity-purified antibodies were used at 1 μ g/ml; commercial antibodies were used as directed by the manufacturers. DAPI was added to the secondary antibody staining solution at 0.3 μ g/ml. Coverslips were mounted in Mowiol 4-88 mounting medium (EMD Millipore). Fixed samples on glass slides were imaged using a 60 \times /1.35 NA oil immersion objective on an upright microscope (model

BX61; Olympus) with filtersets for DAPI, GFP/Alexa 488, -555, -568, and -647 (Chroma Technology Corp.), a camera (CoolSNAP HQ²; Roper Scientific), and MetaMorph 7.5 imaging software (Molecular Dynamics Inc.). Illumination was provided by a Lumen 200-Watt metal halide light source (Prior Scientific, Inc.). Image stacks of 12–35 planes with a spacing of 0.2–0.4 μ m through the cell volume were taken. Image stacks were maximum intensity projected and then merged to create 24-bit RGB TIFF files in MetaMorph. Images in 24-bit RGB format were then cropped in Photoshop CS3 and placed into Illustrator CS3 (Adobe Systems Inc.) to produce the figures.

For live-cell imaging using spinning-disk confocal microscopy, cells were plated in 35-mm dishes with a 14-mm no. 1.5 coverglass window in the bottom (MatTek Corporation). For imaging, the dishes were placed in a 37°C and 5% CO₂ environment chamber (Tokai Hit) on the microscope stage. Imaging was performed at 37°C in 5% CO₂ using an inverted microscope (model IX81; Olympus) with a 60 \times /1.42 NA oil immersion objective coupled to an Ultraview Vox spinning-disk confocal system (PerkinElmer) fitted with an EM-CCD camera (model C9100-13; Hamamatsu Photonics). Exposure times were 50 ms using 6% laser power. Image stacks of six planes spaced 0.2 μ m apart were taken at the time intervals shown in the figure for up to 1 h. A bright-field reference image was also taken to visualize cell shape. Maximum intensity projection of the fluorescent channels was performed in Velocity (PerkinElmer) to create 24-bit RGB TIFF files. Images in 24-bit RGB TIFF format were then placed into Adobe Illustrator CS3 to produce the figures.

Lipid storage assays

Oleate-BSA complexes were formed by incubating 2.1 mM fatty acid-free bovine serum albumin with 12.3 mM oleic acid in 100 mM Tris-HCl, pH 8.0, at 22°C for 5 h. Oleate-BSA stock solution was sterilized by passage through a 0.2- μ m filter and stored at –20°C in small aliquots. To induce lipid droplet formation, cells were incubated with 400 μ M oleate in DME containing 10% bovine calf serum for 18 h. For experiments where lipid droplet turnover was studied, cells were then washed three times in fresh growth medium and then grown for a further 12–36 h. The cells were then fixed with PLP and processed using the standard immunofluorescence protocol described already. Lipid droplets were detected with 1 μ g/ml BODIPY 493/503 (4,4-difluoro-1,3,5,7,8-pentamethyl-4-bora-3a,4a-diaza-s-indacene; Molecular Probes) added to the secondary antibody-staining step.

Online supplemental material

Fig. S1 shows the biochemical analysis of Rab3GAP1 specificity and confirms depletion of the Rab18 and Rab3GAP complex using specific antibodies. Fig. S2 shows the effects of Rab18 and Rab3GAP depletion and additional ER and Golgi markers. Fig. S3 compares the localization of Rab18 and Rab10 to the ER in HeLa and COS7 cells. Figs. S4 and S5 show lipid storage dynamics in cells depleted of Rab18, Rab3GAP complex, or TBC1D20. Videos 1–5 show ER and Rab18 dynamics in control and Rab3GAP- and Rab18-depleted cells. Videos 6–8 show the rescue of ER tubular network dynamics by re-expressing mCherry-Rab18 in cells depleted of endogenous Rab18. Video 9 shows a comparison of lipid droplet and Rab18 dynamics on the ER. Table S1 contains details of the sequences used for RNA interference. Online supplemental material is available at <http://www.jcb.org/cgi/content/full/jcb.201403026/DC1>.

A Wellcome Senior Investigator Award (097769/Z/11/Z) to F.A. Barr supported this work. M.T. Handley and I. Aligianis were supported by the Newlife foundation for disabled children (07-08/12) and the MRC (RA1631 and RA1905).

The authors declare no competing financial interests.

Submitted: 7 March 2014

Accepted: 15 April 2014

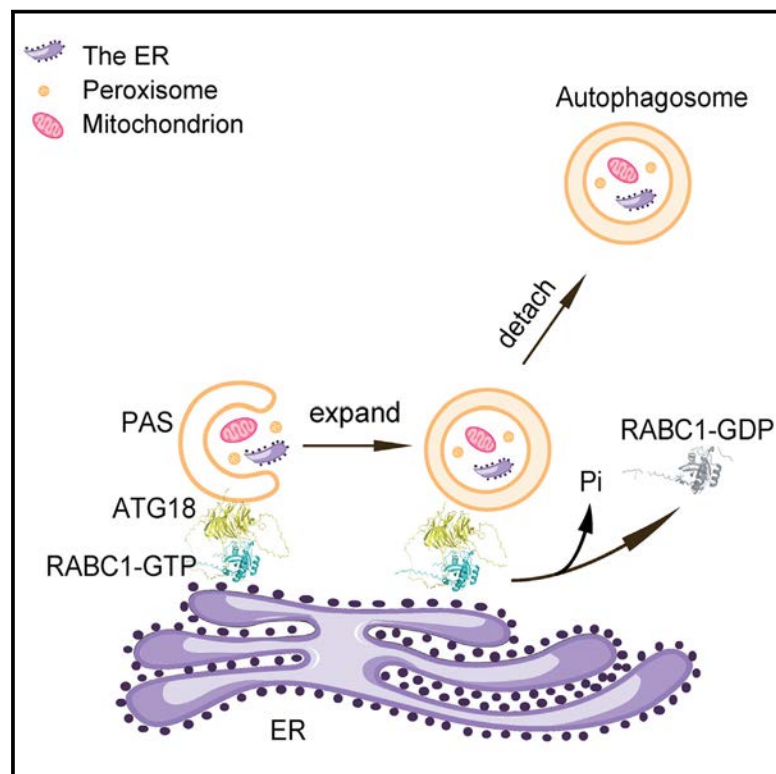
References

- Aligianis, I.A., C.A. Johnson, P. Gissen, D. Chen, D. Hampshire, K. Hoffmann, E.N. Maina, N.V. Morgan, L. Tee, J. Morton, et al. 2005. Mutations of the catalytic subunit of RAB3GAP cause Warburg Micro syndrome. *Nat. Genet.* 37:221–223. <http://dx.doi.org/10.1038/ng1517>
- Aligianis, I.A., N.V. Morgan, M. Mione, C.A. Johnson, E. Rosser, R.C. Hennekam, G. Adams, R.C. Trembath, D.T. Pilz, N. Stoodley, et al. 2006. Mutation in Rab3 GTPase-activating protein (RAB3GAP) noncatalytic subunit in a kindred with Martsolf syndrome. *Am. J. Hum. Genet.* 78:702–707. <http://dx.doi.org/10.1086/502681>

Developmental Cell

An Arabidopsis Rab18 GTPase promotes autophagy by tethering ATG18a to the ER in response to nutrient starvation

Graphical abstract



Authors

Jiaqi Sun, Yang Shao,
Songyang Wang, ..., Pierre Leroy,
Chengyang Li, Huanquan Zheng

Correspondence

jiaqi.sun@sdu.edu.cn (J.S.),
hugo.zheng@mcgill.ca (H.Z.)

In brief

The regulation of autophagy in plant response to stresses is not well defined. Sun and Shao et al. have found that RABC1, an Arabidopsis Rab18, interacts with and recruits ATG18a to the ER to facilitate autophagosome expansion on the ER in plant response to nutrient starvation.

Highlights

- In *rabc1* mutant cells, autophagy is compromised under nutrient starvation
- RABC1 plays a role in autophagosome expansion in response to nutrient starvation
- Active RABC1 specifically interacts with ATG18a
- RABC1 regulates ER association of ATG18a and its subsequent detachment from the ER

Article

An Arabidopsis Rab18 GTPase promotes autophagy by tethering ATG18a to the ER in response to nutrient starvation

Jiaqi Sun,^{1,2,4,*} Yang Shao,^{1,4} Songyang Wang,¹ Xunzheng Li,¹ Shuqing Feng,¹ Weinan Wang,² Pierre Leroy,² Chengyang Li,³ and Huanquan Zheng^{2,5,*}

¹Key Laboratory of Plant Development and Environmental Adaptation Biology, Ministry of Education, School of Life Sciences, Shandong University, Qingdao 266237, Shandong, China

²Department of Biology, McGill University, Montreal, QC H3B 1A1, Canada

³Key Laboratory of Horticultural Plant Biology, Ministry of Education, Huazhong Agricultural University, Wuhan 430070, Hubei, China

⁴These authors contributed equally

⁵Lead contact

*Correspondence: jiaqi.sun@sdu.edu.cn (J.S.), hugo.zheng@mcgill.ca (H.Z.)

<https://doi.org/10.1016/j.devcel.2023.11.006>

SUMMARY

The expansion of autophagosomes requires a controlled association with the endoplasmic reticulum (ER). However, the mechanisms governing this process are not well defined. In plants, ATG18a plays a key role in autophagosome formation in response to stress, yet the factors regulating the process are unknown. This study finds that ATG18a acts as a downstream effector of RABC1, a member of the poorly characterized Rab18/RabC GTPase subclass in plants. Active RABC1 interacts with ATG18a on the ER, particularly under nutrient starvation. In *rabc1* mutants, autophagy is compromised, especially under nutrient deprivation, affecting the ER association and expansion of ATG18a-positive autophagosomes. Furthermore, both dominant-negative and constitutively active RABC1 forms inhibit autophagy. The dominant inactive RABC1 impedes the ER association of ATG18a, whereas the constitutively active RABC1 delays ATG18a detachment from the ER. Collectively, RABC1 regulates the ER association and the subsequent detachment of ATG18a-positive autophagosomes during nutrient starvation.

INTRODUCTION

Rab GTPases constitute the largest family of Ras-like small GTPases in eukaryotic cells. They are the master regulators of various membrane trafficking pathways in the endomembrane system. Rab GTPases function as molecular switches mainly in the tethering of transport vesicles to the targeting membranes but are also involved in the formation, transport, docking, and fusion of transport vesicles during membrane trafficking.¹ A Rab GTPase cycles between inactive guanosine diphosphate (GDP)-bound form and active guanosine triphosphate (GTP)-bound form through the exchange of GTP and GDP via interactions with Rab GEFs (guanine nucleotide exchange factors) and Rab GAPs (GTPase activating proteins).² In the active GTP-bound form, Rab GTPases recruit their downstream effectors to coordinate membrane trafficking. Once the action is completed, the active GTP-bound form switches to the GDP-bound form; therefore, its activity is turned off.

In Arabidopsis, at least 57 Rab GTPases have been identified, which are divided into 8 distinct clades—RabA to RabH.^{1,3} The primary functions of most clades of Arabidopsis Rab GTPases in membrane trafficking have been defined in plant development, hormone signaling, cell-wall biosynthesis, and stress re-

sponses,^{1,4,5} except for the RabC clade, whose functions remain elusive. In Arabidopsis, there are 3 RabCs—RABC1, RABC2a, and RABC2b.³ RabCs are homologs of mammalian Rab18.³ Mammalian Rab18 is found in a wide range of tissues and cell lines in mouse.⁶ Solid evidence now exists that Rab18 plays a crucial role in animal and human development, yet the exact molecular roles Rab18 plays are still not well defined owing to the complicated subcellular localizations revealed in different cell types.⁷ Studies over the past 30 years have provided evidence that Rab18 plays a role in endocytic transport in polarized epithelial cells,⁸ in endoplasmic reticulum (ER)-Golgi transport,⁹ in the morphology of the ER,¹⁰ lipid droplets (LD),¹¹ and most recently in autophagy by promoting autolysosome maturation.¹²

Autophagy is a conserved cellular process for the continuous renovation of cytoplasmic components through the degradation of damaged/dysfunctional components/organelles either under basal condition or in response to external stress.¹³ For instance, the damaged/dysfunctional ER can be targeted by selective autophagy for degradation, a process termed ER-phagy.^{14–16} In plants, numerous stresses, including carbon starvation, salt stress, and ER stress, can induce ER-phagy.^{17,18} In autophagy, damaged/dysfunctional components/organelles, including the ER (cargo), are encased in the autophagosome, a double-membrane

structure generated by a series of dedicated processes, including the initiation, expansion, and closure of a cup-shaped membrane. Autophagosomes are then matured and fused to lysosome/vacuole for cargo degradation.^{19,20} The regulation of autophagy is highly conserved in eukaryotic cells, and more than 40 conserved autophagy-related (ATG) proteins have been identified.^{21,22} For example, the Atg1 kinase promotes the nucleation of autophagosomes. Atg8, a ubiquitin-like protein, is crucial for the expansion of autophagosomes, which requires the action of the Atg5-Atg12-Atg16 E3-like ligase complex.^{13,23,24} There is a complex interplay between the autophagosome expansion and the ER. The ER serves as a membrane source for the autophagosome expansion.²⁵ In mammalian cells, Atg18 plays a role in the tethering of autophagosomes to the ER.²⁶ Yet, how the activity of Atg18 is modulated is not known. In plants, ATG18 is crucial for autophagy, including ER-phagy in plant responses to nutrient deficiency, salt stress, oxidative stress, ER stress, and drought.^{27–30} ATG18a has a phospholipid binding ability that is important for the growth of autophagosomes,³¹ yet it is not known if plant ATG18 associates with the ER for the expansion of autophagosomes.

A recent study in plants has suggested an interesting role of RABC1 in stomatal development.³² It is reported that when plants are treated oleic acid, an LD inducer, RABC1 in guard cells momentarily relocates to the surface of LDs. The absence of RABC1 leads to a deficiency in LD mobilization in guard cells when treated with oleic acid. Given that RABC1 is ubiquitously expressed in plant tissues,³³ it is possible that RABC1 performs additional functions in plants. We reported here that RABC1 plays a role in plant response to nutrient (carbon and nitrogen) starvation during seedling growth. We revealed that RABC1 is localized to the ER and autophagosomes. It promotes autophagy in plant response to nutrient starvation but not under ER stress. We demonstrated that Arabidopsis ATG18a is associated with the ER. Active RABC1 specifically interacts with ATG18a and promotes the association of ATG18a to the ER and therefore the expansion of ATG18a-positive autophagosomes in autophagy.

RESULTS

***rabc1* mutant is hypersensitive to nutrient starvation but not ER stress**

In order to determine what function RABC1 might have in plants, we first identified an intron transfer DNA (T-DNA) insertional *rabc1* line (SALK_012129) (Figure S1A), which exhibited a significantly reduced expression of the *RABC1* gene (Figure S1B). It is worth noting that the same Salk line was reported as a knockout line.³² The *RABC1* gene is expressed ubiquitously in various tissues³³ (Figures S1C and S1D). We found that, in comparison with wild type (WT), *rabc1* only displayed a subtle growth defect during seedling growth under normal conditions on 1/2 Murashige Skoog (MS) medium containing 1% sucrose (Figure 1A). However, under the carbon starvation condition on 1/2 MS medium without sucrose supply, the growth of *rabc1* seedlings was significantly affected (Figure 1A). There were ~50% of seedlings that turned yellow or died (Figures 1A and 1B). Moreover, we conducted a transient carbon starvation experiment involving 5-day-old seedlings grown on 1/2 MS medium supplemented with sucrose, which were subsequently transferred to 1/2 MS medium devoid of sucrose and kept in darkness. Compared with WT seedlings, *rabc1* mutant

seedlings displayed a notable yellowing phenotype within 10 days (Figures 1C and S1F). Additionally, upon transferring normal-grown seedlings to nitrogen-deficient 1/2 MS medium, *rabc1* mutant seedlings exhibited a brownness phenotype resembling that of *atg5-1* mutant seedlings, which was in contrast to the appearance of WT seedlings (Figure 1C). Expression of YFP-RABC1 under either the native or the 35S promoter in the *rabc1* mutant rescued the growth defect of *rabc1* on the 1/2 MS medium without sucrose or under the transient carbon starvation treatment (Figures 1A, 1B, S1E, and S1F). We then conducted an investigation into the expression level of *RABC1* during carbon starvation. We revealed a transient upregulation of the *RABC1* expression within 4 to 12 h, followed by a decline after 24 h (Figure S1G). Interestingly, we found that, although *atg5-1* was hypersensitive to dithiothreitol (DTT) (ER stress inducer) treatment, *rabc1* showed no obvious difference from WT when treated with DTT (Figures 1D and 1E), suggesting that RABC1 has a specific role in plant response to nutrient (carbon and nitrogen) starvation but not to ER stress.

RABC1 is localized to the ER, Golgi, and autophagy compartments

In order to comprehend the cellular basis of the function of RABC1 in the plant response to nutrient starvation, we investigated the subcellular localization of RABC1 in the rescued *rabc1* lines expressing YFP-RABC1. In addition to being found in the cytoplasm (Figure 2A), YFP-RABC1 was also partially targeted to the ER indicated by mCherry-HDEL (Figure 2A, arrows). Additionally, RABC1 was noticeable in a number of punctae, using mCherry-ATG8e as a marker, we found that some of RABC1 punctae, especially those in the cytoplasmic region of cells, were localized to autophagosomes (Figure 2B, arrows), and some of them were localized to ATG18a-positive autophagosomes (Figure 2C, arrows). In addition, some of punctae, especially those relatively large ones, were co-localized with ST (sialyltransferase)-RFP (Figure 2D), A Golgi marker. When transiently expressed in *N. benthamiana* leaves, YFP-RABC1 distributed similarly to YFP-RABC1 in rescued *rabc1* (Figures S2A–S2C). They were co-localized with the ER (Figure S2A, arrows), some punctae were co-localized with autophagosomes (Figure S2B, arrows), and some were co-localized with Golgi (Figure S2C, arrows) marked by ST-RFP. However, none of them were co-localized with Mito-mCherry (mitochondria) (Figure S2D) or PX-mCherry (peroxisome) (Figure S2E).

RABC1 promotes autophagic flux

Next, we investigated the potential cellular function of RABC1 by the classic dominant-negative (SN)/constitutively active (QL) approach.³⁴ In the dominant-negative approach, a Rab is locked in GDP-binding state, which strongly binds and thus interferes with the action of its GEF(s). In the constitutively active approach, a Rab is locked in GTP-binding form, which exhibits sustained/unregulated activation, thus also allowing researchers to investigate the function of a Rab on cellular processes.¹ Because RABC1 is targeted to the ER and Golgi, we first wondered whether RABC1 is involved in ER-Golgi trafficking. When ST-RFP was co-expressed with YFP-RABC1(S27N), a dominant-negative form of RABC1, and YFP-RABC1(Q71L), a constitutively active form of RABC1, Golgi targeting of ST-RFP was not affected (Figures S2F and S2G), suggesting that RABC1 does not play a role in

Developmental Cell

Article

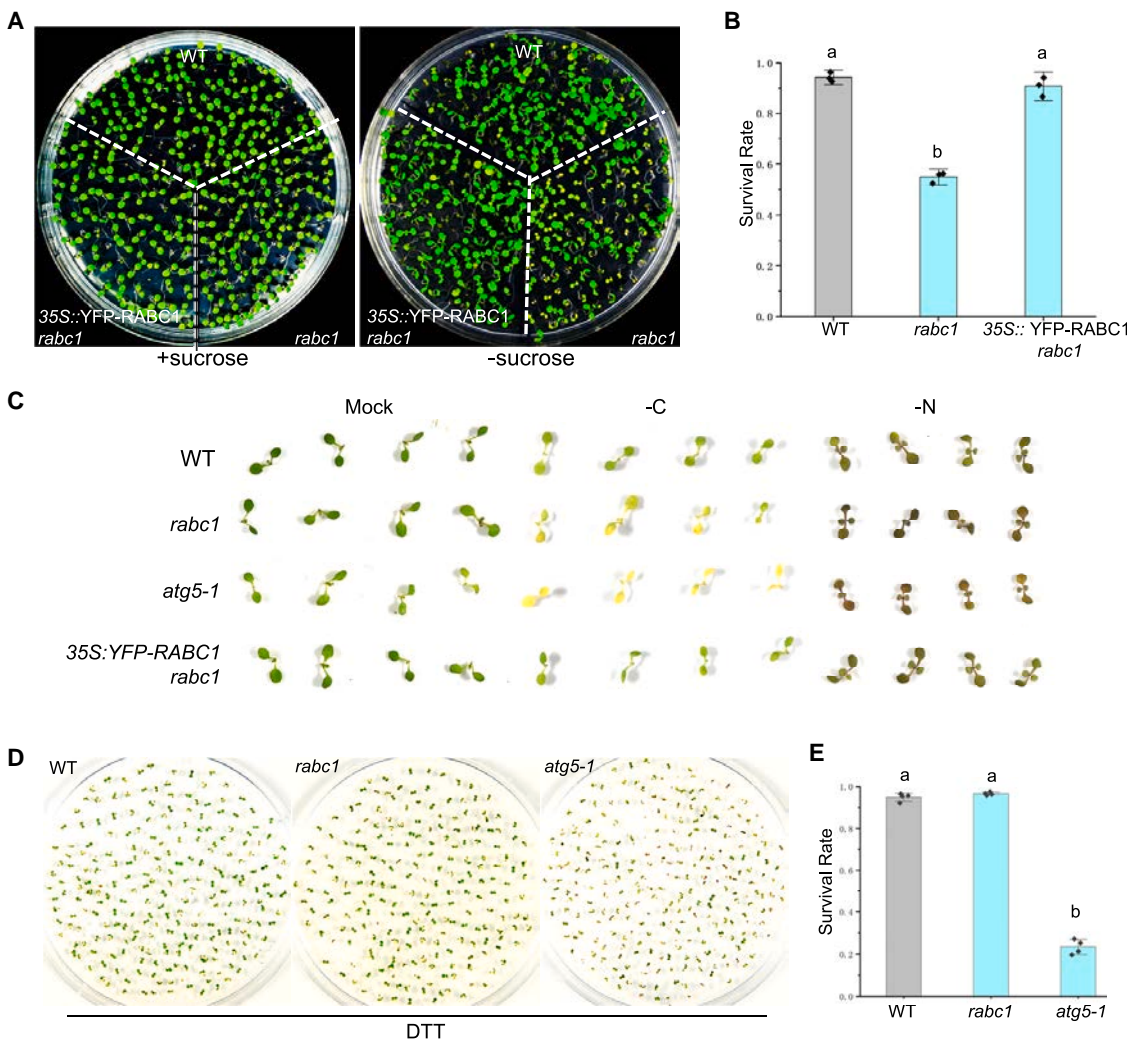


Figure 1. *rabc1* mutant is hyposensitive to nutrient starvation but not ER stress

(A) Seedlings of wild type (WT), *rabc1*, and 35S::YFP-RABC1 *rabc1* grown on 1/2 MS with (the left side) or without (the right side) sucrose for 7 days.

(B) The quantification of survival rate of seedlings grown without sucrose (A). Each time, about 120 seedlings were quantified, and 3 repeats were performed. Error bars represent mean \pm SD. Different letters indicate statistically significant differences (ANOVA, Fisher's least significant difference test, $p < 0.05$).

(C) Seedlings of WT, *rabc1*, *atg5-1*, and 35S::YFP-RABC1 *rabc1* grown on 1/2 MS with sucrose for 7 days, moved to 1/2 MS without sucrose and kept in the dark ($-C$), or moved to 1/2 MS without nitrogen ($-N$) for 10 days.

(D) 7-day-old seedlings of WT, *rabc1*, and *atg5-1* grown on 1/2 MS in the presence of 1 mM DTT.

(E) The quantification of survival rate of (D). Each time, about 200 seedlings were quantified, and 4 repeats were performed. Error bars represent mean \pm SD. Different letters indicate statistically significant differences (ANOVA, Fisher's least significant difference test, $p < 0.05$).

See also Figure S1.

ER-Golgi trafficking. We also noticed that dominant-negative YFP-RABC1(S27N) was mainly cytosolic (Figure S2F), whereas constitutively active YFP-RABC1(Q71L) was cytosolic, as well as on punctae larger than average YFP-RABC1 punctae (compare Figure S2G with Figure S2C). None of the YFP-RABC1(Q71L) punctae were co-localized with ST-RFP (Figure S2G). To investigate the potential involvement of RABC1 in the post-Golgi trafficking pathway, we conducted a co-expression experiment involving Sec-mCherry along with YFP-RABC1, YFP-RABC1(S27N), or YFP-RABC1(Q71L). Sec-mCherry is a mCherry variant that is secreted into the apoplast, and if the post-Golgi trafficking process is impaired, Sec-mCherry should be visible in the interior of the

cell.³⁴ However, we observed no retention of sec-mCherry inside cells in the presence of RABC1 variants (Figure S3). This observation suggests that RABC1 may not play a significant role in the post-Golgi trafficking pathway.

We then co-expressed mCherry-ATG8e together with free YFP, YFP-RABC1, YFP-RABC1(S27N), or RABC1(Q71L), and the number of autophagosomes was quantified. In the presence of YFP-RABC1, there were more mCherry-ATG8e punctae than that in the presence of YFP only (compare Figure 3B with Figures 3A and 3E), and many mCherry-ATG8e punctae were co-localized with YFP-RABC1 (Figure 3B). Fewer mCherry-ATG8e punctae were observed in the presence of

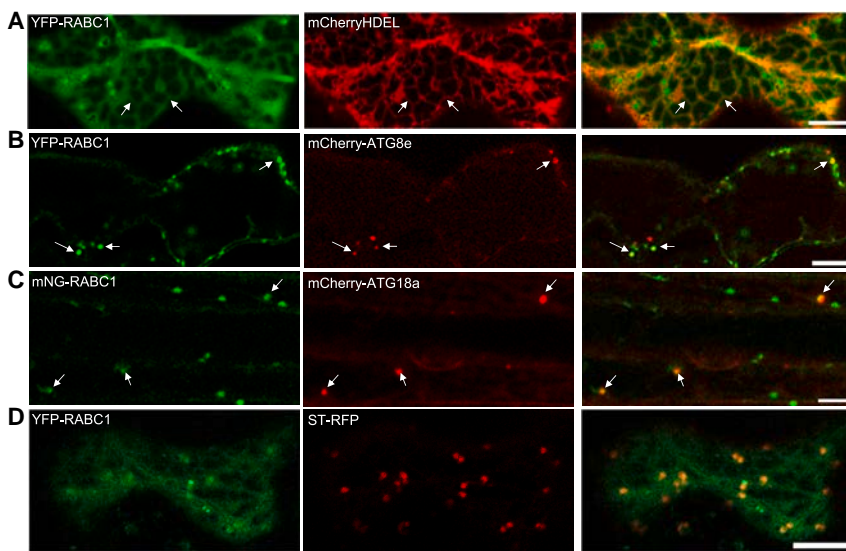


Figure 2. Subcellular localization of RABC1

(A) RABC1 is partially localized to the ER marked by mCherryHDEL. Seedlings expressing both YFP-RABC1 driven by the 35S promoter and mCherryHDEL were used for imaging. Arrows indicate RABC1 (shape line) on the ER. Scale bars: 10 μm.
(B) RABC1 is partially localized to autophagosomes marked by mCherry-ATG8e. Seedlings expressing both YFP-RABC1 driven by the 35S promoter and mCherry-ATG8e were used for imaging. Arrows indicate the co-localization between YFP-RABC1 and mCherry-ATG8. Scale bars: 10 μm.
(C) RABC1 is partially localized to ATG18a-positive autophagosomes. Seedlings expressing both mNeonGreen-RABC1 driven by the native RABC1 promoter and mCherry-ATG18a were used for imaging. Arrows indicate the co-localization between mNeonGreen-RABC1 and mCherry-ATG18a. Scale bars: 10 μm.
(D) RABC1 is partially localized to Golgi. Seedlings expressing both YFP-RABC1 driven by the native RABC1 promoter, and ST-RFP were used for imaging. Scale bars: 10 μm.

See also [Figure S2](#).

RABC1(S27N) or YFP-RABC1(Q71L) than in the presence of YFP (compare [Figures 3C](#) and [3D](#) with [Figures 3A](#) and [3E](#)). In the case of YFP-RABC1(Q71L), YFP-RABC1(Q71L) punctae were not co-localized with mCherry-ATG8e punctae ([Figure 3D](#)). These results suggested that the formation of autophagosomes is promoted by YFP-RABC1 but inhibited by YFP-RABC1(S27N) and YFP-RABC1(Q71L). Furthermore, we found that mCherry cleavage of mCherry-ATG8e was also promoted in the presence of YFP-RABC1 (compare lane 2 with lane 1 in [Figures 3F](#) [top] and [3G](#)) but inhibited in the presence of YFP-RABC1(S27N) or YFP-RABC1 (Q71L) (compare lane 3–4 with lane 1 in [Figures 3F](#) [top] and [3G](#)). Moreover, we also observed an impaired efficiency of YFP cleavage in YFP-RABC1(S27N) and YFP-RABC1(Q71L) mutants, compared with WT YFP-RABC1 ([Figures 3F](#) [lower] and [3H](#)). Together, these data indicated that RABC1 promotes autophagic flux.

To further confirm this notion, we investigated the impact of the expression of different versions of RABC1 on ER-phagy using mCherry-TMC (transmembrane domain and C-terminal tail of the yeast Sey1p protein). We have previously reported that the ER membrane marker TMC is excellent for monitoring ER-phagy both microscopically and biochemically.^{35–37} Co-expression of HA-RABC1 with mCherry-TMC resulted in an enhanced flux of ER-phagy, as evidenced by an increased number of mCherry-TMC punctae within the vacuole in the presence of the cysteine protease inhibitor E64d ([Figures S4A](#) and [S4B](#)) and a more pronounced cleaved free mCherry band ([Figures S4C](#) and [S4D](#)). Conversely, when HA-RABC1(S27N) and HA-RABC1(Q71L) mutants were present, the efficiency of ER-phagy was found to be inhibited both microscopically ([Figures S4A](#) and [S4B](#)) and biochemically ([Figures S4C](#) and [S4D](#)). These findings confirm that RABC1 promotes autophagic flux.

RABC1 promotes carbon-starvation-induced autophagy, including ER-phagy

Because *rabc1* is hypersensitive to nutrient (carbon and nitrogen) starvation but not ER stress, we wondered how autophagy

may be affected in *rabc1* under either nutrient deficient or ER stress. To this end, we examined ER-phagy under carbon starvation and ER stress because it was reported that both carbon starvation and ER stress induce ER-phagy in plants.^{18,30} First of all, we wondered if YFP-RABC1 is targeted, along with the ER (mCherryHDEL) to the vacuole by autophagy in carbon starvation treatment using concanamycin A (ConcA). ConcA is a specific inhibitor of the V-ATPase activity that inhibits acidification of the vacuole, promoting the accumulation of autophagic bodies for YFP visualization.³⁸ After a 6-h carbon-starvation treatment, YFP-RABC1 punctae were clearly visible in the vacuole and were partially co-localized with mCherryHDEL-labeled punctae in cells of the transgenic plants co-expressing YFP-RABC1 and mCherryHDEL ([Figure 4B](#), arrows). In mock samples, neither YFP-RABC1 nor mCherryHDEL was seen in the vacuole ([Figure 4A](#)). The result indicates that YFP-RABC1, together with mCherryHDEL is transported to the vacuole. The YFP-RABC1 punctae observed were co-localized with mCherry-ATG8e within the vacuole following carbon starvation ([Figure S5A](#)), indicating that these punctae are autophagic bodies. Intriguingly, the DTT treatment triggered ER-phagy as shown by the accumulation of mCherryHDEL in the vacuole ([Figure 4C](#), arrows), but few YFP-RABC1 were found co-localized with mCherryHDEL punctae in the vacuole ([Figure 4C](#), arrowhead). Similarly, we observed minimal co-localization between YFP-RABC1 and mCherry-ATG8e following DTT treatment, suggesting that RABC1 specifically promotes carbon-starvation-induced but not DTT-induced ER-phagy. This notion was further supported by our quantification, which revealed that there were more YFP-RABC1 punctae ([Figure 4D](#)) and stronger association of YFP-RABC1 with mCherryHDEL punctae ([Figure 4E](#)) in cells under carbon starvation than that treated with DTT ([Figures 4D](#) and [4E](#)).

Subsequently, we compared the cleavage efficiency of free YFP from YFP-RABC1 in cells under carbon starvation and DTT treatment. We found that the cleavage of free YFP from YFP-RABC1 in WT was enhanced under carbon starvation

Developmental Cell

Article

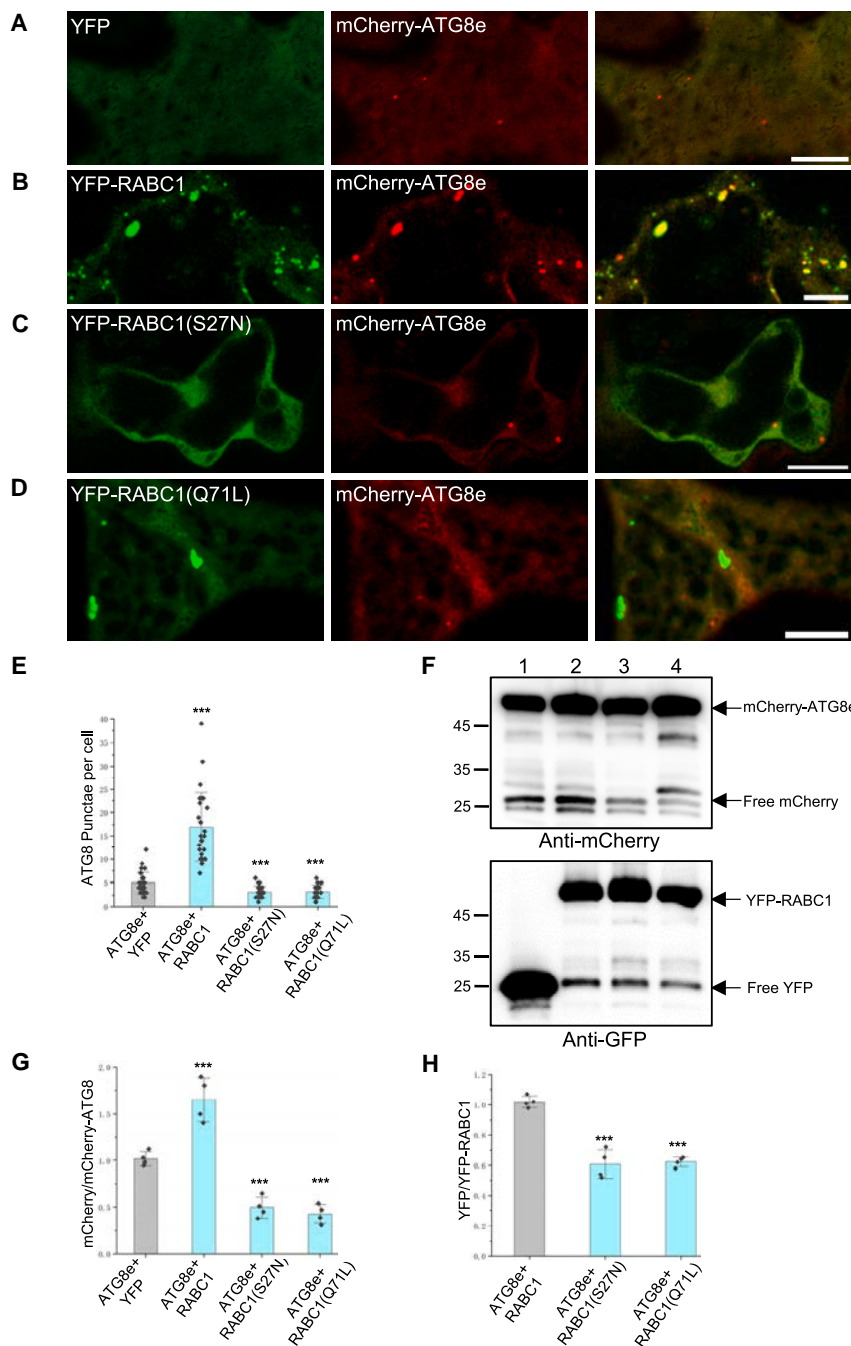


Figure 3. RABC1 promotes autophagic flux

(A–D) Transient co-expression of mCherry-ATG8e with YFP (A), YFP-RABC1 (B), YFP-RABC1(S27N) (C), or YFP-RABC1(Q71L) (D) in *N. benthamiana* leaves. Scale bars: 10 μ m.

(E) The quantification of the number of mCherry-ATG8e punctae in (A)–(D). Error bars represent SD, and *** represents significant difference from the YFP control ($p < 0.001$).

(F) Western blot of total proteins extracted from (A) to (D) samples with anti-mCherry (the upper blot) and anti-GFP (the lower blot). Lane (1–4): mCherry-ATG8e + YFP (1), mCherry-ATG8e + YFP-RABC1(S27N) (2), mCherry-ATG8e + YFP-RABC1(Q71L) (3), and mCherry-ATG8e + YFP-RABC1(Q71L) (4).

(G) The quantification of the ratio between free mCherry and mCherry-ATG8e in (F). Error bars represent mean \pm SD, *** represents significant difference from the YFP control ($p < 0.001$).

(H) The quantification of the ratio between free YFP and YFP-RABC1 in (F). Error bars represent mean \pm SD, *** represents significant difference from the YFP control ($p < 0.001$).

See also Figures S3 and S4.

RABC1 relies on conventional autophagy pathway. In summary, a greater amount of RABC1 is directed to the vacuole for degradation by autophagy together with the ER during carbon starvation but not under DTT treatment.

To further confirm that RABC1 plays a role in the ER-phagy, we employed YFP-TMC to compare the efficiency of ER-phagy in *rabc1* grown under carbon starvation with DTT treatment. The YFP cleavage from YFP-TMC was significantly increased in WT plants under carbon starvation treatment (Figure 4H). In comparison, the YFP cleavage efficiency was compromised in the *rabc1* mutant under carbon starvation (Figure 4H). By contrast, both WT and *rabc1* mutant plants treated with DTT had almost identical YFP cleavage efficiency of YFP-TMC (Figure 4I). Moreover, our microscopy data aligned very well with these biochemical data, showing that there was a significant reduction in YFP-TMC punctae within the vacuole of *rabc1* mutant cells following carbon starvation but not during ER stress induced by TM (Figures S5C and S5D).

Finally, in *rabc1* treated with carbon starvation, we observed compromised degradation not only of an ER protein (BIP2) but also of peroxisomal and mitochondrial proteins (PEX12 and CYC1, respectively) in *rabc1* mutants (Figures S5E–S5H). This observed impairment of protein degradation across multiple organelle proteins indicates that RABC1 extends its role beyond ER-phagy and encompasses a broader function in autophagy in general.

(Figure 4F), but not under DTT treatment (Figure 4G). We further compared YFP-RABC1 cleavage under tunicamycin (TM), another ER stress inducer that inhibits protein glycosylation in the ER³⁹ to that under DTT and carbon starvation. We found that only carbon starvation but not DTT nor TM promoted cleavage of YFP-RABC1 (Figure S5B), suggesting that RABC1 plays an exclusive role in response to carbon starvation rather than in response to ER stress induced by either TM or DTT. Furthermore, no significantly increased cleavage of free YFP from YFP-RABC1 was observed in *atg5-1* under carbon starvation (Figure 4F), suggesting that the cleavage of YFP from YFP-

TMC punctae within the vacuole of *rabc1* mutant cells following carbon starvation but not during ER stress induced by TM (Figures S5C and S5D).

Finally, in *rabc1* treated with carbon starvation, we observed compromised degradation not only of an ER protein (BIP2) but also of peroxisomal and mitochondrial proteins (PEX12 and CYC1, respectively) in *rabc1* mutants (Figures S5E–S5H). This observed impairment of protein degradation across multiple organelle proteins indicates that RABC1 extends its role beyond ER-phagy and encompasses a broader function in autophagy in general.

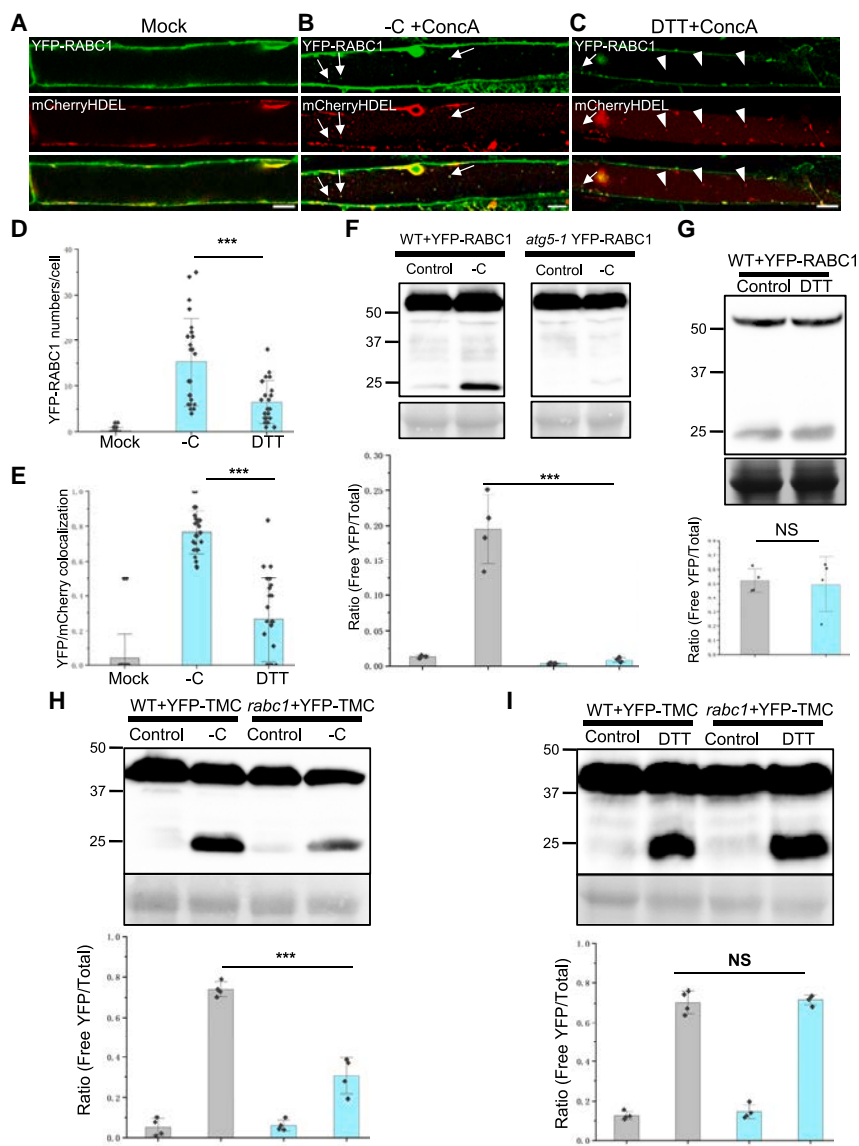


Figure 4. RABC1 promotes carbon-starvation-induced autophagy including ER-phagy

(A–C) Confocal imaging of the middle section cells from 5-day-old *rabc1* seedlings expressing YFP-RABC1 and mCherryHDEL after being treated with liquid MS with DMSO (mock) (A), carbon starvation + ConcA (B), or with DTT + ConcA (C). Arrows in (B) and (C) point the co-localization of YFP-RABC1 and mCherryHDEL punctae in the vacuole, and arrowheads in (C) point mCherryHDEL punctae in the vacuole that are not with YFP-RABC1. Scale bars: 10 μ m.

(D) The quantification of the number of YFP-RABC1 punctae in (A)–(C). The number of YFP-RABC1 within the vacuole (in the middle focus of each cell) was quantified. Error bars represent SD, and *** represents significant difference ($p < 0.001$).

(E) The quantification of the percentage of YFP-RABC1 co-localized with mCherryHDEL punctae in (A)–(C). Error bars represent SD, and *** represents significant difference ($p < 0.001$).

(F) Western blot of total proteins extracted from 5-day-old WT (top left image) or *atg5-1* (top right image) seedlings expressing YFP-RABC1 treated with carbon starvation for 12 h. Ponceau S staining was used as the loading control. The bottom graph indicates the cleavage efficiency of free YFP quantified. Error bars represent SD, and *** represents significant difference ($p < 0.001$).

(G) Western blot of total proteins extracted from 5-day-old WT seedlings expressing YFP-RABC1 treated with 2 mM DTT for 12 h. Coomassie blue staining was used as the loading control. The bottom graph shows the cleavage efficiency of free YFP quantified. Error bars represent SD, and NS represents no significant different ($p > 0.05$).

(H and I) Western blot of total proteins extracted from 5-day-old WT or *rabc1* seedlings expressing YFP-TMC treated with carbon starvation for 12 h (H) or with 2 mM DTT for 12 h (I). Ponceau S staining was used as the loading control. The bottom graphs in (H) and (I) show the cleavage efficiency of free YFP quantified. Error bars represent SD, and *** represents significant difference ($p < 0.001$, t test). NS represents no significant different ($p > 0.05$).

See also Figure S5.

Active RABC1 specifically interacts with ATG18a on the ER

To determine how RABC1 is involved in autophagy, we proceeded to investigate whether RABC1 interacts with any of the autophagy-related (ATG) core proteins by performing co-immunoprecipitation (coIP). When YFP-RABC1 was co-expressed with mCherry-ATG8e, mCherry-ATG18a, and mCherry-ATG5, only mCherry-ATG18a was efficiently co-purified with YFP-RABC1. By contrast, neither mCherry-ATG8e nor mCherry-ATG5 exhibited such interactions (Figure 5A). Furthermore, *in vitro* pull-down experiment revealed that ATG18a interacted with WT RABC1 and had an even stronger interaction with constitutively active form of RABC1 (Q71L) but did not interact with dominant-negative form of RABC1(S27N) (Figure 5B). Furthermore, we also observed a significant enhancement of the interaction between RABC1 and ATG18a following carbon starvation but not ER stress

(Figures 5C and 5D). This result indicated that the RABC1-ATG18a interaction is finely modulated by specific cellular stress conditions. Using BiFC (Bimolecular fluorescence complementation), we found that RABC1 interacted with ATG18a near (Figure 5E, row 1, arrowhead) or on the ER (Figure 5E, row 1, arrow). Our quantification found that 60% of BiFC punctae were on the ER (Figure 5F). Remarkably, over 85% of the interactions between RABC1(Q71L) and ATG18a took place on the ER (Figure 5E, row 2, arrows, and 5F). RABC1(S27N) did not interact with ATG18a (Figure 5E, row 3). There were no interactions revealed in cVenus and nVenus controls either (Figure S6A, rows 1–4). The specific interaction of ATG18a with WT and constitutively active RABC1(Q71L) suggested that ATG18a might be an effector protein of RABC1. Moreover, we performed a 3D structural simulation of ATG18a and RABC1 based on the Alphafold database and found that the contact between ATG18a and RABC1

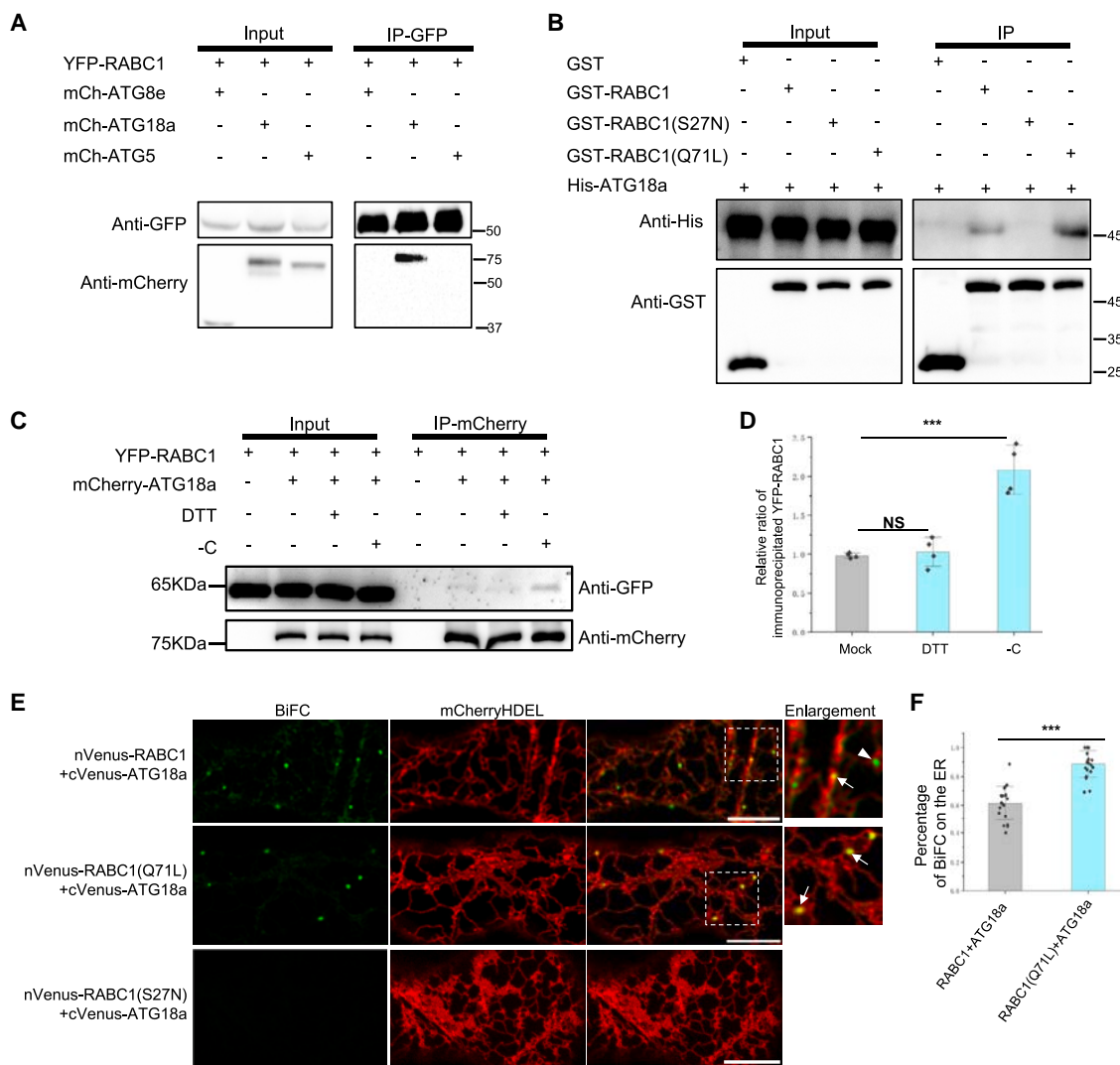


Figure 5. Active RABC1 interacts specifically with ATG18a

- (A) Co-immunoprecipitation of mCherry-ATG8e, mCherry-ATG18a, and mCherry-ATG5 with YFP-RABC1. Only mCherry-ATG18a (lane 2), but not mCherry-ATG8 (lane 1) nor mCherry-ATG5 (lane 3) was co-purified with YFP-RABC1.
- (B) *In vitro* protein interaction test between His-ATG18a and GST-RABC1, GST-RABC1(S27N), or GST-RABC1(Q71L). His-ATG18a interacts with GST-RABC1 and GST-RABC1(Q71L) but not with GST-RABC1(S27N).
- (C) Co-immunoprecipitation of YFP-RABC1 and mCherry-ATG18a expressed in seedlings subjected to indicated treatments, including mock control, DTT treatment, and carbon starvation. Co-immunoprecipitation experiments were conducted using anti-mCherry beads. Seedlings expressing YFP-RABC1 were used as the negative control.
- (D) Relative ratio of immunoprecipitated YFP-RABC1 by mCherry-ATG18a quantified in (C). Error bars represent mean \pm SD, *** represents significant difference ($p < 0.001$). NS represents no significant difference ($p > 0.05$).
- (E) BiFC analysis of the interaction between ATG18a and RABC1. Scale bars: 10 μ m. Arrows indicate the co-localization between YFP-RABC1 and mCherry-ATG8. The arrowhead indicates the presence of punctate that are not associated with the ER.
- (F) The quantification of BiFC signals on the ER from (E). BiFC signals in each cell (from 20 cells) were quantified, and experiments were repeated three times. Error bars represent SD, and *** represents significant difference ($p < 0.001$).

See also Figure S6.

may be mediated by the hydrogen bond between Ser311 (on ATG18a) and Asn36 (on RABC1) (Figures S6B and S6C).

RABC1 regulates the growth of ATG18a structures

ATG18a participates in the expansion of autophagosomes.^{31,40} Next, we investigated how RABC1 might act on ATG18a in the expansion of autophagosomes. To this end, we expressed

mNeonGreen-ATG18a in WT and *rabc1*, and we found that ATG18a punctae were smaller and more in number in *rabc1* mutant cells than that in WT cells under carbon starvation, but there was no significant difference in the mock control (Figure 6A). This notion was supported by our quantification of the size (Figure 6B) and the number (Figure 6C) of ATG18a punctae. Similarly, when compared with WT, we saw a reduction in size

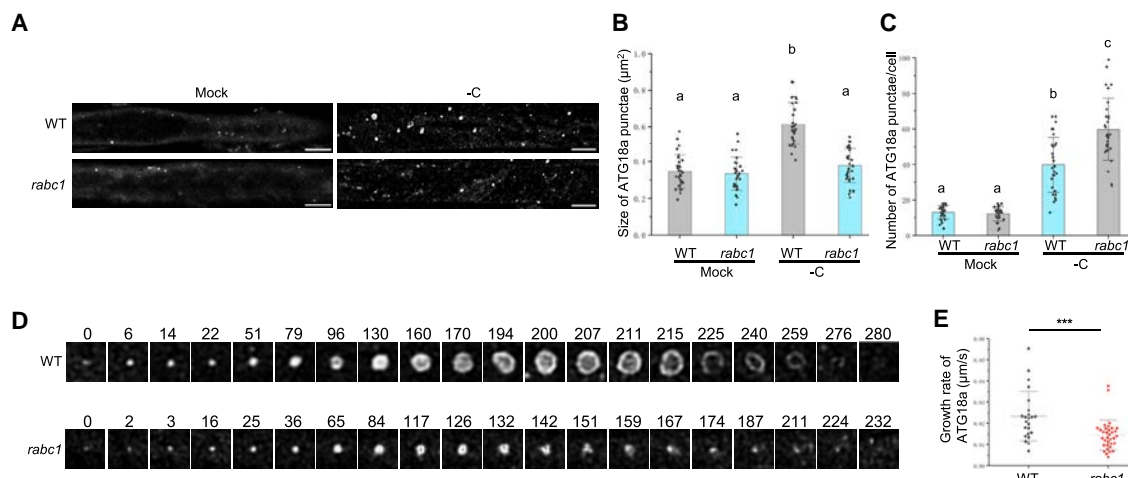


Figure 6. The growth of ATG18a-positive autophagosomes is defective in rabc1 mutant

(A) Confocal analysis of cells of WT (top two images) or rabc1 (bottom two images) seedlings expressing UBQ10pro::mNeonGreen-ATG18a in the mock control (left two images) and under carbon starvation (right two images). Scale bars: 10 μm.

(B and C) The quantification of the size (B) and number (C) of ATG18a-positive autophagosomes in WT and rabc1. Error bars represent SE, and *** represents significant difference ($p < 0.001$). About 25 cells were quantified for WT or rabc1.

(D) Living imaging of the growth of an ATG18a-positive autophagosome in WT and rabc1. The time units indicated are seconds.

(E) The quantification of the growth rate of ATG18a-positive autophagosomes in WT and rabc1. Error bars represent SD, and *** represents significant difference ($p < 0.001$).

See also Figure S7.

and an increase in the number of ATG18a punctae in the rabc1 mutant under nitrogen starvation, whereas no significant difference in the size and number of ATG18a punctae was observed under ER stress (Figures S7A–S7C). Detailed live imaging of the growth of mNeonGreen-ATG18a punctae revealed that, in WT cells, many ATG18a punctae formed, grew, and became fully expanded in 200 s (Figure 6D). Subsequently, they started to decay and quickly disappeared after around 250–280 s (Figure 6D). In rabc1 cells, many of ATG18a punctae did not become well expanded before they started to decay and eventually disappeared within 230 s (Figure 6D). Our quantification of the growth rate of ATG18a punctae revealed that the growth of ATG18a punctae in WT cells was $0.023 \mu\text{m}^2/\text{s}$ in average (Figure 6E). In rabc1, it was reduced to $0.014 \mu\text{m}^2/\text{s}$ (Figure 6E). We also quantified the lifetime of ATG18a punctae in WT and rabc1 cells. We found that there was no significant difference between WT and rabc1 (Figure S7D). Taken all together, we conclude that RABC1 regulates the expansion of ATG18a-positive autophagosomes.

RABC1 plays a role in tethering ATG18a to the ER

Atg18 has been reported to tether pre-autophagosomal membrane to the ER and facilitate the lipid transfer for autophagosome formation in mammalian cells,²⁶ although it is not known if Arabidopsis ATG18a plays a similar role or not. Because RABC1 regulates the expansion of ATG18a punctae, and ATG18a may be an effector protein of RABC1, we wondered if ATG18a is tethered to the ER and if RABC1 plays a role in tethering ATG18a to the ER for autophagosome expansion. In order to investigate these, we first co-expressed mNeon-Green-ATG18a and mScarletHDEL in both WT and in rabc1. Our analysis of projected image stacks over 5 μm revealed

that a large portion of mNeonGreen-ATG18a punctae were located on the ER in WT cells (Figure 7A, arrows), whereas many mNeonGreen-ATG18a punctae were found off the ER in rabc1 mutant cells (Figure 7A, arrowheads). Our quantification revealed that in WT cells, there were more than 60% ATG18a punctae on the ER, whereas in rabc1 cells there were only less than 40% ATG18a punctae on the ER (Figure 7B). Furthermore, our TEM analysis also revealed a higher abundance of unclosed autophagosome structures that were smaller in rabc1 cells than that in WT (Figure S7E, arrows). Notably, a significant proportion of these observed autophagosomes in rabc1 mutant cells appeared to be away from the ER (Figure S7E). The result collectively indicated that ATG18a is tethered to the ER, and RABC1 plays a role in tethering ATG18a to the ER.

Subsequently, we transiently co-expressed mNeonGreen-ATG18a and mCherryHDEL with HA-RABC1, HA-RABC1(S27N), and HA-RABC1(Q71L) in the *N. benthamiana* leaves to compare the different effects between the WT and two mutant forms of RABC1. Similar expression of HA-RABC1, HA-RABC1(S27N), and HA-RABC1(Q71L) was confirmed by western blot (Figure 7F). Compared with HA-RABC1 (Figure 7C), in the presence of HA-RABC1(S27N), more mNeonGreen-ATG18a signal was retained in the cytosol, with fewer but smaller mNeonGreen-ATG18a punctae associated with the ER (Figure 7D, arrowheads). This was verified by quantifying the size of ATG18a punctae, the ratio of ATG18a punctae/cytosol signal, and the percentage of ER-associated ATG18a punctae (Figures 7G–7I). It is interesting that in the presence of HA-RABC1(Q71L), although the ratio of ATG18a punctae/cytosol signal was similar to that in HA-RABC1 (compare Figure 7E with Figures 7C and 7H), mNeonGreen-ATG18a punctae in the presence of HA-RABC1(Q71L) appeared lesser in

Developmental Cell

Article

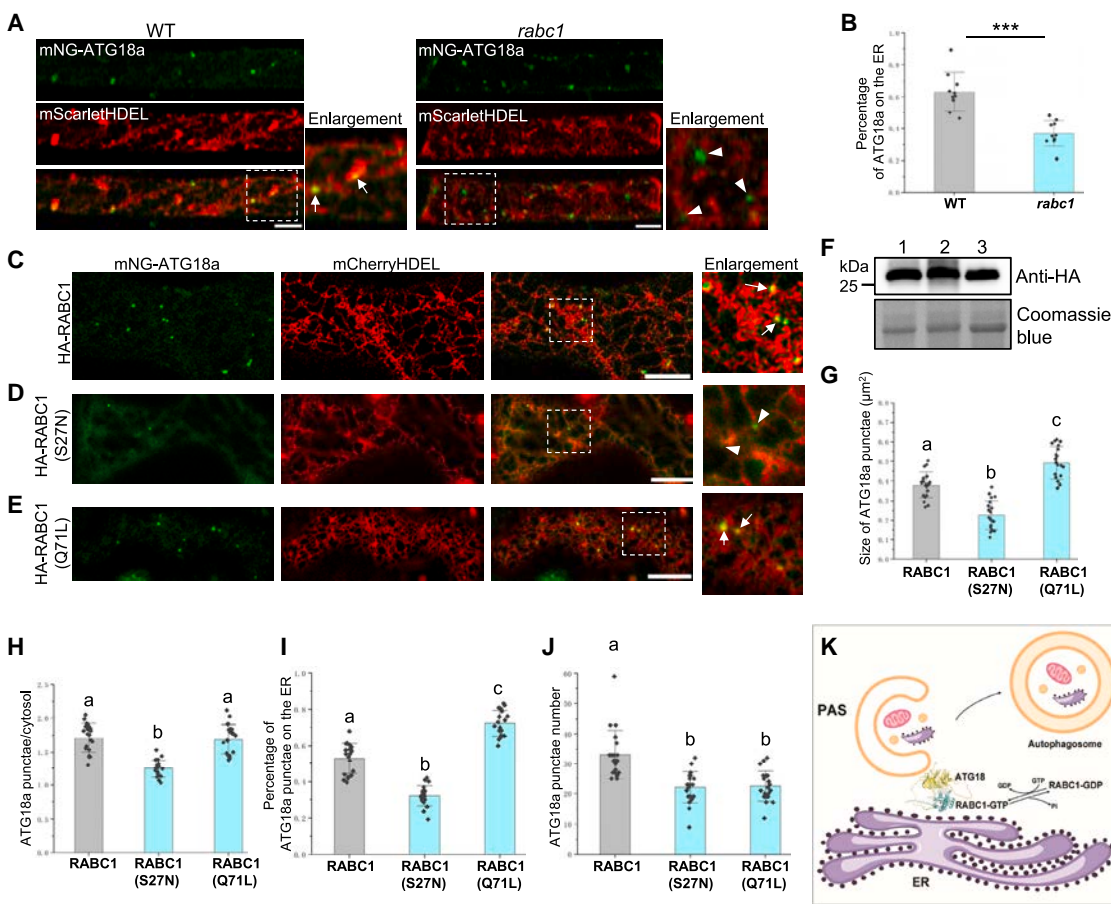


Figure 7. RABC1 plays a role in tethering ATG18a to the ER

(A) The projection of confocal images of WT and *rabc1* seedlings expressing mNeonGreen-ATG18a and mScarletHDEL. Arrows point mNeonGreen-ATG18a punctae on the ER, and arrowheads point mNeonGreen-ATG18a punctae off the ER. Scale bars: 10 μm .

(B) The percentage of ATG18a punctae on the ER in WT and *rabc1* quantified. Error bars represent SD, and *** represents significant difference ($p < 0.001$).

(C–E) Confocal imaging of mNeonGreen-ATG18a and mCherryHDEL transiently co-expressed with HA-RABC1 (C), HA-RABC1(S27N) (D), or HA-RABC1(Q71L) (E). Arrows point mNeonGreen-ATG18a punctae on the ER, and arrowheads point mNeonGreen-ATG18a punctae off the ER. Scale bars: 10 μm .

(F) The expression levels of HA-tagged RABC1 variants in (C)–(E) assessed using anti-HA. Lines 1, 2, and 3 represent (C)–(E), respectively.

(G–J) The size (G) of ATG18a punctae, the ratio of ATG18a punctae to cytosolic signal (H), the percentage of ATG18a punctae on the ER (I) and the number of ATG18a punctae (J) were quantified in the presence HA-RABC1, HA-RABC1(S27N), and HA-RABC1(QL) as observed in (C)–(E). The non-punctate and diffusing signal was defined as cytosolic signal. Error bars represent SD. Different letters indicate statistically significant differences (ANOVA, Fisher's least significant difference test, $p < 0.05$).

(K) Proposed working model for RABC1 in autophagy. Inactive GDP-RABC1 is normally in the cytosol. GDP-RABC1 recruited onto the ER is activated with a switch to GTP-RABC1. Active GTP-RABC1 on the ER interacts with and tethers ATG18a to the ER so autophagosomes are expanded on the ER. The expansion is likely facilitated by material transfer from the ER. At a certain point, active GTP-RABC1 is turned off by GTP hydrolysis. Inactive GDP-RABC1 is recycled back to the cytosol, and expanding autophagosomes are detached from the ER for further expansion or maturation.

number but larger in size than that in HA-RABC1 (compare Figure 7E with Figures 7C, 7G, and 7J). More mNeonGreen-ATG18a in presence of HA-RABC1(Q71L) were associated with ER (Figure 7E, arrows) than that in the presence of WT RABC1, which was supported by the quantification (Figure 7I). Taken all together, we conclude that RABC1 serves as one of the molecules that governs the tethering of ATG18a to the ER, as well as the subsequent detachment of ATG18a from the ER.

DISCUSSION

Despite of recent advances in our knowledge of the actions of different Rab GTPases, the precise cellular function of RabC

Rab18 is not well defined both in plant and in mammalian cells. Here, we report that Arabidopsis RABC1, a member of the RabC clade, is required for plant responses to nutrient (carbon and nitrogen) starvation. RABC1 is localized in the cytosol and in multiple cellular compartments, including the ER, Golgi, and autophagosomes. However, RABC1 does not appear to participate in ER-Golgi and post-Golgi transport processes. Instead, it is primarily involved in autophagy triggered by nutrient deficiency. We find that active RABC1 specifically interacts with ATG18a, either on or near the ER, whereas inactive RABC1 does not display such interaction. In addition, the interaction between RABC1 and ATG18a is enhanced by carbon starvation but not in response to ER stress. It is interesting that the expression

of *RABC1* is also transiently upregulated by carbon starvation. In *rabc1* mutant cells, the ER association of ATG18a is impaired in nutrient-deficient conditions, leading to reduced size and the growth rate of ATG18a. Therefore, we propose that RABC1 promotes nutrient starvation-induced autophagy, including ER-phagy, by tethering ATG18a to the ER to facilitate the expansion of ATG18a-positive autophagosomes (Figure 7K). This promotion is likely a result of the enhanced interaction between RABC1 and ATG18a, along with transient upregulation of the *RABC1* gene expression. Ge et al.³² recently reported that RABC1 contributes to the mobilization of LDs during stomatal development.³² Upon being treated with oleic acid, an LD formation inducer, RABC1 is transiently localized to the LDs in guard cells where it recruits AtSEIPIN2 as an effector, a stomatal-specific protein involved in LD development.³² However, it remains unclear whether RABC1 functions in a similar manner in the absence of oleic acid or in tissues other than stomata. Notably, RABC1 is ubiquitously expressed in plant tissues. Furthermore, autophagy is known to be involved in making LD contents accessible to the cell.⁴¹ Therefore, it is possible that the LD mobilization defect observed in the *rabc1* mutant is explained by defective autophagy revealed here. In this regard, Ge et al.³² reported that aberrantly enlarged LDs present in *rabc1* mutant cells, a sign that the degradation of LDs is defective in *rabc1* mutant cells.

It is known that the expansion of autophagosomes requires a supply of membrane materials from the ER. In yeast and mammalian cells, the Atg18-Atg2 complex tethers growing autophagosomes to the ER, facilitating the lipid transfer from the ER to autophagosomes.^{26,40} However, the existence of any factor(s) that facilitate the tethering of ATG18-ATG2 to the ER is unknown. In plants, ATG18a is crucial for the formation of autophagosomes under a variety of stress conditions.^{28,29,42} Nonetheless, the specific mechanisms by which ATG18a is involved in this process and how its actions are regulated remain unclear. Our findings provide insights into these questions by demonstrating that ATG18a is associated with the ER and is a downstream effector of RABC1. The ER association of ATG18a is facilitated by active RABC1 on the ER. We note that, in *rabc1* mutant cells, the ER association of ATG18a is not completely blocked, and potentially, the residual expression of *RABC1* in the knockdown *rabc1* mutant contributes to the still observed association. However, it is also possible that there are additional mechanisms for ER-autophagosome association; therefore, the linkage between ATG18a and the ER still operates in *rabc1*, although less effectively. For example, it has been recently reported in plants that VAMP724 (Vesicle Associated Membrane Protein724) and VAMP726, two soluble N-ethylmaleimide-sensitive factor attachment protein receptor (SNARE) proteins, work together with ATG9 in regulating autophagosome progression from the ER.^{43,44} The lipid-binding protein ORP2A interacts with VAMP-associated protein (VAP)27-1 to mediate ER-autophagosomal membrane contact for autophagy.⁴⁵ These pathways may compensate the ER-autophagosome association defect when RABC1 is defective. As such, autophagy in the *rabc1* mutant is not completely blocked.

To regulate membrane trafficking precisely, a Rab protein continually cycles between active and inactive forms, allowing its activity to be turned on and off in a timely manner. In *rabc1* mutant cells, there are more but smaller ATG18a-labeled autophagosomes but fewer ATG8-positive autophagosomes. A similar

ATG18a phenotype is also observed when persulfidation of ATG18a, which is important for the phospholipid binding of ATG18a, is disrupted.³¹ It is noteworthy that overexpression of dominant active form of RABC1 leads to an enhanced ER association of ATG18a, as well as enlarged ATG18a punctae, whereas it reduces the number of ATG8 punctae. Yet, dominant active RABC1 does not co-localize with ATG8e. Our interpretation of these results is that ATG18a is the direct effector of RABC1, whereas ATG8 acts in the subsequent step. It has been shown that ATG8 is recruited after ATG18a is nucleated, but ATG8 is co-localized with ATG18a for around 60 s during the formation of autophagosomes.³¹ Because constitutively active RABC1 cannot be turned off, it would lead to a prolonged ER retention of ATG18a-positive autophagosomes, thus potentially delaying their detachment from the ER. This would result in enlarged ATG18a-positive autophagosomes but fewer ATG8-positive autophagosomes as the secondary effect. Therefore, RABC1 is a master regulator of ATG18a, controlling the loading of ATG18a to the ER for expansion and its subsequent detachment from the ER for further expansion or maturation (Figure 7K).

Autophagy is one of the cellular mechanisms plant cells use to respond to various stresses.^{18,31} It is noteworthy that RABC1 promotes carbon-starvation-induced autophagy including ER-phagy, but it does not participate in ER-phagy induced by ER stress. In plants, the protein kinase TOR (target of rapamycin) regulates autophagy induced by nutrient starvation, salt, and osmotic stress but not autophagy induced by ER stress or oxidative stress.⁴⁶ Therefore, it is possible that the action of RABC1-ATG18a in autophagy, including ER-phagy under nutrient starvation, is TOR signaling pathway dependent. Although TOR-regulated autophagy is dependent on ATG18a,⁴⁷ ATG18a is reported to be involved in ER-phagy induced by ER stress.^{30,31,46} Thus, TOR may modulate the action of RABC1-ATG18a through RABC1. Indeed, we found that the AZD8055 (a TOR inhibitor) treatment significantly increased the size and number (doubled in average) of ATG18a punctae in WT. In the *rabc1* mutant, only ~60% increase in the size of ATG18a punctae was observed along with a greater increase (tripled in average) in the number of ATG18a punctae in response to the AZD8055 treatment (Figures S7F–S7H).

Last but not least, ER-phagy is a highly selective process mediated by specific ER-phagy receptors. In plants, several ER-phagy receptors have been recently identified. AtSec62, a constituent of the protein translocator in the ER, is an ER-phagy receptor required for ER stress tolerance.¹⁷ Two ATG8-interacting proteins, ATI1 and ATI2, have been shown to function as ER-phagy receptors in plant responses to carbon starvation.¹⁸ C53, a soluble protein, also serves as an ER-phagy receptor when ribosomes stall on the ER under ER stress.⁴⁸ Most recently, it has been shown that RHD3 serves as an ER-phagy receptor to alleviate ER stress.³⁵ It will be interesting to examine if RABC1 works together with any of the ER-phagy receptors under the carbon starvation condition.

Limitations of the study

Although our research has elucidated a role of RABC1 in facilitating the attachment of ATG18a to the ER and its subsequent detachment from the ER during autophagy, several critical questions remain unanswered. It remains to be determined what other factors are involved in the ER association of ATG18a in autophagy in plant cells. In mammalian cells, the ULK1/FIP200-VAPs

Developmental Cell

Article



complex is known to play a role in ER contact of WIPI2/Atg18.⁴⁹ In addition, it is not clear whether RABC1 also collaborates with ATG9, another membrane supplier for autophagosome expansion. Moreover, the mechanisms that activate and recruit RABC1 to the ER in plant response to nutrient starvation remain incompletely understood. Our data suggest that the action of RABC1 in autophagy is under the regulation of the TOR signaling pathway. It would be interesting to examine if and how TOR may interplay with the guanine exchange factor of RABC1³² to gain crucial insights into this regulation. Additionally, it is not clear whether RABC1 also collaborates with selective autophagy receptors for degradation of the ER or other cargoes.

STAR★METHODS

Detailed methods are provided in the online version of this paper and include the following:

- KEY RESOURCES TABLE

- RESOURCE AVAILABILITY

- Lead contact
 - Materials availability
 - Data and code availability

- EXPERIMENTAL MODEL AND STUDY PARTICIPANT DETAILS

- METHOD DETAILS

- Molecular cloning
 - Real-time quantitative reverse transcription PCR
 - Co-immunoprecipitation
 - In vitro protein affinity assay
 - Western blot
 - Bimolecular fluorescence complementation
 - Transmission electron microscopy
 - Confocal imaging
 - Protein structure simulation

- QUANTIFICATION AND STATISTICAL ANALYSIS

SUPPLEMENTAL INFORMATION

Supplemental information can be found online at <https://doi.org/10.1016/j.devcel.2023.11.006>.

ACKNOWLEDGMENTS

We thank the Cell Imaging and Analysis Network and the Advanced Bio-Imaging Facility at McGill University for the confocal equipment used and Drs. H. Yu, Y. Guo, and X. Zhao at the Analysis and Testing Center of SKLMT (State Key Laboratory of Microbial Technology, Shandong University) for assistance in laser scanning confocal microscopy. We also thank Dr. W. Zhao from the Harbin Institute of Technology for the kind assistance in the Sparse-deconvolution analysis. J.S. acknowledges grant support from the National Natural Science Foundation of China (no. 32200287), a Qilu Scholarship from Shandong University (Qingdao, China), and financial support from the Key Laboratory of Plant Development and Environmental Adaptation Biology, Ministry of Education, School of Life Sciences, Shandong University. The project was supported by a discovery grant from NSERC, Canada (no. 315863) to H.Z.

AUTHOR CONTRIBUTIONS

J.S. and Y.S. performed most of the experiments and analyzed the data. S.W. created the plasmids for *in vitro* pull-down. X.L. and S.F. performed carbon starvation treatments. C.L. performed the TEM experiment. W.W. and P.L.

performed initial cloning of RABC1 and subcellular localization experiments. J.S. and H.Z. designed and supervised the project and wrote the article with the contributions of other authors.

DECLARATION OF INTERESTS

The authors declare no competing interests.

INCLUSION AND DIVERSITY

One or more of the authors of this paper self-identifies as an underrepresented ethnic minority in their field of research or within their geographical location.

Received: January 4, 2023

Revised: July 30, 2023

Accepted: November 10, 2023

Published: December 5, 2023

REFERENCES

1. Nielsen, E. (2020). The small GTPase superfamily in plants: a conserved regulatory module with novel functions. *Annu. Rev. Plant Biol.* **71**, 247–272.
2. Stenmark, H. (2009). Rab GTPases as coordinators of vesicle traffic. *Nat. Rev. Mol. Cell Biol.* **10**, 513–525.
3. Rutherford, S., and Moore, I. (2002). The Arabidopsis Rab GTPase family: another enigma variation. *Curr. Opin. Plant Biol.* **5**, 518–528.
4. Mayers, J.R., Hu, T., Wang, C., Cárdenas, J.J., Tan, Y., Pan, J., and Bednarek, S.Y. (2017). SCD1 and SCD2 form a complex that functions with the exocyst and RabE1 in exocytosis and cytokinesis. *Plant Cell* **29**, 2610–2625.
5. Zeng, Y., Li, B., Ji, C., Feng, L., Niu, F., Deng, C., Chen, S., Lin, Y., Cheung, K.C.P., Shen, J., et al. (2021). A unique AtSar1D-AtRabD2a nexus modulates autophagosome biogenesis in *Arabidopsis thaliana*. *Proc. Natl. Acad. Sci. USA* **118**, e2021293118.
6. Helen, Y., Leaf, D.S., and Moore, H.H. (1993). Gene cloning and characterization of a GTP-binding Rab protein from mouse pituitary AtT-20 cells. *Gene* **132**, 273–278.
7. Dejgaard, S.Y., and Presley, J.F. (2019). Rab18: new insights into the function of an essential protein. *Cell. Mol. Life Sci.* **76**, 1935–1945.
8. Lütcke, A., Parton, R.G., Murphy, C., Olkkonen, V.M., Dupree, P., Valencia, A., Simons, K., and Zerial, M. (1994). Cloning and subcellular localization of novel rab proteins reveals polarized and cell type-specific expression. *J. Cell Sci.* **107**, 3437–3448.
9. Dejgaard, S.Y., Murshid, A., Erman, A., Kizilay, O., Verbich, D., Lodge, R., Dejgaard, K., Ly-Hartig, T.B., Pepperkok, R., Simpson, J.C., et al. (2008). Rab18 and Rab43 have key roles in ER-Golgi trafficking. *J. Cell Sci.* **121**, 2768–2781.
10. Gerondopoulos, A., Bastos, R.N., Yoshimura, S., Anderson, R., Carpanini, S., Alianian, I., Handley, M.T., and Barr, F.A. (2014). Rab18 and a Rab18 GEF complex are required for normal ER structure. *J. Cell Biol.* **205**, 707–720.
11. Xu, D.J., Li, Y.Q., Wu, L.Z., Li, Y., Zhao, D.Y., Yu, J.H., Huang, T.Z., Ferguson, C., Parton, R.G., Yang, H.Y., et al. (2018). Rab18 promotes lipid droplet (LD) growth by tethering the ER to LDs through SNARE and NRZ interactions. *J. Cell Biol.* **217**, 975–995.
12. Takáts, S., Lévay, L., Boda, A., Tóth, S., Simon-Vecsei, Z., Rubics, A., Varga, Á., Lippai, M., Lőrincz, P., Glatz, G., et al. (2021). The Warburg Micro Syndrome-associated Rab3GAP-Rab18 module promotes autolysosome maturation through the Vps34 complex I. *FEBS Journal* **288**, 190–211.
13. Stolz, A., Ernst, A., and Dikic, I. (2014). Cargo recognition and trafficking in selective autophagy. *Nat. Cell Biol.* **16**, 495–501.
14. Chino, H., and Mizushima, N. (2020). ER-phagy: quality control and turnover of endoplasmic reticulum. *Trends Cell Biol.* **30**, 384–398.

Rab18 localizes to lipid droplets and induces their close apposition to the endoplasmic reticulum-derived membrane

Shintaro Ozeki^{1,*}, Jinglei Cheng^{1,*}, Kumi Tauchi-Sato¹, Naoya Hatano², Hisaaki Taniguchi^{2,3} and Toyoshi Fujimoto^{1,‡}

¹Department of Anatomy and Molecular Cell Biology, Graduate School of Medicine, Nagoya University, 65 Tsurumai, Showa, Nagoya 466-8550, Japan

²Harima Institute at SPring-8, RIKEN, Mikazuki, Sayo, Hyogo 679-5148, Japan

³Institute for Enzyme Research, The University of Tokushima, Tokushima 770-8503, Japan

*These authors contributed equally to this work

‡Author for correspondence (e-mail: tfujimot@med.nagoya-u.ac.jp)

Accepted 17 March 2005

Journal of Cell Science 118, 2601-2611 Published by The Company of Biologists 2005

doi:10.1242/jcs.02401

Summary

Lipid droplets (LDs) are organelles that store neutral lipids, but their regulatory mechanism is not well understood. In the present study, we identified Rab18 as an LD component of HepG2 cells by proteomic analysis, and confirmed its localization by immunohistochemistry and western blotting. Wild-type and dominant-active Rab18 localized to LDs but the dominant-negative form did not. Endogenous Rab18 coexisted with adipocyte differentiation-related protein (ADRP) in LDs, but the labeling intensity of the two proteins showed clear reciprocity. Consistent with this observation, overexpression of Rab18 induced a decrease in the amounts of ADRP in LDs in HepG2 and BALB/c 3T3 cells. Furthermore, Rab18 overexpression caused close

apposition of LDs to membrane cisternae connected to the rough ER. Two other procedures that decrease ADRP, i.e. RNA interference and brefeldin A treatment, induced the same morphological change, indicating that decrease in ADRP was the cause of the LD-ER apposition. In accordance with similar structures found between ER and other organelles, we propose that the ER membrane apposed to LDs should be named the LD-associated membrane, or LAM. The present results suggested that Rab18 regulates LAM formation, which is likely to be involved in mobilizing lipid esters stored in LDs.

Key words: Lipid droplet, Mass spectrometry, Rab18, Endoplasmic reticulum, Membrane apposition

Introduction

Lipid droplets (LDs) are found in many kinds of cells. Their surface is composed of a phospholipid monolayer containing free cholesterol, and the core is a mixture of lipid esters, mostly triglyceride and cholesterol ester (Murphy and Vance, 1999; Tauchi-Sato et al., 2002). In adipocytes, LDs store triglyceride, which is used as the source of energy production; in steroid-producing cells, cholesterol ester is stored in LDs for the synthesis of steroid hormones. However, the physiological function of LDs in other cell types has attracted little attention until recently, and LDs were generally thought to be inert and static organelles for storage of excess lipid.

LDs in non-adipose cells have been shown to harbor adipocyte differentiation-related protein (ADRP) and TIP47, both of which show sequence similarity to perilipin expressed in adipose cells (Londos et al., 1999). However, studies performed over the past several years have revealed that LDs contain a number of other functional molecules including major eicosanoid-forming enzymes (Bozza et al., 1997), MAP kinase, cytosolic phospholipase A2 (Yu et al., 1998), caveolins (Fujimoto et al., 2001; Ostermeyer et al., 2001; Pol et al., 2001), α -synuclein (Cole et al., 2002), Nir2 (Litvak et al.,

2002), NAD(P)H steroid dehydrogenase (Ohashi et al., 2003), and σ -1 receptor (Hayashi and Su, 2003). In conjunction with the mobility and rapid transport of various lipids in and out of LDs (Frolov et al., 2000; Pratess et al., 2000; Pol et al., 2004), it is becoming clear that LDs are much more dynamic and functionally active organelles than originally thought.

To elucidate the physiological functions of LDs in molecular terms, we attempted to identify molecules involved in LD function by a proteomic approach. After our preliminary report (T.F., Noriko Nakamura, S.O. and Hiroshi Kogo, The 75th Annual Meeting of the Japanese Biochemical Society, Kyoto, Japan, 2002), three groups published the results of proteomic studies of LDs from various cell types (Fujimoto et al., 2004; Liu et al., 2004; Umlauf et al., 2004). One of a number of proteins identified by the proteomic analysis is Rab18, which we have investigated and found to be highly concentrated in LDs, and that its expression reduced ADRP from LDs. Furthermore, Rab18 induced close apposition of LDs to an ER-derived membrane. These observations implied that Rab18 plays a crucial role in controlling the relationship between LDs and the ER, which may be important for lipid transport between the two organelles.

Materials and Methods

Cells and antibodies

Human HepG2 and mouse BALB/c 3T3 cells were obtained from the Japanese Collection of Research Bioresources Cell Bank. The cells were maintained in Dulbecco's minimum essential medium supplemented with 10% fetal calf serum (FCS), 50 U/ml penicillin and 0.05 mg/ml streptomycin at 37°C under 5% CO₂/95% air.

Anti-Rab18 antibody was raised in rabbits by injecting an antigen peptide (ESENQNKGVKLSH), corresponding to amino acids 177-189 of human Rab18, bound to keyhole limpet hemocyanin, and affinity-purified by an antigen column. We verified that the antibody does not react with Rab1, Rab2, Rab3, Rab5, Rab7, Rab9 or Rab10 by immunofluorescence microscopy and western blotting using cells transfected with the respective Rab cDNA. Antibodies to lysobisphosphatidic acid (LBPA) (Kobayashi et al., 1998), and LC3 (Kabeya et al., 2000) were kindly provided by Toshihide Kobayashi and Yasuo Uchiyama, respectively. Antibodies: ADRP (Progen, Darra, Australia), Lamp1 and Myc (Developmental Studies Hybridoma Bank, the University of Iowa, USA), EEA1 (Transduction Lab., Lexington, KY, USA), transferrin receptor (Cymbus Biotech., Flanders, NJ, USA), GFP (Molecular Probes, Eugene, OR, USA), and FLAG (Sigma-Aldrich, St Louis, MO, USA). Secondary antibodies conjugated with fluorochromes (Molecular Probes) and colloidal gold (BioCell, Cardiff, UK) were also used.

Expression vectors and siRNA

cDNAs of human Rab1, Rab9 and Rab18 were amplified from HepG2 or human fibroblast total RNA by RT-PCR, checked by sequencing and cloned in pEGFP-C (Clontech, Palo Alto, CA, USA) and pFLAG-C (Sigma-Aldrich) vectors. pEFBOS-Myc-Rab2, pCMV5-FLAG-Rab5, pEGFP-Rab7 and pEGFP-Rab10 were kindly provided by Yoshimi Takai, Toshiaki Katada, Takuya Sasaki and Mitsunori Fukuda, respectively. Small interfering RNA (siRNA) for ADRP knockdown was produced by either in vitro transcription using an siRNA construction kit (Ambion, Austin, TX, USA) or by chemical synthesis by Japan BioService (Saitama, Japan). Both plasmid expression vectors and siRNAs were transfected into cells by Lipofectamine2000 (Invitrogen, San Diego, CA, USA) according to the manufacturer's instruction. Cells were used 24–48 hours after transfection of plasmid vectors, and 48–72 hours after siRNA treatment.

Isolation of LDs by subcellular fractionation

LDs were isolated from HepG2 cells as described (Fujimoto et al., 2001). Briefly, cells were disrupted by nitrogen cavitation at 800 psi for 15 minutes at 4°C. After the nuclei were sedimented, the supernatant, adjusted to 0.54 M sucrose (3 ml), was overlaid with 0.27 M sucrose (3 ml), 0.135 M sucrose (3 ml) in disruption buffer, and buffer without sucrose (3 ml), followed by centrifugation for 60 minutes at 154,000 *g* in an SW41 rotor (Beckman, Fullerton, CA, USA). The LD fraction recovered at the top of the tube was used for mass analysis. For western blotting, eight fractions (1.5 ml each) were obtained from the top, mixed with 6× sample buffer, and subjected to electrophoresis and electrotransfer.

Proteomic analysis

The LD fraction purified from HepG2 cells was subjected to proteomic analysis as described previously (Kikuchi et al., 2004). Briefly, the sample electrophoresed in SDS-PAGE was stained with Coomassie Brilliant Blue, destained, and subjected to in-gel digestion with trypsin after reduction by dithiothreitol and alkylation by iodoacetamide. The resulting peptides were extracted and subjected to liquid chromatography/mass spectrometry (LC/MS) and data-dependent tandem mass (LC-MS/MS) analyses using a Q-ToF-type

hybrid mass spectrometer (Micromass, Manchester, UK) interfaced on-line with a capillary HPLC (Waters-Micromass modular CapLC, Micromass). Peak lists obtained from the MS/MS spectra were used to identify proteins using the Mascot search engine (Matrixscience, London, UK).

Immunofluorescence microscopy

Cells cultured on coverslips were observed by immunofluorescence microscopy as described previously (Fujimoto et al., 2001). For most experiments, cells were fixed with 3% formaldehyde and 0.05–0.1% glutaraldehyde, permeabilized with 0.01% digitonin, and treated with 3% bovine serum albumin (BSA) before immunolabeling. LDs were visualized using BODIPY493/503 (Molecular Probes) in most experiments (Gocze and Freeman, 1994). When triple labeling was necessary, LDs were stained with Sudan III. Although the procedure for Sudan III staining could cause some morphological changes in the LDs, correlations with antigen localization were preserved (Fukumoto and Fujimoto, 2002). Images were acquired using a Zeiss PASCAL confocal laser scanning microscope, or a Zeiss Axiohot2 fluorescence microscope equipped with an AxioCam digital camera.

Conventional and immunoelectron microscopy

For conventional electron microscopy, cells on coverslips were fixed with 2.5% glutaraldehyde, post-fixed with 1% osmium tetroxide, stained en bloc with uranyl acetate, and embedded in Epon for thin sectioning. For some specimens, 0.7% potassium ferrocyanide was added to the osmium tetroxide solution to enhance membrane contrast. For immunoelectron microscopy, cells were fixed with 3% formaldehyde for 60 minutes, infiltrated with a mixture of sucrose and polyvinylpyrrolidone, and frozen in liquid nitrogen. Ultrathin cryosections were prepared, labeled with antibodies, and embedded in methylcellulose (Liou et al., 1996). The specimens were observed using a JEOL 1200CX electron microscope operated at 100 kV.

Results

Identification of Rab18 as an LD constituent

LDs were purified from HepG2 cells, and their purity was verified by western blotting as described in the following section. Proteins were electrophoresed, cut into slices, subjected to in-gel digestion, and the resulting peptide mixtures were analyzed by LC-MS/MS (Kikuchi et al., 2004). Besides adipocyte differentiation-related protein (ADRP) and TIP47 (Londos et al., 1999; Miura et al., 2002), which have been shown to be LD components, more than 50 proteins were identified using the Mascot search engine. The overall profile was similar to the result reported recently by two other groups (Liu et al., 2004; Umlauf et al., 2004). The results regarding some of these proteins will be discussed in separate papers.

A number of Rab proteins were identified by proteomic analysis, i.e. Rab1, Rab2, Rab5, Rab6, Rab7, Rab8, Rab10, Rab11, Rab14, Rab18 and Rab32. To examine the extent to which the Rab proteins exist in LDs, we transfected cells with tagged Rab cDNAs and observed their distribution in comparison with LDs stained with BODIPY493/503 or Sudan III. Six Rabs, Rab1, Rab2, Rab5, Rab7, Rab10 and Rab18, were examined. Among these Rab proteins, only Rab18 showed conspicuous and almost exclusive labeling around LDs, whereas other Rabs were generally distributed in other parts of the cell or were distributed rather diffusely in the cytoplasm, and only a small number were seen around LDs (Fig. 1A). The LD localization of Rab18 was seen when either

FLAG or EGFP was used as a tag, and even when EGFP-Rab18 was observed without permeabilization. These results excluded the possibility of artifacts caused by the tag or the labeling procedure.

To compare the LD localization of the Rabs objectively, quantification was performed by two methods. First, the proportion of the LDs stained with BODIPY493/503 that were Rab-positive was determined. Only those LDs encircled completely by Rab labeling were counted as positive, and those seen adjacent to these Rabs or only partially surrounded by labeling were not included (Fig. 1B). Second, the proportion of cells in which more than 10% of the LDs were Rab-positive was determined (Fig. 1C). By either method, a high percentage of Rab18 was found to be localized to LDs. The other Rabs were also found around LDs, but only in much lower ratios than Rab18. Despite their less frequent LD localization, the functions of these Rabs may be related to LDs in some way. However, in the present study, we concentrated on Rab18 because of its conspicuous localization to LDs.

Fig. 1. (A) Double labeling of Rab proteins (red) and LDs (green) in HepG2 cells. Cells were transfected with cDNA of tagged Rab proteins. LDs were stained with BODIPY 493/503. Rab1, Rab5, Rab7, Rab10 and Rab18 were tagged with FLAG, and Rab2 was tagged with Myc.

Rab18 was consistently concentrated around LDs, whereas other Rabs were observed in the vicinity of LDs only infrequently. Bars, 10 μ m.
 (B) The proportion of Rab-positive LDs among all the LDs stained with BODIPY 493/503. Only cells showing positive Rab labeling were selected and counted. More than 500 LDs in 10 random areas were counted in two independent experiments.

(C) The proportion of cells in which the Rab-positive LDs were more than 10% of the total detected LDs. Only cells showing positive Rab labeling were selected and counted. More than 30 cells in 10 random areas were counted in two independent experiments. (D) Double labeling of EGFP-tagged Rab18 (green) and LDs (red) in HepG2 cells. The distributions of wild-type Rab18(WT) and GTPase-deficient Rab18(Q67L) were confined to LDs stained with Sudan III, while constitutively GDP-bound Rab18(S22N) was observed diffusely in the cytoplasm. Scale bars: 10 μ m.

We next examined whether the LD localization of Rab18 was dependent on its activation. Based on the highly conserved sequence among Rab proteins, we constructed a GTPase-deficient mutant (Q67L) and a constitutively GDP-bound mutant (S22N) of Rab18, and observed the distribution of EGFP- and FLAG-tagged molecules in HepG2 cells. Rab18(Q67L) showed localization to LDs in the same way as Rab18(WT: wild-type), whereas Rab18(S22N) was seen diffusely in the cytoplasm and did not show any concentration around LDs (Fig. 1D). These observations implied that the localization of Rab18 to LDs

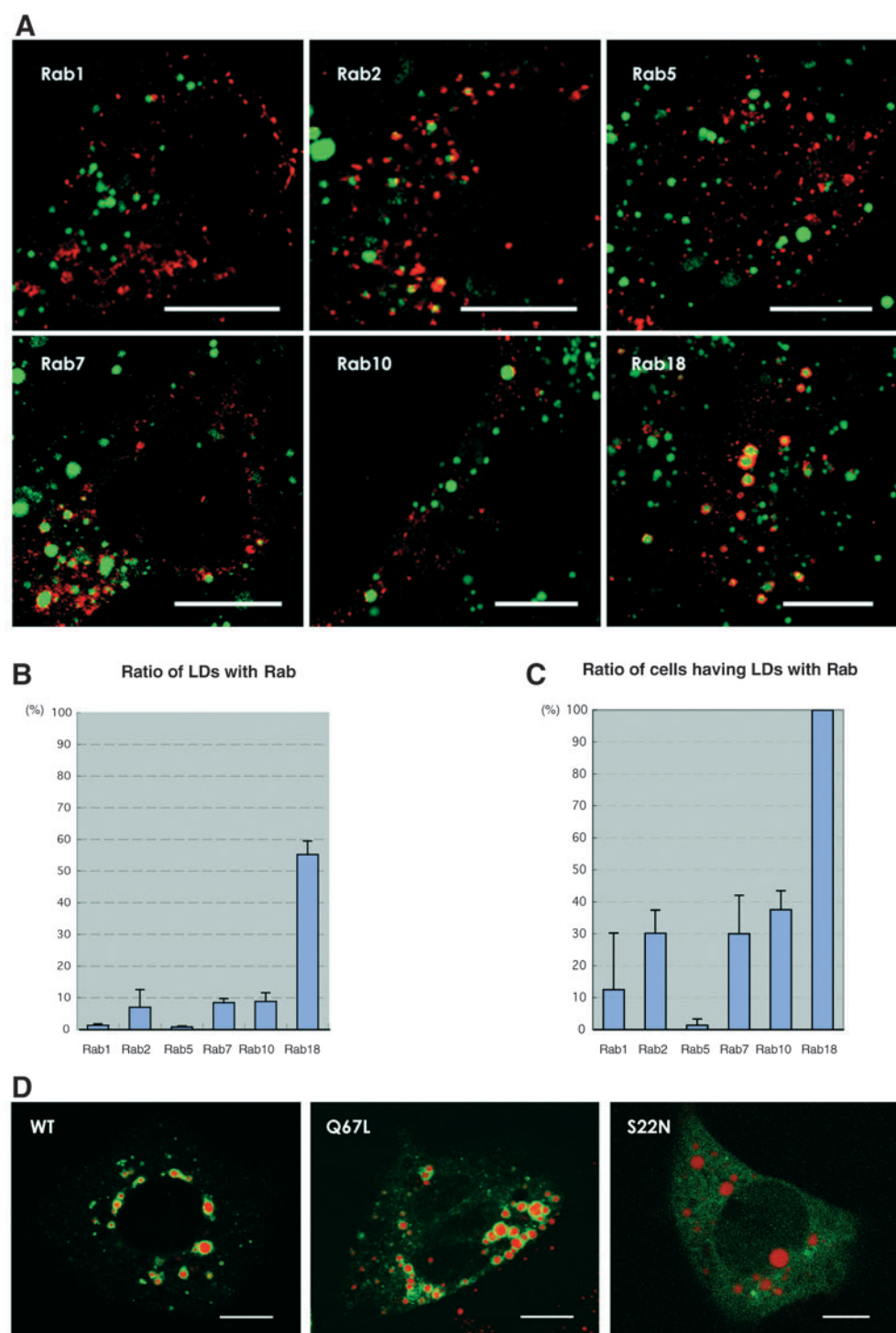


Fig. 2. (A) Western blotting of sucrose density-gradient fractions from HepG2. An equal volume from each fraction was loaded. Both ADRP and Rab18 were strongly present in the top floating LD fraction (#1). There was also some Rab18 in the bottom fractions containing soluble and membrane proteins (#7, #8). EEA1, Lamp1, syntaxin 6, and calnexin were detected only in the bottom fractions (#6-8). (B) Double labeling of endogenous Rab18 (red) and LDs (green) in HepG2 cells. LDs were stained with BODIPY 493/503. Antibody labeling for Rab18 was concentrated around LDs. Note that there were LDs that were not associated with anti-Rab18 (arrowheads). Scale bar: 10 µm. (C) Double labeling of endogenous Rab18 (green) and endosomal markers (red). EEA1 and transferrin receptor (Tf-R) (upper panel), and lysobisphosphatidic acid (LBPA) and Lamp1 (lower panel) were used as markers for early and late endosomes, respectively. Rab18 did not show co-distribution with any of the endosomal markers. Scale bars: 10 µm.

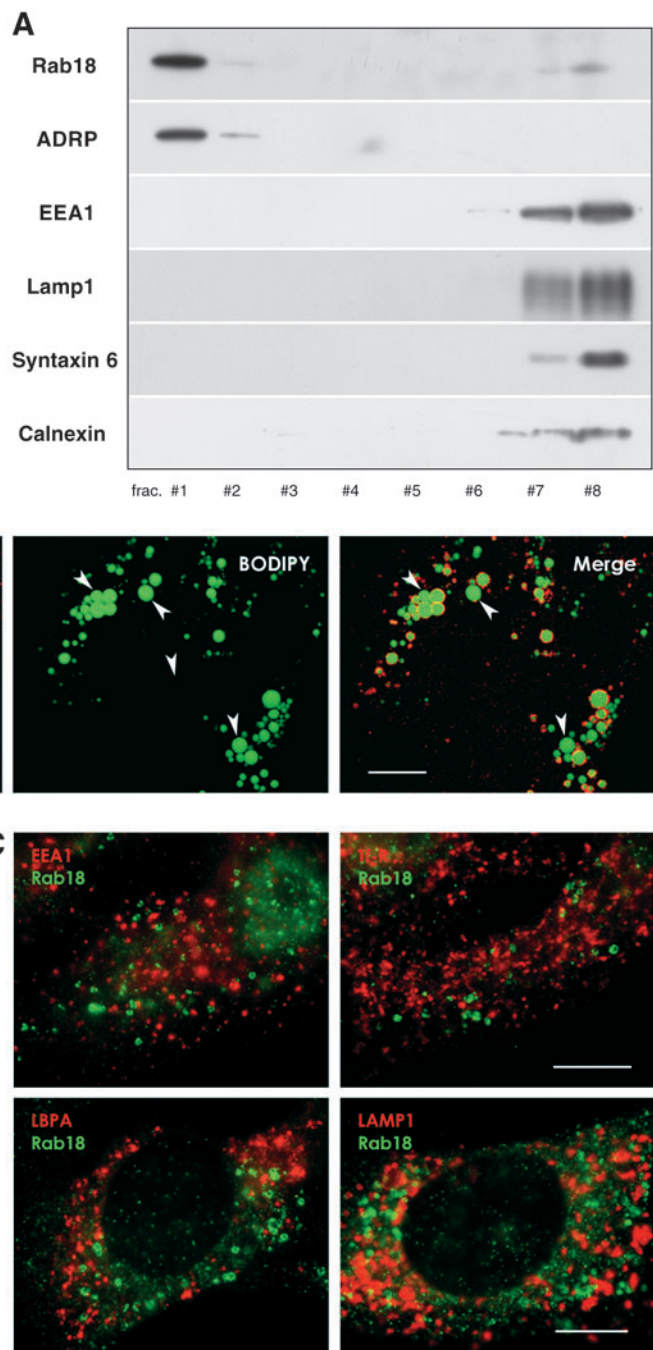
is regulated by its guanine nucleotide status.

Localization of endogenous Rab18

We raised a polyclonal anti-Rab18 antibody in rabbits using a synthetic peptide as the antigen. On western blotting, the antibody reacted specifically with a 23 kDa band from human and mouse samples. Cross-reactivity with other Rabs was checked by applying the antibody to cell samples transfected with tagged Rab proteins (i.e. Rab1, Rab2, Rab3, Rab5, Rab7, Rab9 and Rab10); in both immunofluorescence microscopy and western blotting, the antibody was confirmed not to react with the other Rabs (data not shown).

Western blotting of subcellular fractions of HepG2 showed that the anti-Rab18 antibody reacted intensely with the top floating fractions, which were highly enriched with LDs, as shown by its reactivity with anti-ADRP (Fig. 2A). When gels were loaded with an equal volume from each fraction, the immunoreactivity for Rab18 was also seen in the bottom fractions containing membrane and soluble proteins. The purity of the LD fraction was confirmed by the absence of other organelle markers; EEA1 for the early endosome, Lamp1 for the late endosome/lysosome, syntaxin 6 for the trans-Golgi network, and calnexin for the ER were only detected in the bottom fractions. In our previous study we also showed that markers for the Golgi apparatus, ER and the plasma membrane were not found in the LD fraction (Fujimoto et al., 2001).

Using immunofluorescence microscopy of HepG2 and 3T3 cells, the anti-Rab18 antibody was shown to be present in a ring around BODIPY493/503-stained LDs (Fig. 2B). Notably, a subpopulation of LDs were not labeled by anti-Rab18 antibody (arrowheads in Fig. 2B). The labeling was abolished by pre-absorption of the anti-Rab18 antibody with the antigen peptide or when it was omitted from the procedure (data not shown). These observations supported the results of LC-MS/MS and immunofluorescence microscopy of tagged Rab18, and demonstrated that endogenous Rab18 was localized to LDs.



A previous study showed that Rab18 was distributed in the endosomal vesicles of MDCK cells (Lutcke et al., 1994). To examine this possibility, double labeling for Rab18 and endosomal markers was performed. For the late endosome, we labeled for LBPA and Lamp1, and for the early endosome, we labeled for EEA1 and transferrin receptor. However, Rab18 did not overlap with any of the endosomal markers (Fig. 2C). Based on the result of immunofluorescence microscopy and western blotting, we concluded that Rab18 was localized to the LDs in the cell types examined. The disparity between the present result and those reported previously (Lutcke et al., 1994) cannot be explained easily, but it is notable that a similar disparity with regard to the localization of TIP47 has been

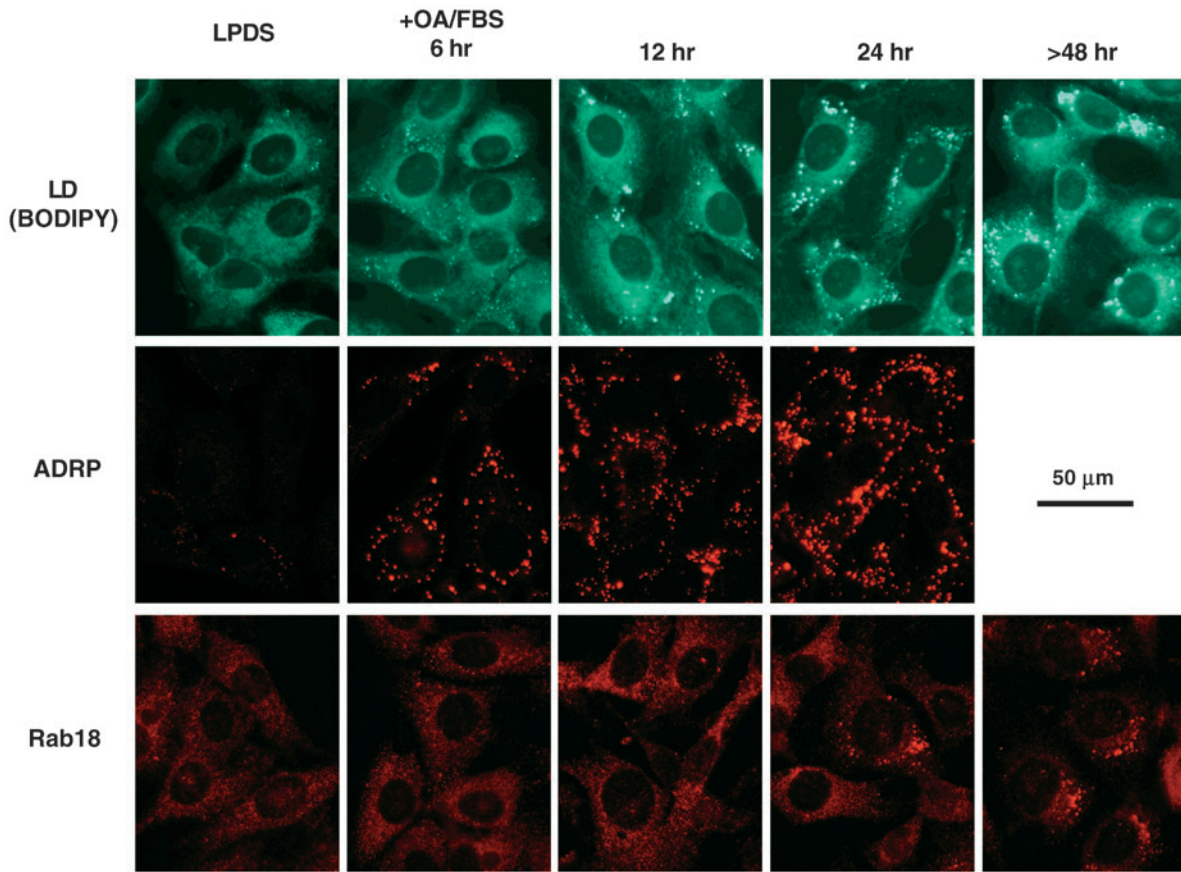


Fig. 3. Time course of LD formation (stained with BODIPY 493/503) in relation to ADRP and Rab18 in 3T3 cells loaded with oleic acid. Cells were cultured in medium containing 2% LPDS for 2 days, and then transferred to medium with 10% FBS with 200 μ M oleic acid-BSA complex (OA/FBS). LDs, ADRP and Rab18 were not detected in the cells kept in LPDS. As early as 6 hours after transfer to OA/FBS medium, LDs and ADRP were observed as bright dots that increased in number and brightness thereafter. In contrast, Rab18 was barely visible as dots at 6 or 12 hours in OA/FBS medium, and was seen clearly only after 24 hours in OA/FBS medium.

reported by other groups (Barbero et al., 2001; Wolins et al., 2001; Miura et al., 2002). Proteins that have a propensity to localize to LDs may be affected by subtle differences in experimental conditions, and may be distributed in other locations under some circumstances.

To examine the time course of ADRP and Rab18 appearance in relation to de novo LD formation, 3T3 cells were cultured in the presence of 2% lipoprotein-deficient serum (LPDS) for 2 days, followed by the addition of 200 μ M oleic acid (OA) complexed to BSA in 10% FCS. Before the addition of OA and FCS, none of the labels were detected as fluorescent dots (Fig. 3). Six hours after the addition of OA and FCS, LDs appeared, and ADRP was observed as ring-shaped fluorescence around them. In contrast, Rab18 fluorescence was very weak at 6 hours; although it became detectable at later time points, the frequency of labeling was far less than that of ADRP.

Effect of Rab18 overexpression on LDs

When triple labeling of endogenous Rab18, ADRP and LDs was performed in HepG2, both Rab18 and ADRP were shown to be associated with BODIPY 493/503-positive LDs as expected. However, the labeling intensity of Rab18 and ADRP showed clear reciprocity in most cases, i.e. in LDs where the Rab18

labeling was intense, ADRP labeling was relatively weak, and vice versa (Fig. 4A). These results suggested that the presence of Rab18 may decrease the amount of ADRP in LDs. Therefore, we examined the consequences of Rab18 overexpression on ADRP. When EGFP-Rab18(WT) was introduced, it was distributed around Sudan III-positive LDs in HepG2 cells, but EGFP-Rab18(WT) and ADRP hardly overlapped (Fig. 4B). The reduction of ADRP expression in the Rab18-overexpressing cell was also detected by western blotting of the total cell lysate. The cells transfected with non-tagged Rab18 cDNA expressed lower levels of ADRP than those transfected with empty vector (Fig. 4C). Similar results were obtained when cells transfected with EGFP-Rab18 cDNA were compared with those transfected with EGFP cDNA (data not shown).

The reduction of ADRP in LDs expressing Rab18 was further confirmed by triple labeling (Fig. 4D): BODIPY 493/503-positive LDs harboring EGFP-Rab18(WT) lacked or showed little ADRP labeling, and those with intense ADRP labeling were devoid of EGFP-Rab18(WT). The exclusion of ADRP from LDs was also observed when FLAG-tagged Rab18(WT) was introduced, verifying that the EGFP tag was not the cause of the phenomenon (data not shown). EGFP-Rab18(Q67L) gave the same result, but neither EGFP alone nor EGFP-Rab18(S22N) affected the labeling of ADRP in LDs.

(Fig. 4D). Reciprocity of EGFP-Rab18 and ADRP was also seen when isolated LDs were labeled with anti-ADRP and observed in comparison with EGFP-Rab18 (Fig. 4E). These results indicated that overexpression of Rab18 reduces the amount of ADRP in LDs.

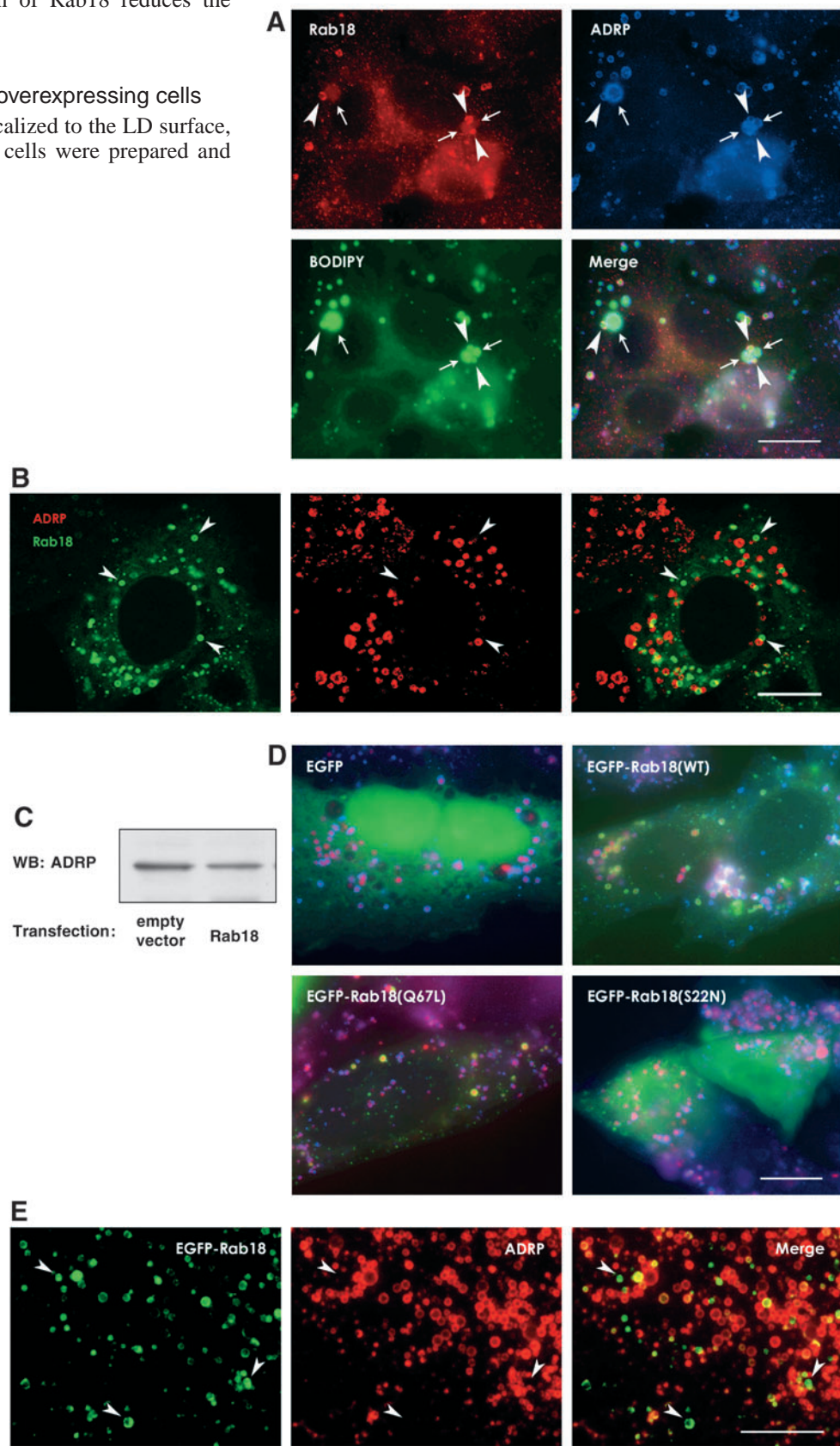
Ultrastructural analysis of Rab18-overexpressing cells

To confirm that EGFP-Rab18 was localized to the LD surface, ultrathin cryosections of transfected cells were prepared and

Fig. 4. (A) HepG2 cells were triple labeled for endogenous Rab18 (red), ADRP (blue), and LDs (green). BODIPY 493/503-stained LDs were labeled for Rab18 and ADRP, but the labeling intensity for Rab18 and ADRP appeared to be reciprocal in most cases. LDs showing strong Rab18 and weak ADRP staining are indicated by arrowheads, and those with the reverse pattern are indicated by arrows. Scale bar: 10 μm. (B) HepG2 cells transfected with EGFP-Rab18(WT) cDNA were labeled with anti-ADRP. Both EGFP-Rab18(WT) (green) and ADRP (red) are visible as small rings of fluorescence, but there is very little overlap. Some Rab18-positive, ADRP-negative ring-shaped fluorescent signals are marked by arrowheads. Scale bar: 10 μm. (C) Western blotting of ADRP. HepG2 cells were transfected with empty vector or Rab18 cDNA. Equal amounts (20 μg) of the total cell lysates were electrophoresed and probed with anti-ADRP antibody. Expression of Rab18 caused a reduction of ADRP. (D) 3T3 cells, expressing EGFP, EGFP-Rab18(WT), EGFP-Rab18(Q67L), or EGFP-Rab18(S22N) (green), were further labeled with anti-ADRP (blue) and Sudan III (red). Merged images of the three colors are shown. EGFP and EGFP-Rab18(S22N) were distributed diffusely in the cytoplasm, and all the Sudan III-positive LDs were labeled with anti-ADRP. In contrast, in cells expressing EGFP-Rab18(WT) or EGFP-Rab18(Q67L), LDs were labeled for either EGFP-Rab18 or ADRP, and those showing both labels were scarce. Scale bar: 10 μm.

(E) LDs isolated from HepG2-expressing EGFP-Rab18(WT) (green) were labeled with anti-ADRP (red). LDs with strong EGFP-Rab18(WT) fluorescence generally showed weak ADRP labeling. EGFP-Rab18(WT)-positive, ADRP-negative LDs are indicated by arrowheads. Scale bar: 10 μm.

labeled with anti-GFP. Immunogold labeling was indeed seen along the surface of LDs, although LDs were usually observed



as an empty round space because of the difficulty of retaining lipid ester in ultrathin cryosections (Fig. 5A). At the same time, we often noticed thin membrane cisternae in the vicinity of EGFP-Rab18-positive LDs (arrows in Fig. 5A).

To clearly delineate the membrane cisterna, we examined resin-embedded sections of 3T3 cells transfected with EGFP-Rab18(WT). As observed in ultrathin cryosections, the cell frequently showed LDs apposed closely to thin membrane cisternae; occasionally LDs were encircled completely by the cisterna (Fig. 5B). The cisterna was often found to be continuous with the rough endoplasmic reticulum (ER) or was studded with ribosomes. In contrast, such extensive membrane apposition to LDs was seen only rarely in cells transfected with EGFP cDNA or in untreated control cells (Fig. 5C). The frequency of cells with LDs apposed to the membrane cisterna was counted in electron micrographs (Fig. 5F); more than 30 cells were taken at random, and LDs with closely apposed membranes over more than half of the perimeter were defined as positive. The frequencies were 41.4% in cells transfected with EGFP-Rab18(WT) cDNA and 3.4% in cells transfected with EGFP cDNA. In the present study, cells were used after transient transfection because more than 60% of the cells were transfected as judged by fluorescence microscopy. Several stably transfected cell lines were also prepared, but even after subcloning only 20–50% of the cells showed fluorescence. They showed LD-membrane apposition, but the frequency was lower than that of the transiently transfected cells.

The ER-derived membrane apposed to LDs was not likely to be the autophagic vacuole, because LC3, a marker of early autophagic vacuoles (Kabeya et al., 2000), was not detected around the EGFP-Rab18-positive LDs by immunofluorescence microscopy, and autophagic vacuoles did not appear to be increased in cells expressing EGFP-Rab18 as determined by electron microscopy (data not shown).

Down-regulation of ADRP induces membrane apposition to LDs

The above results demonstrated that overexpression of Rab18 causes a decrease in the level of ADRP in LDs as well as close membrane apposition between LDs and the ER-derived membrane. To examine whether the decrease in ADRP in LDs was the cause of the membrane apposition, we applied two different methods to decrease ADRP and examined whether similar structural changes were induced: one was knockdown of ADRP by RNA interference, and the other was brefeldin A (BFA) treatment.

For RNA interference, cells transfected with siRNA for ADRP knockdown were compared with those transfected with control scrambled siRNA. About 50% reduction of ADRP expression was verified by western blotting (Fig. 5D-1). By electron microscopy, cells treated with ADRP siRNA frequently showed LDs surrounded by the neighboring membrane cisternae (48.1%), which were very similar to the structure in Rab18-overexpressing cells. In contrast, such structures were hardly observed in cells treated with control siRNA (3.7%) (Fig. 5D-2,F).

In a previous study, we observed that the amount of ADRP in LDs was reduced significantly by treating cells with BFA (Nakamura et al., 2004). Electron microscopy of cells treated

with BFA for 5 hours showed that LDs were surrounded by thin membrane cisternae in the majority of cells (82.8%). Such a disposition was seldom observed in control untreated cells (6.9%; Fig. 5E,F). Virtually all LDs in BFA-treated cells showed apposition to the ER, whereas in cells transfected with pEGFP-Rab18 cDNA or ADRP siRNA, LDs showing apposition to the ER coexisted with those without such a disposition. This difference can be explained at least partly by the penetration ratio of the procedures: BFA should affect all the cells and LDs with the same strength, but the ratio of transfected cells was about 60–70% with variable intensity as estimated by fluorescence microscopy.

Discussion

Rab proteins in LDs

By proteomic analysis of purified LDs, we found that a number of Rab proteins exist in LDs, observations that were similar to the reports by two other groups (Liu et al., 2004; Umlauf et al., 2004). Tagged Rabs were distributed around LDs to variable degrees, but with the exception of Rab18, they were mostly distributed to locations other than the LDs, and only a fraction of the labeling was found around LDs. The relative scarcity of these Rabs in LDs does not necessarily exclude their functional significance, and they might be further recruited to LDs under some circumstances. However, owing to the unique characteristics of the LD surface (Tauchi-Sato et al., 2002), it is possible that some of the Rabs adhered to the LDs during the purification procedure. Further studies are required to determine whether the existence of a variety of Rabs in the purified LD samples has any physiological significance.

Mechanism by which Rab18 causes elimination of ADRP from LD

When cells were transfected with Rab18 cDNA, LDs harboring exogenous Rab18 showed weaker ADRP labeling than the others. This observation can be explained if expression of Rab18 induces de novo formation of LDs containing little ADRP, but the following results indicated that Rab18 was recruited to pre-existing LDs and replaced ADRP. First, overexpression of Rab18 did not increase the number or the total volume of LDs observed by fluorescence microscopy (data not shown); second, even when HepG2 cells were cultured in 2% LPDS to minimize de novo LD formation, recruitment of Rab18 to remaining LDs occurred to a similar extent.

These observations raise the question of how Rab18 decreases ADRP in LDs. Interestingly, ADRP is also eliminated from LDs by expression of perilipin (Brasaemle et al., 1997) and hepatitis C virus (HCV) core protein (data cited in McLauchlan, 2000). We also observed that the N-terminal truncation mutant of caveolin-3 that is distributed to LDs (Pol et al., 2001) also displaced ADRP (K.T.-S. and T.F., unpublished). However, it is unlikely that these proteins compete with ADRP for common specific binding sites in LDs for several reasons. First, in the case of perilipin, despite some similarity to ADRP in the N-terminal PAT-1 domain (Londos et al., 1999), binding to LDs is not mediated by the domain, but by the adjacent short hydrophobic segments (Garcia et al., 2003; Garcia et al., 2004). Second, targeting of HCV core protein and caveolins to LDs requires a long

hydrophobic domain (Hope and McLauchlan, 2000; Fujimoto et al., 2001; Ostermeyer et al., 2004), which is not found in ADRP or perilipin. Third, Rab18 does not appear to have any structural similarity to ADRP, perilipin, or HCV core protein. These properties suggest that any proteins recruited to the

LDs in large amounts could replace pre-existing ADRP sterically. Alternatively, the above proteins could recruit a common protein(s), which competes with ADRP in adherence to LDs. In the case of Rab18, effector proteins may also be involved.

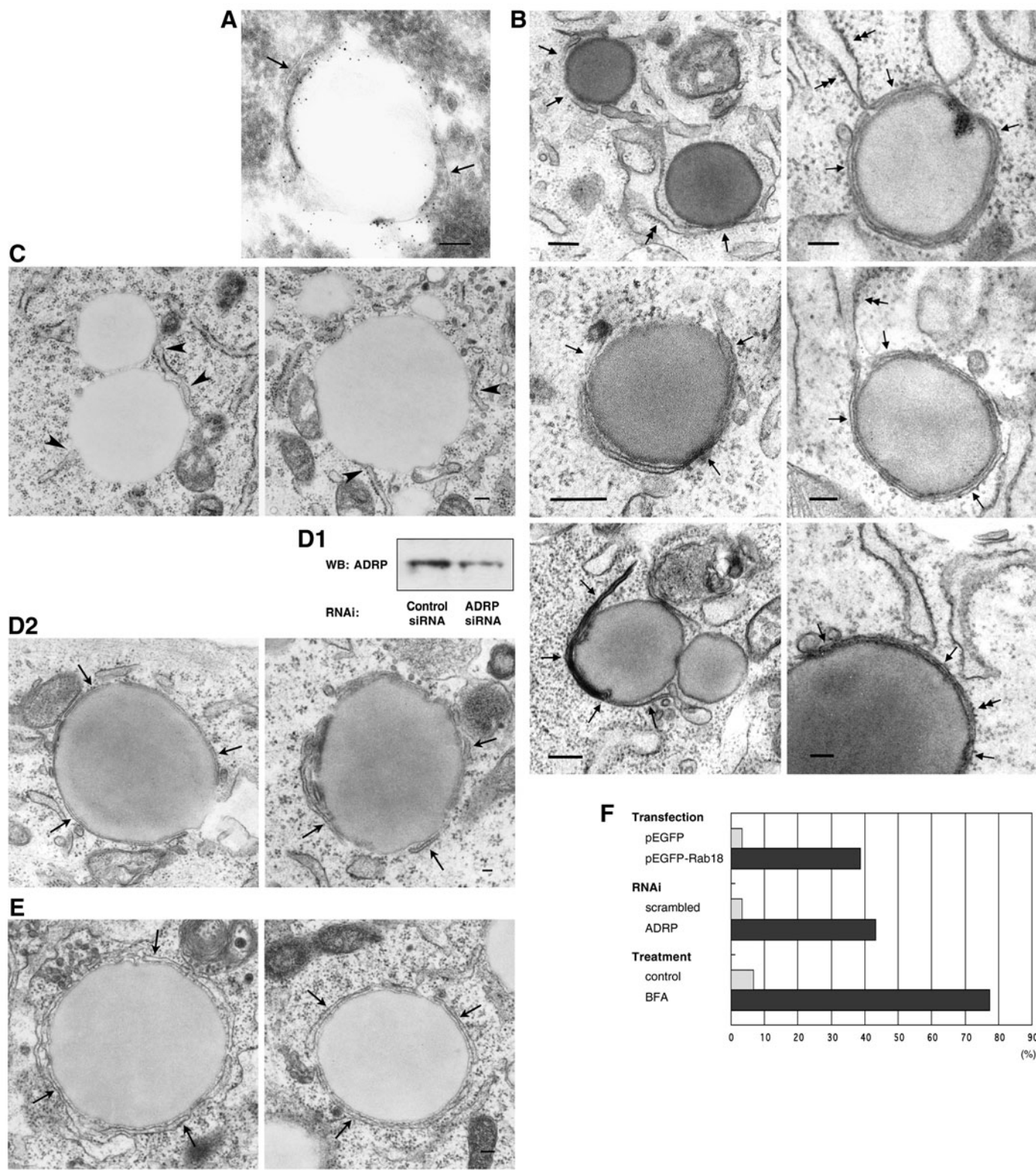


Fig. 5. See next page for legend.

Mechanism by which reduction of ADRP induces LD-ER apposition

We showed that reduction of ADRP in LDs causes close apposition of LDs and the ER-derived membrane. The detailed function of ADRP in LDs has not been determined, but its overexpression was shown to stimulate LD formation (Imamura et al., 2002; Nakamura and Fujimoto, 2003) and its reduction was reported to result in a decrease in LDs detectable by fluorescence labeling (Nakamura et al., 2004). These results suggested that ADRP is important for the maintenance of the LD structure, and that its reduction may compromise the stability of LDs.

Thus, the elimination of ADRP from LDs may be the only function of Rab18, i.e. reduction of ADRP may induce exactly the same results as Rab18 activation. However, it is also possible that Rab18 may activate specific effectors, which then exert downstream functions. For example, Rab18 itself or Rab18 effectors may bind to particular proteins in the ER membrane, and cause the apposition of LDs to a specific sub-compartment of the ER, whereas simple reduction of ADRP may induce nonspecific apposition to bulk ER. This kind of specificity may be important because the LD-ER apposition may be related to lipid transport as discussed in the following section.

Apposition of ER and other organelles

In hepatocytes, LDs are believed to form in an ER sub-compartment enriched with lipid ester-synthesizing enzymes; LDs are likely to be detached from the ER, and then to dock to another ER sub-compartment where lipid esters in the LDs are utilized to generate very low-density lipoproteins (VLDL)

Fig. 5. (A) Immunogold electron microscopy of HepG2 cells expressing EGFP-Rab18(WT). Ultrathin cryosections were labeled with anti-GFP antibody. Most LDs appeared as vacant round spaces because lipid esters were not retained well in the sections. Gold labeling was observed along the rim of LDs. Notably, thin membrane cisternae were often seen adjacent to the labeled LD (arrows). Scale bar: 100 nm. (B) Conventional electron microscopy of 3T3 cells expressing EGFP-Rab18(WT). LDs were frequently apposed to thin membrane cisternae (arrows). The direct continuity of the membrane cisterna and the rough ER (double arrows in the upper left, upper right and middle right figures), and the ribosomes in the membrane cisterna (double arrows in the lower right figure) were observed in many cases. Scale bars: 100 nm. (C) Conventional electron microscopy of control 3T3 cells. Small ER cisternae were occasionally found adjacent to LDs (arrowheads), but contacts between them were seldom extensive. Scale bar: 100 nm. (D) 3T3 cells treated with siRNA for knockdown of the expression of ADRP. (D-1) Western blotting of ADRP. Cells were treated with control random siRNA or ADRP siRNA, and equal amounts of the total cell lysates (20 µg) were electrophoresed. The expression of ADRP was reduced by more than 50% by this procedure. (D-2) In cells treated with ADRP siRNA, LDs in apposition with thin membrane cisternae were frequently observed (arrows). Scale bar: 100 nm. (E) Conventional electron microscopy of 3T3 cells treated with brefeldin A for 5 hours. Most LDs were surrounded by thin membrane cisternae (arrows). Scale bar: 100 nm. (F) Frequency of 3T3 cells with LDs in close membrane apposition. More than 30 cells were chosen randomly, and only LDs with membrane cisternae apposed to more than half its circumference were counted as positive. The transfection efficiency was no less than 60% as determined by fluorescence microscopy.

(Gibbons et al., 2000; Murphy, 2001) [for a different possible mechanism of LD formation in other cell types, see Robenek et al. (Robenek et al., 2004)]. Thus, LDs and the ER could exist in proximity in two situations: LD formation and LD docking. If the Rab18-induced LD-ER apposition is involved in LD formation, recruitment of Rab18 should be observed concomitantly with lipid esterification. However, upon addition of oleic acid, Rab18 was detectable only at much later times than LDs or ADRP (Fig. 3). This observation suggests that the LD-ER apposition induced by Rab18 may not be related to the LD formation process.

ER has been shown to appose to other organelles (Voelker, 2003; Levine, 2004). The specialized ER region in contact with mitochondria is referred to as the mitochondria-associated membrane, or MAM (Pickett et al., 1980; Rusinol et al., 1994). MAM is enriched with phosphatidylserine synthase (Vance, 1990), and is thought to be involved in transport of phosphatidylserine from the ER to the mitochondria (Voelker, 2003). More recently, close contact with the plasma membrane was reported in yeast, and the apposed ER region is called the plasma membrane-associated membrane, or PAM (Pichler et al., 2001). The apposition between the ER and LDs is observed frequently in various steroidogenic cells, and has been suggested to be involved in mobilization of stored cholesterol esters for steroid synthesis (Rhodin, 1974; Fawcett, 1981). The present result is consistent with this hypothesis. In accordance with the nomenclature of MAM and PAM, we propose that the ER region apposed to LDs should be called the lipid droplet-associated membrane, or LAM.

Although the mechanism of phosphatidylserine transport between MAM and mitochondria is beginning to be elucidated, it is not yet known how the apposition between the ER and other organelles is formed (Voelker, 2003). The present study showed, for the first time, that a Rab protein is involved in apposition of the ER membrane. It would be of interest to determine whether other GTP-binding proteins are also involved in the formation of MAM, PAM and other membrane appositions. A number of questions remain to be answered regarding the apposition: e.g. how stable is it?; how is it regulated?; what kind of proteins and lipids are involved?, etc. Elucidation of the molecular mechanism responsible for the apposition would also lead to an understanding of its function.

Functional heterogeneity of LD

The present results showed that LDs in a cell could have ADRP and Rab18 in variable ratios, which probably reflects the diverse functional states of the LDs. As speculated above, ADRP is likely to stabilize LDs, and its reduction may lead to mobilization of the lipid content. We suppose that Rab18 may offer a physiological mechanism to regulate the amount of ADRP. ARF1 may also be involved in regulation by dissociation of ADRP from LDs (Nakamura et al., 2004). The conjecture that the amount of ADRP is correlated with LD function was supported by the observation that ER-linked LDs lacked ADRP, while independent LDs contained it (Hayashi and Su, 2003).

It is becoming clear that the LD is not a static organelle involved only in storing excessive lipids. The contents of LDs and their relationship to other organelles are regulated by intricate mechanisms, and LDs in different functional states

must coexist in the cell. The physiological significance of LDs, especially in relation to intracellular lipid homeostasis, should be clarified through further studies of their regulatory mechanisms.

We are grateful to Toshihide Kobayashi (RIKEN), Yasuo Uchiyama (Osaka University), Yoshimi Takai (Osaka University), Toshiaki Katada (Tokyo University), Takuya Sasaki (Tokushima University) and Mitsunori Fukuda (RIKEN) for providing reagents, and to Tetsuo Okumura for technical assistance. This work was supported by Grants-in-Aid for Scientific Research (T.F. and H.T.), the 21st Century COE Program 'Integrated Molecular Medicine for Neuronal and Neoplastic Disorders' (T.F.), and CLUSTER Project 'Tokushima Proteomics Factory' (H.T.) of the Japanese Ministry of Education, Culture, Sports, Science and Technology.

References

- Barbero, P., Buell, E., Zulley, S. and Pfeffer, S. R. (2001). TIP47 is not a component of lipid droplets. *J. Biol. Chem.* **276**, 24348-24351.
- Bozza, P. T., Yu, W., Penrose, J. F., Morgan, E. S., Dvorak, A. M. and Weller, P. F. (1997). Eosinophil lipid bodies: specific, inducible intracellular sites for enhanced eicosanoid formation. *J. Exp. Med.* **186**, 909-920.
- Brasaemle, D. L., Barber, T., Wolins, N. E., Serrero, G., Blanchette-Mackie, E. J. and Londos, C. (1997). Adipose differentiation-related protein is an ubiquitously expressed lipid storage droplet-associated protein. *J. Lipid Res.* **38**, 2249-2263.
- Cole, N. B., Murphy, D. D., Grider, T., Rueter, S., Brasaemle, D. and Nussbaum, R. L. (2002). Lipid droplet binding and oligomerization properties of the Parkinson's disease protein alpha-synuclein. *J. Biol. Chem.* **277**, 6344-6352.
- Fawcett, D. W. (1981). *The Cell*. Philadelphia, USA: W. B. Saunders.
- Frolov, A., Petrescu, A., Atshaves, B. P., So, P. T., Gratton, E., Serrero, G. and Schroeder, F. (2000). High density lipoprotein-mediated cholesterol uptake and targeting to lipid droplets in intact L-cell fibroblasts. A single- and multiphoton fluorescence approach. *J. Biol. Chem.* **275**, 12769-12780.
- Fujimoto, T., Kogo, H., Ishiguro, K., Tauchi, K. and Nomura, R. (2001). Caveolin-2 is targeted to lipid droplets, a new "membrane domain" in the cell. *J. Cell Biol.* **152**, 1079-1085.
- Fujimoto, Y., Itabe, H., Sakai, J., Makita, M., Noda, J., Mori, M., Higashi, Y., Kojima, S. and Takano, T. (2004). Identification of major proteins in the lipid droplet-enriched fraction isolated from the human hepatocyte cell line HuH7. *Biochim. Biophys. Acta* **1644**, 47-59.
- Fukumoto, S. and Fujimoto, T. (2002). Deformation of lipid droplets in fixed samples. *Histochem. Cell Biol.* **118**, 423-428.
- Garcia, A., Sekowski, A., Subramanian, V. and Brasaemle, D. L. (2003). The central domain is required to target and anchor perilipin A to lipid droplets. *J. Biol. Chem.* **278**, 625-635.
- Garcia, A., Subramanian, V., Sekowski, A., Bhattacharyya, S., Love, M. W. and Brasaemle, D. L. (2004). The amino and carboxyl termini of perilipin a facilitate the storage of triacylglycerols. *J. Biol. Chem.* **279**, 8409-8416.
- Gibbons, G. F., Khurana, R., Odwell, A. and Seelaender, M. C. (1994). Lipid balance in HepG2 cells: active synthesis and impaired mobilization. *J. Lipid Res.* **35**, 1801-1808.
- Gocze, P. M. and Freeman, D. A. (1994). Factors underlying the variability of lipid droplet fluorescence in MA-10 Leydig tumor cells. *Cytometry* **17**, 151-158.
- Hayashi, T. and Su, T. P. (2003). Sigma-1 receptors (sigma(1) binding sites) form raft-like microdomains and target lipid droplets on the endoplasmic reticulum: roles in endoplasmic reticulum lipid compartmentalization and export. *J. Pharmacol. Exp. Ther.* **306**, 718-725.
- Imamura, M., Inoguchi, T., Ikuyama, S., Taniguchi, S., Kobayashi, K., Nakashima, N. and Nawata, H. (2002). ADRP stimulates lipid accumulation and lipid droplet formation in murine fibroblasts. *Am. J. Physiol. Endocrinol. Metab.* **283**, E775-E783.
- Kabeya, Y., Mizushima, N., Ueno, T., Yamamoto, A., Kirisako, T., Noda, T., Kominami, E., Ohsumi, Y. and Yoshimori, T. (2000). LC3, a mammalian homologue of yeast Apg8p, is localized in autophagosome membranes after processing. *EMBO J.* **19**, 5720-5728.
- Kikuchi, M., Hatano, N., Yokota, S., Shimozawa, N., Imanaka, T. and Taniguchi, H. (2004). Proteomic analysis of rat liver peroxisome: presence of peroxisome-specific isozyme of Lon protease. *J. Biol. Chem.* **279**, 421-428.
- Kobayashi, T., Stang, E., Fang, K. S., de Moerloose, P., Parton, R. G. and Gruenberg, J. (1998). A lipid associated with the antiphospholipid syndrome regulates endosome structure and function. *Nature* **392**, 193-197.
- Levine, T. (2004). Short-range intracellular trafficking of small molecules across endoplasmic reticulum junctions. *Trends Cell Biol.* **14**, 483-490.
- Liou, W., Geuze, H. J. and Slot, J. W. (1996). Improving structural integrity of cryosections for immunogold labeling. *Histochem. Cell Biol.* **106**, 41-58.
- Litvak, V., Shaul, Y. D., Shulewitz, M., Amarilio, R., Carmon, S. and Lev, S. (2002). Targeting of Nir2 to lipid droplets is regulated by a specific threonine residue within its PI-transfer domain. *Curr. Biol.* **12**, 1513-1518.
- Liu, P., Ying, Y., Zhao, Y., Mundy, D. I., Zhu, M. and Anderson, R. G. (2004). Chinese hamster ovary K2 cell lipid droplets appear to be metabolic organelles involved in membrane traffic. *J. Biol. Chem.* **279**, 3787-3792.
- Londos, C., Brasaemle, D. L., Schultz, C. J., Segrest, J. P. and Kimmel, A. R. (1999). Perilipins, ADRP, and other proteins that associate with intracellular neutral lipid droplets in animal cells. *Semin. Cell Dev. Biol.* **10**, 51-58.
- Lutcke, A., Parton, R. G., Murphy, C., Olkkonen, V. M., Dupree, P., Valencia, A., Simons, K. and Zerial, M. (1994). Cloning and subcellular localization of novel rab proteins reveals polarized and cell type-specific expression. *J. Cell Sci.* **107**, 3437-3448.
- McLauchlan, J. (2000). Properties of the hepatitis C virus core protein: a structural protein that modulates cellular processes. *J. Viral Hepat.* **7**, 2-14.
- Miura, S., Gan, J. W., Brzostowski, J., Parisi, M. J., Schultz, C. J., Londos, C., Oliver, B. and Kimmel, A. R. (2002). Functional conservation for lipid storage droplet association among Perilipin, ADRP, and TIP47 (PAT)-related proteins in mammals, Drosophila, and Dictyostelium. *J. Biol. Chem.* **277**, 32253-32257.
- Murphy, D. J. (2001). The biogenesis and functions of lipid bodies in animals, plants and microorganisms. *Prog. Lipid Res.* **40**, 325-438.
- Murphy, D. J. and Vance, J. (1999). Mechanisms of lipid-body formation. *Trends Biochem. Sci.* **24**, 109-115.
- Nakamura, N. and Fujimoto, T. (2003). Adipose differentiation-related protein has two independent domains for targeting to lipid droplets. *Biochem. Biophys. Res. Commun.* **306**, 333-338.
- Nakamura, N., Akashi, T., Taneda, T., Kogo, H., Kikuchi, A. and Fujimoto, T. (2004). ADRP is dissociated from lipid droplets by ARF1-dependent mechanism. *Biochem. Biophys. Res. Commun.* **322**, 957-965.
- Ohashi, M., Mizushima, N., Kabeya, Y. and Yoshimori, T. (2003). Localization of mammalian NAD(P)H steroid dehydrogenase-like protein on lipid droplets. *J. Biol. Chem.* **278**, 36819-36829.
- Ostermeyer, A. G., Paci, J. M., Zeng, Y., Lublin, D. M., Munro, S. and Brown, D. A. (2001). Accumulation of caveolin in the endoplasmic reticulum redirects the protein to lipid storage droplets. *J. Cell Biol.* **152**, 1071-1078.
- Ostermeyer, A. G., Ramcharan, L. T., Zeng, Y., Lublin, D. M. and Brown, D. A. (2004). Role of the hydrophobic domain in targeting caveolin-1 to lipid droplets. *J. Cell Biol.* **164**, 69-78.
- Pichler, H., Gaigg, B., Hrastnik, C., Achleitner, G., Kohlwein, S. D., Zellnig, G., Perktold, A. and Daum, G. (2001). A subfraction of the yeast endoplasmic reticulum associates with the plasma membrane and has a high capacity to synthesize lipids. *Eur. J. Biochem.* **268**, 2351-2361.
- Pickett, C. B., Montisano, D., Eisner, D. and Cascarano, J. (1980). The physical association between rat liver mitochondria and rough endoplasmic reticulum. I. Isolation, electron microscopic examination and sedimentation equilibrium centrifugation analyses of rough endoplasmic reticulum-mitochondrial complexes. *Exp. Cell Res.* **128**, 343-352.
- Pol, A., Luetterforst, R., Lindsay, M., Heino, S., Ikonen, E. and Parton, R. G. (2001). A caveolin dominant negative mutant associates with lipid bodies and induces intracellular cholesterol imbalance. *J. Cell Biol.* **152**, 1057-1070.
- Pol, A., Martin, S., Fernandez, M. A., Ferguson, C., Carozzi, A., Luetterforst, R., Enrich, C. and Parton, R. G. (2004). Dynamic and regulated association of caveolin with lipid bodies: modulation of lipid body motility and function by a dominant negative mutant. *Mol. Biol. Cell* **15**, 99-110.
- Prattes, S., Horl, G., Hammer, A., Blaschitz, A., Graier, W. F., Sattler, W., Zechner, R. and Steyrer, E. (2000). Intracellular distribution and mobilization of unesterified cholesterol in adipocytes: triglyceride droplets are surrounded by cholesterol-rich ER-like surface layer structures. *J. Cell Sci.* **113**, 2977-2989.

- Rhodin, J. A. G.** (1974). *Histology, A Text and Atlas*. New York: Oxford University Press.
- Robenek, M. J., Severs, N. J., Schlattmann, K., Plenz, G., Zimmer, K. P., Troyer, D. and Robenek, H.** (2004). Lipids partition caveolin-1 from ER membranes into lipid droplets: updating the model of lipid droplet biogenesis. *FASEB J.* **18**, 866-868.
- Rusinol, A. E., Cui, Z., Chen, M. H. and Vance, J. E.** (1994). A unique mitochondria-associated membrane fraction from rat liver has a high capacity for lipid synthesis and contains pre-Golgi secretory proteins including nascent lipoproteins. *J. Biol. Chem.* **269**, 27494-27502.
- Tauchi-Sato, K., Ozeki, S., Houjou, T., Taguchi, R. and Fujimoto, T.** (2002). The surface of lipid droplets is a phospholipid monolayer with a unique Fatty Acid composition. *J. Biol. Chem.* **277**, 44507-44512.
- Umlauf, E., Csaszar, E., Moertelmaier, M., Schuetz, G. J., Parton, R. G. and Prohaska, R.** (2004). Association of stomatin with lipid bodies. *J. Biol. Chem.* **279**, 23699-23709.
- Vance, J. E.** (1990). Phospholipid synthesis in a membrane fraction associated with mitochondria. *J. Biol. Chem.* **265**, 7248-7256.
- Voelker, D. R.** (2003). New perspectives on the regulation of intermembrane glycerophospholipid traffic. *J. Lipid Res.* **44**, 441-449.
- Wolins, N. E., Rubin, B. and Brasaemle, D. L.** (2001). TIP47 associates with lipid droplets. *J. Biol. Chem.* **276**, 5101-5108.
- Yu, W., Bozza, P. T., Tzizik, D. M., Gray, J. P., Cassara, J., Dvorak, A. M. and Weller, P. F.** (1998). Co-compartmentalization of MAP kinases and cytosolic phospholipase A2 at cytoplasmic arachidonate-rich lipid bodies. *Am. J. Pathol.* **152**, 759-769.



RAB18 Loss Interferes With Lipid Droplet Catabolism and Provokes Autophagy Network Adaptations

Fazilet Bekbulat^{1,†}, Daniel Schmitt^{1,†}, Anne Feldmann¹, Heike Huesmann¹, Stefan Eimer², Thomas Juretschke³, Petra Beli³, Christian Behl¹ and Andreas Kern¹

1 - Institute of Pathobiochemistry, University Medical Center of the Johannes Gutenberg University Mainz, Duesbergweg 6, 55128 Mainz, Germany

2 - Department of Structural Cell Biology, Institute for Cell Biology and Neuroscience, Goethe University Frankfurt, Max-von-Laue-Str. 13, 60438 Frankfurt, Germany

3 - Institute of Molecular Biology (IMB), Ackermannweg 4, 55128 Mainz, Germany

Correspondence to Andreas Kern and Christian Behl: Institute of Pathobiochemistry, University Medical Center of the Johannes Gutenberg University Mainz, Duesbergweg 6, Mainz, D-55128, Germany. cbeh@uni-mainz.de, akern@uni-mainz.de

<https://doi.org/10.1016/j.jmb.2019.12.031>

Edited by Martens Sascha

Abstract

Autophagy is dependent on appropriate lipid supply for autophagosome formation. The regulation of lipid acquisition and the autophagy network response to lipid-limiting conditions are mostly elusive. Here, we show that the knockout of the RAB GTPase RAB18 interferes with lipid droplet catabolism, causing an impaired fatty acid release. The resulting reduced lipid-droplet-derived lipid availability influences autophagy and provokes adaptive modifications of the autophagy network. These adjustments include increased expression and phosphorylation of ATG2B as well as augmented formation of the ATG12-ATG5 conjugate. Moreover, ATG9A shows an enhanced phosphorylation at amino acid residues tyrosine 8 and serine 14, resulting in an increased ATG9A trafficking. Via pharmacological inhibition of Y8 phosphorylation, we demonstrate that this ATG9A modification is important to maintain basal autophagy under RAB18 knockout conditions. However, while the network adaptations are sufficient to maintain basal autophagic activity, they are incapable of ensuring autophagy induction upon starvation, which is characterized by an enhanced lipid demand. Thus, here, we define the molecular role of RAB18 in connecting lipid droplets and autophagy, emphasize the significance of lipid droplets as lipid sources for the degradative pathway, and uncover a remarkable autophagy network plasticity, including phosphorylation-dependent ATG9A activation, to compensate reduced lipid availability in order to rescue basal autophagic activity.

© 2019 The Author(s). Published by Elsevier Ltd. This is an open access article under the CC BY license (<http://creativecommons.org/licenses/by/4.0/>).

Introduction

Macroautophagy (hereafter referred to as autophagy) is the eukaryotic lysosomal degradation pathway that mediates protein and organelle turnover and maintains cellular homeostasis [1]. Autophagic cargo is transported in vesicles, the so-called autophagosomes, to lysosomes for degradation and recycling of building blocks. The generation of

autophagosomes is highly dynamic and increases within minutes upon autophagy induction. Several conditions, including nutrient deprivation or rapamycin treatment, stimulate autophagy and result in activation of the AMP-activated kinase PRKAA1 and/or inhibition of the kinase MTOR [2]. Subsequently, ULK1 kinase is activated by phosphorylation, which is required for autophagosome generation in canonical autophagy [3].

The synthesis of double-membraned autophagosomes starts with a precursor membrane, the phagophore, which originates from specific omega-shaped domains (omegasomes) in the ER membrane [4–6]. The phagophore elongates by the addition of substantial amounts of lipids until it finally closes to form an autophagosome, fully engulfing the autophagic cargo. This process involves a cascade of proteins, including two ubiquitin-like conjugations systems, that mediate the formation of the ATG12-ATG5/ATG16L1 protein complex as well as the lipidation of Atg8 family members, such as MAP1LC3B (shortly LC3) [7]. The phosphatidylinositol-3-phosphate (PI(3)P)-binding protein WIPI2 is targeted to the omegasome and remains associated with the phagophore, where it recruits ATG16L1,

which forms a complex with the ATG12-ATG5 conjugate [8]. This complex shows E3 ligase-like activity that promotes the final step of Atg8 lipidation [9–12]. Lipid-conjugated Atg8 proteins associate with the growing phagophore and are essential for autophagosome formation [13]. The proteins stay (partially) attached to autophagic vesicles, resulting in their subsequent lysosomal degradation.

Besides protein processing, phagophore elongation is highly dependent on sufficient lipid supply [3]. Several cellular organelles or compartments, including the ER, plasma membrane, mitochondria, the Golgi complex, the ER-Golgi intermediate compartment, recycling endosomes [3,14], as well as lipid droplets (LDs) [15–17], have been suggested as sources that donate lipids via vesicles or membrane

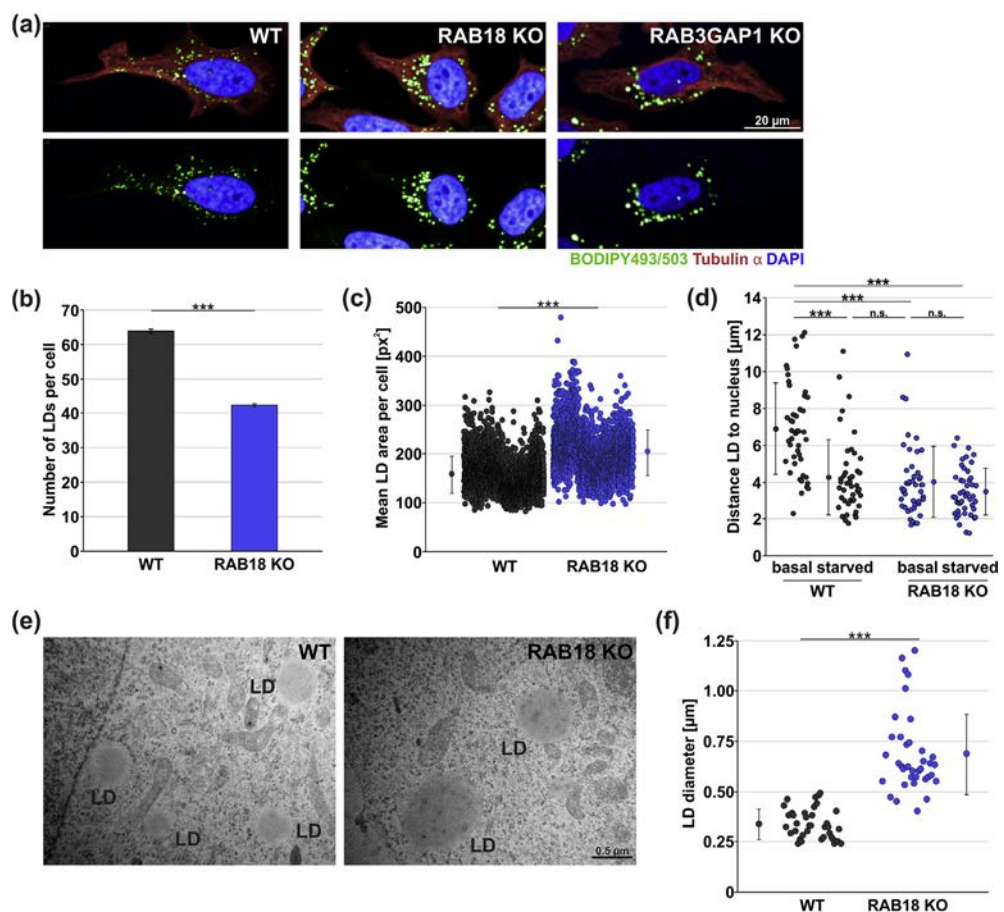


Fig. 1. The loss of RAB18 function results in an altered LD phenotype. (a) Representative confocal fluorescence images of LDs stained with BODIPY493/503 (green). Tubulin α staining (red) served to visualize cell area and DAPI (blue) stained nuclei. Approx. 2500 cells from six independent experiments have been analyzed. **(b)** Statistical analyses of LD number in approx. 2500 single WT and RAB18 KO cells. Statistics are depicted as mean \pm SEM. n = 6, t-test, ***P \leq 0.001. **(c)** Analyses of mean LD area in approx. 2500 single WT and RAB18 KO cells. Statistics are depicted as mean \pm SD. n = 6, t-test, ***P \leq 0.001. **(d)** Distance of LDs to the nucleus under basal and lipolytic conditions (2 h EBSS) has been analyzed in approx. 45 single WT and RAB18 KO cells from three independent experiments. Statistics are depicted as mean \pm SD. n = 3, t-test, ***P \leq 0.001. **(e)** Representative TEM images of LDs in WT and RAB18 KO cells. **(f)** For statistics of LD diameter, approx. 35 individual LDs have been analyzed and statistics are depicted as mean \pm SD. t-test, ***P \leq 0.001.

contact sites. However, the detailed process and regulation of autophagic lipid acquisition remain unresolved and the role and importance of LDs as lipid donors for autophagy have been discussed [18].

A key protein involved in autophagic lipid transfer is the multipass transmembrane protein ATG9A that connects the peripheral cellular compartments to autophagosome formation [19–22]. ATG9A directs vesicles from the cellular periphery to the site of phagophore maturation and supplies essential proteins and lipids [23–25]. Under basal autophagy

conditions, the majority of ATG9A is located at the Golgi complex and switches to a dispersed vesicular localization when autophagy is increased. Upon autophagy induction, the specific phosphorylations of ATG9A, mediated by ULK1 and SRC kinase [26,27], are enhanced and foster ATG9A trafficking dynamics, facilitating autophagosome formation.

LDs are lipid sources supporting phagophore elongation that act independently of ATG9A but in close functional association with the ER [15–17]. These cytoplasmic lipid stores are found in virtually all eukaryotic cells and contain neutral lipids, mainly

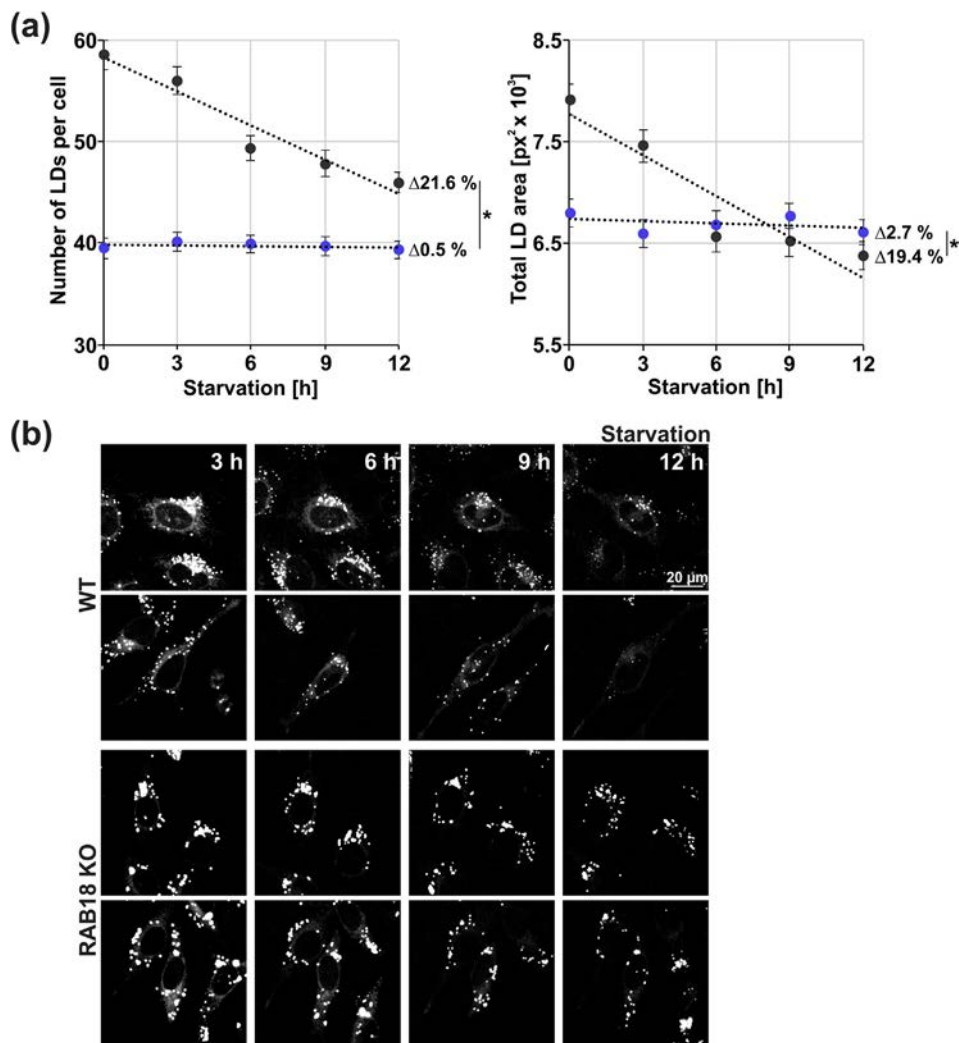


Fig. 2. The loss of RAB18 impedes fatty acid mobilization from LDs. (a) LD consumption upon lipolytic conditions (EBSS) in WT (gray) and RAB18 KO cells (blue). LDs were stained with BODIPY493/503. At each indicated time point, the number and total area of LDs in approx. 240 single WT or KO cells from three independent experiments were evaluated. By linear regression comparison, significant differences between the regression coefficients of each condition were analyzed: R^2 LD number: WT = 0.936, KO = 0.162, *** $P \leq 0.001$; R^2 LD area: WT = 0.871, KO = 0.137, ** $P \leq 0.01$. The absolute changes (Δ) in LD number and total area from time point 0 h–12 h were evaluated. $n = 3$, t -test, * $P \leq 0.05$. (b) Confocal fluorescence live cell imaging of cells treated with BODIPY558/568 C₁₂ during EBSS treatment. Cells were preprobed with 5 nM BODIPY558/568 C₁₂ for 24 h and incubated in fresh medium for 1 h before microscopy. The depicted cells are representative for approx. 20 imaged cells per condition from three independent approaches.

triacylglycerides (TAGs) and sterol esters, which are separated from the cytosol by a phospholipid monolayer, and are coated by a distinct set of proteins [28]. Under lipolytic conditions, TAGs are hydrolyzed by the activity of various lipases and the

generated fatty acids are utilized for energy metabolism or are modified to appropriate lipids within the ER [29]. Importantly, recent studies employing yeast or human cell lines have demonstrated that specific LD-associated lipases, including PNPLA2/ATGL

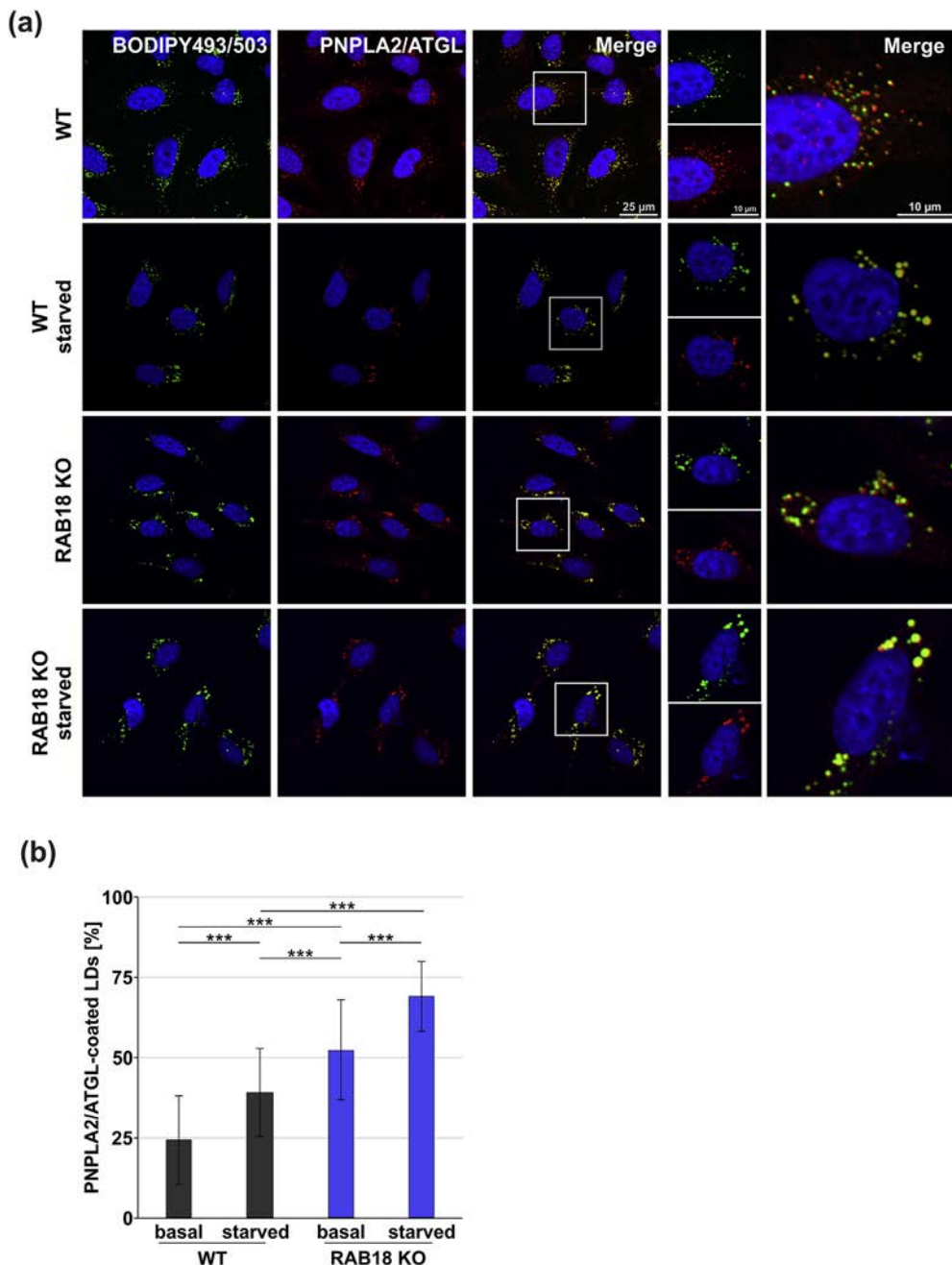


Fig. 3. The loss of RAB18 enhances the localization of PNPLA2/ATGL at LDs. (a) Representative confocal fluorescence images of cells stained with PNPLA2/ATGL (red), BODIPY493/503 (green), and DAPI (blue). WT cells are shown under basal and lipolytic conditions (2 h EBSS). For each condition, approx. 15 images from three independent approaches were obtained. (b) PNPLA2/ATGL colocalization with LDs under basal and lipolytic conditions (2 h EBSS) have been analyzed in approx. 45 single WT and RAB18 KO cells. Statistics are depicted as mean \pm SD. n = 3, t-test, ***P \leq 0.001.

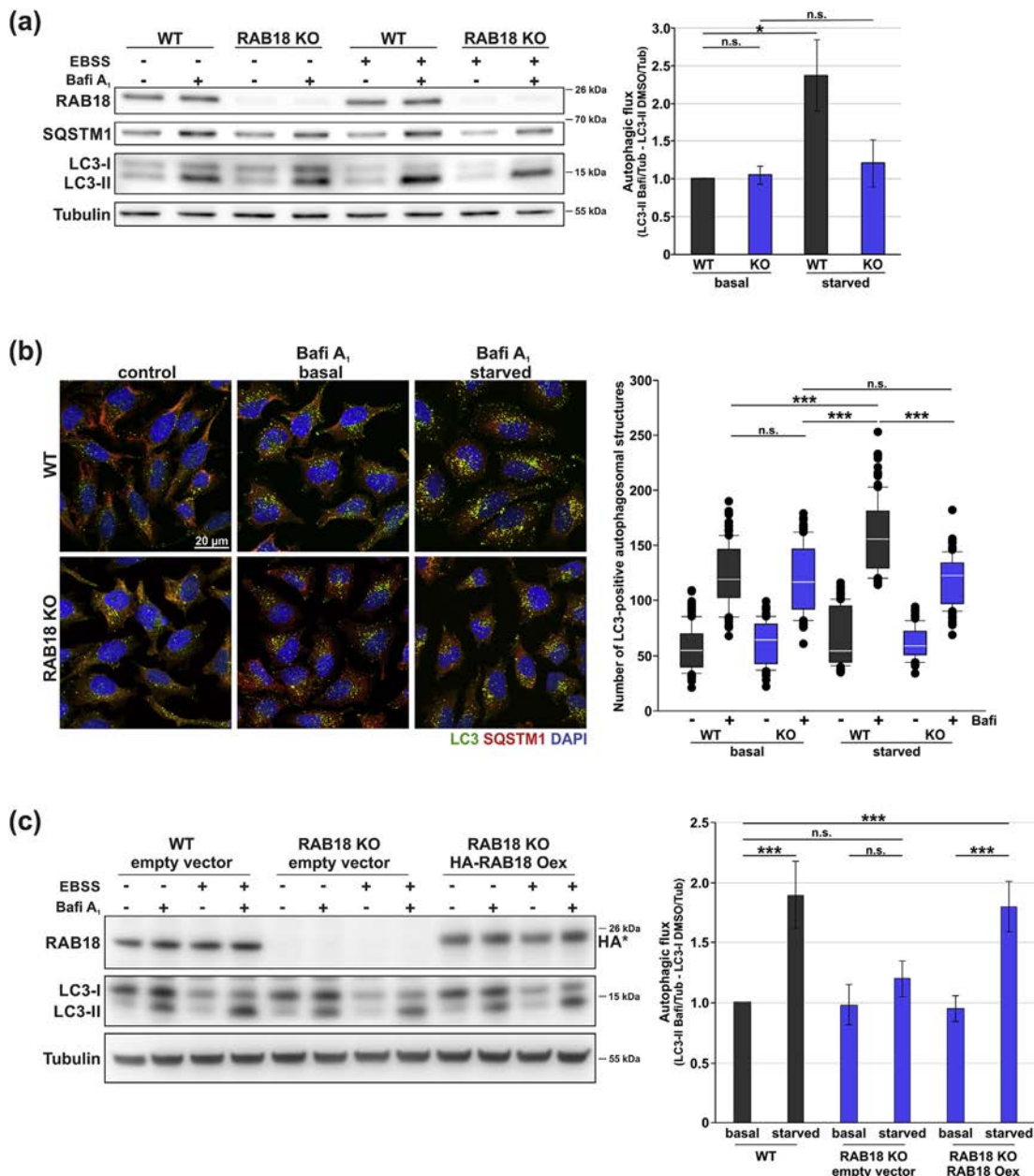


Fig. 4. Limited lipid availability affects autophagy in RAB18 KO cells. **(a)** Immunoblot analyses of autophagic activity under basal and induced conditions (2 h EBSS). Cells were treated with DMSO (control) or bafilomycin A₁ (Bafi A₁) for 2 h to allow LC3-II flux evaluation. LC3-II levels were corrected over the loading control Tubulin. Statistics are depicted as mean \pm SD. n = 4, One-Way ANOVA, n. s. = not significant, *P \leq 0.05. **(b)** Immunocytochemical stainings of LC3 (green) and SQSTM1/p62 (red). Nuclei were stained with DAPI (blue). Cells were treated with DMSO (control) or Bafi A₁ under basal conditions or upon EBSS treatment (2 h). For statistical analysis, autophagosomal structures (LC3) were quantified in approx. 120 single cells per cell line and condition from four independent experiments. One-Way ANOVA, n. s. = not significant, ***P \leq 0.001. Single channels as well as quantification of SQSTM1-positive structures are presented in Supplementary Fig. 7. **(c)** Immunoblot analyses of autophagic activity upon reintroduction of RAB18 under basal and induced conditions (2 h EBSS). Cells were transfected with empty vector or HA-tagged wild-type RAB18 and were treated with DMSO (control) or Bafi A₁ for 2 h. LC3-II levels were corrected over Tubulin. Statistics are depicted as mean \pm SD. n = 4, One-Way ANOVA, n. s. = not significant, ***P \leq 0.001.

and PNPLA5, modulate autophagy and that LD-derived lipids support the formation of autophagosomes [15–17,30].

The RAB GTPase RAB18 has functionally been associated with LD metabolism [31] and is a positive modulator of autophagy [32]. RAB18 localizes to LDs, and this association has been linked to a function in LD biogenesis and/or consumption [31,33–35]. The interaction of RAB18 with ER-linked tethering factors mediates the connection of LDs with the ER membrane and facilitates LD maturation [35–37]. In a human mammary carcinoma cell line (SUM159), however, an involvement of RAB18 in LD metabolism could not be observed [38]. Importantly, loss-of-function mutations in *RAB18* cause Warburg Micro syndrome (WARBM) [39], a severe human autosomal recessive (neuro-)developmental disorder. The molecular basis responsible for the pathogenesis remains unclear, yet, WARBM patient cells are characterized by an altered LD homeostasis [40].

In this study, we examined the impact of RAB18 on LD metabolism and autophagy. The stable knockout of the RAB GTPase provoked an LD phenotype that resembled WARBM patient cells. In-depth analysis revealed that fatty acid release was impaired in the absence of RAB18. The resulting insufficient LD-derived lipid availability influenced autophagy, causing adaptations in the autophagy network, which included an increased expression and altered phosphorylation of ATG2B as well as augmented levels of ATG12-ATG5 conjugates. Additionally, the phosphorylation of ATG9A and its trafficking were enhanced in RAB18 KO cells under basal autophagy conditions, which supported the maintenance of autophagic activity.

Thus, we were able to directly associate the role of RAB18 in LD catabolism with autophagy and to demonstrate the significant impact of LD-derived lipids on the degradative pathway. Moreover, we characterized autophagy network adaptations that

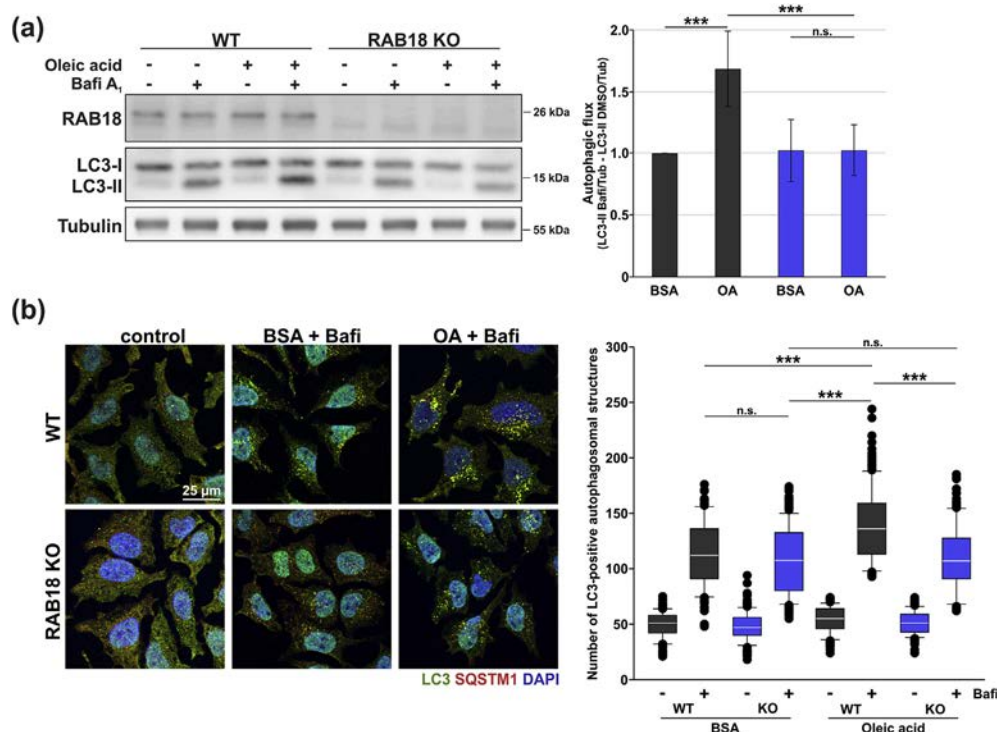
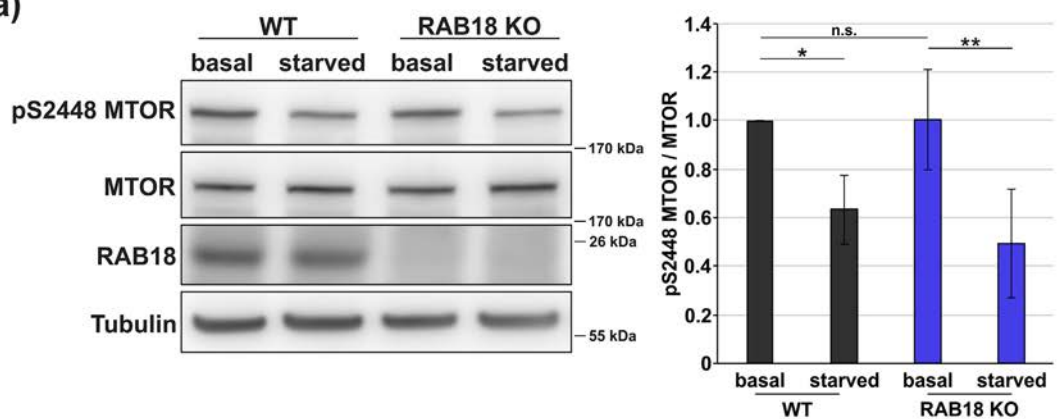
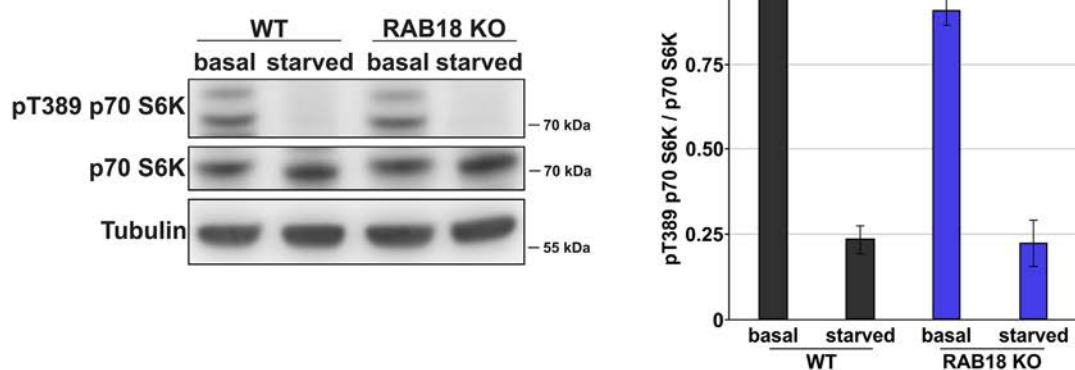


Fig. 5. Abundant lipid availability does not affect autophagy in RAB18 KO cells. (a) Immunoblot analyses of autophagic activity after oleic acid (OA) treatment. Cells were pretreated with BSA (control) or BSA-conjugated oleic acid and with DMSO (control) or baflomycin A₁ (Bafi A₁) for 3 h to allow LC3-II flux evaluation. Statistics are depicted as mean \pm SD, n = 4; One-Way ANOVA, n. s. = not significant, **P \leq 0.01. (b) Immunocytochemical stainings of LC3 (green) and SQSTM1 (red). Nuclei were stained with DAPI (blue). Cells were treated with DMSO (control) or Bafi A₁ under control conditions or upon OA treatment (2 h). Shown here are merged images, single channels are presented in Supplementary Fig. S9. For statistical analysis, autophagosomes (LC3) were quantified in approx. 150 single cells per cell line and condition from three independent experiments. One-Way ANOVA, n. s. = not significant, ***P \leq 0.001. In Supplementary Fig. S9 SQSTM1-positive autophagosomes are statistically analyzed.

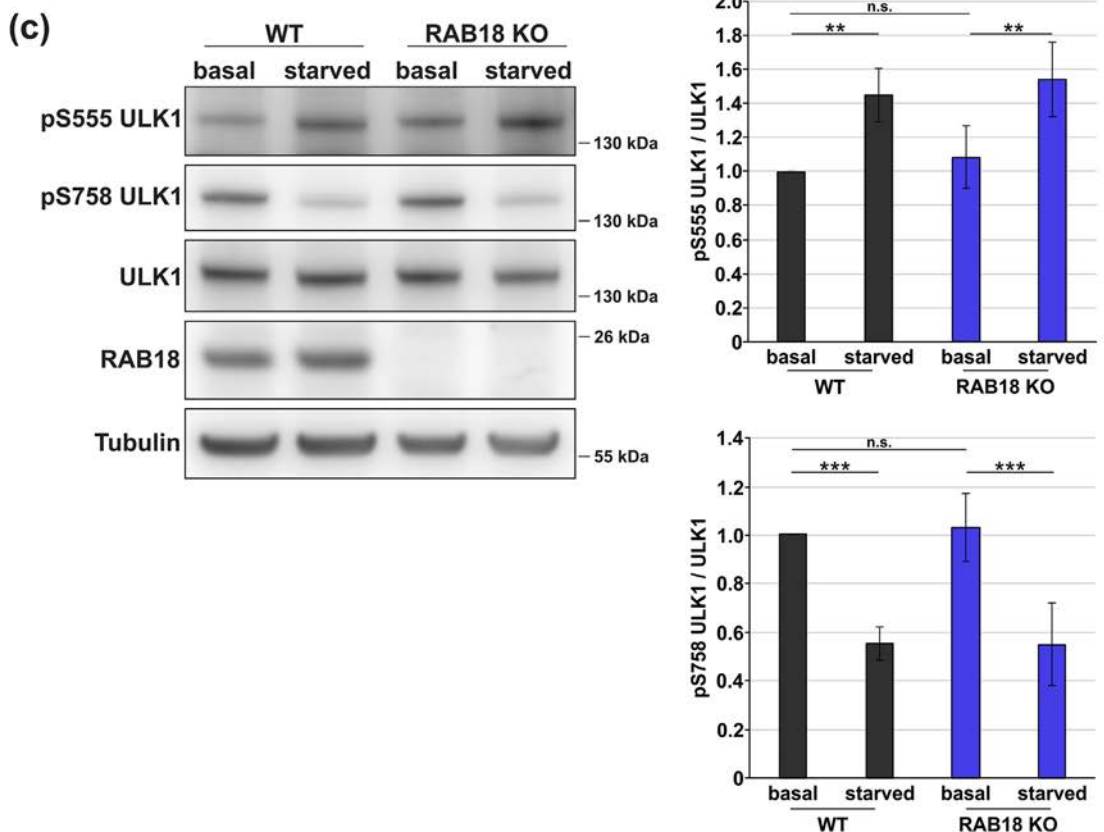
(a)



(b)



(c)



rescue basal autophagic activity under conditions of decreased lipid availability.

Results

Previously, employing transient genetic manipulations, we have characterized RAB18 as a positive modulator of autophagy [32]. To conduct more detailed analyses on RAB18 function, we generated stable KO HeLa cells of the RAB GTPase, employing the CRISPR/Cas9 technology, and selected two independent clonal cell lines ([Supplementary Fig. S1](#)).

Initially, we focused on the impact of the RAB18 KO on LDs and visualized the lipid reservoirs with BODIPY493/503, which stains neutral lipids. Fluorescence imaging revealed a striking LD appearance in the absence of RAB18 ([Fig. 1a](#), [Supplementary Fig. 2](#)), similar to WARB patient cells [40]. LDs were reduced in number and enlarged in size and accumulated in the perinuclear region of the cell with a reduced mean distance from the nucleus when compared to HeLa wild-type (WT) cells ([Fig. 1a–d](#)). This result was further strengthened by transmission electron microscopy (TEM), showing enlarged LDs in KO cells ([Fig. 1e, f](#)), which were mostly localized close to the nucleus. Importantly, reintroducing RAB18 into the KO cells reversed the LD alterations ([Supplementary Fig. S3](#)). Overexpression of wild-type RAB18 resulted in small, dispersed LDs in WT as well as RAB18 KO cells, confirming the findings of Xu et al. [35].

Notably, the CRISPR/Cas9-mediated stable RAB3GAP1 KO caused a similar LD appearance as observed in RAB18 KO cells ([Fig. 1a](#), [Supplementary Fig. S2](#)). RAB3GAP1 functions as an upstream regulator of RAB18, acting as a RAB GEF, activating the RAB GTPase [32,35,41]. Loss-of-function mutations in *RAB3GAP1* have likewise been associated with WARB [42]. Thus, we detected an altered LD appearance in cell lines with a KO in different genes that encode functionally associated proteins, emphasizing the relevance of RAB18 and RAB3GAP1 in LD homeostasis.

Presuming that the LD phenotype originates from an altered LD metabolism, we investigated their consumption under starvation conditions. Nutrient

deprivation results in the hydrolysis of TAGs and the release of fatty acids for mitochondrial energy metabolism [43]. Indeed, starvation triggered a time-dependent reduction in LD numbers and total area in WT cells, while this process was clearly repressed in KO cells ([Fig. 2a](#)).

In order to directly investigate fatty acid release from LDs, we employed the dye-conjugated fatty acid BODIPY558/568 C₁₂ and live cell imaging, following an established method [43]. As expected, in WT cells, the fatty acid efficiently migrated out of LDs under lipolytic conditions ([Fig. 2b](#)). The LD-located fluorescence signal decreased and the area of single LDs progressively declined during the starvation period. In contrast, the fatty acid was largely immobile in KO cells, emphasizing that its mobilization is disturbed in the absence of RAB18.

One key component of LD turnover is the lipase PNPLA2/ATGL, which is responsible for the release of fatty acids from TAGs. Under lipolytic conditions, the enzyme localizes to LDs and mediates the hydrolysis of TAGs, generating diacylglycerides [44,45]. Here, we analyzed the association of PNPLA2/ATGL with LDs, employing immunocytochemistry ([Fig. 3a, b](#)). Remarkably, the lipase showed an enhanced localization at LDs in RAB18 KO cells already under basal conditions, which we observed in WT cells only after inducing lipolysis. This showed that the permanent loss of RAB18 did not affect the transfer of PNPLA2/ATGL to LDs. However, the enhanced LD localization of the lipase was not linked to an efficient fatty acid release ([Fig. 2a, b](#)), underlining the specific importance of RAB18 for LD catabolism.

The KO of RAB18 interferes with LD turnover. To investigate whether it also affects LD formation, we monitored the dynamics of LD buildup upon oleic acid supplementation ([Supplementary Fig. S4](#)). Fatty acid treatment resulted in the rapid increase in LD numbers as well as total LD area, and importantly, we observed no significant differences between WT and KO cells. This demonstrated that the induced generation of LDs was unaffected by the stable loss of RAB18. The protein BSCL2/Seipin is functionally relevant for LD biogenesis [46]. BSCL2/Seipin forms ER-LD contact sites and regulates the stable association of forming LDs with the ER, facilitating the transfer of lipid cargo and

Fig. 6. The phospho-regulation of MTOR and ULK1 is unaffected in RAB18 KO cells. (a) Immunoblot analyses of MTOR levels and phosphorylation of residue S2448 under basal and starved conditions (2 h EBSS). Statistics are depicted as mean \pm SD. n = 4, One-Way ANOVA, n. s. = not significant, *P ≤ 0.05, **P ≤ 0.01. Statistical analysis of total MTOR levels is shown in [Supplementary Fig. S10](#). (b) Immunoblot analyses of p70 S6K levels and phosphorylation of T389 under basal and starved conditions (2 h EBSS). Statistics are depicted as mean \pm SD. n = 4, One-Way ANOVA, n. s. = not significant, **P ≤ 0.01. (c) Immunoblot analyses of ULK1 levels and phosphorylation of residues S555 and S758 under basal and starved conditions (2 h EBSS). Statistics are depicted as mean \pm SD. n = 4, One-Way ANOVA, n. s. = not significant, **P ≤ 0.01, ***P ≤ 0.001. Statistical analysis of total ULK1 levels is shown in [Supplementary Fig. S10](#).

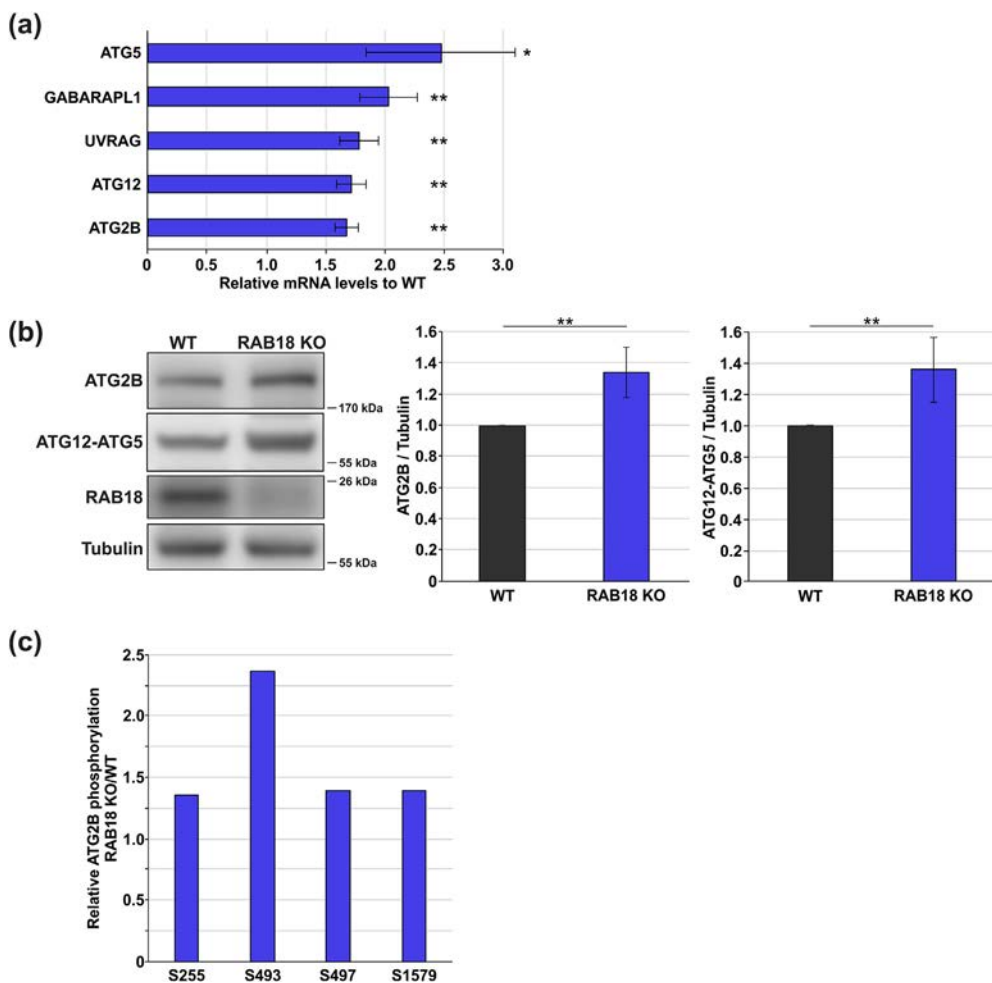


Fig. 7. Autophagy network alterations in RAB18 KO cells. (a) Genes showing altered expression levels in RAB18 KO compared to WT cells as evaluated using the qPCR array ([Supplementary Table 2](#)). mRNA levels were evaluated in relation to the respective levels in WT cells and the threshold for upregulation was set to 1.5-fold. n = 3, t-test, *P ≤ 0.05, **P ≤ 0.01. (b) Immunoblot analyses of ATG2B protein and ATG12-ATG5 conjugate levels in WT and RAB18 KO cells. Statistics are depicted as mean ± SD. n = 4, t-test, **P ≤ 0.01. (c) Phosphorylation levels of ATG2B (Q96BY7) serine residues in RAB18 KO compared to WT cells, determined by SILAC-based phosphoproteomics and depicted as mean values of two replicates.

proteins [47]. To further support the finding that LD formation is indeed unaffected in RAB18 KO cells, we investigated the localization of BSCL2/Seipin and observed no difference comparing WT and KO cells ([Supplementary Fig. S5](#)). The ER-located protein closely associated with small LDs upon conditions preferring LD formation. Thus, in contrast to LD consumption, we gained no indication that the biogenesis of the lipid reservoirs was affected by RAB18 loss.

Next, we analyzed the influence of alterations in LD turnover on autophagy, considering that autophagosome synthesis is strongly dependent on a sufficient lipid supply. In contrast to our previous findings analyzing transient genetic manipulations of RAB18 [32], here, using stable RAB18 KO cells, we

found that basal autophagic activity was actually unaffected ([Fig. 4](#)). In fact, immunoblot analyses of the lipidated LC3-II showed no differences when comparing WT and KO cells under basal, uninduced, autophagy conditions ([Fig. 4a](#), [Supplementary Fig. S6a](#)). This result was confirmed by confocal fluorescence microscopy of LC3- and SQSTM1-positive autophagosomes ([Fig. 4b](#), [Supplementary Figs. S7a, b](#)). The amount of LC3- as well as SQSTM1-positive autophagosomal structures and their baflomycin A₁-mediated accumulation was comparable in WT and KO cells under basal autophagy conditions.

Intriguingly, starvation increased autophagic activity in WT cells as expected; however, it failed to induce autophagy in RAB18 KO cells ([Fig. 4a, b](#),

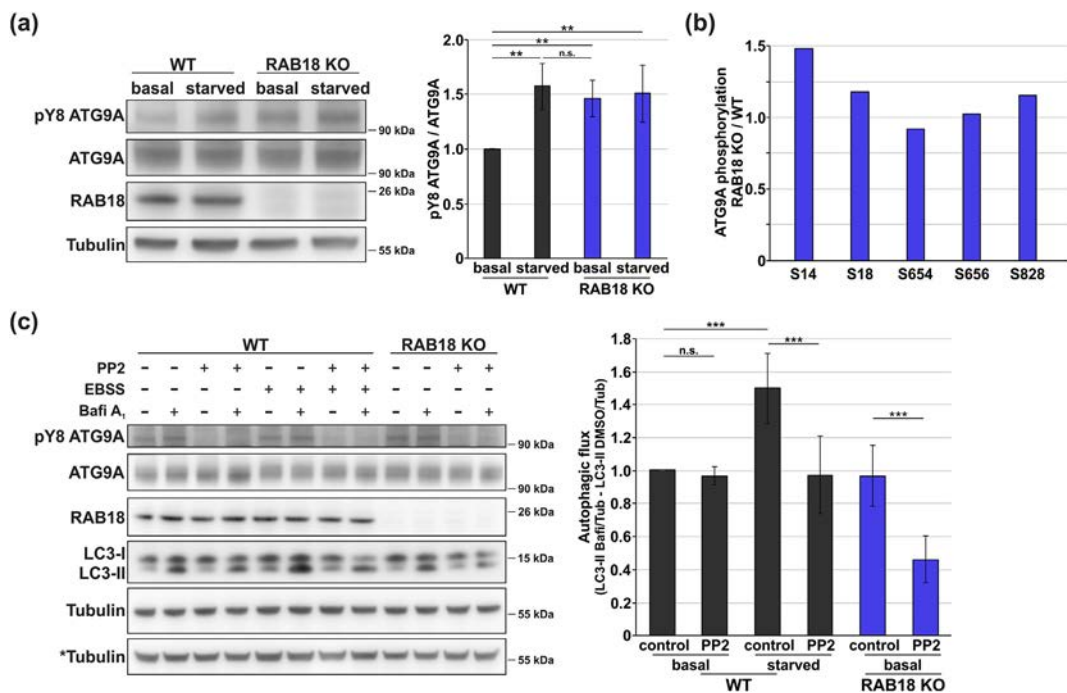


Fig. 8. ATG9A phosphorylation is altered in RAB18 KO cells and impacts autophagy. **(a)** Immunoblot analyses of Y8 phosphorylation of ATG9A in RAB18 KO and WT cells under basal and starved conditions (2 h EBSS). Statistics are depicted as mean \pm SD. n = 4, One-Way ANOVA, n. s. = not significant, **P \leq 0.01. **(b)** Phospho-levels of serine residues of ATG9A (Q7Z3C6) in RAB18 KO compared to WT cells, determined by SILAC-based phosphoproteomics and depicted as mean values of two replicates. **(c)** Immunoblot analyses of autophagic activity upon SRC kinase inhibition via PP2 treatment (5 μ M for 12 h). WT cells were examined under basal and starved conditions (2 h EBSS). All cells were treated with DMSO (control) or bafilomycin A₁ (Bafi A₁) for 2 h to allow evaluation of LC3-II flux. LC3-II loading was corrected over Tubulin. *indicates Tubulin loading control corresponding to parallel ATG9A blot. Statistical analyses are depicted as mean \pm SD. n = 5, One-Way ANOVA, n. s. = not significant, ***P \leq 0.001.

Supplementary Figs. S6a, S7a, b: immunoblotting as well as immunocytochemical analyses of autophagosomal structures showed that the KO cells did not respond to nutrient deprivation with the usually observed increased autophagic activity. Notably, we confirmed these findings in RAB3GAP1 KO cells (**Supplementary Fig. S8**). The stable loss of RAB3-GAP1 had no impact on basal autophagic activity, but impeded the induction-mediated increased autophagic flux.

Again, as observed for LDs, reintroduction of RAB18 restored the KO effect (**Fig. 4c, Supplementary Fig. S6b**). Expression of wild-type RAB18 facilitated autophagy induction upon starvation and resulted in increased autophagic activity, emphasizing the direct relevance of RAB18 function for the detected alterations.

RAB18 KO cells are characterized by reduced fatty acid release from LDs (**Figs. 1–3**), which might result in an insufficient lipid supply for autophagosome formation. To analyze the significance of LD-derived lipids for autophagy, we investigated autophagic activity after treatment with oleic acid, in accordance with a previous study [15]. The

enhanced availability of LD-derived lipids stimulated autophagy in WT cells and facilitated the flux of LC3-II as shown by immunoblotting as well as immunocytochemistry (**Fig. 5a, b, Supplementary Figs. S9a, b**). Strikingly, in RAB18 KO cells, the treatment with oleic acid did not result in an increased autophagic activity. This data again indicates that the fatty acid transfer from LDs to the autophagic pathway is disturbed when RAB18 is absent and clearly accentuates the relevance of LD-derived lipids for autophagy.

Interestingly, in contrast to induced autophagy as well as our previous transient genetic manipulations [32], basal autophagic rates were unaffected in stable RAB18 KO cells. This indicated that the autophagy network adapted to compensate the reduced LD-derived lipid availability to maintain basal autophagic activity. In order to analyze these adaptive adjustments, we investigated the canonical autophagy induction system and analyzed phosphoregulations of the kinases MTOR and ULK1.

MTOR is regulated via phosphorylation at multiple sites, and we focused on amino acid residue S2448 [48]. Interestingly, we found no differences in its

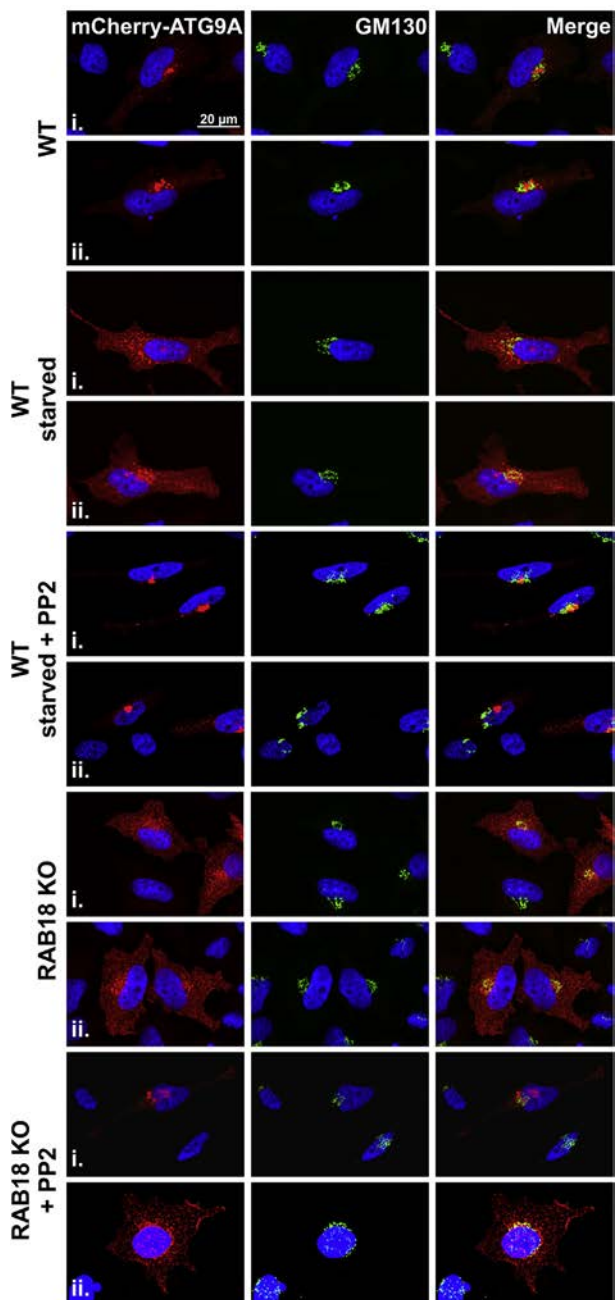


Fig. 9. ATG9A trafficking dynamics are enhanced under basal conditions in RAB18 KO cells. Representative confocal fluorescence images of cells expressing mCherry-ATG9A (red), stained with GM130 (Golgi, green), and DAPI (nuclei, blue). Cells were examined under basal conditions, upon starvation (2 h EBSS), and/or upon PP2 treatment (5 μ M for 8 h). Approx. 20 images for each condition were obtained from three independent experiments.

starvation-mediated phosphorylation as well as in total MTOR protein levels when comparing KO and WT cells (Fig. 6a, *Supplementary Fig. S10*). Additionally, we examined the phosphorylation of the MTOR substrate p70 S6 kinase at amino acid residue T389 and found no differences in its phospho-levels under basal conditions and upon starvation (Fig. 6b). Thus, the loss of RAB18 had no impact on the activity of MTOR kinase. ULK1 activity is modulated via several phosphorylations upon starvation, and we examined the MTOR-mediated, inactivating, phosphorylation at S758 as well as the AMP kinase PRKAA1-mediated, activating, phosphorylation at S555 [49,50]. Importantly, both regulations as well as total ULK1 protein levels were comparable in KO and WT cells (Fig. 6c, *Supplementary Fig. S10*). Thus, MTOR and ULK1 phosphoregulations were unaffected by the RAB18 KO, demonstrating that the adaptations of the autophagy network were not linked to modifications in canonical autophagy induction. In addition, we conducted a SILAC-based quantitative phosphoproteomics approach, which confirmed that the phospho-levels of these amino acid residues were unaltered when comparing KO and WT cells, while other residues showed alterations under basal conditions (*Supplementary Table S1, Supplementary Fig. S11*).

Next, we investigated direct modifications of the autophagy network in RAB18 KO cells and analyzed expression levels of key autophagy proteins employing a qPCR array (Fig. 7a, *Supplementary Table S2*). Interestingly, mRNA levels of a discrete number of autophagy factors were upregulated in KO cells, whereas actually no downregulations were observed. This underlines the positive adaptation of the autophagy network with the aim to rescue the activity of the degradative pathway under unfavorable conditions. Remarkably, all regulated proteins can be allocated to early steps of the autophagy process, suggesting that the network responded to the stable RAB18 loss with alterations that facilitate autophagosome formation. In fact, expression levels of ATG2B as well as ATG5 and ATG12 were enhanced in RAB18 KO cells, and importantly, this directly correlated with increased ATG2B protein and ATG12-ATG5 conjugate levels when compared to WT cells (Fig. 7b).

Combined findings from the SILAC-based phosphoproteomics approach and the expression analysis underline the particular regulation of ATG2B. In RAB18 KO cells, in addition to the increased expression levels, ATG2B showed an enhanced phosphorylation of the particular amino acid residue S493 (Fig. 7c, *Supplementary Fig. S11, Supplementary Table S1*). Since ATG2 proteins have recently been described as lipid transfer factors that promote autophagosome formation [51,52], the detected regulation of ATG2B emphasizes that adaptational autophagy network alterations are specifically

targeted and include distinct factors related to autophagosome formation and potentially lipid transfer.

Within the autophagy network, ATG9A is well acknowledged to function in the transfer of vesicles from the cellular periphery to the site of autophagosome formation to supply required proteins as well as lipids [22,24,25]. Thus, the protein is indeed an important candidate to compensate reduced LD-derived lipid availability. Notably, mRNA and protein levels of ATG9A were not altered in RAB18 KO cells (Supplementary Fig. S12). However, the activity of ATG9A is regulated via phosphorylation at amino acid residues Y8 and S14, which direct the protein to the autophagy pathway and facilitate autophagosome formation [26,27]. We analyzed the phospho-status of the Y8 residue by immunoblotting and found that its phosphorylation levels were enhanced in RAB18 KO cells already under basal autophagy conditions, which we observed in WT cells solely upon induction (Fig. 8a). Again, this data point was confirmed in RAB3GAP1 KO cells, which showed basally enhanced Y8 phosphorylation (Supplementary Fig. S13).

Due to the lack of a specific antibody directed against the phosphorylated S14 residue, we employed the quantitative phosphoproteomics approach to analyze S14 phosphorylation levels and found that they were in fact slightly, but reproducibly, enhanced in RAB18 KO cells (Fig. 8b, Supplementary Fig. S11, Supplementary Table S1). Since the phosphoproteomics exclusively detected the serine residues on ATG9A, confirmation for Y8 by this approach was not possible.

Y8 phosphorylation of ATG9A is mediated by SRC kinase [27]. To confirm this link and to gain insight into the functional importance of this ATG9A modification, we employed the two SRC kinase inhibitors PP2 (Fig. 8c) and SU6656 (Supplementary Fig. S14). Indeed, SRC kinase inhibition impeded the autophagy induction mediated increased Y8 phosphorylation in WT cells and prevented induced autophagic activity. Importantly, basal autophagic flux was not significantly affected by SRC kinase inhibition in WT cells. Remarkably, in contrast to WT cells, the decreased Y8 phosphorylation by PP2 as well as SU6656 treatment in RAB18 KO cells resulted in reduced autophagic activity already under basal conditions (Fig. 8c, Supplementary Fig. S14). These findings demonstrate that ATG9A phosphorylation supports the maintenance of basal autophagy in the absence of RAB18.

RAB18 has been shown to affect the function of the Golgi complex [53], which is also a central compartment for ATG9A trafficking. To exclude that phosphorylation of ATG9A is related to functional perturbations of the Golgi, we disrupted its function

and monitored the impact on Y8 phospho-levels by immunoblotting (Supplementary Figs. S15a, b). The treatment with golgicide did not result in enhanced Y8 phosphorylation.

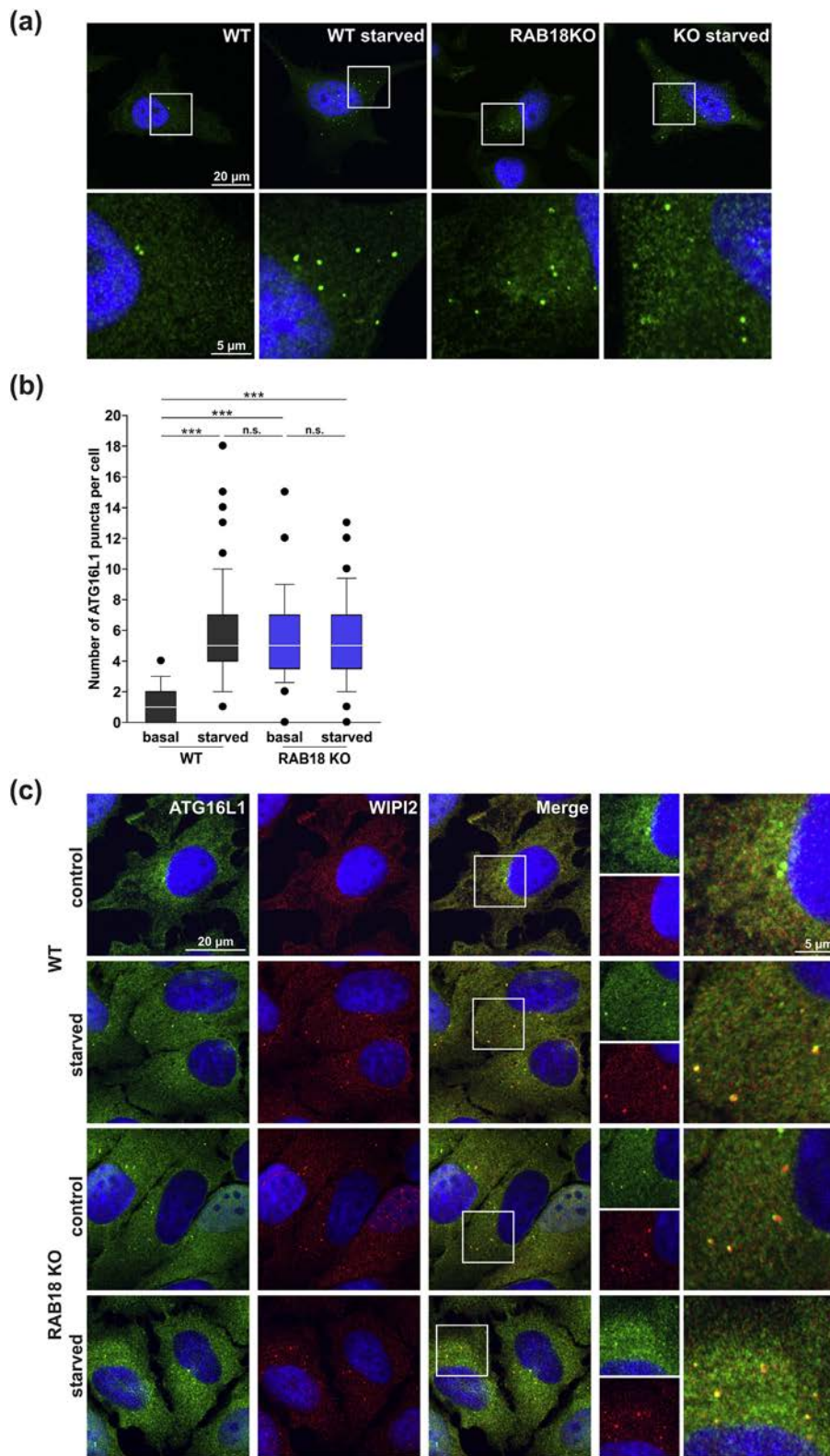
In order to conduct a more detailed investigation into ATG9A dynamics in RAB18 KO cells, we directly analyzed ATG9A trafficking. The protein prominently localizes to the Golgi complex under basal autophagy conditions and changes to a dispersed vesicular distribution upon autophagy induction [23,25]. Employing immunocytochemistry, we analyzed the localization of ATG9A in WT and KO cells (Fig. 9). As expected, the majority of ATG9A was located at the Golgi in WT cells, but changed to a dispersed distribution upon starvation-mediated autophagy induction. Remarkably, in RAB18 KO cells, ATG9A showed the dispersed vesicular distribution already under basal conditions, which is directly related to the observed enhanced phosphorylation. Inhibition of SRC kinase activity affected ATG9A trafficking. The treatment with PP2 reversed the dispersed appearance and resulted in enhanced localization of ATG9A at the Golgi in KO cells under basal conditions as well as in WT cells upon starvation. This indicates an important role of Y8 phosphorylation for ATG9A trafficking dynamics and emphasizes the relevance of this particular modification in RAB18 KO cells.

Autophagy induction and dynamic ATG9A trafficking are associated with the increased appearance of ATG16L1-positive pre-autophagosomal structures. ATG16L1 is targeted to the phagophore, where it forms a complex with the ATG12-ATG5 conjugate, which is required for the lipidation of Atg8 family members [9,11,12]. In fact, starvation resulted in increased numbers of ATG16L1 puncta in WT cells, which were already observed in RAB18 KO cells under basal conditions (Fig. 10a, b). Importantly, these ATG16L1 puncta were also positive for WIPI2 (Fig. 10c). Upon autophagy induction, WIPI2 is recruited to the omegasome at the ER and remains associated with the growing phagophore, where it is essential for the recruitment of ATG16L1 [8].

Thus, the comparison of WT cells upon autophagy induction to RAB18 KO cells under basal conditions showed similar ATG9A trafficking and an enhanced presence of ATG16L1 as well as WIPI2-positive phagophore structures. This further demonstrated that ATG9A activity is increased in RAB18 KO cells, facilitating basal autophagic activity under lipid-limited conditions.

Discussion

In the present study, we connect the impact of RAB18 on LD catabolism with autophagy. The stable



loss of RAB18 results in a reduced LD-derived lipid availability that provokes adaptive alterations of the autophagy network to maintain autophagic activity.

RAB18 has been implicated to function in a broad range of cellular processes, including LD homeostasis [54]. However, its exact role in LDs metabolism remains indistinct. Recent studies range from functionally linking RAB18 to ER-LD tethering, to LD maturation, or to no influence on LD turnover at all [31,33–38]. Here, we show that the stable loss of RAB18 results in functionally inert LDs. The lipid reservoirs are efficiently formed but the fatty acid release on demand is impeded, despite an enhanced localization of the TAG lipase PNPLA2/ATGL at the organelles. Previous studies showed that modulating PNPLA2/ATGL levels reciprocally affects the number of LDs in HeLa cells [55] and that the LD association and activity of the lipase are dynamically regulated [56,57]. Thus, the detailed functional correlation of PNPLA2/ATGL activity and the permanent loss of RAB18 requires further elucidation.

In conclusion, our analyses demonstrate that the stable loss of RAB18 causes a defect in LD catabolism, provoking the prominent LD appearance that, excitingly, is also observed in WARB patient cells carrying loss-of-function mutations in *RAB18* or *RAB3GAP1* [40]. Importantly, the loss of RAB3-GAP1, which is a regulator of RAB18 activity [32,41], results in a similar LD phenotype, emphasizing the relevance of RAB18 function in LD consumption.

The disturbed LD catabolism affects autophagy, which is dependent on an adequate lipid supply to guarantee sufficient autophagosome formation [3,58]. Different cellular organelles and compartments have been recognized as lipid donors [3,14]. However, the specific regulation of autophagosomal lipid acquisition remains elusive. Previous studies have demonstrated a link between LDs and autophagy [15–17], but the functional impact and importance of LD-derived lipids on autophagosome biogenesis have been questioned [18]. It has already been demonstrated that the increased availability of fatty acids from LDs enhances autophagic capacity by facilitating autophagosome formation and, importantly, that this process is dependent on LD-located lipases [15]. Fatty acids are mobilized from LDs and converted into appropriate lipids that are potentially delivered to the site of autophagosome formation.

Here, we confirm that fatty acid supplementation increases autophagic capacity in WT cells. In contrast, the enhanced fatty acid availability does not stimulate autophagy in RAB18 KO cells, demonstrating that in the absence of RAB18 their efficient transfer to the autophagy pathway is impeded, consequently affecting the degradative pathway.

Previously, employing transient genetic manipulations, we have characterized RAB18 and RAB3-GAP1 as positive modulators of autophagy [32,59]. The siRNA-mediated transient reduction of RAB18 or RAB3GAP1 levels cause a decline in autophagic activity, notably, under basal as well as induced autophagy conditions. Excitingly, as demonstrated here, the stable KO of RAB18 (as well as RAB3-GAP1) showed no impact on basal autophagic activity. The flux of LC3-II and the ratio of LC3-II to LC3-I were unaffected. However, autophagy induction, which is associated with an increased lipid demand, indeed failed. These findings indicate that the stable loss of RAB18 function leads to adaptations of the autophagy network, which rescue basal autophagy under conditions of reduced LD-derived lipid availability but are insufficient to enable an increased autophagic activity upon induction.

Indeed, we detected several alterations within the autophagy network, including increased ATG12-ATG5 conjugate and ATG2B levels. These modifications appeared already under basal autophagy conditions in RAB18 KO cells and occurred independently of the autophagy induction system, since the starvation-mediated phospho-regulation and activity of MTOR as well as ULK1 were unaffected.

ATG12 and ATG5 are covalently linked by an ubiquitin-like conjugation process, which is a prerequisite for the formation of the ATG12-ATG5/ATG16L1 complex that is required for the lipidation of Atg8 family members [11,60]. In the absence of ATG5, phagophores are formed but do not mature into fully closed autophagosomes [61,62]. Enhanced ATG5 levels facilitate autophagy; augmented conjugate levels have been linked to increased autophagic activity [63].

The increased protein levels and altered phosphorylation of ATG2B are of particular interest here. Mammalian cells possess two functionally similar ATG2 proteins, ATG2A and ATG2B, which have recently been characterized as lipid transfer factors that support phagophore growth and

Fig. 10. ATG16L1 puncta accumulate under basal conditions in RAB18 KO cells and colocalize with WIPI2. (a) Representative confocal fluorescence images of cells stained with ATG16L1 (green) and DAPI (blue). WT cells were examined under basal and starved conditions (2 h EBSS). (b) Statistical evaluation of (a). Approx. 65 cells for each condition from four independent experiments were analyzed and the total number of ATG16L1 puncta was quantified per cell. One-Way ANOVA, n. s. = not significant, ***P < 0.001. (c) Representative confocal images of immunocytochemical stainings using ATG16L1 (green) and WIPI2 (red). Nuclei were stained with DAPI (blue). Cells were examined under basal conditions and upon starvation (2 h EBSS). Approx. 15 images for each condition were obtained from three independent experiments.

autophagosome closure [51,52,64,65]. Noteworthy, ATG2A/B localize to phagophores as well as LDs and their transient knockdown results in the accumulation of enlarged LDs [64,66]. This indicates that ATG2A/B may be linking LD metabolism and autophagy. We presume that the upregulation of ATG2B expression observed here, together with the enhanced S493 phosphorylation, which has not been functionally characterized yet, is a direct adaptive response to the limited lipid availability.

A further adaptation of the autophagy network we identified is the phosphorylation-dependent increased ATG9A activity, which proved to be important for the maintenance of basal autophagy in RAB18 KO cells. The transmembrane protein transfers vesicles from the cellular periphery to the site of autophagosome formation, delivering proteins and lipids required for the generation of autophagic vesicles [20,22–25]. Therefore, ATG9A is indeed a prime candidate to compensate insufficient lipid availability for autophagosome formation. The activity of ATG9A is regulated by ULK1 and SRC kinase-mediated phosphorylation at amino acid residues S14 and Y8, respectively [26,27]. Both modifications are described to be enhanced upon autophagy induction, which we confirmed here for HeLa WT cells. Importantly, in RAB18 KO cells, the phosphorylation of both residues was increased already under basal, unstimulated, autophagy conditions, indicating that the activity of ATG9A adapted to compensate the reduced LD-derived lipid availability in the absence of RAB18. Indeed, ATG9A showed an enhanced trafficking that was accompanied by increased amounts of ATG16L1 and WIPI2-positive preautophagosomal structures. The pharmacological inhibition of Y8 phosphorylation demonstrated a functional relevance of this ATG9A modification for the maintenance of basal autophagy: reducing Y8 phosphorylation in RAB18 KO cells impeded ATG9A trafficking dynamics and caused a clear decline in autophagic activity already under basal autophagy conditions. Thus, here, we describe the phosphorylation-dependent activation of ATG9A as a cellular adaptation aiming to compensate limited lipid availability and supporting the maintenance of autophagic activity.

In summary, we define the molecular function of RAB18 in connecting LD catabolism and autophagy and emphasize the high-impact role of LDs as lipid sources for autophagosome formation. The loss of RAB18 results in a reduced LD-derived lipid availability that provokes autophagy network adaptations, which reflect changes normally only observed upon autophagy induction, aiming to maintain autophagic activity. Thus, we uncover an exciting autophagy network plasticity, which ensures basal autophagic efficacy under unfavorable—here lipid-limiting—conditions.

Materials and Methods

Cell culture

HeLa cells were cultured in DMEM, supplemented with 10% fetal bovine serum, 1 mM sodium pyruvate, and 1 × antibiotic-antimycotic solution at 37 °C in a 5% CO₂-humidified atmosphere. Cell identity was authenticated via STR analysis and cells were regularly tested negative for the presence of mycoplasma using the Venor GeM Mycoplasma PCR detection kit (Minerva Biolabs, 11-1050). Stock solutions of bafilomycin A₁ (Biozol, TRC-B110000) and rapamycin (Enzo, BML-A275-0025) were prepared in DMSO and employed as described before [59]. Stock solutions of PP2 (Sigma Aldrich, P0042) and SU6656 SRC Inhibitor (Selleck Chemicals, S7774) were prepared in DMSO and cells were treated with 5 μM and 10 μM, respectively, for 8 h (immunocytochemistry) or 12 h (immunoblotting). Cells were transfected with 30 μg of mCherry-ATG9A plasmid and transfections were carried out by electroporation as described previously [59].

CRISPR/Cas9-mediated knockout

Gene-specific CRISPR/Cas9 vectors (pLV-U6g-EPCG) targeting *RAB18* and *RAB3GAP1* were obtained from Sigma Aldrich. Wild-type HeLa cells were transfected with 15 μg of plasmids, and selection of positive clones was performed using culture medium containing 1 μg/ml puromycin. Positive knockout clones were identified via immunoblotting and qPCR.

Immunoblotting

Immunoblot analyses were performed as previously described [32]. Usually 15–30 μg of total protein was subjected to hand-cast 12% Bis-Tris or 4–12% NuPage Bis-Tris gels (Thermo Scientific, MP0335) and transferred onto nitrocellulose membranes. Membranes were blocked with 5% milk powder in TBS-Tween 20 and probed with the appropriate primary and secondary antibodies. Proteins were detected by chemiluminescence and developed using the Amersham Imager 600 (GE Healthcare Life Science). Primary antibodies: MAP1LC3B (Sigma, L7543), SQSTM1 (Progen, GP62-C), RAB18 (Proteintech, 11304-1-AP), RAB18 (Santa Cruz Biotechnology, sc-393168), RAB3GAP1 (Sigma, SAB4500914), RAB3GAP2 (Sigma, HPA026273), Tubulin (Sigma, T9026), ATG2B (abcam, ab116215), ATG5 (Novus, NB110-53818), ATG9A (Cell Signaling, 135095), p-Y8-AT9A (kindly provided by Yushan Zhu and Quan Chen, Nankai, China, or, alternatively, obtained from Proteintech), ULK1 (Cell Signaling, 8054), p-ULK1 Ser555 (Cell Signaling, 5869), p-ULK1 Ser757 (Cell Signaling, 6888), mTOR (Cell Signaling, 2972S), p-mTOR S2448 (Cell Signaling, 2971), p70 S6 kinase (Cell Signaling, 9202), p-p70 S6 kinase Thr389 (Cell Signaling, 9206).

Immunocytochemistry

Immunocytochemistry was performed as previously described [32]. Briefly, cells were grown on glass cover slips, fixed with 4% PFA, and were permeabilized in 90% methanol, 0.02% Triton X-100, or 0.01% Saponin. Unspecific binding sites were blocked with 3% BSA in PBS. Cells were incubated with primary antibodies and fluorophore-conjugated secondary antibodies followed by DAPI. Primary antibodies: ATGL/PNPLA2 (Cell Signaling, 2138), ATG16L1 (MBL, PM040), CLIMP63 (Enzo, ENZ-ABS660), GM130 (BD biosciences, 610823), MAP1LC3B (nano Tools, 0260-100), BSCL2/Seipin (Thermo Fisher, PAS-47922), SQSTM1 (Progen, GP62-C), Tubulin (Sigma, T9026), WIPI2 (Millipore, MABC91). Stock solutions of BODIPY493/503 (Thermo Fisher, D3922) and BODIPY558/568 C₁₂ (Thermo Fisher, D3835) were prepared according to the supplier. Cells were imaged using the laser scanning microscope LSM710 (Zeiss). Live cell imaging and imaging of autophagosomal structures for quantification were performed via the Opera Phenix High-Content Screening System (Perkin-Elmer).

Lipid droplet analysis

For LD analyses, cells were stained with Tubulin α , DAPI, and BODIPY493/503 and were imaged via the Opera Phenix High-Content Screening System (Perkin-Elmer). Single cells and cell area were defined via DAPI and Tubulin α staining, respectively. LD number and size were quantified through BODIPY493/503 fluorescence, employing Harmony High-Content Imaging and Analysis software (Perkin-Elmer). Distance analyses as well as PNPLA2/ATGL colocalization were conducted with ImageJ plugin DiAna [67].

Autophagic activity analysis

Autophagic activity was analyzed in accordance with "Guidelines for the use and interpretation of assays for monitoring autophagy" [68]. Cells were treated with baflomycin A₁ for 2–4 h or DMSO for control and the flux of autophagic substrates was calculated by the subtraction of accumulated levels upon baflomycin A₁ treatment and DMSO control after correction of equal loading using Tubulin. Additionally, the ratio of LC3-II to LC3-I was calculated.

Quantitative real-time PCR

RNA extraction, reverse transcription, and real-time PCR were performed as described previously [59]. Primer sequences for the autophagy array are listed in Supplementary Table 2.

Transmission electron microscopy

For transmission electron microscopy, cells were grown on 7.8 mm thick Aclar discs (Ted Pella Inc.) and fixed by 2.5% glutaraldehyde in 0.1 M sodium cacodylate buffer pH 7.4. Discs were washed in 0.1 M cacodylate buffer. After

treatment with 1% OsO₄, the sections were stained with uranyl acetate, dehydrated, and flat-embedded in epon resin (Araldite 502). 35 nm ultrathin cross sections were cut using an Ultracut S ultramicrotome (Reichert) and analyzed using a CM12 TEM (Philips) operated at 80 kV and equipped with an ES500W Erlangshen (782) CCD camera (Gatan).

Quantitative phosphoproteome analysis

Quantitative phosphoproteome analysis was performed as described previously [69]. Briefly, cells were cultured in SILAC media containing L-arginine and L-lysine, L-arginine [¹³C₆] and L-Lysine [²H₄], or L-arginine [¹³C₆–¹⁵N₄] and L-lysine [¹³C₆–¹⁵N₂] (Cambridge Isotope Laboratories). Cells were lysed and proteins were precipitated, redissolved, and digested. Thereafter, peptides were purified using reversed-phase Sep-Pak C18 cartridges (Waters). Phosphorylated peptides were enriched and fractionated. Peptide fractions were analyzed on a quadrupole Orbitrap mass spectrometer (QExactive Plus, Thermo Scientific) equipped with a UHPLC system (EASY-nLC 1000, Thermo Scientific). Survey full-scan MS spectra were acquired in the Orbitrap. The 10 most intense ions were sequentially isolated and fragmented by higher energy C-trap dissociation (HCD). Fragment spectra were acquired in the Orbitrap mass analyzer. Raw data files were analyzed using MaxQuant (dev. version 1.5.2.8). Parent ion and MS2 spectra were searched against a database containing 95,057 human protein sequences obtained from the UniProtKB released in May 2018 using Andromeda search engine. Site localization probabilities were determined by MaxQuant using the PTM scoring algorithm as described previously [70]. The dataset was filtered based on posterior error probability to arrive at a false discovery rate below 1% estimated using a target-decoy approach [71]. Only phosphorylated peptides with a score ≥ 40 , delta score ≥ 8 , score difference ≥ 5 , and localization probability ≥ 0.75 were considered for downstream analysis. The mass spectrometry proteomics data have been deposited to the ProteomeXchange Consortium via the PRIDE [72] partner repository with the dataset identifier PXD013719.

Statistics

Statistical significance was determined by One-Way ANOVA or *t*-test in dependence of the normal distribution or variance differences of the samples using SIGMA STAT (SPSS Science). Statistical significance was accepted at a level of $P \leq 0.05$. The results are expressed as mean \pm standard deviation (SD) or standard error of the mean (SEM).

Acknowledgments

We kindly thank Drs Yushan Zhu and Quan Chen (Nankai, China) for supplying the ATG9A phospho-specific antibody and Sandra Ritz (IMB, Mainz,

Germany) for her support with the live cell imaging. We also thank Marion Basoglu from the Electron Microscopy Facility of the Biology department, Frankfurt, for her help with the TEM sample preparation and imaging. This work is supported by the Collaborative Research Center CRC1177 of the DFG (to AK, CB, PB and SE), the Heller Foundation (to CB), and the Emmy Noether Program BE 5342/1-1 of the DFG (to PB).

Credit Author Statement

FB, DS, AF, and HH carried out the experiments. SE conducted the electron microscopy. TJ and PB performed the phosphoproteomics analysis. FB, DS, TJ, PB, CB, and AK analyzed the data. CB and AK designed the study and wrote the manuscript with contributions from FB and DS.

Conflicts of Interest

The authors declare no conflict of interest.

Appendix A. Supplementary data

Supplementary data to this article can be found online at <https://doi.org/10.1016/j.jmb.2019.12.031>.

Received 7 August 2019;
Received in revised form 16 December 2019;
Accepted 16 December 2019
Available online 24 December 2019

Keywords:
autophagy;
lipid droplets;
autophagosome formation;
ATG9A phosphorylation;
adaptation

[†]F.B. and D.S. contributed equally to this work.

Abbreviations used:

ATG, autophagy related; ER, endoplasmic reticulum; KO, knockout; LC3, microtubule-associated protein 1 light chain 3 beta; LD, lipid droplet; TAG, triacylglyceride; WARBM, Warburg micro syndrome; WT, wild type.

References

- [1] T. Kawabata, T. Yoshimori, Beyond starvation: an update on the autophagic machinery and its functions, *J. Mol. Cell. Cardiol.* 95 (2016) 2–10.
- [2] C. He, D.J. Klionsky, Regulation mechanisms and signaling pathways of autophagy, *Annu. Rev. Genet.* 43 (2009) 67–93.
- [3] T.J. Mercer, A. Gubas, S.A. Tooze, A molecular perspective of mammalian autophagosome biogenesis, *J. Biol. Chem.* 293 (2018) 5386–5395.
- [4] E.L. Axe, S.A. Walker, M. Manifava, P. Chandra, H.L. Roderick, A. Habermann, et al., Autophagosome formation from membrane compartments enriched in phosphatidylinositol 3-phosphate and dynamically connected to the endoplasmic reticulum, *J. Cell Biol.* 182 (2008) 685–701.
- [5] M. Hayashi-Nishino, N. Fujita, T. Noda, A. Yamaguchi, T. Yoshimori, A. Yamamoto, A subdomain of the endoplasmic reticulum forms a cradle for autophagosome formation, *Nat. Cell Biol.* 11 (2009) 1433–1437.
- [6] E. Karanasios, E. Stapleton, M. Manifava, T. Kaizuka, N. Mizushima, S.A. Walker, et al., Dynamic association of the ULK1 complex with omegasomes during autophagy induction, *J. Cell Sci.* 126 (2013) 5224–5238.
- [7] D.J. Klionsky, B.A. Schulman, Dynamic regulation of macroautophagy by distinctive ubiquitin-like proteins, *Nat. Struct. Mol. Biol.* 21 (2014) 336–345.
- [8] H.C. Dooley, M. Razi, H.E. Polson, S.E. Girardin, M.I. Wilson, S.A. Tooze, WIP12 links LC3 conjugation with PI3P, autophagosome formation, and pathogen clearance by recruiting Atg12-5-16L1, *Mol. Cell* 55 (2014) 238–252.
- [9] N. Fujita, T. Itoh, H. Omori, M. Fukuda, T. Noda, T. Yoshimori, The Atg16L complex specifies the site of LC3 lipidation for membrane biogenesis in autophagy, *Mol. Biol. Cell* 19 (2008) 2092–2100.
- [10] J. Geng, D.J. Klionsky, The Atg8 and Atg12 ubiquitin-like conjugation systems in macroautophagy. 'Protein modifications: beyond the usual suspects' review series, *EMBO Rep.* 9 (2008) 859–864.
- [11] T. Hanada, N.N. Noda, Y. Satomi, Y. Ichimura, Y. Fujioka, T. Takao, et al., The Atg12-Atg5 conjugate has a novel E3-like activity for protein lipidation in autophagy, *J. Biol. Chem.* 282 (2007) 37298–37302.
- [12] A.H. Lystad, S.R. Carlsson, L.R. de la Ballina, K.J. Kauffman, S. Nag, T. Yoshimori, et al., Distinct functions of ATG16L1 isoforms in membrane binding and LC3B lipidation in autophagy-related processes, *Nat. Cell Biol.* 21 (2019) 372–383.
- [13] H. Weidberg, E. Shvets, T. Shpilka, F. Shimron, V. Shinder, Z. Elazar, LC3 and GATE-16/GABARAP subfamilies are both essential yet act differently in autophagosome biogenesis, *EMBO J.* 29 (2010) 1792–1802.
- [14] D.C. Rubinsztein, T. Shpilka, Z. Elazar, Mechanisms of autophagosome biogenesis, *Curr. Biol.* 22 (2012) R29–R34.
- [15] N. Dupont, S. Chauhan, J. Arko-Mensah, E.F. Castillo, A. Masedunskas, R. Weigert, et al., Neutral lipid stores and lipase PNPLA5 contribute to autophagosome biogenesis, *Curr. Biol.* 24 (2014) 609–620.
- [16] F. Moretti, P. Bergman, S. Dodgson, D. Marcellin, I. Claerr, J.M. Goodwin, et al., TMEM41B is a novel regulator of autophagy and lipid mobilization, *EMBO Rep.* (2018), <https://doi.org/10.15252/embr.201845889>.
- [17] T. Shpilka, E. Welter, N. Borovsky, N. Amar, M. Mari, F. Reggiori, et al., Lipid droplets and their component triglycerides and sterol esters regulate autophagosome biogenesis, *EMBO J.* 34 (2015) 2117–2131.
- [18] A.P. Velazquez, T. Tatsuta, R. Ghillebert, I. Drescher, M. Graef, Lipid droplet-mediated ER homeostasis regulates



Expression dynamics and a loss-of-function of *Arabidopsis RabC1* GTPase unveil its role in plant growth and seed development

Uzma Khatoon^{1,2} · Vivek Prasad² · Samir V. Sawant¹

Received: 18 November 2022 / Accepted: 16 March 2023 / Published online: 29 March 2023
© The Author(s), under exclusive licence to Springer-Verlag GmbH Germany, part of Springer Nature 2023

Abstract

Main conclusion Transcript isoform dynamics, spatiotemporal expression, and mutational analysis uncover that *Arabidopsis RabC1* GTPase is required for root length, flowering time, seed size, and seed mucilage.

Abstract Rab GTPases are crucial regulators for moving different molecules to their specific compartments according to the needs of the cell. In this work, we illustrate the role of RabC1 GTPase in *Arabidopsis* growth and seed development. We identify and analyze the expression pattern of three transcript isoforms of *RabC1* in different development stages, along with their tissue-specific transcript abundance. The promoter activity of *RabC1* using promoter-GUS fusion shows that it is widely expressed during the growth of *Arabidopsis*, particularly in seed tissues such as chalazal seed coat and chalazal endosperm. Lack of RabC1 function led to shorter roots, lesser biomass, delayed flowering, and sluggish plant development. The mutants had smaller seeds than the wildtype, less seed mass, and lower seed coat permeability. Developing seeds also revealed a smaller endosperm cavity and shorter integument cells. Additionally, we found that the knock-out mutant had downregulated expression of genes implicated in the transit of sugars and amino acids from maternal tissue to developing seed. The seeds of the loss-of-function mutant had reduced seed mucilage. All the observed mutant phenotypes were restored in the complemented lines confirming the function of RabC1 in seed development and plant growth.

Keywords Chalazal endosperm · Chalazal seed coat · Seed mucilage · Seed size · Transcript isoforms

Abbreviations

DAG	Day after germination
DAP	Day after pollination
UMAMIT	Usually multiple acids move in an out transporter

Introduction

Membrane trafficking is essential for a number of cellular processes in plant growth and development, such as the manufacture of cell walls, uptake of nutrients, hormone signaling, and various other cell activities (Geldner et al. 2001; Takano et al. 2005; Harpaz-Saad et al. 2011). The communication between different cell compartments is mediated by membrane trafficking, a crucial process for transporting molecules. Membrane trafficking functions through various steps comprising budding, transport, targeting, tethering, and vesicle fusion via effector proteins to the target organelles (Zerial and McBride 2001). Spatiotemporal regulation and specificity of membrane trafficking during development and various cellular activities are mainly mediated by Rab GTPases, belonging to the family of small GTPases (Stenmark 2009; Ebine 2015; Gu et al. 2020).

Rab GTPases represent a molecular switch, and their regulatory module relies on the GTP-binding and hydrolysis process. Rab GTPases are operative when associated with GTP, and upon hydrolysis, they become inactive (Stenmark

Communicated by Dorothea Bartels.

✉ Samir V. Sawant
samirsawant@nbri.res.in

¹ Plant Molecular Biology and Biotechnology Division, CSIR-National Botanical Research Institute, Rana Pratap Marg, Lucknow 226001, India

² Department of Botany, University of Lucknow, Lucknow 226007, India

et al. 1994; Markgraf et al. 2007). The activation, as well as inactivation of Rab GTPases, depends on the particular guanine nucleotide exchange factors (GEFs) and GTPase-activating proteins (GAPs) (Olkonen and Stenmark 1997; Pereira-Leal and Seabra 2001; Vernoud et al. 2003; Woollard and Moore 2008). In Arabidopsis, 57 Rab GTPases are reported that are divided into eight clades, namely, RabA/Rab11, RabB/Rab2, RabC/Rab18, RabD/Rab1, RabE/Rab8, RabF/Rab5, RabG/Rab7, and RabH/Rab6 based on their similarity with the yeast and the animal GTPases (Pereira-Leal and Seabra 2001; Rutherford and Moore 2002; Nielsen 2020). Numerous plant Rab GTPases of the different groups are predicted to be localized to a distinct compartment in various stages of membrane trafficking. Proteins belonging to RabB and RabD have been involved in the initial phases of trafficking to Golgi-associated structures, whereas members of RabF (RabF1 and RabF2) and RabG3 subclass have been associated with transport to the vacuole (Batoko et al. 2000; Rojo et al. 2001; Cheung et al. 2002; Vernoud et al. 2003; Woollard and Moore 2008; Nielsen 2020). Several pieces of research have revealed the role of Rab GTPases, mainly belonging to RabA, RabE, and RabF clades, in post-Golgi secretory and endocytic processes (Zheng et al. 2005; Foucart et al. 2008; Huang et al. 2021). Members of the RabH clade, such as RabH1b and RabH1c, have been implicated in the trafficking between Golgi and plasma membrane (He et al. 2018; Jia et al. 2018). The RabC family in plants is closest to the Rab18 GTPase-like family of animals, and RabC2a of this family seems to recruit myosin motors to peroxisomes (Hashimoto et al. 2008).

Since the discovery, numerous Rab GTPases have been known to play a crucial role in plant growth, plant–microbe interaction, biotic stress, drought stress, and adaptation processes (Kotzer et al. 2004; Szumlanski and Nielsen 2009; Ambastha et al. 2021; Huang et al. 2021). In Arabidopsis, RabH1b appears to be involved in cellulose biosynthesis during hypocotyls growth by engaging in the trafficking of CELLULOSE SYNTHASE 6 (CESA6) across intracellular compartments to the plasma membrane (He et al. 2018). Further, a mutation in *RabA5c* disturbs cell geometry during lateral organ development suggesting its role in wall stiffening and cell shape (Kirchhelle et al. 2016). RabE1 seems to be implicated in exocytosis and PIN2-GFP endocytosis by interacting with SCD1(STOMATAL CYTOKINESIS DEFECTIVE 1 and SCD2 (Mayers et al. 2017). Rab GTPases also play a critical role in pollen development and the polarized growth of pollen tubes (Cheung et al. 2002). Specifically, RabD along with RabA appears to be involved in these processes (De Graaf et al. 2005; Peng et al. 2011). A lack of RabA4d activity leads to abnormalities in pollen tube growth polarization due to impairment in delivering the components essential for pollen tube growth. Also, it shows decreased pollen tube guidance towards micropyle

(Szumlanski and Nielsen 2009). *RabA4b* is expressed explicitly at the apex of developing root hair cells during cell expansion and is implicated in releasing cell wall elements required to expand the tip (Preuss et al. 2004). A double mutant of *AtRabD2b* and *AtRabD2c* genes has deformed pollen, furcate and swollen pollen tube ends and produces smaller siliques than the wildtype (Peng et al. 2011). We asked which RabGTPases are explicitly expressed in the seed and its function during seed development.

Seed development commences with double fertilization, producing a diploid embryo and triploid endosperm. The embryo is formed after several cell divisions, elongation, and differentiation, while the endosperm developmental progression involves the coenocyte phase, cellularization, and differentiation of cells (Wang et al. 2021). In Arabidopsis, expansion and growth of the embryo rely on endosperm breakdown, which is regulated by the endosperm-specific gene, *ZHOUPI* (Denay et al. 2014). Embryo and endosperm development coupled with the development of integument that later turns to mature seed coat after differentiation, pigments accumulation, and cell death. For a proper seed formation, these three structures must coordinate through cell–cell communications that require the secretion of signaling molecules (Wang et al. 2021).

This study focused on a Rab GTPase, which is involved in plant growth and seed development. Based on its high seed-preferential expression, we selected the RabC1 GTPase. Isoform identification, transcript abundance analysis, tissue-specific localization via GUS transcriptional fusion, and mutants' analysis implicate its contribution to cellular functions required for plant growth and seed formation.

Materials and methods

Plant materials, growth condition and transformation

Arabidopsis thaliana Col-0 plants were grown on autoclaved soilrite under long-day conditions (22 °C, 16 h light, 8 h dark) after three days of stratification of seeds at 4°C. For the seedling experiment, sterilized seeds, after three days of stratifications at 4°C, were germinated on a 0.7% agar medium comprising 0.5 × Murashige and Skoog salts (Sigma, St. Louis, MO, USA) at pH 5.75 for 5–6 days; after that five seedlings of each genotype in six replicates were transferred on square plates containing 0.8% agar medium, transferred to growth chamber and placed vertically. For the *RabC1_{prom}:GUS* reporter line, the construct was transformed in the *Agrobacterium* GV3101 strain, and plant transformation was done on the Col-0 background using the floral dipping method (Clough and Bent 1999). Seeds were grown on selection media containing 50 µg/ml of kanamycin.

RNA extraction, cDNA synthesis, and expression analysis

Total RNA was extracted from the different plant stages: mature leaf, rosette 30-day-old, stem, flower, bud, and root, and various stages of developing seeds, 3 days after pollination (DAP), 4DAP, 5DAP, 6DAP, 8DAP, 10DAP, and 16DAP siliques. According to the manufacturer's instructions, RNA was extracted utilizing Sigma spectrum™ total RNA kit and then subjected to DNase treatment (TURBO™ DNase kit; Ambion, Austin, TX, USA). Using Superscript III (Invitrogen, Waltham, MA, USA), first-strand complementary DNA (cDNA) was created from 2 µg of total RNA subjected to DNase treatment. The PCR was carried out using a Fast SYBR™ Green Master Mix (Applied Biosystems, Waltham, MA, USA) on an ABI 7500 Fast Real-Time PCR Machine (Applied Biosystems). The experiment used at least two distinct biological and 2–3 technical replicates. Relative expression was determined using the $2^{-\Delta\Delta Ct}$ method (Livak and Schmittgen 2001). Ubiquitin 10 was taken as an endogenous reference gene.

For the determination of the expression level of genes involved in seed size and seed filling for the validation of seed phenotypes (*UMAMIT25*, *UMAMIT24*, *CYP714A*, *CYCB1-4*, *SWEET11*, and *SWEET15*) in Col-0 and *rabc1-2*, RNA was extracted from the seeds dissected from 25 to 30 5DAP siliques of each genotype in two biological replicates. In addition, ubiquitin 10 and actin were taken as reference genes. The primer sequences are listed in Supplementary Table S1.

Plasmid construction and *in-silico* promoter analysis

To generate the *RabC1_{prom}::GUS* reporter line, 1202 bp promoter sequence from the upstream region of ATG was amplified and cloned into the pBluescript SK(+). From the sequenced clone, the HindIII and BamHI digested promoter region was ligated into the pBI121 binary vector (Chen et al. 2003) in front of the *GUS* gene. Primer sequences for cloning were given in Supplementary Table S1. *Agrobacterium*-mediated transformation in *Arabidopsis* Col-0 was performed as mentioned above. A minimum of seven lines were analyzed, and all showed consistent results. Two lines with single T-DNA insertion showing a 1:3 Mendelian segregation pattern were taken for the experiment.

For the analysis of the cis-regulatory motif in the promoter of *RabC1*, sequences were scanned in PlantCARE and PLACE (Higo et al. 1999; Lescot et al. 2002). In addition, the promoter's diagrammatic representation of selected cis-regulatory motifs was done using TB tools (Chen et al. 2020).

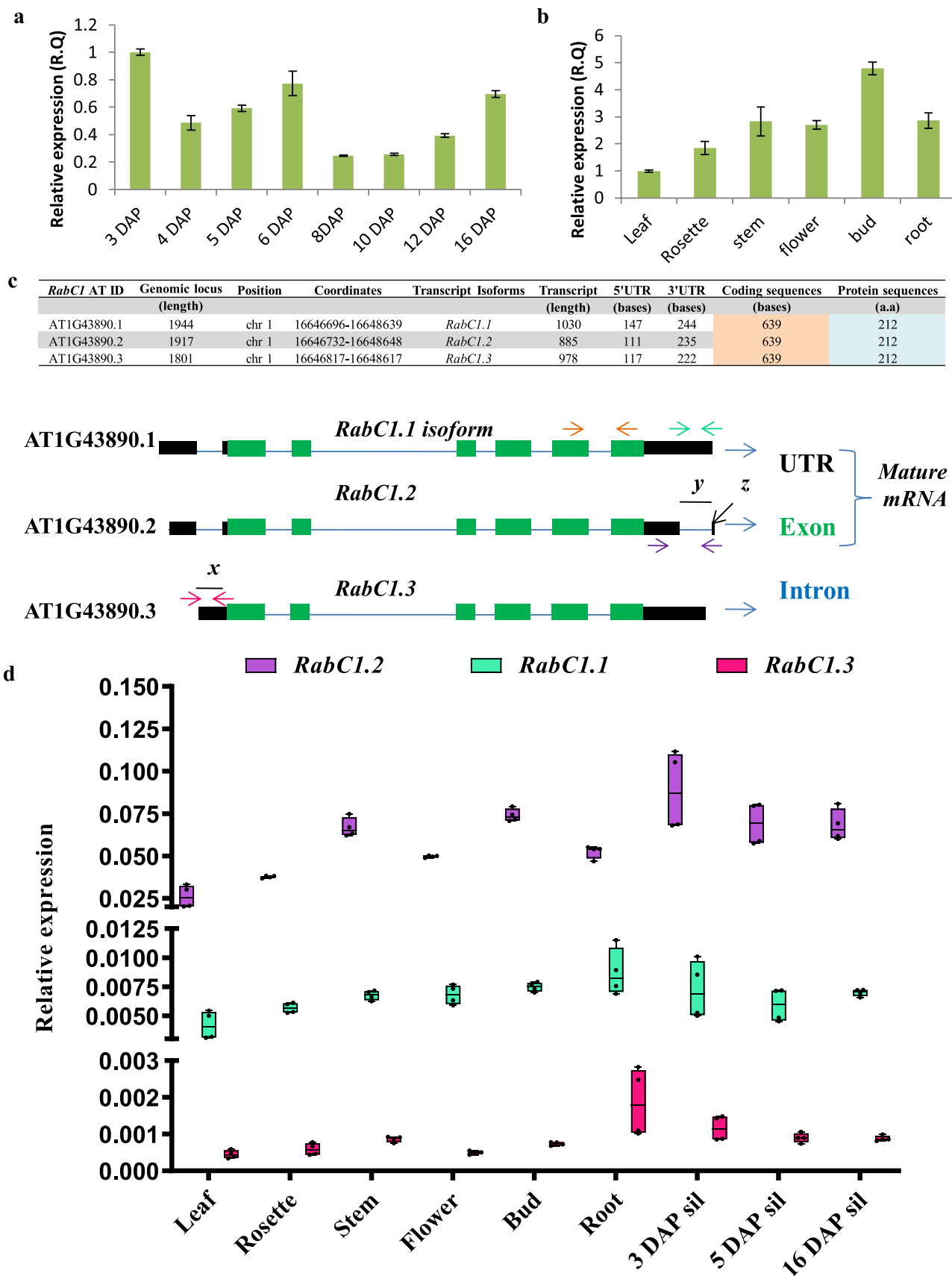
Histochemical GUS staining and quantitative fluorimetry assay

The spatiotemporal expression of *AtRabC1* in the *RabC1_{prom}::GUS* lines was analyzed by GUS staining (Jefferson et al. 1987), with a few alterations by adding 2 mM each of potassium ferrocyanide and potassium ferricyanide. Samples were incubated at 37 °C for 12–16 h and then cleared in a series of ethanol. Images were captured under a stereomicroscope (Leica microsystem). To detect the staining in the seed, freshly harvested siliques of a particular stage were slit longitudinally. Dissected seeds were incubated overnight in a GUS staining solution at 37 °C. After incubation and clearing in 1:2 acetic acid: ethanol and chloral hydrate solution, images were visualized under the light microscope (Leica microsystem).

GUS activity was quantified in plant extracts (Jefferson et al. 1987). In brief, 15-day-old seedlings (12–15 mg) (with and without induction of GA3 and salicylic acid, SA) in 3–8 replicates were crushed in 0.2 ml of GUS extraction buffer (50 mM Na₂HPO₄ pH-7.0, 10 mM DTT, 1 mM EDTA, 0.1% SLS, 0.1% Triton X-100) with micropestle in 1.5 ml Eppendorf tubes at 4°C. Tissue extracts were centrifuged at 16,200 g for 20 min at 4 °C. The supernatant was collected into fresh tubes. Then, 90 µl of the extract was mixed with 10 µl of 10X GUS assay buffer [4-methylumbelliferyl-β-D-glucuronide (MUG) suspended in GUS extraction buffer] and incubated at 37 °C for 2 h. After that, the reaction was terminated by adding 900 µl of 0.2 M sodium carbonate solution and was mixed adequately by vortexing. The reaction mixture was 2 times diluted. Fluorescence was measured using a Tecan spectrofluorometer with an excitation of 365 nm and emission at 455 nm. The specific GUS activity was calculated as nM 4-methylumbelliferone (MU) min⁻¹ mg protein⁻¹. Total protein was estimated using Bio-Rad dye.

Mutant characterization and genotyping

We obtained two T-DNA insertion lines, SALK_114305C (*rabc1-1*) and SALK_012129 (*rabc1-2*), from ABRC. The T-DNA in *rabc1-1* was positioned in the promoter, 335 nucleotides upstream of the translational start site. The T-DNA in *rabc1-2* was inserted in the intron, as mentioned in the figure (cf. Supplementary Fig. S7b). In both mutants, the left border was situated towards the 5' end of the gene. The T-DNA insertions and homozygosity were confirmed using a combination of primers (cf. Supplementary Fig. S7b, c, and d).



◀Fig. 1 Expression profile of *RabC1*. **a** qRT-PCR validation of *RabC1* transcript in different seed developing stages: 3 DAP, 4 DAP, 5 DAP, 6 DAP, 8 DAP, 10 DAP, 12 DAP, and 16 DAP siliques (primers designed from the exonic region, indicated by orange color arrows). A total of six replicates were taken (two biological and three technical replicates). Error bars denote the standard error (SE). **b** Relative expression of *RabC1* in different tissues: leaf, rosette, stem, flower, bud, and root. Error bars denote SE. Four replicates were taken (two biological and two technical replicates). **c** Gene structure and diagrammatic representation of transcript isoforms of *RabC1*. The black, blue, and green boxes represent the UTRs, introns, and exons (different color arrows represent the primers for different isoforms; common primers which recognize all three variants are indicated by orange arrows). The x indicates the portion of intron retained in the *RabC1.3* isoform, y represents the region of intron spliced out in the *RabC1.2* transcript, and z is denoted by the six extra adenine in the *RabC1.2* transcript isoform. **d** Relative expression for three transcript isoforms of *RabC1* in different vegetative and reproductive tissues: leaf, rosette, stem, flower, bud, root, 3 DAP siliques, 5 DAP siliques, and 16 DAP siliques. A total of four replicates were taken (two biological and two technical replicates)

Root length, seed mass, and seed size measurement

For comparative quantitative analysis of root length, plates were photographed, and root length was measured using ImageJ software. Boxplots were generated using Graph Pad Prism 8.4.2.

Mature, dry seeds were collected from the homozygous plants, and the weight of 250 seeds per aliquot of five different replicates was measured in each genotype. To determine seed size variables, seeds of multiple genotypes were photographed under a stereomicroscope at identical magnification. ImageJ software measured the area, perimeter, length, width, and length/width ratio of seeds. Boxplots were plotted in GraphPad Prism 8.4.2 software. Two-tailed Student's *t*-test and one-way ANOVA were carried out in excel and GraphPad Prism.

Differential interference contrast microscopy of developing seeds

The differences in the internal structure of seeds at different developing stages were analyzed, individual open flowers (marked as zero DAP) were tagged, and self-fertilized siliques of desired stages were collected, cut on both ends, slit longitudinally, and opened to dissect the seeds. Seeds were fixed in ethanol: acetic acid (9:1, v/v) solution for 1–2 h, then transferred to 70% and 90% ethanol for washing. Seeds were then cleared in chloral hydrate solution, visualized by DIC microscopy in Zeiss Meta 510 confocal microscope.

Tetrazolium staining

Seed coat integrity was assessed by permeability test by incubating seeds in 1% 2, 3, 5-triphenyl tetrazolium chloride (Sigma) prepared in 50 mM phosphate buffer (pH 7.0) overnight at 30°C. After that image was captured with a stereomicroscope (Leica Microsystems) and quantification of red-pigmented seeds was performed. The experiment was performed in five replicates containing 50 seeds of different genotypes. In addition, a two-tailed Student's *t*-test was performed to check the significance.

Complementation line in the mutant *rabc1*-background

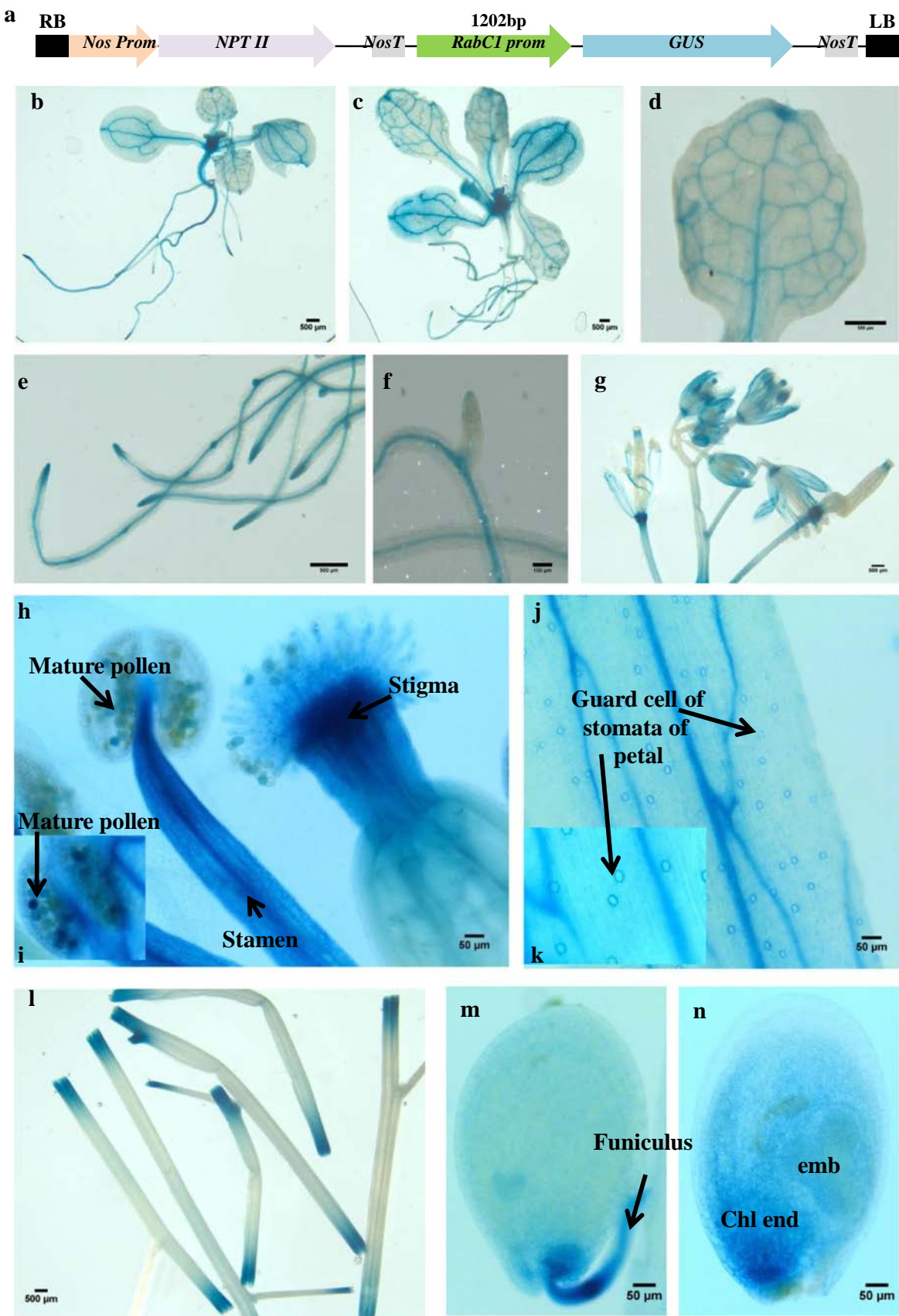
The complementation lines were developed in the mutant background, and a construct was prepared in the modified pBI121 having SmaI site at the 3' end of the *GUS* gene. In brief, the coding sequence of 639 bp having BamHI and SmaI sites was sub-cloned in pBluescript SK(+), and the clones were confirmed by Sanger sequencing. Digested promoters having HindIII and BamHI together with a digested fragment of coding sequences from Bluescript SK were triply ligated in HindIII, and SmaI digested pBI121 vector (without *GUS* gene). The positive construct was further confirmed by digestion with restriction enzyme HindIII (cf. Supplementary Fig. S8a, and b). The construct was transformed in *Agrobacterium*, followed by the transformation in *Arabidopsis* using the floral dipping method. Restoration of *RabC1* expression in transgenic lines in the mutant background was confirmed by qRT-PCR. The complementation line having the wild-type equivalent expression of *RabC1* in the mutant background was further selected for phenotypic analysis.

Staining of seed mucilage

Dry seeds were stained per the described protocol (Willats et al. 2001; Harpaz-Saad et al. 2011). Briefly, seeds were imbibed in water for 30–90 min and then stained with dye. For the visualization of acidic pectin, pre-hydrated seeds were stained with 0.01% ruthenium red (Sigma) with shaking for 20–30 min. Next, the cellulose and β-glucans were visualized by staining seeds with calcofluor white (Sigma) at a concentration of 25 µg/ml for 10 min. Stained seeds were washed multiple times and then visualized in the Leica fluorescence microscope under UV light.

Statistics

Biological replicates, sample size, and significance level were mentioned in all the figures, figure legends, and



◀Fig. 2 Tissue-specific expression of *RabC1* in different tissues. **a** Schematic representation of *RabC1_{prom}::GUS* construct. **b** GUS staining in a ten-day-old seedling. **c** A 15-day-old seedling. **d** Enlarged view of 15-day-old leaf. **e** Enlarged view of primary and secondary roots of 15-day-old seedling. **f** GUS staining at the tip of the secondary lateral root. **g** Inflorescence, bud, flower, and early stage of siliques. **h** Anther, stamen, and stigma. **i** An enlarged view of the anther. **j, k** Accumulation of GUS in guard cells and veins of petals. **l** Sections of cutted stem. **m** 4 DAP seed with funiculus. **n** 7 DAP seed. The experiment was performed in seven lines

supplemental data. Two-tailed *t*-tests and ANOVA have been performed in excel and GraphPad Prism 8.4.2 software.

Accession numbers

The accession numbers of genes specified in this study are as follows: AT1G43890 (*RabC1*), AT1G09380 (*UMAMIT25*), AT1G25270 (*UMAMIT24*), AT5G24910 (*CYP714A1*), AT2G26760 (*CYCB1-4*), AT3G48740 (*SWEET11*), AT5G13170 (*SWEET15*), AT4G05320 (*UBI10*), AT5G03530 (*RabC2A*), AT3G09910 (*RabC2B*).

Results

Identification and expression profiling of *Arabidopsis RabC1*

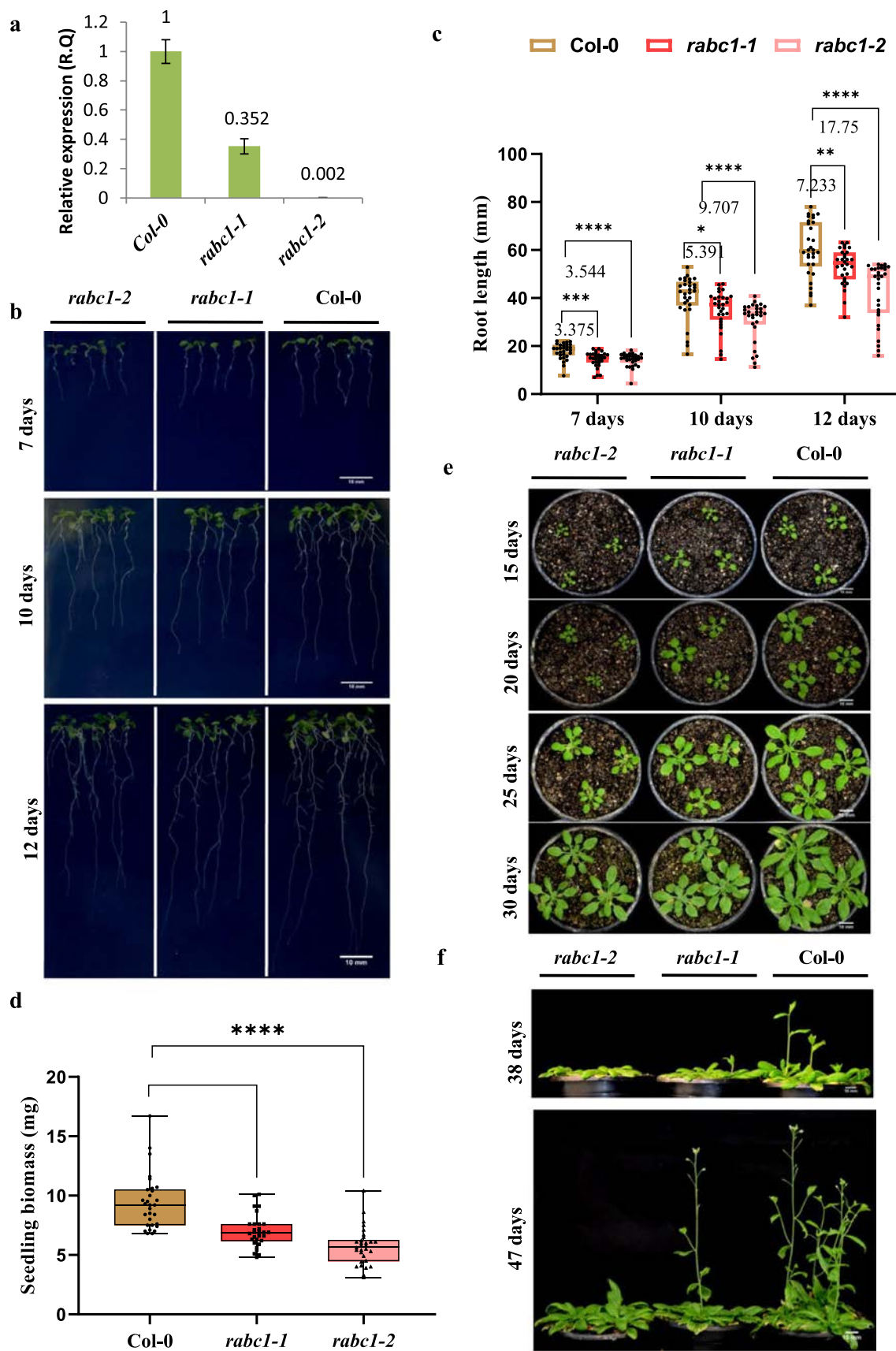
The *in silico* gene expression of 57 identified *Arabidopsis* Rab GTPases was performed in different plant developmental stages using Genevestigator to identify candidate GTPase with seed preferential expression. The developmental expression analysis revealed that most Rab GTPases were expressed differentially in various tissues (Supplementary Fig. S1). However, *RabC1*, *RabB1a*, and *RabH1a* have the highest expression in the chalazal endosperm stage (Supplementary Fig. S1). Furthermore, the expression of *RabC1* was significantly higher than *RabB1a* and *RabH1a* (Supplementary Fig. S2). It is also noteworthy that the expression of *RabC1* was elevated considerably in the seed-developing stages comprising chalazal endosperm, chalazal seed coat, and micropylar endosperm (Supplementary Fig. S1). Earlier studies suggested that chalazal endosperm mediates the delivery of nutrients between the maternal parent and growing embryo (Nguyen et al. 2000). Thus, we speculated that *RabC1* might have a role in cellular processes affecting the seed size and seed development.

RabC1 transcript variants and dynamics in their expression pattern along the developmental stages

The expression of *RabC1* transcript was assessed using qRT-PCR in three stages of developing seeds in *Arabidopsis* viz.,

early seed development stages at 3, 4, 5, and 6 DAP siliques; maturation stage at 8, 10, and 12 DAP; and late maturation stages at 16 DAP and also in other tissues (Fig. 1a, and b; primers indicated by orange color arrows, Fig. 1c). First, the transcript level of *RabC1* was highest at 3 DAP siliques; then it fell sharply at 4 DAP siliques. Further, it gradually increased up to 6 DAP siliques and decreased again at 8 DAP and then steadily increased afterward until the late phase (Fig. 1a). The expression pattern of the *RabC1* transcript was elevated at three developmental stages, i.e., the early coenocyte phase of endosperm (3 DAP); endosperm cellularization stage (6 DAP) which is important for the final seed size (Zhang et al. 2020) together with seed filling during seed maturation and late maturation (16 DAP) stage (Fig. 1a). We also analyzed transcript levels in various vegetative tissues: leaf, rosette, stem, flower, bud, and root, and the expression was found to be highest at the bud stage, followed by root, flower, stem, rosette, and least at the mature leaf (Fig. 1b).

The *RabC1* gene consists of three transcript isoforms viz., *RabC1.1*, *RabC1.2*, and *RabC1.3* that translate to identical proteins (Fig. 1c). The transcription start sites (TSS) of each isoform seem to be at a different position (Fig. 1c). These isoforms have differences in 3' and 5' UTR sequences (Supplementary Fig. S3). Considering the differences, at the 5' UTR of *RabC1.3*, there was intron retention (Fig. 1c indicated by 'x') which appears to be spliced out in the mature mRNA of *RabC1.1* and *RabC1.2* isoforms. The occurrence of intron retention might be due to the TSS switching for the generation of different splice variants. Furthermore, 3' UTR of isoform *RabC1.1* and *RabC1.3* was similar except for the addition of 22 nucleotides at the end of 3' UTR of *RabC1.1*. However, *RabC1.2* poses a relatively shorter 3' UTR due to some portion spliced out (Fig. 1c indicated by 'y') in the form of an intron in the mature mRNA, and besides this, it also contains six extra adenine at the 3' UTR (Fig. 1c indicated by 'z'). We thus assessed the expression level of these variants using isoform-specific primers in the qRT-PCR analysis (Fig. 1d, Supplementary Fig. S3a and b). We examined the isoform-specific expression (Fig. 1c primers denoted by arrows with different colors and S3a) in multiple tissues: leaf, rosette, stem, flower, bud, root, and three developing seed stages; 3, 5, and 16 DAP siliques. The expression of the variants *RabC1.1* and *RabC1.3* was lower in all tissues investigated than the cumulative expression of *RabC1*, which demonstrated a high level of expression (Fig. 1d). The *RabC1.2* primers cannot differentiate these isoforms; thus, the expression of *RabC1.2* was higher (app. 75–80%) among all the variants but not equal to the cumulative expression of *RabC1* (Supplementary Fig. S3a, and b). The isoform *RabC1.3* showed relatively higher expression in roots compared to other tissues; while *RabC1.2* or *RabC1* was expressed predominantly in the 3 DAP stages of siliques



◀Fig. 3 Phenotypic characterization of *RabC1*. **a** Relative expression of *RabC1* transcript in Col-0, *rabc1-1*, *rabc1-2*. Transcript level was checked by qRT-PCR from primers designed downstream of T-DNA insertion. A total of two biological replicates in *Arabidopsis* Col-0, five in *rabc1-1*, two in *rabc1-2*, and each with two technical replicates was taken. Standard bars represent SE. **b** Comparative growth analysis of seven-day-old, ten-day-old, and 12-day-old Col-0, *rabc1-1*, and *rabc1-2* seedlings. The image is representative of six biological replicates. Each plate contains five seedlings of all three genotypes, Col-0, *rabc1-1*, and *rabc1-2*. **c** Quantitative analysis of root length of seven-day-old, ten-day-old, and 12-day-old Col-0, *rabc1-1*, and *rabc1-2* seedlings. Box plots are represented by median (lines), interquartile ranges (boxes), and whiskers of root length of various genotypes (Col-0, *rabc1-1*, and *rabc1-2*; $n=30$). Each dot represents the sample. **d** Biomass determination of 12-day-old Col-0, *rabc1-1*, and *rabc1-2* seedlings. Box plots showing median (lines), interquartile ranges (boxes), and whiskers of seedling biomass of the genotypes as mentioned above. **e** Morphological analysis of 15-day-old, 20-day-old, 25-day-old, and 30-day-old Col-0, *rabc1-1*, *rabc1-2* plants. Scale bar = 10 mm. **f** Comparison of flowering time of 38-day-old and 47-day-old Col-0, *rabc1-1*, *rabc1-2* plants. The image is representative of three independent replicates. Seedling experiments were performed three times and showed consistent results. Scale bar = 10 mm. Significance denoted by asterisks * at $P < 0.05$, ** at $P < 0.01$, *** at $P < 0.001$, and **** at $P < 0.0001$

development (Fig. 1d). Apart from *RabC1*, the *RabC* family contains two other members, *RabC2A* and *RabC2B*. All three *RabC* proteins show a high degree of homology among their isoforms (Hashimoto et al. 2008). However, the transcript abundance of *RabC2A* and *RabC2B* in different tissues reveals its preferential expression in the root and stem in contrast to *RabC1*, which showed their highest expression in siliques (Supplementary Fig. S4a, and b; and Fig. 1a, and d).

Tissue-specific expression of *RabC1* and the analysis of cis-regulatory motifs in the promoter region

The spatiotemporal expression of *RabC1* was further investigated by fusing 1202 bp promoter sequence (Supplementary Fig. S5a), including 5' UTR from upstream of the ATG to *GUS* reporter gene (Fig. 2a, and Supplementary Fig. S5a) as previous studies in *Arabidopsis* suggests that 500 bp-1kb is sufficient to emulate transcription behavior of a promoter (Maston et al. 2006; Srivastava et al. 2014; Mishra et al. 2022; Prasad et al. 2022). The promoter construct was stably transformed in *Arabidopsis*, and several independent lines were analyzed for GUS expression using histochemical staining. In the vegetative development stage, GUS staining was observed in the shoot and roots of 10-day-old seedlings, and expression was more prominent in the leaf veins and nodes (Fig. 2b). We also observed GUS staining in the primary and secondary roots (Fig. 2b, c, e, and f). In 15-day-old seedlings, expression was persistent in the shoot, roots, leaf veins, nodes, and the leaf tip (Fig. 2c, and d). We also found a strong expression at the primary and secondary root tips (Fig. 2e and f). In the reproductive stage, strong

GUS expression was observed in the petal, the base of the flower (Fig. 2g), the stamen, the anther, mature pollen, and the stigma (Fig. 2h and i). We also detected prominent staining in the petals' guard cells and veins (Fig. 2j and k). GUS expression was also apparently strong at the cut part of the stem (Fig. 2l).

In the developing seed, maximum GUS expression was observed at the chalazal endosperm, followed by the chalazal seed coat. A low but distinct expression was also seen in the embryo (Fig. 2m and n). Interestingly, intense GUS staining was also observed in the funiculus tissue (Fig. 2m) that connects the developing seeds to the maternal parent and is known to be responsible for the direct transport of nutrients and the developmental signal from maternal tissues to seeds (Khan et al. 2015). Thus, it can be concluded that *RabC1* is widely expressed in all organs, with its maximum expression in the chalazal endosperm suggesting its role during seed development.

The *in-silico* promoter analysis using PlantCARE (Lescot et al. 2002) and PLACE (Higo et al. 1999) indicated several *cis*-regulatory elements involved in plant development, hormonal regulation, and stress response in the promoter of *RabC1* (Supplementary Fig. S5b). Further, light responsiveness motifs that include ACE, G-box, GT1-motif, and P-CMA2a were also enriched in the promoter regulatory region. The endosperm-specific skn-1 motif (Supplementary Fig. S5b) correlated with *RabC1*'s maximum expression in seed (Fig. 1a and 2n), suggesting its role in seed development. A significant number of GA responsive elements (GARE-motif and TATC-box) were located at various positions (+ 242, + 893, + 414, and - 93) and predicted to be involved in plant signaling. *RabC1* promoter also harbors two TCA elements required for salicylic acid responsiveness at positions + 396 and - 1056. Different *cis*-regulatory elements were identified as associated with abiotic stress responses that included ABRE, DRE, HSE, and MBS were also present in the *RabC1* promoter (Supplementary Fig. S5b).

The high number of gibberellin responsive (Four, GARE-motif, and TATC-box) and SA-responsive elements (two TCA elements) in the *RabC1* promoter indicates its responsiveness towards these phytohormones. We thus subjected *RabC1* promoter-GUS fusion lines to 200 μ M GA3 and 2 mM SA treatment. The histochemical and quantitative enzyme activity assay showed that the *RabC1* promoter does not respond to GA3 despite having a significant number of conserved GA-responsive elements (Supplementary Fig. S6). However, we identified intense histochemical GUS staining and elevated but insignificant quantitative GUS activity increase in response to SA compared to control (Supplementary Fig. S6a, and b).

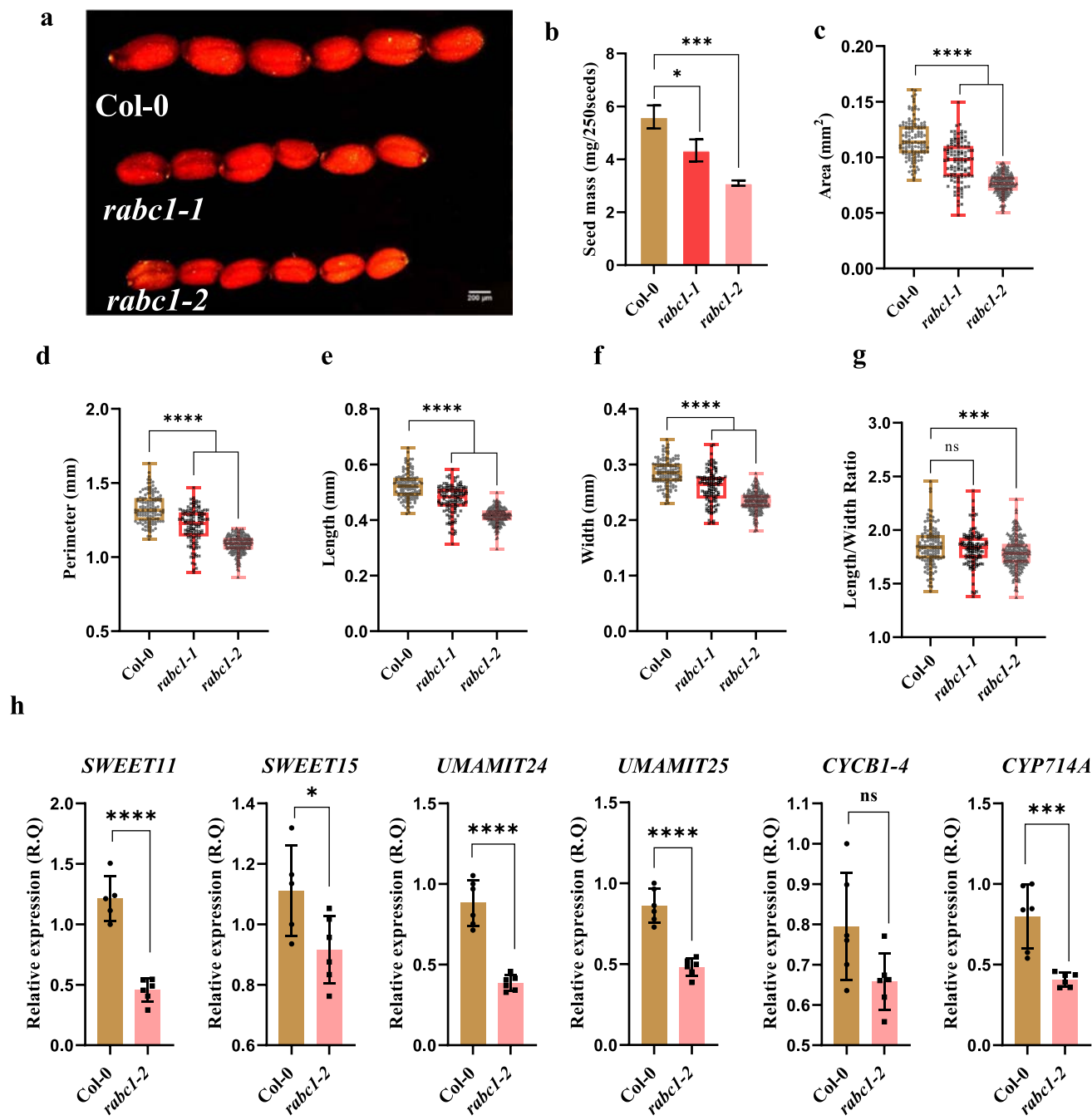


Fig. 4 Differences in the seed phenotype of Col-0, *rabc1-1*, and *rabc1-2*. **a** Seed size of different genotypes (Col-0, *rabc1-1*, *rabc1-2*). Scale bar = 200 μm. **b** Determination of seed mass of 250 seeds of each Col-0, *rabc1-1*, and *rabc1-2* in five biological replicates. Error bars denote standard deviation (SD). **c–g** Quantitative analysis of seed parameters in Col-0, *rabc1-1*, and *rabc1-2*. **c** Area. **d** Perimeter. **e** Length. **f** Width. **g** Length/width ratio (Col-0, $n=128$; *rabc1-1*, $n=110$; *rabc1-2*, $n=225$). Box plots indicate the median (lines), interquartile ranges (boxes), and whiskers of the above seed size variables, area, perimeter, length, and width. Each point represents the

sample. The experiment was repeated two times with similar results. **h** Validation of seed phenotypes by expression analysis of sugar transporters genes, *SWEET11*, and *SWEET15*, amino acid transporters *UMAMIT24*, and *UMAMIT25*, *CYCB1-4*, and *CYP714A* in 5DAP seeds of *rabc1-2* and Col-0. The experiment was executed in six replicates with two biological and three technical replicates. Error bars denote the standard deviation (SD) among replicates. Significance denoted by * at $P < 0.05$; ** at $P < 0.01$; *** at $P < 0.001$; and **** at $P < 0.0001$.

Mutation in *RabC1* affects plant growth, root length, and flowering time

RabC1 encodes a protein of 212 amino acids that belongs to the Rab family of small GTPases (Supplementary Fig. S7a). To demonstrate the role of *RabC1* in plant growth and development, we assessed the expression of *RabC1* in T-DNA insertional mutants. The qRT-PCR for the *RabC1* gene confirmed that the transcript level was reduced significantly to 35% compared to WT in *rabc1-1*, while in intronic mutant *rabc1-2*, no transcript was detected (Fig. 3a). Thus, *rabc1-1* is a knock-down mutant while *rabc1-2* is a knock-out mutant. We compared the seedling growth and root length in *rabc1-1* and *rabc1-2* with that of the wildtype (WT) Col-0 at seven-day-old, ten-day-old, and 12-day-old seedlings. It was apparent that the seedling growth and root length in *rabc1-1* and *rabc1-2* were compromised as compared to WT (Fig. 3b). The quantitative analysis of root length also indicated that root length was highly reduced in *rabc1-2* than in *rabc1-1*, with a significant difference of 7.233 mm in the case of *rabc1-1* and 17.75 mm in the case of *rabc1-2* at 12 days after germination (DAG) as compared to WT (Fig. 3c). However, seedling biomass was comparable in *rabc1-1* and *rabc1-2* to WT, with relatively lesser biomass in *rabc1-2* (Fig. 3d). The qualitative and quantitative analysis of root length strongly suggests that *rabc1-2* phenotype was more profound than *rabc1-1* (Fig. 3b, and c), which was highly correlated with the expression pattern of *RabC1* in mutant's *rabc1-1*, and *rabc1-2* (Fig. 3a). Collectively, these results suggest that *RabC1* is required for plant growth and root development.

To further gain insight into the importance of *RabC1* in the later stages of plant development, the *rabc1-1*, *rabc1-2*, and Col-0 phenotypic analyses were performed in multiple replicates before and after the flowering stages of plant development (Fig. 3e, and f). Before flowering stages, such as 15-day, 20-day, 25-day, and 30-day-old, plants of *rabc1-1* and *rabc1-2* exhibited comparatively dwarf phenotypes with less expanded leaves and smaller rosette size than WT (Fig. 3e). Later, we observed delayed flowering in *rabc1-1* and *rabc1-2* compared to WT (Fig. 3f). In the case of *rabc1-1*, we have seen a few replicates flowered normally which may be due to the knock-down expression of *RabC1*. However, in the case of *rabc1-2*, flowering was delayed comparatively which correlates with their complete loss of transcript because of their T-DNA insertion in the genic region (Fig. 3a, and f). Overall, these results highlight the crucial role of *RabC1* in cellular processes important for normal plant development.

RabC1 affects seed size and cell expansion during seed development

Our expression analysis implies that *RabC1* exhibited a maximum expression at early seed development; 3 DAP and 6 DAP and specifically at chalazal endosperm, chalazal seed coat, and funiculus that are essential tissue for the transport of nutrients to the developing embryo (Fig. 2m, 2n, and Supplementary Fig. S1). Thus, to define the role of *RabC1*, seeds collected from homozygous mutants *rabc1-1* and *rabc1-2* were examined. We observed a smaller seed size in the mutants of *RabC1* compared to WT, with *rabc1-2* exhibiting the smallest seed size compared to *rabc1-1* (Fig. 4a). Furthermore, seed weight was also significantly lesser in the *rabc1-1* and *rabc1-2* compared to WT (Fig. 4b). The quantitative analysis also revealed that seed area, perimeter, length, and width of *rabc1-1* and *rabc1-2* were significantly reduced compared to WT (Fig. 4c, d, e, and f). The length/width ratio of *rabc1-1* was similar to WT while *rabc1-2* showed a significantly reduced ratio (Fig. 4g). Together, these results suggest that mutation in the *RabC1* gene affects seed size. The knockout mutant displayed a more pronounced phenotype of reduced seed size and weight than the knock-down mutant.

Expression analysis was performed by taking previously reported marker genes to validate the seed phenotypes of mutants. We analyze the expression of genes implicated in seed size and seed filling in knockout mutant *rabc1-2* and WT at 5 DAP seeds. In Arabidopsis, developing embryos rely on the nutrition provided by the maternal tissues through the activity of various sugar transporters located in the seed coat and endosperm (Chen et al. 2012, 2015). We determined the expression of *SWEET11* and *SWEET15*, and we found that the expression of both genes was significantly downregulated in *rabc1-2* (Fig. 4h).

Furthermore, several reports suggest that numerous UMAMIT proteins are expressed in the developing seeds during the seed-filling process, participate in the transport of amino acids, and contribute to the seed yield (Mu et al. 2015; Besnard et al. 2018). We found that the expression of *UMAMIT24* and *UMAMIT25* was affected and significantly downregulated in *rabc1-2* (Fig. 4h). We also analyze the expression of some known seed size regulators reported previously to validate the seed phenotypes (Ren et al. 2019). In Arabidopsis, *CYCB1; 4*, a positive seed size regulator. We found its expression was downregulated in *rabc1-2* (Fig. 4h). Further, Arabidopsis *CYP714A1* or *ELA1* encodes a cytochrome p450 monooxygenase which is a negative seed size regulator that deactivates the bioactive GAs, thus affecting cell wall expansion (Zhang et al. 2011; Creff et al. 2015). We analyzed the transcript abundance of *ELA1*, which was also downregulated (Fig. 4h). Collectively, the above results point toward the role of *RabC1* during seed development.

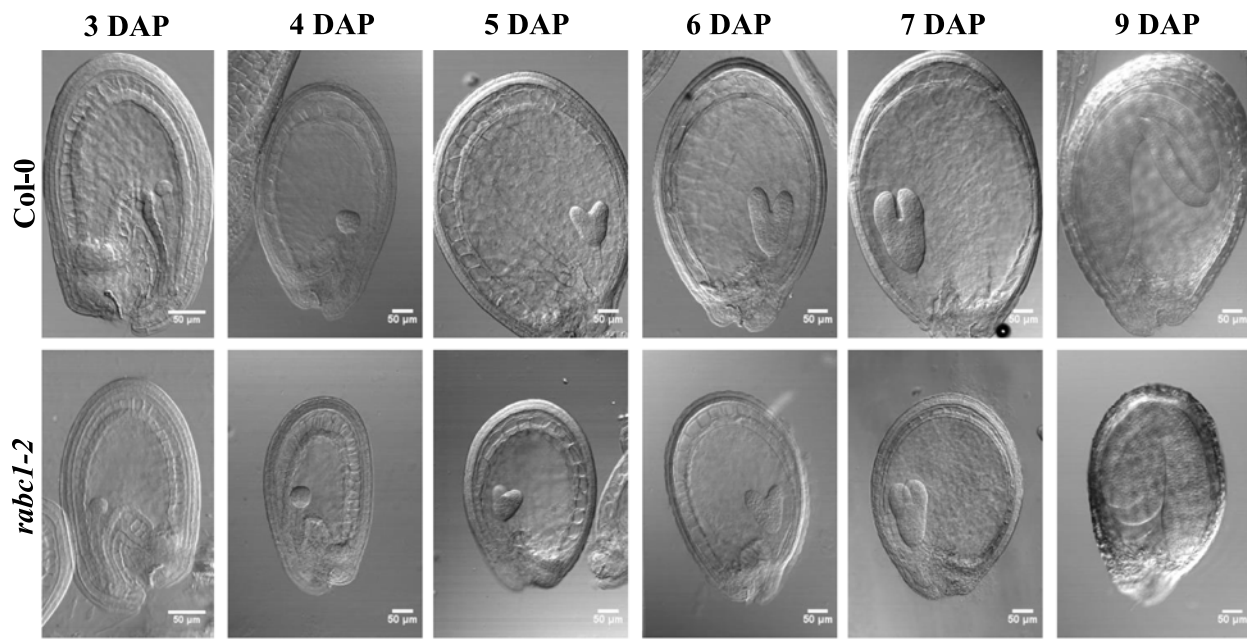
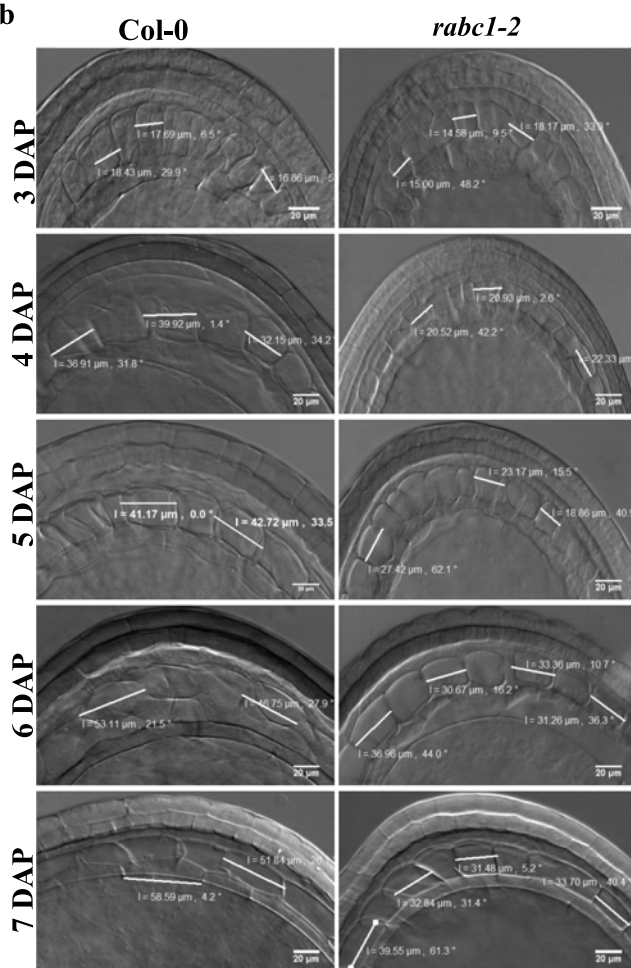
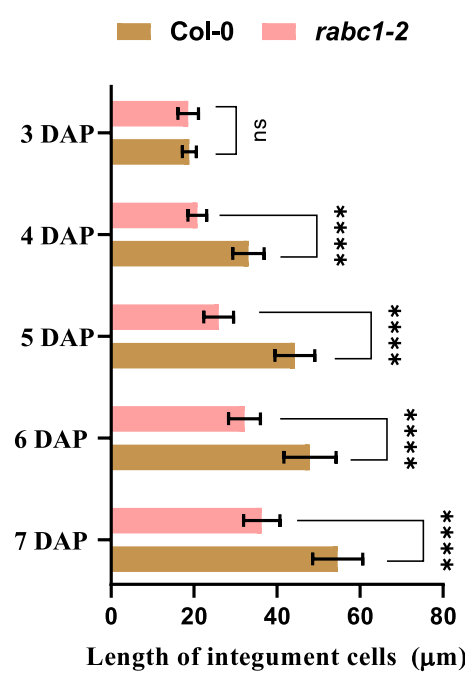
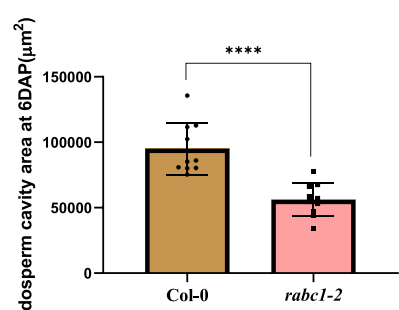
a**b****c****d**

Fig. 5 RabC1 is required for cell expansion during seed development. **a** Differential interference contrast microscopy (DIC) of randomly selected seeds at various stages of seed development (3DAP, 4DAP, 5DAP, 6DAP, 7DAP, and 9DAP) in WT and *rabc1-2*. Scale bars = 50 μ m. **b** Microscopical image of an enlarged view of integument cells of different genotypes, WT and *rabc1-2* in several seed developing stages (3DAP–7DAP). Scale bars indicate 20 μ m. **c** Quantitative measurement of the length of integument cells in genotypes, WT, and *rabc1-2*, at numerous stages of seed development 3DAP to 7DAP (WT at 3–7DAP, $n=30, 25, 19, 14, 13$; and *rabc1-2* at 3DAP to 7 DAP, $n=20, 18, 16, 23, 17$). **d** Comparative analysis of endosperm cavity area of WT and *rabc1-2* at 6DAP stage (WT and *rabc1-2*, $n=10$). The experiment was performed two times and showed similar results. Asterisks represent significance level (two-tailed *t*-test), where * at $P<0.05$, ** at $P<0.01$, *** at $P<0.001$, and **** at $P<0.0001$

and is positively implicated in the seed-filling process by an unknown mechanism.

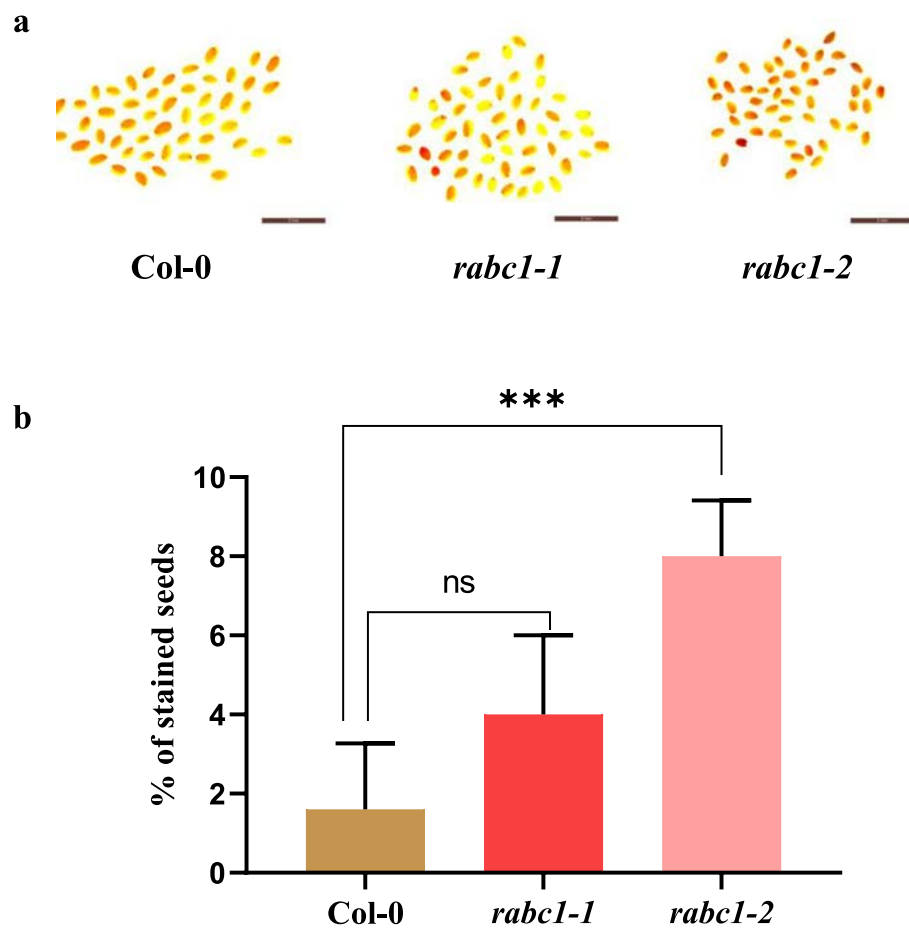
To further gain insight into the details of the internal structure of developing seeds, differential interference contrast (DIC) microscopy was performed at various stages of seed development, comprising 3, 4, 5, 6, 7, and 9 DAP. The cytological study revealed that embryo development in *rabc1-2* was proper and similar to WT in all stages of

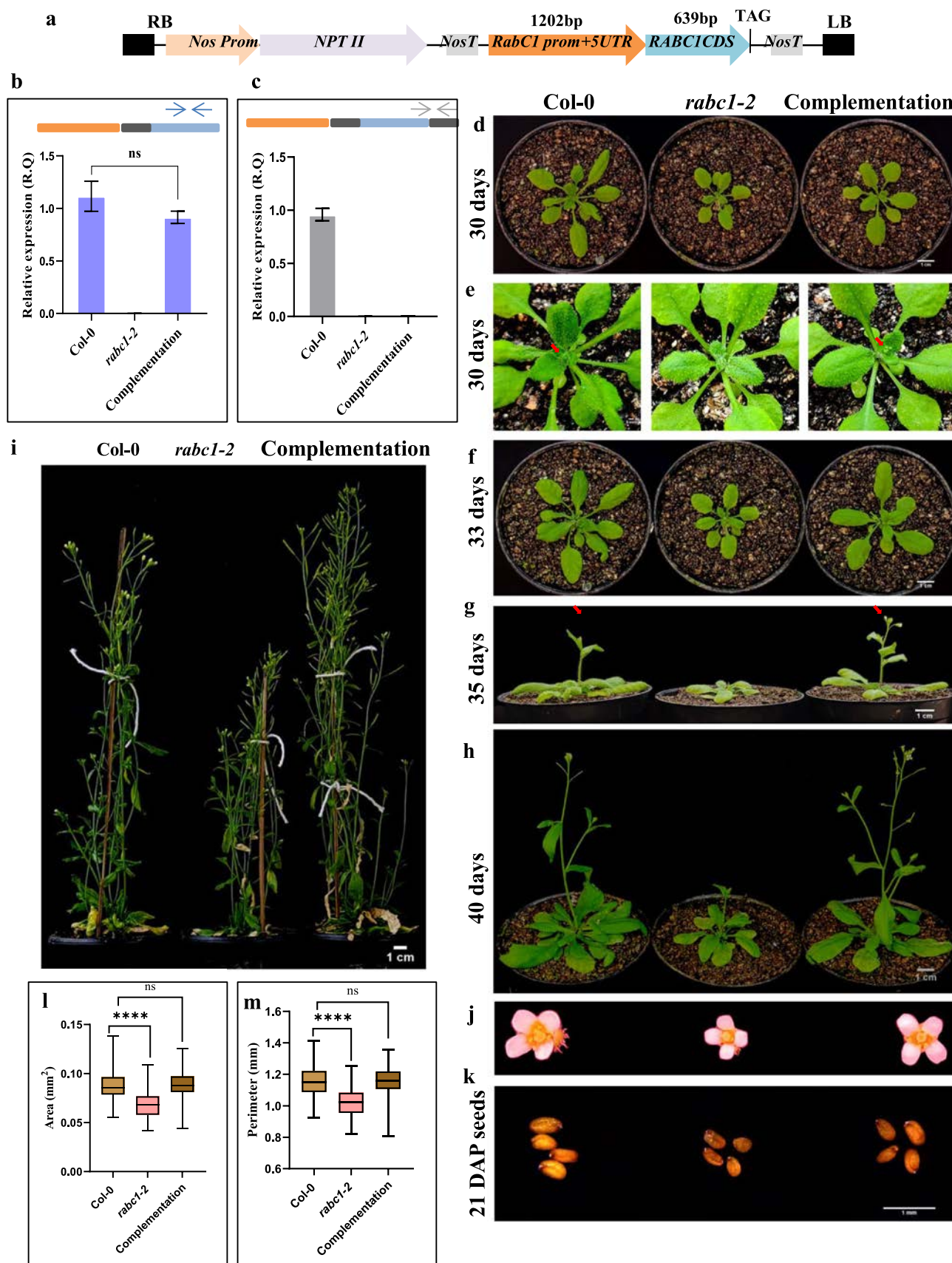
developing seeds (Fig. 5a). We found a reduced expansion of the endosperm cavity from 4 to 7 DAP in *rabc1-2* compared to WT (Fig. 5a). At 3 DAP, cell integument length was almost similar in *rabc1-2* and WT (Fig. 5b, and c). Beyond 3 DAP, we observed less cell expansion in the integument from 4 to 7 DAP of developing seeds (Fig. 5b). The quantitative analysis of cell integument length from 3 to 7 DAP stages also indicated that *rabc1-2* showed significantly decreased cell integument length than WT (Fig. 5c). Since at 6 DAP the endosperm cavity almost attains its full size, which determines the final seed size, we performed a quantitative analysis of the endosperm cavity area in *rabc1-2* with WT. Notably, we found a significantly smaller area of the endosperm cavity in *rabc1-2* compared to WT (Fig. 5d). The cumulative results suggest that RabC1 GTPase contributes to cellular processes required for the expansion of the endosperm cavity and integument cells.

Mutation in *RabC1* affects seed coat permeability

The RabC1 was hypothesized to play role in nutrient transport and seed coat permeability because of high expression in the chalazal seed coat and funiculus (Fig. 2m, and n).

Fig. 6 Mutation in *RabC1* affects seed coat permeability. **a** Seeds of WT, *rabc1-1*, and *rabc1-2* after overnight incubation in tetrazolium chloride dye. **b** Quantitative analysis of stained seeds of WT, *rabc1-1*, and *rabc1-2* in five biological replicates, each containing 50 seeds. Asterisks indicate * as a significant difference between mutants and WT (two-tailed *t*-test). * at $P<0.05$, ** at $P<0.01$, *** at $P<0.001$, and **** at $P<0.0001$





◀Fig. 7 Restoration of phenotypes in the complementation line generated in *rabc1-2*. **a** Schematic representation of *RabC1_{prom}::CDS* restorer construct. **b** Relative expression of *RabC1* in Col-0, *rabc1-2*, and complementation line. Arrows represent the position of the primers, and error bars indicate the standard deviation. **c** Relative expression of *RabC1* of WT specific allele in the Col-0, *rabc1-2*, and complementation line for confirming mutant background. Arrows represent the position of the primers (orange, blue, and grey bars indicate the promoter, coding sequence, 3' and 5' UTR). **d** Phenotype of Col-0, *rabc1-2*, and complementation line at 30DAG. **e** Zoom image showing initiation of flowering in Col-0, complementation line in contrast to *rabc1-2*. **f, g, h**, and **i** Morphological analysis of Col-0, *rabc1-2*, and complementation line in 33-day-old, 35-day, 40-day-old and mature plants. **j** Comparison of flower phenotype in Col-0, *rabc1-2*, and complementation line. **k** Seed phenotype of Col-0, *rabc1-2*, and complementation line at 21 DAP stage. **l, m** Comparison of area and perimeter of Col-0, *rabc1-2*, and complementation line seeds ($n=174, 120$, and 160)

The seed coat permeability was assessed by staining seeds with tetrazolium chloride, a colorless dye. Upon exposure to enzymes of live tissue, it gets reduced to red formazan. We observed a significantly higher number of stained seeds in the knockout mutant *rabc1-2* compared to WT (Fig. 6a, and b). On the other hand, there was no significant difference in the knock-down mutant *rabc1-1* compared to WT (Fig. 6b). These results indicate that the lack of function of RabC1 increases the permeability of the seed, which may be due to defects in the seed coat integrity.

Functional complementation in the *rabc1-2* mutant

Complementation lines were generated in the knock-out *rabc1-2* mutant background (Supplementary Fig. S8). The complementation lines with a functional copy of RabC1 driven by the native promoter showed RabC1 transcript abundance comparable to that of the WT in the quantitative RT-PCR analysis (Fig. 7a, Supplementary Fig. S8 and S9). The complementation line in which the expression of RabC1 was equivalent to WT was subjected to phenotypic analysis (Fig. 7b, c and Supplementary Fig. S8 and S9). The detailed phenotypic study at 30, 33, 35, and 40 DAG, showed that the rosette diameter, flowering time, flower size, bolting, and plant height of the complementation line were similar to that of the WT (Fig. 7d–j). In addition, we also observed the restoration of seed development defects in 21 DAP siliques of the complemented line, with an average seed size comparable to that of the WT (Fig. 7k, l, and m).

The correlation of gene expression among the three members of the RabC family was also assessed. The transcripts level of *RabC2A* was similar in the Col-0, *rabc1-2*, and complemented lines, implying no compensation at the transcript level (Supplementary Fig. S10a). In contrast, the transcript level of *RabC2B* was reduced in *rabc1-2* as compared to Col-0, and it got partially restored in the complemented lines (Supplementary Fig. S10b), suggesting that there is

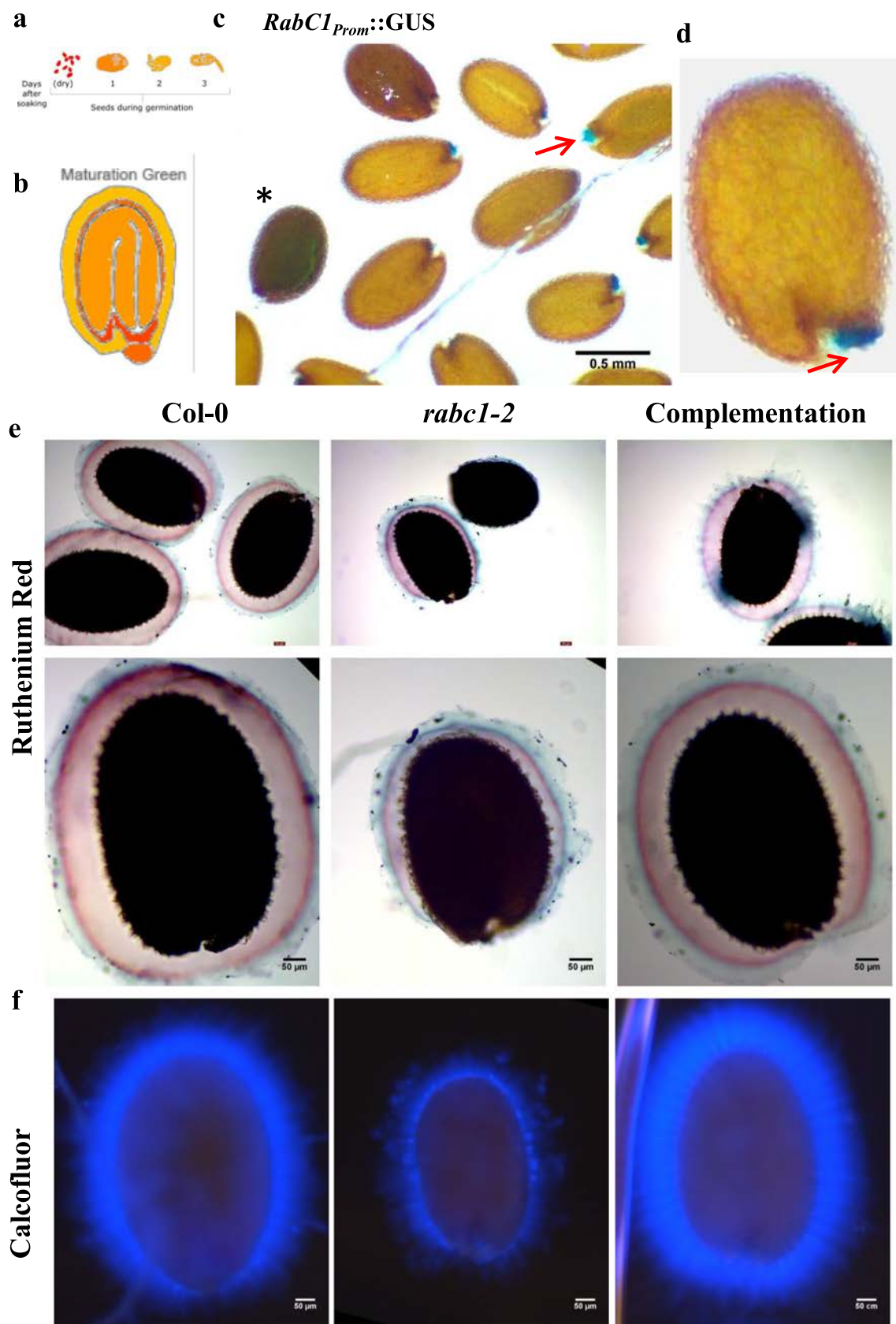
some unknown mechanism that correlates the expression of *RabC1* and *RabC2B*. However, the elevated expression level of *RabC2B* in the complemented lines was not similar to the WT level that might be due to some experimental variation. Overall, the complementation experiment showed that RabC1 with its native promoter could rescue plant growth and seed defects of the mutant supporting functional complementation.

RabC1 is required for seed mucilage formation

The *in-silico* expression using the eFP browser (Winter et al. 2007) showed the expression of *RabC1* in the green maturation seed stage and the dry seed (Fig. 8a and b). We also observed GUS expression in the ruptured dry seed beneath the brown seed coat (Fig. 8c, denoted by an asterisk) and the chalazal seed coat region in the GUS-promoter reporter lines (Fig. 8c, and d). Thus, the expression of *RabC1* in the different seed tissues prompted us to analyze the status of seed mucilage in *rabc1-2*. First, we stained the seeds with ruthenium red to examine the seed mucilage in the WT and *rabc1-2*. The *rabc1-2* mutants showed reduced seed mucilage staining compared to WT. However, the seed mucilage staining was comparable to WT in the complemented line, indicating that the mucilage defects were rescued (Fig. 8e). To examine cellulose, which is the critical constituent of seed mucilage, we stained the seeds with calcofluor white. The WT seeds showed broad, intense fluorescence, while the fluorescence was reduced in *rabc1-2*. However, in the complemented line, we observed fluorescence similar to WT suggesting the involvement of *RabC1* in the trafficking of mucilage components during seed mucilage synthesis and deposition (Fig. 8f).

Discussion

Angiosperms are the most dominant life form of the plant due to their ability to develop seeds that house the next generation. Seeds germinate and revive into the fully grown plant on receiving appropriate conditions. Plant growth and development need numerous signaling pathways to be activated precisely temporally and spatially by key regulators. Rab GTPases are key regulators that mediate the transport of molecules to their respective compartments according to the demand (Olkkinen and Slenmark 1997; Pereira-Leal and Seabra 2001; Nielsen 2020). Several Rab GTPases have been reported to localize to distinct compartments. The localization of RabC1 is uncharacterized (Wang et al. 2022). Few reports predict its localization to post Golgi/endosome, but its functional characterization has not yet been done (Rutherford and Moore 2002; Zhou et al. 2020).



◀Fig. 8 RabC1 is required for seed mucilage. **a** Expression of *RabC1* in the dry seed via eFP browser. **b** At the maturation green stage. **c** GUS expression in the dry seed. **d** Enlarged image showing GUS expression at the chalazal seed coat region in the *RabC1_{prom}::GUS* reporter line. The mature, dry seeds were kept in GUS solution overnight and then visualized under a microscope. **e** Ruthenium red staining in the pre-hydrated seeds of Col-0, *rabc1-2*, and complementation line. **f** Calcofluor white staining in the pre-hydrated seeds of Col-0, *rabc1-2*, and complementation line. The experiment was performed two times with similar results

Among the three Rab GTPases preferentially expressed in seed tissue, *RabC1* showed the highest expression level, indicating its substantial role in the seed (Supplementary Fig. S1, and S2). Besides, among the three members of the RabC family, *RabC1* shows the highest expression (Fig. 1a, b, d, and Supplementary Fig. S3). The expression of *RabC1* in different stages of the plant development also suggests its involvement in various processes (Fig. 1a, b, Supplementary Fig. S1 and S2). Furthermore, its pattern of expression during different developing stages of seed also reveals that it is involved in the three transition stages; early seed development, endosperm cellularization, and seed maturation (Fig. 1a, and b).

Several reports indicate that housekeeping genes harbor a single UTR and are expressed constitutively in numerous processes (Eisenberg and Levanon 2003). Some studies also emphasize that most of the ubiquitously transcribed genes produce various 3' UTRs through tissue-specific alternative polyadenylation to gain specificity. The 3' UTR isoform ratios appear to be cell type-specific and crucial for particular pathways (Kesari et al. 2012; Lianoglou et al. 2013; Zheng 2018). We found that *RabC1* consists of three isoforms that produce identical proteins. These isoforms have differences in their 5' UTRs and 3' UTRs (Fig. 1c, Supplementary Fig. S3a).

Furthermore, isoform-specific expression analysis in different stages of plant development and developing seeds indicates their expression pattern and level dynamics (Fig. 1d). A comparative analysis of the expression level of isoforms showed that *RabC1.2* showed the highest transcript abundance at 3 DAP siliques (Fig. 1d). Several findings reveal that shorter 3' UTR have more regulatory functions, as lengthy 3' UTR occlusive topologies make regulatory components less accessible (Lianoglou et al. 2013). Furthermore, these 3' UTR have relatively short UTR due to using the closest polyadenylation (pA) site (Kim et al. 2014; Mayr 2017). Interestingly, the *RabC1.2* isoform has a shorter 3' UTR (Fig. 1c, and Supplementary Fig. S3a) and exhibits high expression, too (Fig. 1d). With the help of publicly available tools (Weigel and Mott 2009), we found that *RabC1.2* genomic locus carried single nucleotide polymorphism (SNPs) towards 3' end of the gene in 10 natural ecotypes (Supplementary Table S2). The particular SNPs

are categorized under splice acceptor variant, and their effect is considered high, indicating their importance towards the 3' end of the gene (Supplementary Table S2). The above findings suggest that abundantly expressed *RabC1* likely controls tissue-specific functions through the generation of isoform under the tight regulation by 3' UTR.

Spatiotemporal expression using the GUS promoter line further confirmed the tissue-specific localization of *RabC1* (Fig. 2). We observed GUS staining in almost all tissue: seedling, root, secondary lateral root, leaf, leaf tip, veins, and reproductive tissues, suggesting *RabC1*'s role in all aspects of development (Fig. 2b, c, d, e, f, and g). GUS staining at the cut part of stems further indicates its involvement in wound responsiveness (Fig. 2l). Specific expression in the guard cell of flower petals documents its role in stomatal biology (Fig. 2j, and k). During seed development, GUS staining was found to accumulate at the chalazal endosperm, embryo, and funiculus, which was strong evidence of its role in seed development and seed size (Fig. 2m, and n). Overall, expression analysis prompted us further to characterize the role of *RabC1* in plant development.

To further characterize the phenotype of *RabC1*, a comparative study was performed on *rabc1-1*, *rabc1-2*, and WT at the different seedling stages, revealing that *rabc1-1* and *rabc1-2* were comparatively smaller than WT (Fig. 3b). Its root length and seedling biomass were also significantly reduced compared to WT (Fig. 3c, and d). Comparative phenotypic analysis at later stages of plant growth showed that the development of *rabc1-1* and *rabc1-2* lines was slow compared to WT (Fig. 3e). We also observed a delayed flowering phenotype in the later stage of plant growth in *rabc1-1* and *rabc1-2* (Fig. 3f). Collectively, reduced root length, less biomass, and delayed flowering suggest that *RabC1* is involved in multiple developmental pathways through controlling the vesicle trafficking events.

RabC1 expression was seen in the seed tissue during seed development, including chalazal endosperm, funiculus, chalazal seed coat, and embryo (Fig. 2m, and n). We observed that the seed size of *rabc1-1* and *rabc1-2* was significantly smaller than WT (Fig. 4a). Quantitative seed size and mass analysis further validate the results (Fig. 4b, c, d, e, f, and g). Numerous studies suggest that multiple sugar and amino acid transporters play a crucial role in seed filling and thus govern seed size (Chen et al. 2012, 2015; Mu et al. 2015; Besnard et al. 2018). The expression of *SWEET11* and *SWEET15* was significantly downregulated in *rabc1-2* seeds (Fig. 4h). The reported GUS expression pattern of *SWEET11* in leaves and seeds (Chen et al. 2012, 2015) was highly similar to the *RabC1* (Fig. 2b, c, and d). However, further work is needed to validate the relation between *RabC1* and *SWEET* genes. Similarly, the expression of amino acid transporters *UMAMIT24* and *UMAMIT25* was also significantly downregulated in *rabc1-2* seeds (Fig. 4h). *UMAMIT24* and

UMAMIT25 are expressed in the chalazal seed coat in developing seeds and help transport amino acids from maternal tissue to seeds through the chalazal seed coat (Besnard et al. 2018). The above findings indicate that the transportation of amino acids in the seed and the seed-filling process were affected by the disruption of RabC1 GTPase signaling.

The *rabc1-2* has a reduced endosperm cavity and smaller integument cell length, contributing to the smaller seed size (Fig. 5a). We observed lesser expansion in the integument cell wall of *rabc1-2* compared to WT (Fig. 5b). The reduction in the endosperm cavity area and integument cell length expansion in different stages of developing seeds further validates and illustrates the role of *RabC1* in seed development (Fig. 5c, and d). Together, the above results suggest that disruption of trafficking events leads to failure in the coordination among the seed tissues, i.e., embryo, seed coat, and endosperm that made the seed smaller, considering the role of Rab GTPase in nutrient transport. Furthermore, the percentage of tetrazolium red stained seeds was significantly high in *rabc1-2*, indicating that seed coat integrity was compromised in *rabc1-2* (Fig. 6a, and b), and RabC1 plays a role in regulating seed size and seed coat integrity.

The above results were further verified by restoring the mutant phenotype in the complementation line (Fig. 7, S8, and S9). A recent study suggests that TERMINAL FLOWER 1 (TFL1) plays a vital role in flowering and seed size regulation as its loss-of-function mutants also exhibited early flowering and prominent seed size phenotype (Zhang et al. 2020). The *rabc1-2* mutant showed smaller seed size and delayed flowering, and those phenotypic developmental defects were rescued in the complementation line (Fig. 7, S8, and S9). Thus, our results also suggest that RabC1 is involved in processes affecting both seed size and flowering.

Seed coat epidermal cells, which develop from the outer ovule integument, produce mucilage in *Arabidopsis*. The synthesis of cellulose occurs on the plasma membrane, while pectin and hemicelluloses are formed within the Golgi apparatus, which are eventually secreted to the apoplast (Young et al. 2008; Zhang et al. 2022). Plasma membrane-localized cellulose synthase (CESA) complexes are necessary for cellulose biosynthesis and cell wall formation. The synthesis and assembly of CESA proteins occur in the endoplasmic reticulum and Golgi. Hence, the trafficking of these complexes between organelles and their regulation is crucial for proper cell wall formation. Reportedly, Rab GTPase, such as Golgi localized RabH1b, is involved in the trafficking of CESAs to the plasma membrane (He et al. 2018).

Interestingly, we confirmed that the impairment of RabC1 function affects the secretion or deposition of mucilage. We observed reduced staining of ruthenium red in the *rabc1-2*, which depicted the declined pectin content (Fig. 8e). Additionally, reduced calcofluor staining in the *rabc1-2* showed decreased cellulose content (Fig. 8f). The

defective phenotype gets restored in the complementation line (Fig. 8e, and f). Overall, this result implies that RabC1 is involved in the trafficking of seed mucilage components.

Altogether, our work demonstrates the role of abundantly expressed *RabC1* in plant growth and especially in seed development. We showed that *RabC1* generates different isoforms to perform the function. RabC1 regulates root length and flowering time and is also involved in the regulation of seed size and seed filling process by affecting unknown steps of vesicle trafficking during seed development. Further detailed work is required to uncover the molecular characterization of *RabC1* that will help in the deep understanding of Rab GTPase signaling during growth and seed development. While this article was under review, a publication on RabC1 regarding its role in stomatal development was published (Ge et al. 2022). Similar to our work (Figs. 3 and 7), Ge et al. 2022 showed lesser biomass and reduced plant height in RabC1 (*lds1*) mutant, a single amino acid substitution mutant. In contrast, seed mass in the *lds1* mutant was unaffected compared to WT, compared to our results on T-DNA insertional knock-out mutant *rabc1-2* (Fig. 4), which showed lesser biomass than WT. Since we used knock-out mutant *rabc1-2* compared to their single amino acid substitution mutant *lds1*, this could be a possible reason for the contrasting results obtained in both studies.

Author contribution statement UK designed and performed all the experiments. First draft manuscript prepared by UK. SVS and VP supervised the study. SVS and UK analyzed and wrote the final manuscript. All authors read and approved the manuscript.

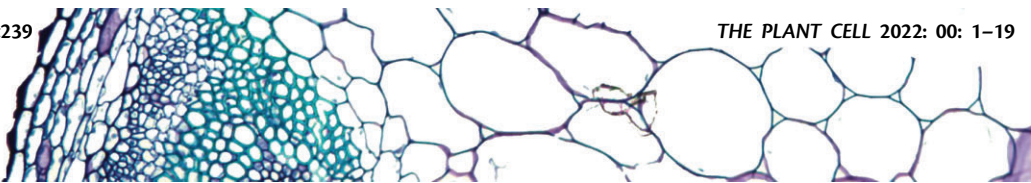
Supplementary Information The online version contains supplementary material available at <https://doi.org/10.1007/s00425-023-04122-2>.

Acknowledgements This work was supported by a grant from the Department of Biotechnology (DBT), India (Project Code, GAP-3361). We acknowledge the Director, CSIR-NBRI, for the resources and assistance. In addition, UK acknowledges the Department of Science and Technology, Government of India, for a research fellowship (DST/ INSPIRE Fellowship/2015/IF150279), and the University of Lucknow, Lucknow, U.P, India for Ph.D. registration. The institution manuscript number allotted to this manuscript is CSIR-NBRI_MS/2022/07/11.

Availability of data and materials All data generated or analyzed during this study are provided in this published article and its supplementary data files.

Declarations

Conflict of interest The authors declare no conflict of interest.



The Arabidopsis Rab protein RABC1 affects stomatal development by regulating lipid droplet dynamics

Shengchao Ge ^{1,2} Ruo-Xi Zhang ^{1,2} Yi-Fei Wang ^{1,2} Pengyue Sun ^{1,2} Jiaheng Chu ¹ Jiao Li ¹,
Peng Sun ¹, Jianbo Wang ¹ Alistair M. Hetherington ³ and Yun-Kuan Liang ^{1,2,*}

1 State Key Laboratory of Hybrid Rice, Department of Plant Sciences, College of Life Sciences, Wuhan University, Wuhan 430072, China

2 Hubei Hongshan Laboratory, Wuhan 430070, China

3 School of Biological Sciences, Life Sciences Building, University of Bristol, 24 Tyndall Avenue, Bristol, BS8 1TQ, UK

*Author for correspondence: ykliang@whu.edu.cn

These authors contributed equally (S.G. and R.-X.Z.)

Y.-K.L. conceived the project; S.G., Y.-F.W., P.Y.S., J.H.C., and J.L. conducted experiments; Y.-K.L., A.M.H., J.B.W., S.G., R.-X.Z., and P.S. analyzed data and wrote the manuscript. All authors read and approved the manuscript.

The author responsible for distribution of materials integral to the findings presented in this article in accordance with the policy described in the Instructions for Authors (<https://academic.oup.com/plcell>) is: Yun-Kuan Liang (ykliang@whu.edu.cn).

Abstract

Lipid droplets (LDs) are evolutionarily conserved organelles that serve as hubs of cellular lipid and energy metabolism in virtually all organisms. Mobilization of LDs is important in light-induced stomatal opening. However, whether and how LDs are involved in stomatal development remains unknown. We show here that *Arabidopsis thaliana* LIPID DROPLETS AND STOMATA 1 (LDS1)/RABC1 (At1g43890) encodes a member of the Rab GTPase family that is involved in regulating LD dynamics and stomatal morphogenesis. The expression of RABC1 is coordinated with the different phases of stomatal development. RABC1 targets to the surface of LDs in response to oleic acid application in a RABC1GEF1-dependent manner. RABC1 physically interacts with SEIPIN2/3, two orthologues of mammalian seipin, which function in the formation of LDs. Disruption of RABC1, RABC1GEF1, or SEIPIN2/3 resulted in aberrantly large LDs, severe defects in guard cell vacuole morphology, and stomatal function. In conclusion, these findings reveal an aspect of LD function and uncover a role for lipid metabolism in stomatal development in plants.

Introduction

Stomata are microscopic pores mainly located in the leaf epidermis of most terrestrial plants. Their role is to simultaneously regulate CO₂ uptake, water loss, and transpirational cooling, thus directly influencing photosynthetic capacity and transpiration rates (Hetherington and Woodward, 2003; Duckett and Pressel, 2018). Stomatal formation is a result of a tightly regulated developmental sequence culminating in the symmetrical division of a guard mother cell (GMC) and the ensuing separation of the cell walls of the two resultant guard cells (GCs) to form a central pore (Zhao and Sack,

1999; Lee and Bergmann, 2019; Torii, 2021). Various transcriptional regulators and signaling components have been demonstrated to be involved in the control of stomatal development and function. These allow the plant to adapt its gas exchange to suit the prevailing conditions (Zoulias et al., 2018; Lawson and Matthews, 2020). Growing concern over the detrimental effects of climate change on food security has prompted great interest in understanding the control of stomatal development and function. Manipulation of stomatal traits has resulted in crop improvement. For example, a

moderate reduction in stomatal density improves stress resilience and yield stability in barley (*Hordeum vulgare*), wheat (*Triticum aestivum*), and rice (*Oryza sativa*; Yu et al., 2008; Franks et al., 2015; Hughes et al., 2017; Caine et al., 2019; Dunn et al., 2019; Lu et al., 2019; Buckley et al., 2020).

All eukaryotic and some prokaryotic cells accumulate lipid droplets (LD) to survive periods of scarcity, protect cells against lipotoxicity and, in oil seeds, to provide a source of triacylglycerols (TAGs) that are broken down to provide energy after germination (Martin and Parton, 2006; Pyc et al., 2017; Walther et al., 2017; Huang, 2018). Cytoplasmic LDs are endoplasmic reticulum (ER)-derived multifunctional organelles consisting of a hydrophobic core of neutral lipids, mainly TAGs and sterol esters, coated with a protein-studded phospholipid monolayer (Guo et al., 2009; Wilfling et al., 2014; Rotsch et al., 2017; Zhang and Liu, 2019). Oilseeds accumulate large numbers of LDs that are mobilized during post-germinative growth, to fuel seedling growth, and intriguingly, up to 20% of LD degradation during germination takes place in the vacuoles (Poxleitner et al., 2006; Siloto et al., 2006; Graham, 2008; Chapman et al., 2012; Fan et al., 2019; Ischebeck et al., 2020). Despite the fact that LDs were observed by Hanstein in plant cells as early as 1880 (Chapman et al., 2012), most research on LDs has focused on oil seeds (Huang, 1992) and the important roles of LDs in other tissues such as pollen tubes and leaves have come to light only recently (Ischebeck et al., 2020).

In nonseed tissues, for example, in growing pollen tubes, LDs may be used as a way to transport lipids to the tip region for the synthesis of membrane lipids as well as for the provision of energy. In leaves, many genes involved in TAG metabolism are rapidly upregulated in the presence of abiotic stress and pathogen infection, suggesting they are related to cellular stress responses (Chapman et al., 2012; Ischebeck, 2016; Yang and Benning, 2018). A functional study on roots suggested that plants transfer lipids rather than sugars to sustain colonization by mutualistic mycorrhizal and parasitic fungi (Jiang et al., 2017). LDs are common in GCs and their abundance is diurnally regulated (Rutter and Willmer, 1979; Wanner et al., 1981; Sack, 1987; Gidda et al., 2016; McLachlan et al., 2016). LD mobilization followed by β -oxidation of fatty acids (FAs) is an important source of ATP during light-induced stomatal opening, a process which is evolutionarily conserved from basal plant lineages to angiosperms (McLachlan et al., 2016).

Proteomic studies of LDs in a variety of organisms have revealed a general role for LDs as transient or permanent depots for storing or sequestering proteins and identified a large number of regulatory proteins residing at the surface of LDs. These surface proteins control LD functions including TAG synthesis and breakdown, nutrient sensing, signal integration, and membrane trafficking (Cermelli et al., 2006; Yang et al., 2012; Kretzschmar et al., 2018; Zhang and Liu, 2019; Kretzschmar et al., 2020; Roberts and Olzmann, 2020; Pyc et al., 2021; Krawczyk et al., 2022). Rab proteins are small membrane-associated GTP-binding proteins involved in

vesicular trafficking pathways that act as molecular switches, cycling between GDP-bound (inactive) and GTP-bound (active) states to transmit upstream signals to downstream effectors (Takai et al., 2001; Zerial and McBride, 2001). Accumulating evidence suggests that Rab proteins regulate LD formation, catabolism, and interaction with other subcellular organelles (Rasineni et al., 2014; Li and Yu, 2016; Xu et al., 2021). More than 30 Rab proteins have been suggested to be associated with LDs (Turro et al., 2006; Larsson et al., 2012; Krahmer et al., 2013; Rasineni et al., 2014; Li and Yu, 2016), however, to date the direct involvement of Rab proteins in plant LD biology, particularly with respect to stomatal development, has yet to be investigated.

During the process of stomatal development, there is considerable cell expansion and this is associated with an increased requirement for the new membrane to increase surface area (Zhao and Sack, 1999; Kaiser and Scheuring, 2020). Given LDs are hubs of cellular lipid metabolism (Martin and Parton, 2006; Walther and Farese, 2012), we reasoned that plants mobilize LDs and liberate lipids for membrane synthesis during stomatal formation. Here we report that LD abundance is highly dynamic during stomatal development. In addition, an LD genetic screen in *Arabidopsis thaliana* resulted in the isolation of the *lds1* (*lipid droplets and stomata 1*) mutant, also known as *Rab18* and *RABC1* (Vernoud et al., 2003), that breaks the programmed LD dynamics in stomatal lineage cells (SLCs). *LDS1/RABC1/Rab18*, which we will henceforth refer to as *RABC1*, is distinctly expressed in SLCs and its expression level is correlated with the different phases of stomatal development. *RABC1* deficiency resulted in compromised LD size, stomatal morphology, and functionality. We conclude that the *RABC1* protein, together with its partner, a Guanine Exchange Factor (GEF), controls the dynamics and size of LDs in young stomata. We show that *RABC1* does this by regulating its effector factors *SEIPIN2* and *SEIPIN3*.

Results

The lds1 mutant displays aberrant LD size and LD dynamics during stomatal development

In *Arabidopsis*, stomata are produced by a tightly coordinated series of cell divisions that give rise to specialized SLCs, namely, M (meristemoid), GMC, and Young1-stoma (at this stage, symmetric division of GMC has been completed, stomatal length approximately equals stomatal width and the pore of the stoma does not appear or just starts to appear), Young2-stoma (at this stage, the stomatal complex has yet to achieve its full size but the stomatal pore is clearly visible), and M-stoma (Mature-stoma) according to the nomenclature used by Carter et al. (2017) and Torri (2021; Figure 1A). To test whether LDs are involved in stomatal development, we first used the neutral lipid stain, Nile red (NR) to monitor the dynamics of LDs in the SLCs (Fowler and Greenspan, 1985). As shown in Figure 1A and Supplemental Figure S1A, conspicuous staining of LDs was detected in the small triangular cell meristemoid (M), and

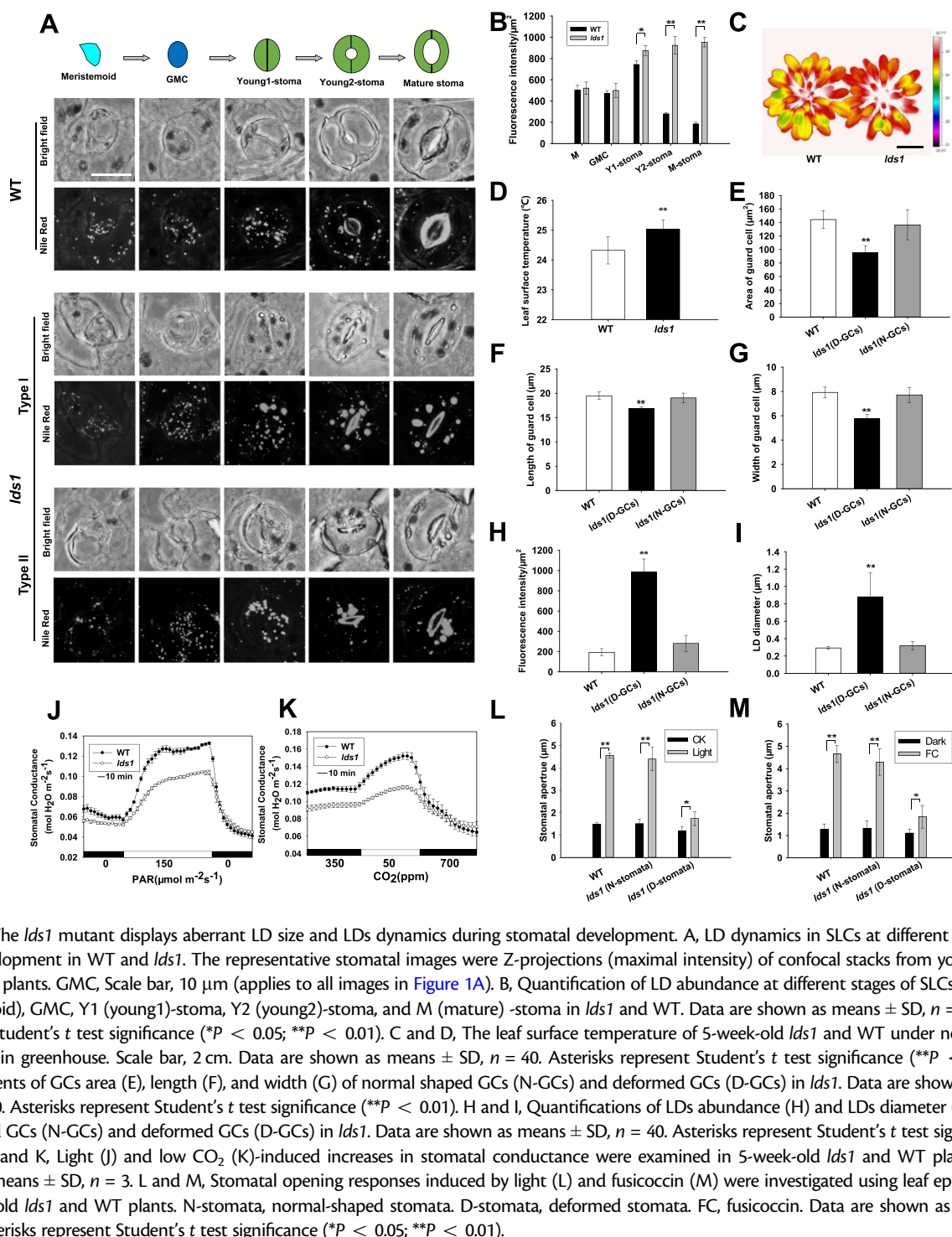


Figure 1 The *lds1* mutant displays aberrant LD size and LD dynamics during stomatal development. **A**, LD dynamics in SLCs at different stages of stomatal development in WT and *lds1*. The representative stomatal images were Z-projections (maximal intensity) of confocal stacks from young leaves of 4-week-old plants. GMC, Scale bar, 10 μm (applies to all images in Figure 1A). **B**, Quantification of LD abundance at different stages of SLCs, including M (meristemoid), GMC, Y1 (young1)-stoma, Y2 (young2)-stoma, and M (mature) -stoma in *lds1* and WT. Data are shown as means \pm SD, $n = 50$. Asterisks represent Student's *t* test significance (* $P < 0.05$; ** $P < 0.01$). **C** and **D**, The leaf surface temperature of 5-week-old *lds1* and WT under normal growth conditions in greenhouse. Scale bar, 2 cm. Data are shown as means \pm SD, $n = 40$. Asterisks represent Student's *t* test significance (** $P < 0.01$). **E–G**, Measurements of GCs area (E), length (F), and width (G) of normal shaped GCs (N-GCs) and deformed GCs (D-GCs) in *lds1*. Data are shown as means \pm SD, $n = 300$. Asterisks represent Student's *t* test significance (** $P < 0.01$). **H** and **I**, Quantifications of LDs abundance (H) and LDs diameter (I) in the normal shaped GCs (N-GCs) and deformed GCs (D-GCs) in *lds1*. Data are shown as means \pm SD, $n = 40$. Asterisks represent Student's *t* test significance (** $P < 0.01$). **J** and **K**, Light (J) and low CO_2 (K)-induced increases in stomatal conductance were examined in 5-week-old *lds1* and WT plants. Data are shown as means \pm SD, $n = 3$. **L** and **M**, Stomatal opening responses induced by light (L) and fusicoccin (M) were investigated using leaf epidermal strips of 4-week-old *lds1* and WT plants. N-stomata, normal-shaped stomata. D-stomata, deformed stomata. FC, fusicoccin. Data are shown as means \pm SD, $n \geq 60$. Asterisks represent Student's *t* test significance (* $P < 0.05$; ** $P < 0.01$).

the fluorescence intensity of the dye (as a proxy of the neutral lipid content) progressively increases during differentiation, reaching a peak in stage Young1 stomata, before decreasing rapidly at the Young2 stage. In mature stomata, the signal becomes much weaker (Figure 1, A and B). When the cells were stained with Bodipy 493/503 (Thumser and Storch, 2007), we observed similar LD dynamics in SLCs (Supplemental Figure S1B). A very recent finding by Liwen

Jiang's group lends strong support to our observation that LD abundance is higher in the young stomatal cells compared with other SLCs (Cao et al., 2022).

To identify the molecular regulator(s) involved in controlling the dynamics of LDs during stomatal development we performed a two-step, forward genetic screen, using infrared thermography and NR staining. Infrared thermography has been extensively used to noninvasively isolate mutant plants

that are defective in stomatal function (Merlot et al., 2002; Wang et al., 2004; Xie et al., 2006; Hashimoto et al., 2006; He et al., 2018; Sun et al., 2022). We first screened 2,700 individual plants and isolated 32 candidates that displayed altered leaf surface temperature. Then we subjected these candidates to a second round of screening using NR to stain LDs in detached epidermis. This resulted in the isolation of one mutant plant designated *lds1* (*lipid droplets and stomata 1*), which exhibited much enlarged GC LDs and increased leaf surface temperature compared with WT (Figure 1, A–D). Morphologically, more than half of the stomata examined (cotyledon $51.2 \pm 5.5\%$, $n = 500$; rosette leaf $53.9 \pm 3.5\%$, $n = 500$) were of irregular shape in *lds1*, with one or two deformed GCs (Figure 1A; Supplemental Figure S1C).

Since cotyledons and rosette leaves display a comparable phenotype, we focused on the stomata of rosette leaves. We divided the abnormal stomatal complexes into two categories based on the degree of deformity. When both GCs were deformed we classified these as “Type I” stomata ($78.2 \pm 5.2\%$, $n = 500$). The second category, “Type II” stomata ($22.8 \pm 3.4\%$, $n = 500$) consists of one seemingly normal and one impaired GC (Figure 1A). On closer inspection, in “Type II” stomata, we found that the irregular GC is smaller than the normal-shaped GC, and the symmetric layout of the two GCs was compromised (Figure 1, E–G; Supplemental Figure S1C). Type I stomatal complexes were characterized by a “thin shape” in contrast to the roundish shape of the normal stomata both in *lds1* and in WT (Figure 1A). Importantly, only deformed GCs had enlarged LDs (Figure 1, A, H, and I). Not unexpectedly, the pattern of LD dynamics, during stomatal differentiation was also affected by the *lds1* mutation. At M and GMC stages there was no detectable difference in either LD abundance or LD size between *lds1* and WT (Figure 1A). However, on the basis of NR staining, at the Young1-stomata stage, we found that 27 of 50 stomata accumulated much more lipid and larger LDs in *lds1* compared with wild type (Figure 1, A and B). In contrast to the progressive decrease of NR fluorescence in WT, the increase in NR fluorescence remained constant when the *lds1* Young1-stomata differentiate into the Young2-stomata and subsequently into the M-stomata (Figure 1A). Consistently, we saw significant increases in the levels of 16:0, 18:0, 18:1, 18:2, and 18:3 FA molecular species in the *lds1* mutant when compared with WT (Supplemental Figure S1D). These data indicate that LD defects and deformed GC morphology are two linked phenotypes in *lds1*. FDA staining (Krasnow et al., 2008) demonstrated that all deformed GCs were living, suggesting that the *lds1* mutation does not result in significant damage to GC membrane integrity (Supplemental Figure S1E).

Given that SCAP1 is expressed from young stomata to mature stomata, and disruption of SCAP1 resulted in defective stomata, which are seemingly comparable to those in *lds1* mutant (Negi et al., 2013), we therefore next investigated the relationship between the aberrant stomatal development and LD defects in the *scap1* mutant. As shown in

Supplemental Figure S1, O and P, there were no detectable LD defects in GCs of *scap1* in contrast to *lds1*. Consistently, when we sequenced the SCAP1 gene in the *lds1* mutant, we detected no mutation in SCAP1 gene. These results indicate that SCAP1 is not the causal gene for *lds1* phenotypes, and by extension that stomatal deformations are not necessarily associated with LD defects.

We next investigated stomatal function and found that light and low [CO₂]-induced changes in stomatal conductance were reduced substantially in the *lds1* mutant compared with WT (Dark to light: 321.8 ± 41.2 in WT vs $231.3 \pm 53.5\%$ in *lds1*; high to low [CO₂]: $236.4 \pm 30.4\%$ in WT vs. $163.6 \pm 44.1\%$ in *lds1*; Figure 1, J and K). The inhibitive effect of the *lds1* mutation on stomatal opening was confirmed for both light and fusicoccin (Turner and Graniti, 1969; Yamauchi et al., 2016; Figure 1, L and M). In wild type, there is a rapid decrease in LD abundance during light-induced opening, this was not observed in the deformed GCs of *lds1* (Supplemental Figure S1F; McLachlan et al., 2016). As we observed no appreciable difference in terms of stomatal density and stomatal index between *lds1* and WT plants, we conclude that *LDS1* is not involved in cell fate determination (Supplemental Figure S1, G and H). We also noted that biomass accumulation and stature of *lds1* are reduced compared with WT (Supplemental Figure S1, I–K), but seed size and seed germination are not affected in the *lds1* mutant (Supplemental Figure S1, L–N).

LDS1/RABC1 is highly expressed in young stomata and *RABC1* targets to the surface of LDs

To identify the causal mutation of *lds1*, we undertook map-based gene cloning and next-generation DNA sequencing and identified a single point mutation (a G to A substitution) at position +508 in the *At1g43890* (RABC1) open reading frame. This causes a substitution from a conserved acidic amino acid to a basic amino acid (E170K; Figure 2A; Supplemental Figure S2A). Next, the wild-type RABC1 cDNA was introduced into *lds1* driven by RABC1 promoter and the transgene fully restored the phenotypic defects in LD size and stomatal morphology (Supplemental Figure S2, B–E). Furthermore, a T-DNA insertion mutant SALK_012129, which had no detectable RABC1 mRNA, exhibited similar defects to *lds1*, indicating that *lds1* and SALK_012129 are allelic to each other (Supplemental Figure S2, C–E). These data demonstrate that a mutation in *LDS1/RABC1* is responsible for the phenotypes described in this paper. For brevity, *LDS1/RABC1* is hereafter referred to as RABC1. We renamed *lds1* and SALK_012129 as *lds1-1* and *lds1-2*, respectively, and subjected them to further investigation.

Arabidopsis RABC1 has been suggested to be the counterpart of mammalian Rab18 (Vernoud et al., 2003). As shown in Supplemental Figure S2A, the putative amino acid sequence of RABC1 exhibited 63% identity and 61% identity to mouse MmRab18 and human HsRab18, respectively. Mutations in Rab18 impair lipid metabolism and result in enlarged LDs in several cell types, including HEK293T cells,

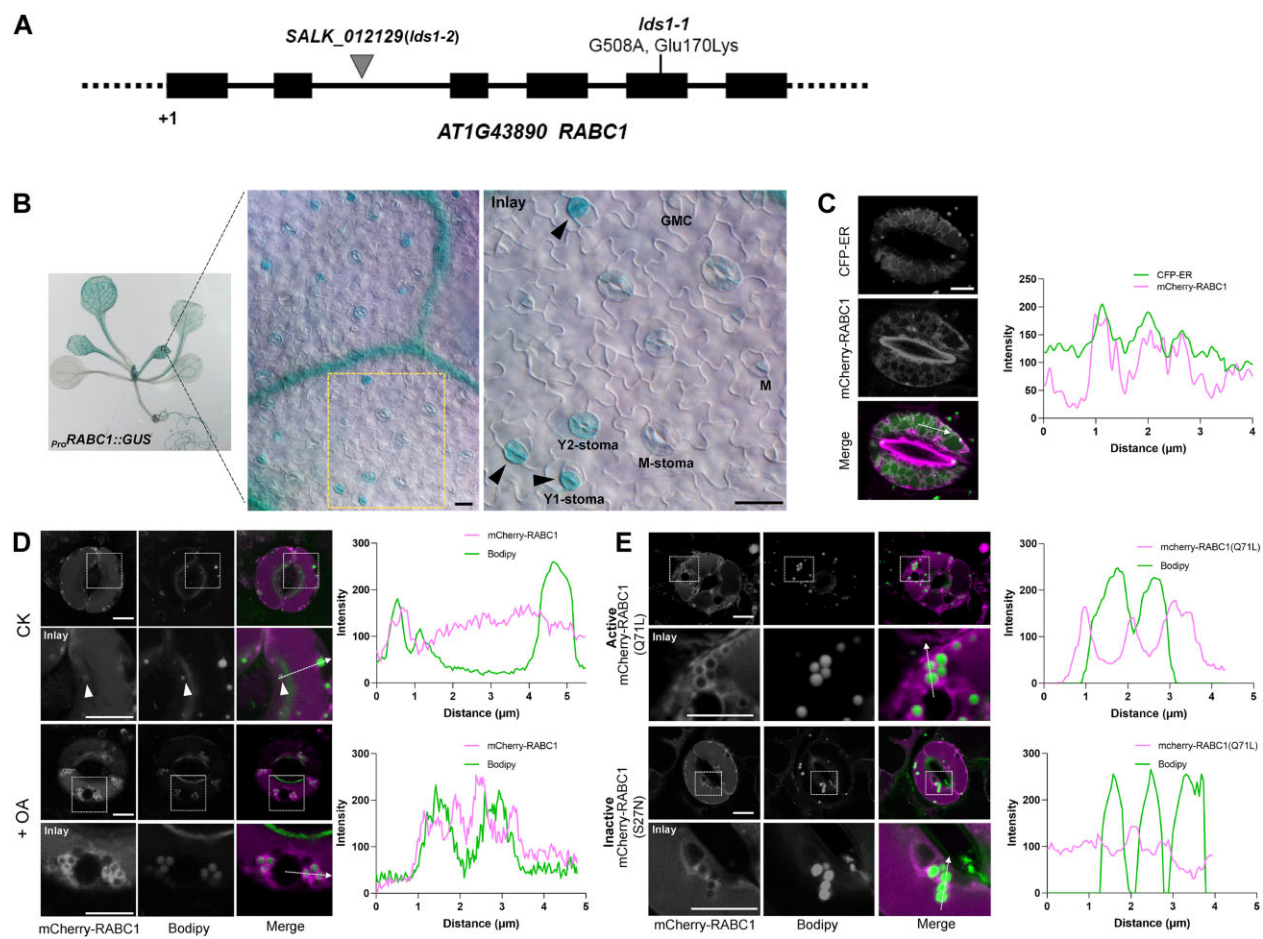


Figure 2 *LDS1/RABC1* is highly expressed in young stomata and *RABC1* targets to the surface of LDs. **A**, Schematic view of mutation site determination of two independent lines of *lds1* mutants. **B**, GUS staining of a 2-week-old seedling of *ProRABC1:GUS* transformant. *RABC1* is highly expressed in leaf veins and SLCs. The inset image shows that *RABC1* is highly expressed in young GCs. Arrowheads indicate Y1-stomata. M (meristemoid), GMC, Y1 (young1), Y2 (young2), M (mature) -stoma. Scale bars, 20 μm . **C**, mCherry-RABC1 transformants were used to determine whether *RABC1* localized to the ER. mCherry-RABC1 co-localized with CFP-ER. The fluorescence intensity profile plot of mCherry-RABC1 and CFP-ER is quantified along the dotted arrow. Scale bar, 5 μm . **D**, mCherry-RABC1 transformants were used to determine the relationship between *RABC1* localization and LDs. Oleic acid (OA) application induces LD production. Arrowheads indicate ring-like signals surrounding LDs. The fluorescence intensity profile plots of mCherry-RABC1 and Bodipy were quantified along the dotted arrows, respectively. Scale bar, 5 μm . **E**, Activity status of *RABC1* dictates the subcellular localization of *RABC1*. The fluorescence intensity profile plots of mCherry-RABC1 and Bodipy were quantified along the dotted arrows, respectively. Scale bar, 5 μm .

human fibroblasts, and 3T3-L1 adipocytes. However, the causal basis for this is not clear (Li et al., 2017; Xu et al., 2018; Dejgaard and Presley, 2019). To investigate whether *RABC1* and mammalian Rab18 have similar functions *in vivo*, we performed cross-species complementation tests. Ectopic expression of HsRab18 in Arabidopsis fully rescued the defects caused by *lds1* mutation (Supplemental Figure S2, F–H). The Arabidopsis genome contains two homologs of *RABC1*. These are *RABC2a* (At5g03530) and *RABC2b* (At3g09910) which share 73% and 67% identity with *RABC1*, respectively (Supplemental Figure S2A). Neither single gene mutant caused defects in LD size or stomatal morphogenesis (Supplemental Figure S2, I–K). However, when the expression of either gene was driven by the *RABC1* promoter in *lds1*, both LD size and stomatal morphology could essentially be restored to WT levels (Supplemental Figure S2,

I–K). This result suggests that similarities in protein structure likely account for the interchangeable functions of *RABC2a*, *RABC2b*, and *RABC1*. Their different roles may be related to their tissue expression and, or abundance. Resolving whether this is the case must await further investigation.

Next, a transcriptional reporter, *ProRABC1:GUS* was constructed to evaluate *RABC1* expression patterns. As shown in Figure 2B, *RABC1* is widely expressed. In leaves, GUS production was most abundant in the veins and SLCs, with the highest signal intensity detected in Young1-stomata (Figure 2B), reminiscent of the dynamic changes of LDs in these cells (Figure 1A). *RABC1* subcellular localization was evaluated using the *ProRABC1:mCherry-RABC1* construct, which complemented the *lds1* mutation (Supplemental Figure S2, B, D, and E). As shown in Figure 2C, mCherry-

RABC1 localized to the ER. Next, we sought to establish whether RABC1 could also target to LDs. Under normal circumstances, only a small subset of LDs displayed mCherry fluorescence (Figure 2D). However, in response to treatment with oleic acid (18:1, unsaturated FA, OA), which is known to stimulate the formation of LDs (Xu et al., 2018), an increase in mCherry-RABC1 fluorescence was observed around most LDs (Figure 2D). We found that OA incubation not only significantly increased LD abundance, but also increased LD size in WT GCs. In the GCs of *lds1*, although the abundance and size of LDs also increased when incubated with OA, the increase was much less than seen in WT (Supplemental Figure S2, L and M).

Next, in order to study the effects of the state of the RABC1 protein on its intracellular localization, we used RABC1 (S27N; a dominant-negative form) and RABC1 (Q71L; a constitutively active form), two mutant forms of RABC1 that were generated based on the highly conserved molecular switch motif among Rab proteins (Ozeki et al., 2005; Lee et al., 2009). As shown in Figure 2, D and E, there was almost no OA-induced fluorescence of mCherry-RABC1 (S27N) surrounding LDs. This was in marked contrast to the obvious fluorescence in the constitutively active RABC1 (Q71L) or in OA-induced RABC1. This indicates that RABC1 trafficking to LDs (in response to the lipogenic stimulus, OA) depends on its activity state. This is consistent with the view that the activation status of Rab proteins impacts their subcellular localization (Bhuin and Roy, 2014; Cui et al., 2014).

RABC1GEF1 is a GEF for RABC1

The conversion of Rab proteins from an inactive GDP-bound form to an active GTP-bound form relies on guanine nucleotide exchange factor proteins (GEFs; Zerial and McBride, 2001). To identify RABC1 protein regulators that interact with RABC1, we screened an Arabidopsis cDNA library in yeast using the dominant-negative form of RABC1 (S27N) as bait. Among the 30 candidate proteins that interact with the inactive RABC1, At5g58510 was repeatedly isolated, and a direct yeast two-hybrid (Y2H) assay confirmed that the protein encoded by At5g58510 could directly interact with RABC1 (S27N; Supplemental Data Set S1; Figure 3A; Supplemental Figure S3A). Based on its high sequence similarity to human Rab3GAP1 that works as a GEF for HsRab18 (Supplemental Figure S3B; Xu et al., 2018), it is likely that this protein has GEF activity for RABC1. Based on our characterization described below, we named this protein RABC1GEF1. The subsequent BiFC and Co-IP tests demonstrated that RABC1GEF1 and RABC1 interact in vivo in a RABC1 activity-dependent manner (Figure 3, A–D).

Furthermore, two T-DNA insertion mutant lines (*WiscDsLox393-396G22* and *SALK_116404C*) were identified that harbor no detectable mRNA of At5g58510 (Supplemental Figure S3C). *WiscDsLox393-396G22* shows similar defects in LD size and stomatal morphology to *lds1* (Figure 3, E and F). The ratio ($55.6 \pm 3.2\%$, $n = 500$) of deformed stomata caused by mutation in RABC1GEF1 closely resembles the ratio ($53.9 \pm 3.5\%$, $n = 500$) seen in *lds1*.

RABC1GEF1 deficiency in *SALK_116404C* also causes similar defects to *lds1* (Supplemental Figure S3, D and E).

In addition, the targeting of RABC1 to the LD surface is inhibited by mutation of RABC1GEF1 (Figure 3G). When a dominant-active form of RABC1 (Q71L) was introduced into either *WiscDsLox393-396G22* or *SALK_116404C*, the defective LD size and stomatal morphology could be fully restored (Figure 3, E and F). Of note, although the protein encoded by At5g55060 in Arabidopsis resembles Rab3GAP1 (Supplemental Figure S3B), our data suggest that this protein exerts no GEF function for RABC1, as the corresponding loss-of-function mutant (*SALK_058192C*) displays no similar defects to those of *lds1-1*, *lds1-2*, *WiscDsLox393-396G22* or *SALK_116404C* (Supplemental Figure S3, C–E).

Next, we measured the in vitro GEF activity of RABC1GEF1 towards RABC1 by monitoring the change in intrinsic tryptophan fluorescence upon nucleotide exchange as described (Pan et al., 1995; Antony et al., 2001; Goh et al., 2007; Cui et al., 2014). RABC1GEF1 stimulates the guanine nucleotide exchange of RABC1 in a dose-dependent manner (Figure 3H), but shows almost no guanine nucleotide exchange activity for RHA1, a Rab GTPase used as the experimental control (Supplemental Figure S3F, Cui et al., 2014). Unlike RABC1GEF1, the protein encoded by At5g55060 shows no detectable GEF activity for RABC1 (Supplemental Figure S3F). These data demonstrate that RABC1GEF1 works as a GEF for RABC1.

SEIPIN2 and SEIPIN3 are two effectors for RABC1

Rab GTPases generally work through their downstream effectors (Gillingham et al., 2014). To identify the effector(s) of RABC1, we conducted a second Y2H screen using a dominant-active RABC1 (Q71L) as bait and obtained SEIPIN2 as a possible effector for RABC1 among other 45 candidates (Figure 4A; Supplemental Data Set S2). SEIPIN2 is an orthologue of mammalian seipin (sei1 in yeast), which was originally identified as being deficient in a form of congenital lipodystrophy and has since been suggested to function in regulating the formation and size of LDs (Magre et al., 2001; Szymanski et al., 2007; Fei et al., 2008; Wang et al., 2016). Unlike yeast or mammals, Arabidopsis has three SEIPIN homologs, and their deficiency alters lipid contents and LD size, whereas overexpression of each homolog in either yeast cells or plant leaves influenced the number and size of LDs differently (Cai et al., 2015; Taurino et al., 2018; Huang, 2018; Greer et al., 2020; Pyc et al., 2021). As shown in Figure 4, A–C, SEIPIN2 physically interacts with RABC1 and the interaction depends on the RABC1 activity state.

Through constructing transgenic Arabidopsis that expresses a SEIPIN2 promoter-driven GUS reporter ($p_{SEIPIN2}GUS$), we found that unlike SEIPIN1 and SEIPIN3, SEIPIN2 is preferentially expressed in GCs (Figure 4D; Supplemental Figure S4, A and B), consistent with a previous observation (Greer et al., 2020). Importantly, the highest expression of SEIPIN2 is in Young1 stomata resembling that of RABC1 (Figure 4D). RABC1 also interacts with SEIPIN3 but not SEIPIN1 (Figure 4, A–C). No LD defects were

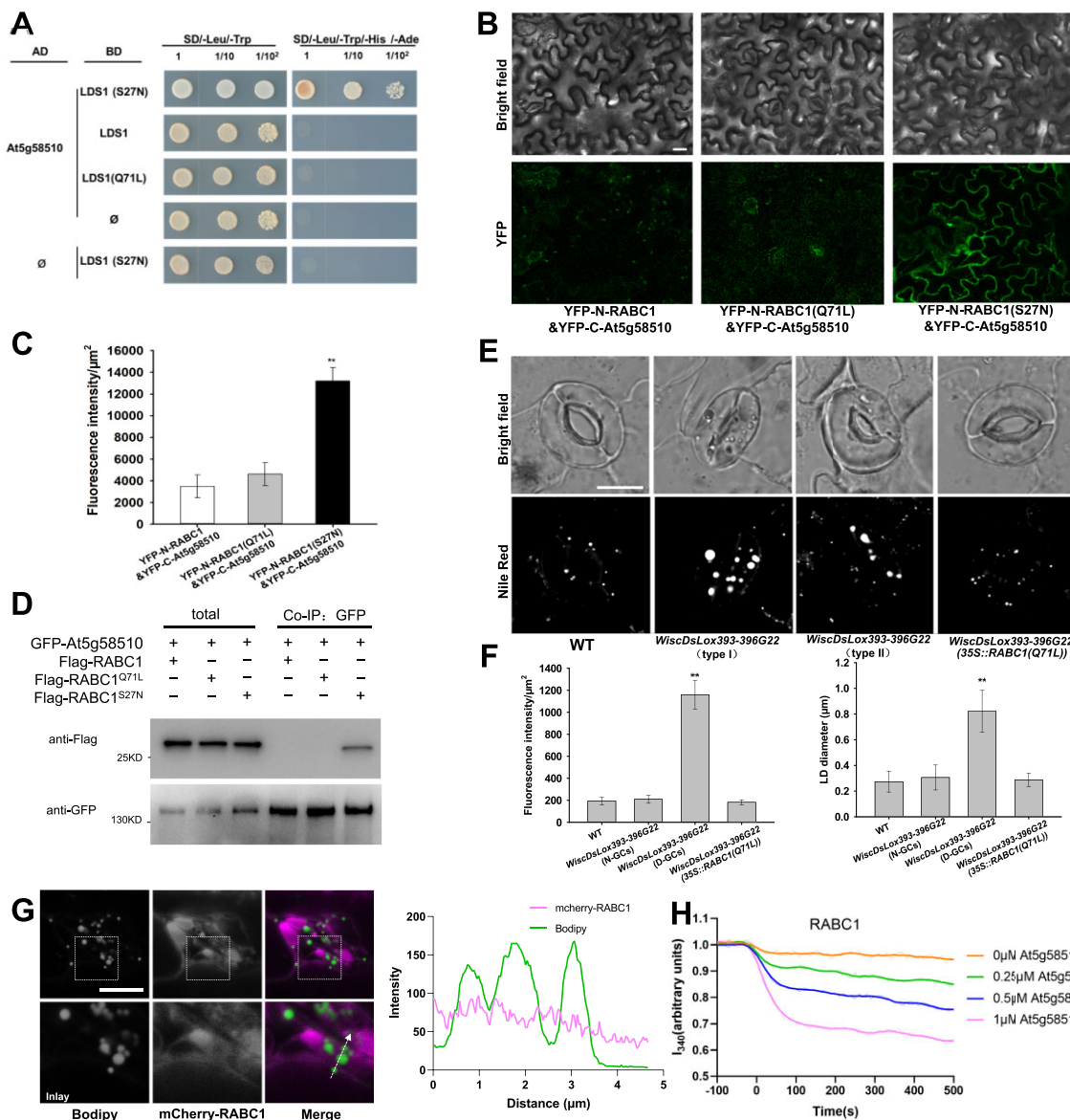


Figure 3 At5g58510 is a GEF for RABC1. **A**, The interaction between At5g58510 and RABC1 was dependent on the activity status of RABC1 in the Y2H system. **B**, BiFC was used to verify the interactions between At5g58510 and RABC1. Scale bar, 30 μm . **C**, Fluorescence intensity of YFP in (B) was quantified. Data are shown as means \pm SD, $n = 3$. Asterisks represent Student's *t* test significance (** $P < 0.01$). **D**, Co-IP was used to verify the interaction between At5g58510 and RABC1. **E** and **F**, Both allelic mutants of At5g58510 showed defective LDs dynamics, LDs size, and stomatal morphology. Introduction of a dominant-active form of RABC1 (Q71L) into the mutants of At5g58510 rescued the defects. The representative stomatal images were single confocal planes from young leaves of 4-week-old plants (E). LD abundance and size of GCs were quantified (F). Data are shown as means \pm SD, $n = 20$. Asterisks represent Student's *t* test significance (** $P < 0.01$). Scale bar, 10 μm . **G**, Localization of RABC1 to LDs is blocked by RABC1GEF1 deficiency. The fluorescence intensity profile plots of mCherry-RABC1 and Bodipy are quantified along the dotted arrow. Scale bar, 10 μm . **H**, In vitro GEF assays of At5g58510. Nucleotide exchange of RABC1 was tested by monitoring tryptophan autofluorescence in the absence or presence of 0.25 mM, 0.5 mM, or 1 mM GST-At5g58510. The raw data are the jagged lines and the bold lines represent the trend lines.

detected in *seipin1*, *seipin2*, or *seipin3* individual gene mutant (Supplemental Figure S4, C–E). However, a comparable number of stomata in *seipin2 seipin3* double mutant ($13.37 \pm 4.2\%$, $n = 500$) and *seipin1 seipin2 seipin3* triple mutant ($11.29 \pm 2.5\%$, $n = 500$) displayed enlarged LDs and deformed GC morphology, whereas no such defects were observed in either *seipin1 seipin2* or *seipin1 seipin3* (Figure 4, E and F). This suggests that functional divergence has

occurred in these paralogous SEIPIN proteins. It seems that SEIPIN2 acts as an important effector for RABC1 in GCs and SEIPIN3 can contribute to stomatal biology, whereas SEIPIN1 has distinct functions.

Considering that GTPases regulate the function of their effectors by affecting their localization (Pylypenko et al., 2018), we next examined whether mutations in RABC1 lead to abnormal localization of SEIPIN2/3. Consistent with the

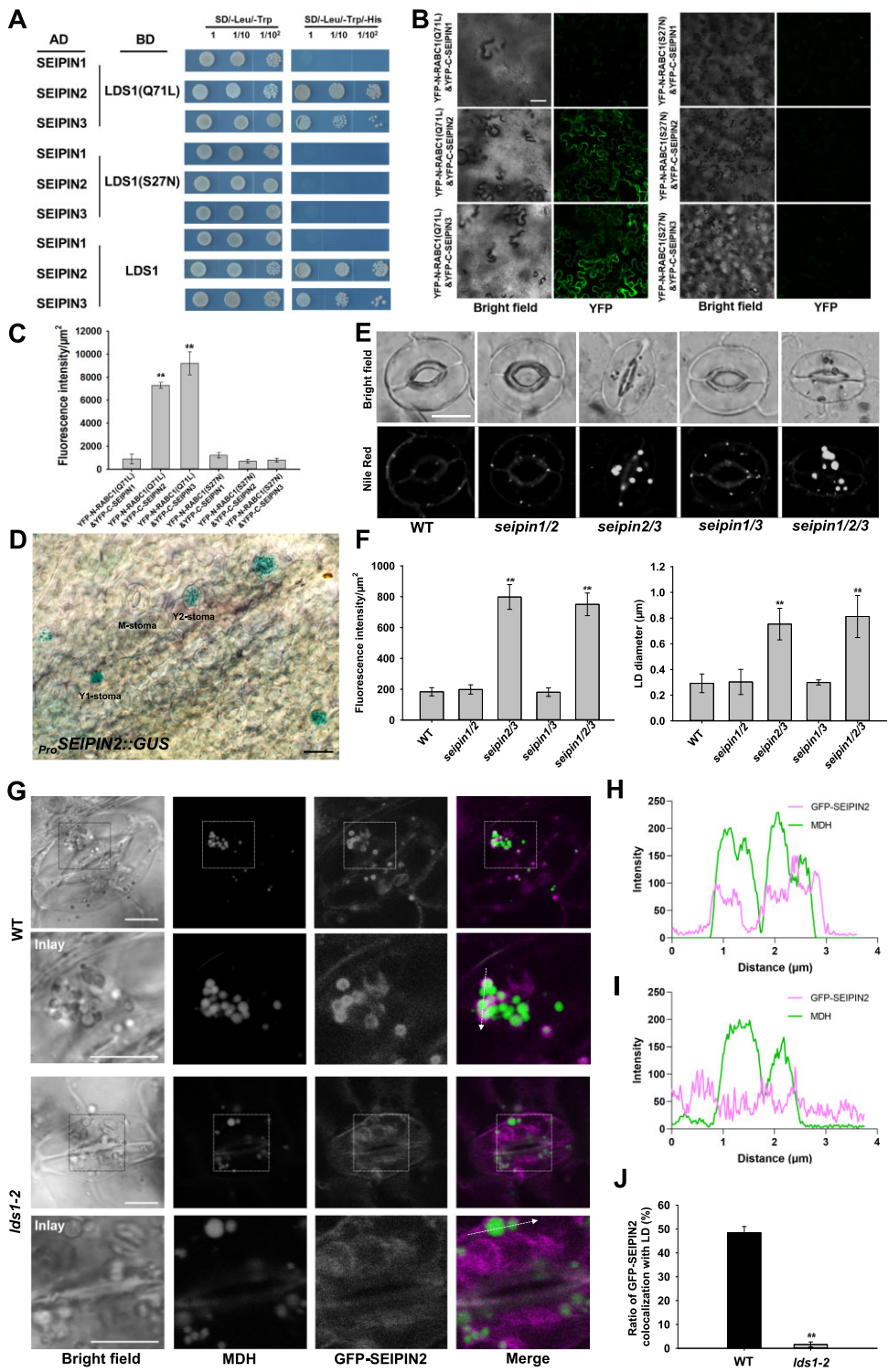


Figure 4 SEIPIN2 and SEIPIN3 are two effectors for RABC1. A, Interaction tests between SEIPINs and different status RABC1 in Y2H system. B, Interaction tests between SEIPINs and different status RABC1 in BiFC tests. Scale bar, 50 μm . C, Fluorescence intensity of YFP in (B) was quantified. Data are shown as means \pm SD, $n = 3$. Asterisks represent Student's *t* test significance (** $P < 0.01$). D, GUS staining of leaves from 2-week-old seedling of *ProSEIPIN2::GUS* transformant. SEIPIN2 is highly expressed in stomatal cells. Scale bar, 20 μm . E and F, Simultaneous disruption of SEIPIN2 and SEIPIN3 resulted in defective LD dynamics, aberrant LD size, and stomatal morphology. The representative stomatal images were single confocal planes from young leaves of 4-week-old plants (E). LD abundance and size of GCs were quantified (F). Data are shown as means \pm SD, $n = 20$. Asterisks represent Student's *t* test significance (** $P < 0.01$). Scale bar, 10 μm . G, Localization of GFP-SEIPIN2 to LDs is blocked by RABC1 deficiency. The LDs were stained with Monodansylpentane (MDH). Scale bar, 5 μm . H and I, Fluorescence intensity profile plots of GFP-SEIPIN2 and LDs in WT (H) and *lds1-2* (I) are quantified along the dotted arrow in (G). J, Quantification of the proportion of GFP-SEIPIN2 localized on LDs in WT and *lds1-2*. Data are shown as means \pm SD, $n = 120$. Asterisks represent Student's *t* test significance (** $P < 0.01$).

observation made in tobacco (Cai et al., 2015; Taurino et al., 2018; Greer et al., 2020; Pyc et al., 2021), we found that GFP-SEIPIN2/3 localizes to ER-like structures but hardly co-localize with LDs in the GCs of both WT and *lds1* (Supplemental Figure S4G). When we used OA to promote LD production, we found that a large proportion of LDs had strong GFP-SEIPIN2/3 signals in WT, but the GFP signal was weak around the LDs in *lds1* mutants (Figure 4, G–J; Supplemental Figure S4, H–K). This result suggests that the localization of SEIPIN2/3 to the LD surface is regulated by RABC1 activity. Since SEIPIN proteins are thought to be mainly responsible for the formation of LDs at the surface of ER, the regulation of their localization on LDs by RABC1 is likely to be related to the size of LDs, but the specific mechanism still needs further study. In addition, when overexpressing SEIPIN2 or SEIPIN3 in *lds1*, we found that defective LDs and stomatal morphology could not be restored in *lds1* (Supplemental Figure S4, L and M). A possible explanation for this result is that RABC1 affects the function of SEIPIN2/3 by regulating their localization which might not be related to their expression levels.

DMP treatment mimics the phenotype of *lds1* and overexpression of SDP1 partly restores the aberrant stomatal morphology of *lds1*

Diphenyl methylphosphonate (DMP) is a potent inhibitor of LD mobilization and in seedlings results in LD retention and the production of large LDs (Brown et al., 2013; Yu et al., 2018). In addition, DMP-treated isolated leaf epidermis exhibited delayed light-induced stomatal opening (McLachlan et al., 2016). When we grew *Arabidopsis* seedlings on half-strength Murashige and Skoog (1/2 MS) agar plates with 25 μM DMP, we found that many GCs contained aberrantly large LDs, and the corresponding stomata were irregular in shape (Figure 5, A and B). Similar to *lds1*, DMP treatment resulted in enlarged LDs in young GCs (Figure 5A), suggesting that blocking LD turnover during stomatal development causes defective stomatal morphology.

To examine whether the enlarged LDs in *lds1* could impair lipolysis, we developed transgenic plants that overexpress SUGAR DEPENDENT1 (SDP1), a major lipase for TAG degradation (Eastmond, 2006; Kelly et al., 2013). As shown in Figure 5, C and D and Supplemental Figure S5A, SDP1 overexpression largely restored LD size and stomatal morphology in *lds1*, suggesting that aberrant LDs caused by RABC1 deficiency likely slowed the access of lipases and, or other degradative enzymes to TAG substrates, reducing the production of free FAs with likely negative effects on ATP production.

Disruption of RABC1 function affects vacuole occupancy and OCL formation

By taking advantage of a tonoplast marker, GFP-VAMP711 (Cui et al., 2014), we found that the area of vacuoles in deformed GCs is much smaller in *lds1* than WT (Figure 6, A and B), suggesting an essential role of RABC1 in the intracellular expansion of the vacuoles. This observation was further

substantiated using transmission electron microscopy (TEM) and FM4-64 staining (Supplemental Figure S5, B–E). Vacuole size defects were also clearly observed in the deformed GCs of *lds1gef1* and *seipin2 seipin3* (Supplemental Figure S5, D–G). Intriguingly, the frequency of LDs appearing in the vacuolar lumen of *lds1* mutants was greatly reduced compared with WT (Figure 6, C and D), suggesting that RABC1 malfunction inhibits LD-vacuole interactions. Finally, the outer cuticular ledge (OCL), an extension of stomatal cell walls that forms an antechamber just above the stomatal pore and is involved in stomatal regulation (Merced and Renzaglia, 2014; Hunt et al., 2017; Hunt and Gray, 2020; Tang et al., 2020) was stained by NR (Figure 6, E and F). Whereas the OCL of deformed GCs in *lds1* is much thinner, indicating that *lds1* mutation impairs OCL formation. This observation reveals a previously unrecognized role of LDs related to OCL formation. In addition, when we examined the vacuole morphology and OCL structure in the GCs of *scap1*, we detected no significant difference between *scap1* and WT (Supplemental Figure S5, D, E, H and I). This further supported our view that stomatal deformations are not necessarily associated with LD defects.

Discussion

The acquisition of stomata was a critical evolutionary innovation that maximized plant survival and fitness through controlling the fundamental tradeoff between carbon dioxide uptake and water loss (Clark et al., 2022). To exploit stomata for crop improvement in the face of global climate change necessitates investigations that reveal essential regulators of stomatal development and function. In this study, we describe the cellular dynamics of LDs during stomatal development and identify RABC1 as a key regulator required for modulating LD dynamics and lipid metabolism during the establishment of functional stomata. Our data suggest a model in which RABC1 deficiency results in compromised LD size, deformed stomata, smaller GC vacuoles, and defective cuticle. We have also shown that RABC1GEF1 and SEIPIN2/3 exert GEF and effector function, respectively, for RABC1. RABC1GEF1 is required for the targeting of LDs by RABC1. Our findings expand the roles of LDs by revealing that LDs are likely required for GC morphogenesis, vacuole growth, and OCL establishment during stomatal development in plants (Figure 7).

Stomata are the end products of a specialized epidermal lineage, and each stoma possesses two seemingly identical GCs. The symmetric layout of the two GCs was disrupted in “Type II” stomata in *lds1* (Figure 1A). Given that the ends of the two GCs of a stoma are connected, it is likely that this asymmetric layout results from the distortion imposed by the larger GC over its smaller neighbor. The distinct morphogenesis of the paired GCs demonstrated in “Type II” stomata confirms and extends previous evidence that while paired stomatal GCs are of same origin they behave autonomously (McAinsh et al., 1990; Pillitteri and Torii, 2012).

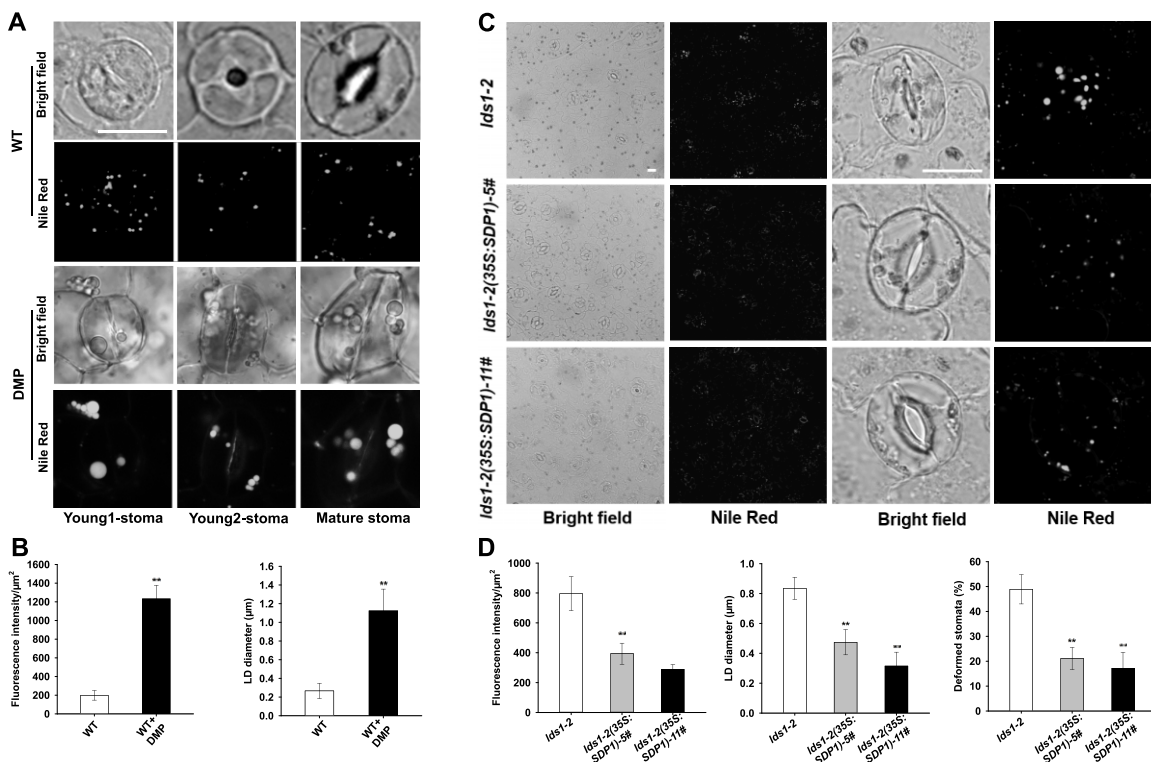


Figure 5 DMP treatment mimics the phenotype of *lds1* and overexpression of *SDP1* partly restores the aberrant stomatal morphology of *lds1*. A and B, DMP treatment resulted in defective LD dynamics and stomatal morphology in WT. The representative stomatal images were single confocal planes from young leaves of 2-week-old plants (A). LD abundance and size of GCs were quantified (B). Data are shown as means \pm SD, $n = 30$. Asterisks represent Student's *t* test significance (** $P < 0.01$). Scale bar, 10 μm . C and D, Overexpression of *SDP1* restored defects in LDs size and stomatal morphology in *lds1-2*. The representative stomatal images were single confocal planes from young leaves of 4-week-old plants (C). LD abundance and size ($n = 30$) of GCs, deformed stomata ratio ($n = 400$), were quantified (D). Data are shown as means \pm SD. Asterisks represent Student's *t* test significance (** $P < 0.01$). Scale bar, 20 μm .

Our observation that the abundance of cytoplasmic LDs changes dramatically during stomatal development (Figure 1, A and B), and perturbing LD dynamics either by pharmacological or genetic means, compromises the formation of fully functional stomata (Figures 1A and 5A), suggests that maintaining LD homeostasis is indispensable for stomatal development. The *lds1* mutant displayed enlarged LDs in the deformed GCs (Figure 1, A and I). This suggests that RABC1 is a negative regulator of LD size. This is likely to be of importance because LD size needs to be strictly controlled, as it is known that small LDs are suitable for fast lipid mobilization, whereas larger LDs are more suitable for long-term lipid storage (Suzuki et al., 2011). The size of LDs is the result of the combined action of LD growth and mobilization. Overexpression of *SDP1* restored LD size and stomatal morphology (Figure 5, C and D), suggesting that the enlarged LDs, caused by the malfunctioning of RABC1, impact the access of the *SDP1* lipase and the mobilization of LDs. It is likely that RABC1 also restricts LD growth as TAG content in the GC-enriched epidermis is significantly higher in *lds1* than in WT (Supplemental Figure S1D). However, whether RABC1 functions in preventing LD coalescence or inhibiting localized synthesis of lipid (or in both processes) remains to be clarified. In the Rab18 knockout 3T3-L1

adipocytes of mammals, although the exact mechanism of LD enlargement remains unclear, the enlarged LDs were not a result of the fusion/coalescence of small LDs (Xu et al., 2018). In contrast to our finding, the TAG content of cultured Rab18 knockout 3T3-L1 adipocytes was decreased to the same extent as the reduction in the normal-sized LDs (Xu et al., 2018). Further dissecting the mechanisms by which RABC1 regulates LD homeostasis will not only help us better understand stomatal function and development but it will also help to provide essential insights into the production of vegetable oils in vegetative tissues which is a field of increasing interest to the biotechnology sector and biofuel industries (Xu and Shanklin, 2016).

The formation of the central vacuole allows metabolically inexpensive plant cell expansion, and interference with vacuolar function evokes severe developmental defects (Schumacher et al., 1999; Rojo et al., 2001; Li et al., 2005; Krüger and Schumacher, 2018). Studies of vacuoles in GCs have revealed a tight correlation between vacuole morphology and stomatal movement (Gao et al., 2005, 2009; Bak et al., 2013; Andrés et al., 2014; Cao et al., 2022). During stomatal development, there is a significant increase in cell size that will require an increase in plasma and vacuolar membrane surface area. Disruption of RABC1 causes defects in

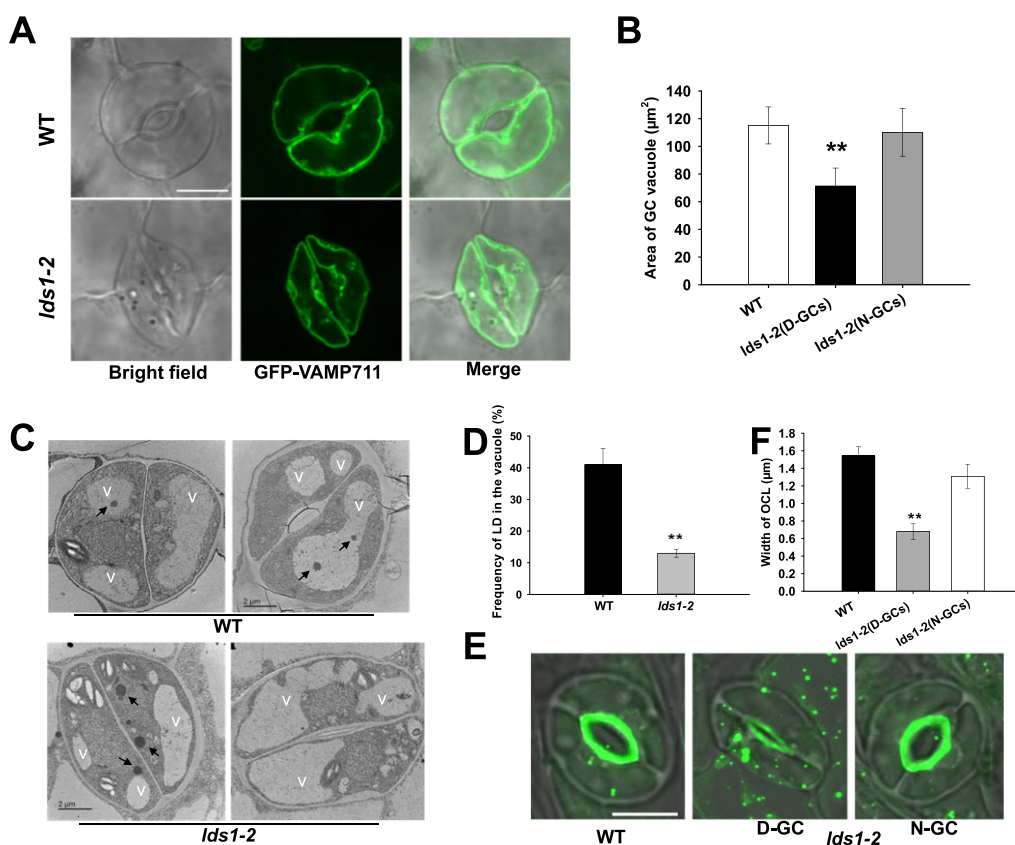


Figure 6 Disruption of RABC1 function affects vacuole occupancy and OCL formation. **A**, Representative images of vacuoles in GCs of WT and *lds1* plants. The representative stomatal images were single confocal planes from young leaves of 4-week-old plants. Scale bar, 10 μm . **B**, Quantification of the area of vacuoles in GCs of WT and *lds1* plants. Data are shown as means \pm SD, $n = 50$. Asterisks represent Student's *t* test significance (** $P < 0.01$). **C** and **D**, The number of LDs in the vacuolar lumen of *lds1* was reduced compared with WT. Representative TEM images of LDs in the vacuolar lumen (C), quantification of LDs in the vacuolar lumen (D). Arrows indicate LDs. V, vacuole. Data are shown as means \pm SD, $n = 30$. Asterisks represent Student's *t* test significance (** $P < 0.01$). **E** and **F**, The OCL of deformed GCs in *lds1-2* is much thinner and narrower. The representative stomatal images were single confocal planes from young leaves of 4-week-old plants. Data are shown as means \pm SD, $n = 40$. Asterisks represent Student's *t* test significance (** $P < 0.01$).

LD mobilization and vacuole size (Figures 1A and 6A), highlighting the relationship between these two organelles. What is less clear is the mechanism by which LDs are able to contribute toward the new membrane required for vacuolar growth. As it is the ER, rather than the vacuole that is the site of *de novo* phospholipid biosynthesis, it seems unlikely that LD TAGs could be used directly by the vacuole to synthesize the new phospholipids required for membrane expansion. Instead, perhaps the vacuole incorporates the phospholipid monolayer surrounding the LD so as to increase the surface area of the tonoplast. This is of course speculation but would be a topic to explore in the future. Another possibility is that RABC1 regulates LD homeostasis and vacuole growth separately, and, or the changes in vacuole occupancy and OCL formation are downstream effects of defective GC development. The final possibility is that LD-vacuole interactions are related to lipophagy whereby lipids can be degraded and recycled (Ischebeck et al., 2020). We observed LDs within vacuoles in GCs and disruption of RABC1 led to a significant decrease of LDs entering the vacuole (Figure 6, C and D). These data indicate that there is

an interaction of the LDs with the vacuole. If lipid recycling underlies the LD-vacuole interactions, it is possible that the lipids or their metabolites could be exported to sites of phospholipid (for membranes) or wax (for OCL) synthesis in the cell. Again, this possibility would be worth further investigation.

RABC1 localizes to the ER and weakly localizes to LDs under normal conditions, however, in OA-induced LD production, RABC1 targets to the surface of the LDs. This mirrors the targeting of Rab18 in mammalian cells. According to Kretzschmar et al. (2018), the tobacco (*Nicotiana tabacum*) counterpart of Rab18 was enriched in LD fractions of seedlings and pollen tubes but not as strongly enriched as canonical LD proteins. This is in line with the dual localization of RABC1 and suggests the localization of Rab18 proteins on LDs is transient and not very strong.

The finding that SEIPIN2 and SEIPIN3 serve as effectors of RABC1 is in accordance with the early work on Rab18 (which is a close homolog of RABC1 in mammalian cells; Li et al., 2019). In contrast to yeast or mammals, plants express three SEIPIN genes. The expansion of SEIPIN isoforms could

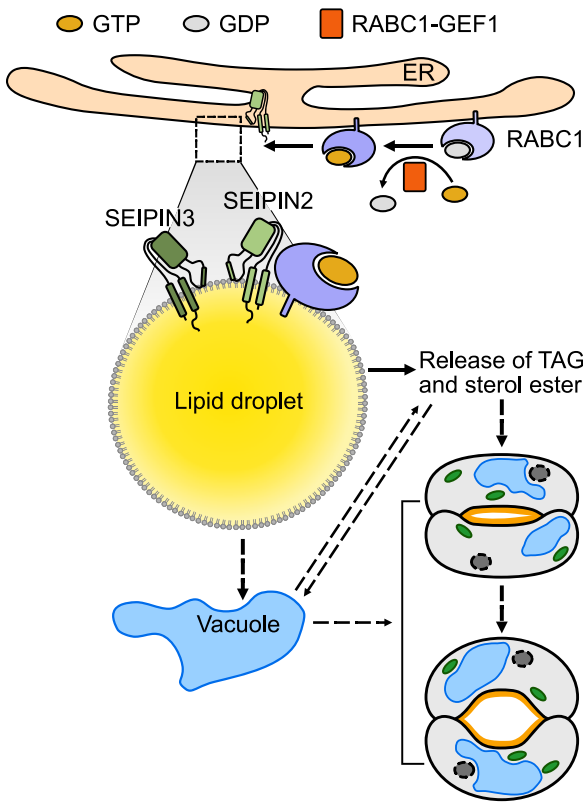


Figure 7 Proposed working model of RABC1 regulating LD dynamics and stomatal development. RABC1, a Rab protein that is preferentially expressed in young stomatal GCs, is activated by the binding of RABC1GEF1 (a specific guanine nucleotide exchange factor of RABC1) in response to a yet unknown developmental cue, and then targeted to the surface of LDs, where it interacts with SEIPIN2 and SEIPIN3, two ER-localized proteins that serve as the downstream effectors of RABC1 to regulate LD mobilization and lipid availability for the establishment of functional stomata. The dashed arrows indicate the possible involvement of the vacuole during RABC1-controlled LD homeostasis. ER, endoplasmic reticulum. For more details, please refer to the “Discussion” section.

have resulted in an expanded capacity to meet the distinct needs of land plants to adapt to an always-changing environment. This suggestion is supported by the fact that we only detected increased LD abundance and LD size in the GCs of the double mutant *seipin2 seipin3* but not in *seipin1 seipin2* and *seipin1 seipin3*. This suggests that SEIPIN1 is unlikely to be involved in the regulation of LDs by RABC1 in GCs. In support of this suggestion, all three SEIPIN proteins have been found to participate in the regulation of LD abundance in seeds/pollen grains (Taurino et al., 2018), whereas only the function of SEIPIN2 and SEIPIN3 depends on their interaction with the vesicle-associated membrane protein-associated protein family member AtVAP27-1 (Greer et al., 2020). One thing that might account for the distinct function of SEIPIN2, SEIPIN3, and SEIPIN1 is the sequence differences between SEIPIN1 and SEIPIN2/3, particularly between their N-terminal regions which have been proposed to be crucial for the functionality of SEIPIN proteins (Greer et al., 2020). It is important to note that the severity of

deformed LDs and defective stomata in *seipin2 seipin3* is much weaker than either *lds1* or *ldsgef1*, and *lds1* and *seipin2 seipin3*. This strongly suggests that there must be other effectors of RABC1.

In humans, Rab18 is correlated with Warburg Micro syndrome, a severe illness characterized by microcephaly, intellectual disability, optical atrophy, and hypogenitalism. However, whether there is a direct causal relationship between LD dysfunction and the disease is currently unknown (Bem et al., 2011; Dejgaard and Presley, 2019). Rab18 was detected at LD-ER contact sites, associated with the NRZ tethering complex and the Q-SNARES Use1, Syntaxin18, and BNIP1 to cooperatively support LD growth in adipocytes (Ozeki et al., 2005; Xu et al., 2018). In COS7 and HeLa cells, a complex of Rab18 and DFCP1 has been found to be important for efficient ER-LD tethering and LD expansion (Li et al., 2019). In addition to being a key factor regulating lipogenesis and lipolysis (Martin et al., 2005; Ozeki et al., 2005; Pulido et al., 2011), Rab18 is also involved in trafficking between the Golgi and ER (Dejgaard et al., 2008), regulating ER structure (Gerondopoulos et al., 2014), and autophagy (Feldmann et al., 2017; Bekbulat et al., 2020). Overall, the mechanistic details by which mutations in Rab18 cause enlarged LDs remain understudied. *Arabidopsis* Rab18 has not been previously ascribed an LD-related function. Our work reveals that RABC1 together with its GEF and effectors are involved in stomatal regulation by modulating LDs.

In summary, the results of the research described here reveal an unexpected role for LDs in the regulation of stomatal development. Underpinning this role is the Rab GTPase family member RABC1. We show that it interacts with SEIPIN2/3, which functions in LD formation. Future research will be directed to understanding whether, how LD-vacuole interactions result in the increase in vacuolar surface area seen during stomatal development.

Materials and methods

Plant materials, growth conditions, and plasmid construction

All *Arabidopsis* (*A. thaliana* L.) lines used in this study are in the Columbia (Col-0) ecotype background. The mutants *lds1-2* (SALK_012129), *rabc2a* (SALK_061001C), *rabc2b* (WiscDsLoxHs095_05E), *lds1gef1-1* (WiscDsLox393-396G22), *lds1gef1-2* (SALK_116404C), SALK_058192C of At5g55060, *seipin1-1*, (SALK_Seq0958), *seipin2-1* (GabiGK_183F09), *seipin3-1* (SALK_019429C) and the marker line *ER-ck* (CS16250; Nelson et al., 2007) were obtained from the *Arabidopsis* Biological Resource Center (ABRC, Ohio State University) and genotyped using specific primers, which are listed in the Supplemental Table S1. The *scap1* mutant is as described by Negi et al. (2013) and was a kind gift from Professor Koh Iba (Kyushu University). The three single mutant lines of SEIPINs, and from which the corresponding double and triple mutants were derived through genetic crossings, are as described by Taurino et al. (2018).

Arabidopsis seeds were sown on half-strength Murashige and Skoog (1/2MS) media with 1% sucrose and 0.6% agar. After a 3-d stratification at 4°C in the dark, the seed plates were transferred to a greenhouse at 22°C with an average light intensity of 120 μmoles photons m⁻² s⁻¹ and relative humidity at 70%–80% with a 10-h-light/14-h-dark photoperiod. 7-d-old seedlings on the plates were transplanted into the potting soil/vermiculite mixture (Zhang et al., 2019). *Nicotiana benthamiana* seeds were directly sown at a depth of 0.5 cm below the soil/vermiculite mixture surface and the seedlings were grown in a greenhouse with 16-h-light/8-h-dark cycles at 28°C. The light source used in the greenhouses is wide-spectrum fluorescent bulb (YZ28-T5-28W, NVC).

The promoter sequence of RABC1 was amplified using the primers listed in *Supplemental Table S1*, while the promoter sequences of SEIPINs used in this study were as previously described (Taurino et al., 2018). The *ProRABC1:GUS* and *ProSEIPINs:GUS* transgenic plants were generated using pENTR/D-TOPO as an entry vector, pKGWFS7 plasmids as the destination vectors. Plasmid of *ProRABC1:GUS* was used to develop *ProRABC1:mCherry-RABC1* (the natural or mutated RABC1), *ProRABC1:RABC2a*, and *ProRABC1:RABC2b* constructs by replacing the GUS gene sequence with the coding sequences of *mCherry-RABC1*, *RABC2a*, and *RABC2b*, respectively. The nucleotide sequences of *mCherry-RABC1* were generated by overlapping PCR using the CDS of *mCherry* and the natural or mutated RABC1. The coding sequences of RABC1(S27N) and RABC1(Q71L) were produced by site-directed mutagenesis PCR. pK2GW7 was used as the destination vector for *Pro35S:MmRAB18*, *Pro35S:HsRAB18*, and *Pro35S:SDP1* constructs after introducing the corresponding CDS of *MmRAB18*, *HsRAB18*, and *SDP1* to the entry vector, respectively. pGWB6 (Nakagawa et al., 2007) was the destination vectors for *Pro35S:GFP-SEIPIN2/3* and *Pro35S:GFP-VAMP711* constructs, respectively. All primers used above are shown in *Supplemental Table S1* and all generated constructs were verified by DNA sequencing.

Mutant screen

Ethyl methane sulfonate mutagenesis of Arabidopsis seeds was performed essentially as described (Kim et al., 2006). The M2 seeds were subjected to a two-step mutant screen based on infrared thermal imaging and NR staining to identify genes involved in LD dynamics and stomatal development/function. Thermal images were obtained using an SC660 (FLIR Systems, Wilsonville, USA). The camera was mounted vertically above the plants. Mean temperature of leaves no. 3, 4, 5, 6, and 7 below the apex were calculated using the customized region of interest (ROI) tool, according to the manufacturer's instructions. Abaxial epidermal strips were detached from rosette leaves for LD staining. Briefly, strips were incubated in KCl/MES buffer (50 mM KCl, 10 mM MES/KOH, pH 6.15) containing 10 μg/mL NR (Sigma) or 10 μM Bodipy 493/503 (Invitrogen) for 10 min and then washed in KCl/MES buffer for 5 min before imaging. Confocal images were collected with a Leica SP8 confocal

microscope. Following the identification of a mutant, it was backcrossed to WT 3 times.

Confocal microscopy

Images were collected using a Leica SP8 confocal microscope with a × 63/1.4 NA oil immersion objective lens. For LD staining, we used three dyes in this study, NR (10 μg/mL), Bodipy 493/503 (10 μM), and MDH (Monodansylpentane, Yang et al., 2012). The excitation wavelength was 405 nm and the emission wavelength was 440–485 nm for MDH; the excitation wavelength was 488 nm and the emission wavelength was 530–590 nm for NR while the emission wavelength was 500–530 nm for Bodipy 493/503. When detecting the LDs abundance and size in GCs, the Z-projections (maximal intensity) of confocal stacks from young leaves of 4-week-old plants was used. Z-series images were taken every 0.5 μm and the same settings of laser power and gain value for all samples examined. Z-projections were generated in Leica Advanced Fluorescence v3.1.0 (Leica) and Image J (NIH) was used for fluorescence intensity quantification. Briefly, images were first converted to 16-bit depth, and ROI (regions of interest) was defined by tracing the outline of cells in Image J. Raw integrated density (the sum of all pixel intensities within an ROI) and area were recorded. Fluorescence intensity was represented as a ratio of raw integrated density to area after minus the background fluorescence intensity. Given that the resolution of confocal microscopy is about 150 nm, it is difficult to observe and quantify smaller LDs, such as nascent LDs. However, this limitation does not have much influence on the conclusions of this paper.

Map-based mutant gene cloning

Candidate *lds1* mutants were outcrossed to WT plants in the Landsberg *erecta* background (*Ler*) and the segregating F2 seedlings were screened using infrared thermography and microscopic observation following NR/Bodipy staining. Segregant analysis of totally 900 *lds1* mutants was performed using simple sequence length polymorphism (SSLP) markers as previously described (Lukowitz et al., 2000; He et al., 2018). The mutation was narrowed down to a ca. 200 kb region of chromosome 1 between SSLP marker 125DW-G and 125DW-J2. T-DNA insertion lines representing all the annotated genes within this region were obtained from ARBC and screened. A T-DNA insertion line (SALK_012129) of At1g43890 which displayed similar LD accumulation defects to *lds1* was identified. Allelism tests were performed using the F1 progeny of the *lds1* x SALK_012129 which confirmed that *lds1* and SALK_012129 are allelic to each other. The presence of a single point mutation in At1g43890 of the *lds1* mutant and a T-DNA insertion in At1g43890 of the SALK_012129 line was validated using PCR-based genotyping and gene sequencing. We renamed the *lds1* and SALK_012129 as *lds1-1* and *lds1-2*, respectively.

Stomatal aperture measurements

Stomatal aperture was determined using the rapid imprinting technique described by Geisler et al. (2000). Light-bodied vinylpolysiloxane dental resin (eliteHD+, Zhermack Clinical, Badia Polesine, Italy) was attached to the abaxial side of the leaflet and then removed as soon as it dried. The resin epidermal imprints were covered with transparent nail polish, which was removed once it dried and served as a mirror image of the resin imprint. The nail-polish imprints were put on glass coverslips and photographed under a model ICC50 W bright-field inverted microscope (Leica Microsystem, Wetzlar, Germany). Stomatal images were later analyzed to determine aperture size using the ImageJ software fit-ellipse tool (<http://rsb.info.nih.gov/ij/>). A microscopic ruler (Olympus) was used for size calibration.

Stomatal conductance measurements

Stomatal conductance of intact leaves of 5-week-old plants to water vapor (g_s) was measured with a Li-6400 gas exchange analyzer with a fluorometer chamber (Li-Cor, Lincoln, NE, USA) as described previously (Negi et al., 2013; He et al., 2018). The g_s response to light was tested under 350 ppm CO₂. Intact leaves were incubated in dark for 3 h first, then kept under light illumination (150 $\mu\text{mol m}^{-2} \text{s}^{-1}$) for 2 h and another 1 h dark. The g_s response to CO₂ was measured at constant light intensity (150 $\mu\text{mol m}^{-2} \text{s}^{-1}$). Temperature and relative humidity in the chamber were held at 22°C and 60%, respectively. All measurements were taken at a rate of one per minute.

Transgene expression analysis

GUS activity of *ProRABC1:GUS* and *ProSEIPIN2:GUS* transformants was performed as described previously (Negi et al., 2013; Taurino et al., 2018). Transformants were fixed in 90% ice-cold acetone for 20 min. After washing, transformants were incubated in 100 mM sodium phosphate (pH 7.4), 10 mM EDTA, 0.5 mM K₃Fe(CN)₆, 0.5 mM K₄Fe(CN)₆, 0.1% Triton X-100, and 1 mM 5-bromo-4-chloro-3-indolyl β-D-glucuronic acid at 37°C in the dark. Plants were bleached in 70% ethanol and mounted in chloral hydrate for imaging. Subcellular localization of mCherry-RABC1 was analyzed using a *ProRABC1:mCherry-RABC1* transformant. After incubation with or without 200 μM OA (oleic acid, Xu et al., 2018) in buffer (50 mM KCl, 10 mM MES/KOH (pH 6.15)) for 6 h, leaf epidermal peels of the transformant were observed with a Leica SP8 confocal microscope. LDs were stained with Bodipy 493/503 (excitation laser 488 nm, emission 530–590 nm). mCherry was excited using a 552 nm laser and its emission is 590–650 nm.

Yeast two-hybrid analysis

The Y2H assay was based on the Matchmaker Gold Yeast Two-Hybrid System User Manual (Clontech). The cDNAs encoding different forms of RABC1 were cloned into pGBKT7 bait plasmid and introduced into Y2H Gold yeast strain. Possible autoactivation of RABC1 was determined according to the manufacturer's protocol. We used the

Mate and Plate Normalize Arabidopsis Universal Library (Clontech) for screening potential interacting proteins of RABC1. Briefly, we first prepared a concentrated overnight culture of the Bait Strain (cell density $>1 \times 10^8$ cells/mL in SD/-Trp) before adding 1 mL of the Library Strain to the Bait Strain (4–5 mL) in a sterile 2 L flask. Next, we added 45 mL of 2 × YPDA liquid medium, and incubated the reaction at 30°C for 20–24 h with gentle agitation (30–50 rpm). After centrifugation to pellet the cells, we resuspended all pelleted cells in 10 mL of 0.5 × YPDA/Kan liquid medium before plating the culture on SD/-Leu/-Trp/-His/-Ade and incubated it at 30°C for 3–5 d. Yeast colonies that were alive on SD/-Leu/-Trp/-His/-Ade medium were streaked. Then plasmids of these colonies were isolated and sequenced. In addition, to further confirm the interactions in yeast, the plasmids pGADT7 and pGBKT7 with corresponding proteins were co-transformed into the yeast strain Y2H Gold. Empty vectors were used for negative controls.

Nucleotide exchange assays

The nucleotide exchange assays were performed to determine GEF for RABC1 as described (Pan et al., 1995; Antonny et al., 2001; Goh et al., 2007; Cui et al., 2014). Briefly, each purified GST-Rab protein was preloaded with a 25 M GDP at 25°C for 2 h. Then, each assay was incubated with or without GST-At5g58510 protein or GST-At5g55060 protein in reaction buffer (20 mM Tris-HCl, pH 8.0, 150 mM NaCl, 0.5 mM MgCl₂) for 100 s at 25°C. The nucleotide exchange reaction was initiated by the addition of 0.1 mM GMP-PNP (guanylyl imidodiphosphate). The Trp intrinsic fluorescence of Rab proteins was detected by fluorescence spectrophotometry at an excitation wavelength of 298 nm and an emission wavelength of 340 nm.

Expression and purification of GST fusion proteins

Vector pGEX-4T-1 was used for expressing GST fusion proteins. After inserting the respective CDS sequence into pGEX-4T-1 and confirming that the cloning was in-frame, the resultant plasmids of pGEX-GST-RABC1, pGEX-GST-RHA1, pGEX-GST-RABC1GEF1, and pGEX-GST-At5g55060 were transformed in BL21 Rosetta and recombinant proteins were purified according to published procedures (Goh et al., 2007; Fukuda et al., 2013; Cui et al., 2014). Briefly, the expression of recombinant proteins was induced by the addition of 1 mM isopropyl β-D-1-thiogalactopyranoside (IPTG) then incubated overnight at 16°C. GST-tagged proteins were purified on a glutathione-Sepharose 4B column (GE Healthcare).

BiFC assays

The constructs for BiFC assays were generated by cloning the coding sequences of RABC1, RABC1GEF1, and SEIPINs into the series of pSAT expression vectors as described (Tzfira et al., 2005). The constructs were introduced into *N. benthamiana* leaves through Agrobacterium (*Agrobacterium tumefaciens*, strain GV3101)-mediated transformation. After incubated for 2–3 d, the leaves were examined using a Leica SP8 microscope (excitation 488 nm,

emission 520–560 nm). Fluorescence intensity quantification was performed in a similar manner to that used for LDs as described above. Images were converted to 16-bit depth, and ROI was defined in Image J. The YFP intensity was represented as a ratio of raw integrated density to area after minus the background fluorescence intensity.

Co-IP reactions

The CDS of *RABC1*, *RABC1(S27N)*, *RABC1(Q71L)*, or *RABC1GEF1* was each separately subcloned into pGWB12 or pGWB6 using LR reaction (Nakagawa et al., 2007). Then the plasmids were electroporated into the GV3101 strain of *A. tumefaciens* and transiently expressed in *N. benthamiana*. Co-IP reactions were performed according to published procedures (Roux et al., 2011; Fukuda et al., 2013). Briefly, leaves were ground in liquid nitrogen and suspended in the extraction buffer (50 mM Tris, 150 mM NaCl, 1 mM EDTA, 5 mM DTT, 0.5% NP40, 1 × protease inhibitor cocktail, pH 7.5) at 2 mL/g tissue powder. Samples were centrifuged at 16,000 g at 4°C for 10–15 min before the supernatant was transferred to a new tube and centrifuged at 16,000 g at 4°C for 5 min. The supernatant (1.5 mL) was incubated with 20 μL GFP Trap-A beads (Chromotek) for 2 h at 4°C. After washing 4 times with the immunoprecipitation buffer (the extraction buffer minus the protease inhibitor cocktail), the beads were then boiled in SDS sample buffer for 5 min before being subjected to western blot analysis using anti-GFP (ProteinTech, HRP-66002) and anti-Flag antibody (ProteinTech, HRP-66008) at a dilution of 1:5,000.

TAG analysis

GC-enriched epidermal strips were isolated essentially as described in McLachlan et al. (2016). Of the GCs, 97.3 ± 4.8% were intact and the epidermal pavement cell viability was 4.5% ± 0.8% using FDA staining. TAGs were extracted from 50 mg fresh-frozen epidermal strips, and analyzed by LC/MS/MS (Burgal et al., 2008).

TEM analysis

Leaf pieces from 3-week-old seedlings were fixed in 2% (v/v) glutaraldehyde in 100 mM phosphate buffer (pH7.4) at 4°C for overnight. The tissue was then rinsed, postfixed in 1% (w/v) osmium tetroxide for 2 h. After dehydration in an alcohol series (15%, 30%, 50%, 70%, 80%, 85%, 90%, and 95% alcohol, each treatment lasted for 30 min), the tissue was embedded in Spurr's epoxy resin after a propylene oxide/Spurr's epoxy resin incubation series (propylene oxide/Spurr's epoxy resin = 2:1, 1:1, 1:2, every 12 h). After polymerizing at 60°C for 48 h, thin resin sections were prepared and stained with aqueous uranyl acetate and lead acetate. A JEM-1400Plus transmission electron microscope was used to visualize the sections.

Statistical analysis

All assays were conducted with three or more biological replicates and analyzed using SigmaPlot (version 12.0, Systat).

Comparison of means was conducted using Student's *t* tests.

Accession numbers

The GenBank accession numbers of the *Arabidopsis* genes used in this study are as follows: *RABC1* (At1g43890), *RABC1GEF1* (At5g58510), *RABC2a* (At5g03530), *RABC2b* (At3g09910), *SEIPIN1* (At5g16460), *SEIPIN2* (At1g29760), *SEIPIN3* (At2g34380), *SDP1* (At5g04040). The NCBI accession numbers for the proteins are as follows: *RAB3GAP1* (NP_001165906), *MmRab18* (NP_001265376), *HsRab18* (NP_067075).

Supplemental data

The following materials are available in the online version of this article.

Supplemental Figure S1. *lds1* mutation caused no alterations in stomatal density and stomatal index but did bring about growth arrest.

Supplemental Figure S2. *RABC1*-mediated LD regulation is conserved across species.

Supplemental Figure S3. Mutant identification, GEF activity analysis of At5g58510 and At5g55060.

Supplemental Figure S4. Localization analysis of *SEIPIN2/3* and overexpression of *SEIPIN2/3* in *lds1-2*.

Supplemental Figure S5. Vacuole area in GCs is affected by *lds1*, *lds1gef1*, and *seipin2 seipin3* mutations.

Supplemental Table S1. Primers used in this study.

Supplemental Data Set S1. Candidates identified during the Y2H screen using *RABC1(S27N)* as bait.

Supplemental Data Set S2. Candidates identified during the Y2H screen using *RABC1(Q71L)* as bait.

Acknowledgments

The authors are grateful to Professor Maoteng Li (Huazhong University of Science and Technology) for the assistance with the neutral lipid analysis.

Funding

This work was supported by the National Natural Science Foundation of China (#31770282 and #31971811).

Conflict of interest statement. None declared.

References

- Andrés Z, Pérez-Hormaeche J, Leidi EO, Schlücking K, Steinhorst L, McLachlan DH, Schumacher K, Hetherington AM, Kudla J, Cubero B (2014) Control of vacuolar dynamics and regulation of stomatal aperture by tonoplast potassium uptake. Proc Natl Acad Sci USA 111: E1806–E1814
- Antony B, Madden D, Hamamoto S, Orci L, Schekman R (2001) Dynamics of the COPII coat with GTP and stable analogues. Nat Cell Biol 3: 531–537
- Bak G, Lee EJ, Lee Y, Kato M, Segami S, Sze H, Maeshima M, Hwang JU, Lee Y (2013) Rapid structural changes and acidification of guard cell vacuoles during stomatal closure require phosphatidylinositol 3,5-bisphosphate. Plant Cell 25: 2202–2216
- Bekbulat F, Schmitt D, Feldmann A, Huesmann H, Eimer S, Juretschke T, Beli P, Behl C, Kern A (2020) RAB18 loss interferes

Regulated Localization of Rab18 to Lipid Droplets

EFFECTS OF LIPOLYtic STIMULATION AND INHIBITION OF LIPID DROPLET CATABOLISM^{*§}

Received for publication, June 20, 2005, and in revised form, September 15, 2005 Published, JBC Papers in Press, October 5, 2005, DOI 10.1074/jbc.M506651200

Sally Martin[†], Kim Driessens[‡], Susan J. Nixon[‡], Marino Zerial[§], and Robert G. Parton[‡]

From the [†]Institute for Molecular Bioscience & Centre for Microscopy and Microanalysis, University of Queensland, Brisbane, Queensland 4072, Australia and the [§]Max Planck Institute for Molecular Cell Biology and Genetics, Pfotenhauerstrasse 108, 01307 Dresden, Germany

Rab GTPases are crucial regulators of membrane traffic. Here we have examined a possible association of Rab proteins with lipid droplets (LDs), neutral lipid-containing organelles surrounded by a phospholipid monolayer, also known as lipid bodies, which have been traditionally considered relatively inert storage organelles. Although we found close apposition between LDs and endosomal compartments labeled by expressed Rab5, Rab7, or Rab11 constructs, there was no detectable labeling of the LD surface itself by these Rab proteins. In contrast, GFP-Rab18 localized to LDs and immunoelectron microscopy showed direct association with the monolayer surface. Green fluorescent protein (GFP)-Rab18-labeled LDs underwent oscillatory movements in a localized area as well as sporadic, rapid, saltatory movements both in the periphery of the cell and toward the perinuclear region. In both adipocytes and non-adipocyte cell lines Rab18 localized to a subset of LDs. To gain insights into this specific localization, Rab18 was co-expressed with Cav3^{DGV}, a truncation mutant of caveolin-3 shown to inhibit the catabolism and motility of lipid droplets. GFP-Rab18 and mRFP-Cav3^{DGV} labeled mutually exclusive subpopulations of LDs. Moreover, in 3T3-L1 adipocytes, stimulation of lipolysis increased the localization of Rab18 to LDs, an effect reversed by β -adrenergic antagonists. These results show that a Rab protein localizes directly to the monolayer surface of LDs. In addition, association with the LD surface was increased following stimulation of lipolysis and inhibited by a caveolin mutant suggesting that recruitment of Rab18 is regulated by the metabolic state of individual LDs.

The maintenance of lipid homeostasis within the cell is controlled through combined synthesis, influx, efflux, and storage. Cells store excess fatty acids and cholesterol in lipid droplets (LDs),² which are dynamic and regulated organelles derived from the endoplasmic reticulum (ER) (1, 2). LDs have been shown to undergo microtubule-based motility (3–5) and to interact with a range of other organelles, including

mitochondria, peroxisomes, and the ER (6, 7). Whereas LDs have been best described in adipocytes and steroidogenic cells of the testis, ovary, and adrenal gland, they are also present in a range of other cell types, and their formation can be induced in cultured cells by oleic acid treatment (3), suggesting that all cells have the ability to generate LDs under conditions of elevated fatty acids. In recent years interest in the regulation of LDs in less specialized cell types has increased significantly, due in part to the observation that a dominant-negative truncation mutant of caveolin, Cav3^{DGV}, is localized to the surface of LDs and induces a cholesterol imbalance in fibroblasts, in addition to inhibiting LD motility and catabolism (3, 8). Caveolins have been shown to bind cholesterol (9) and fatty acids (10), and while predominantly localized to caveolar domains of the cell surface they can be redistributed to LDs upon fatty acid treatment (3). In addition to the inhibitory effects of Cav3^{DGV} on the LD, Cav3^{DGV} also indirectly inhibits signaling from the cell surface through an effect on cholesterol, suggesting a link between the function of the LDs and functional maintenance of cell surface domains.

To begin to define the mechanisms regulating the formation and catabolism of the LD it is important to first identify the nature of the interaction of this organelle with other compartments within the cell. Several recent studies have undertaken proteomic analyses of LDs from a number of different cell types, under conditions of lipolysis or lipid deposition. These analyses identified numerous members of the Rab family of small GTPases associated with the LDs (11–14). The Rab family of proteins are essential regulators of vesicular traffic. Described as molecular switches, Rab proteins undergo conformational changes through cycles of GTP binding and hydrolysis (15, 16). The GTP-bound active form interacts directly with downstream effectors and indirectly with other components of the transport machinery controlling cargo selection, vesicle fusion, cytoskeletal transport, and integration of vesicle traffic with signal transduction pathways. Although the novel nature of the LD hemi-membrane makes it unlikely that proteins spanning the bilayer could associate with this organelle, this would not preclude association of Rab proteins whose attachment to membranes is regulated through prenylation at the C terminus, and protein-protein interactions (15, 16). Indeed, ten Rab GTPases have been found associated with LDs (11–14), several of which have been previously localized to endocytic compartments. On the one hand, this complexity is not unusual, as several distinct Rab proteins can be associated with a single organelle undertaking multiple sorting functions, such as early endosomes and the Golgi complex (16). The predicted association of multiple Rab proteins with the lipid droplet suggests a dynamic interaction between this and other organelles in the cell. On the other hand, out of the Rab proteins associated with LDs, only five, *i.e.* Rab5c, Rab7, Rab10, Rab14, and Rab18, have been identified independently in at least two separate studies.

In the present study we have analyzed the localization of Rab5, Rab7, Rab11, and Rab18, all previously identified in the endosomal system,

* This work was supported by a grant from the National Health and Medical Research Council of Australia (to R. G. P.). Confocal microscopy was performed at the Australian Cancer Research Foundation (ACRF)/Institute for Molecular Bioscience (IMB) Dynamic Imaging Facility for Cancer Biology, established with funding from the ACRF. Electron microscopy was performed at the Centre for Microscopy and Microanalysis at the University of Queensland. The IMB is a Special Research Centre of the Australian Research Council. The costs of publication of this article were defrayed in part by the payment of page charges. This article must therefore be hereby marked "advertisement" in accordance with 18 U.S.C. Section 1734 solely to indicate this fact.

§ The on-line version of this article (available at <http://www.jbc.org>) contains supplemental videos 1–5.

¹ To whom correspondence should be addressed. Tel.: 61-7-3346-2030; Fax: 61-7-3346-2101; E-mail: s.martin@imb.uq.edu.au.

² The abbreviations used are: LD, lipid droplet; ER, endoplasmic reticulum; TVE, tubulovesicular elements; PFA, paraformaldehyde; BHK, baby hamster kidney cells; BSA, bovine serum albumin; GFP, green fluorescent protein; YFP, yellow fluorescent protein; MRFP, monomeric red fluorescent protein; PIPES, 1,4-piperazinediethanesulfonic acid.

Rab18 in Lipid Droplets

with respect to LDs under conditions of neutral lipid synthesis. We have identified Rab18 as a major component of lipid droplets and further explored its role in lipid dynamics and lipid storage activities.

MATERIALS AND METHODS

Cell Culture—3T3-L1 fibroblasts (American Type Culture Collection, Rockville, MD) were maintained in Dulbecco's modified Eagle's medium supplemented with 10% fetal calf serum and 2 mM L-glutamine, and differentiated using insulin, dexamethasone, biotin, and isobutyl-methylxanthine as described previously (17). Adipocytes were used between days 6 and 12 post-differentiation, or at 2-day intervals during the differentiation process as described in the results section. BHK-21 cells (baby hamster kidney cells) and Vero cells (African green monkey kidney epithelial cells) were maintained in Dulbecco's modified Eagle's medium supplemented with 10% (v/v) Serum-Supreme (BioWhittaker) and 2 mM L-glutamine.

Antibodies, Plasmids, and Reagents—Mouse anti-GM130 (catalog no. 610823), monoclonal anti-caveolin-1 (catalog no. 610406), and monoclonal anti-caveolin-2 (catalog no. 610684) were obtained from BD Transduction Laboratories (BD Biosciences). Rabbit anti-perilipin A (catalog no. P1998) and mouse anti- α -tubulin (catalog no. T9026) were obtained from Sigma. Rabbit anti-Rab18 (18) and rabbit anti-GFP (19) have been described previously. Alexa488- and Alexa594-conjugated secondary antibodies were obtained from Molecular Probes Inc. (Eugene, OR). Horseradish peroxidase-conjugated secondary antibodies were obtained from Sigma. Oleic acid was obtained from Calbiochem and conjugated to fatty-acid free bovine serum albumin (Calbiochem) prior to use. Bodipy493/503 and Nile Red were obtained from Molecular Probes and prepared as saturated solutions in ethanol (working dilution, 1:200) and acetone (working dilution, 1:2000), respectively. All other chemicals were obtained from Sigma unless stated otherwise.

GFP-Rab5 and YFP-Rab11 have been described previously (20). GFP-Rab7 was obtained from Dr. Lucas Pelkmans, Max-Planck Institute, Dresden, Germany. mRFP-Cav3^{DGV} was constructed using Cav3^{DGV}-HA (21) as a template to amplify a fragment using the following primers: 5'-G-GGGTACCCGACGGTGTATGGAAGGTG-3' and 5'-CGGGATCCT-AGCCTTCCCTTCGCAG-3'. The PCR product was A-tailed and cloned into pGEM-T Easy (Promega, Madison, WI) and subsequently excised using BamHI and KpnI, and ligated into linearized mRFP-C3. mRFP-C3 was constructed from pRESETb-mRFP1 (supplied by Prof. Roger Tsien, Howard Hughes Medical Institute, University of California (22)).

To generate GFP-Rab18, the mouse Rab18 ORF was excised from myc-Rab18 using NdeI and BamHI (removing the myc tag), ligated into pSL1180 (Amersham Biosciences), and subsequently excised with BamHI and PstI and ligated into pEGFP-C1 (Clontech), resulting in an N-terminal GFP tag. All constructs were sequenced using ABI PRISM BigDye Terminator version 3.1 (Applied Biosystems, Foster City, CA) in the Australian Genome Research Facility, University of Queensland.

Indirect Immunofluorescence Microscopy and Real-time Video Microscopy—For immunofluorescence microscopy cells grown on glass coverslips were fixed with 4% paraformaldehyde (PFA) in PBS. Cells were permeabilized in 0.1% saponin (w/v) for 10 min, quenched for 10 min using 50 mM NHCl₄, and blocked for 10 min using 0.2% bovine serum albumin/0.2% fish skin gelatin in PBS. Primary and secondary antibodies were diluted in blocking solution and incubated with the cells for 30 min at room temperature. Finally the coverslips were washed in PBS and mounted in Mowiol (Calbiochem). Labeling was analyzed using an Axiovert 200M SP LSM 510 META confocal laser scanning microscope (Zeiss) under oil, using either 100 \times or 63 \times oil immersion objectives. The data were processed using the LSM 510 Meta (Zeiss)

software, and images were assembled using Photoshop 7.0 (Adobe Systems, Mountain View, CA). Quantitation of LD Rab18 labeling was performed on fluorescence images collected with identical settings, using ImageJ 1.33 to measure the mean pixel intensity of individual LDs. For each individual experiment between 20 and 70 LDs were analyzed.

Cells for real-time microscopy were plated onto glass-bottom tissue culture dishes (MatTek Corp.) and transferred into CO₂-independent medium supplemented with 0.1% fatty-acid free bovine serum albumin (Calbiochem) in the presence or absence of 100 μ g/ml oleic acid. Time series were collected at 37 °C using an Axiovert 200M SP LSM 510 Meta confocal laser scanning microscope equipped with a heated stage and a 100 \times oil immersion objective. Cells were used for real-time data collection for a maximum of 1.5 h. Time series images were collected using a 488 nm excitation laser line at <20% maximum power using the Zeiss LSM510 Meta software. Images were converted to 8-bit TIFF files and further analyzed using ImageJ software (National Institutes of Health, Bethesda, MD). QuickTime movies were assembled using ImageJ 1.33, and still images were compiled using Adobe Photoshop 7.0.

LD Isolation—LDs were isolated using a modification of the procedure of Yu *et al.* (23). Briefly, cells were scraped into dissociation buffer (25 mM Tris-HCl, pH 7.4, 100 mM KCl, 1 mM EDTA, 5 mM EGTA) containing a mixture of protease inhibitors (250 μ M phenylmethylsulfonyl fluoride, 10 μ g/ml aprotinin, and 10 μ g/ml leupeptin), and lysed by sonication for 10 s. LDs were isolated by sucrose density gradient centrifugation through 18.5%, 9%, and 4.1% sucrose steps and through top buffer (25 mM Tris-HCl, pH 7.4, 1 mM EDTA, 1 mM EGTA). Gradients were analyzed by Western blotting or by electron microscopy.

Immunoprecipitation and Western Blotting—Immunoprecipitation was carried out essentially as described previously (24). Briefly, cells were lysed in 50 mM Tris, pH 7.4, 150 mM NaCl, 5 mM EDTA containing 1% Nonidet P-40, 0.1% SDS, and protease inhibitors. Equal volumes of lysates were immunoprecipitated using either Rab18 antiserum, GFP antiserum, or a non-immune rabbit serum and collected using protein A-Sepharose beads. Immunoprecipitated proteins were solubilized directly into Laemmli sample buffer and analyzed by SDS-PAGE and Western blotting as described previously (25). Immunolabeled proteins were visualized using horseradish peroxidase-conjugated secondary antibodies and developed using the Supersignal ECL reagent (Pierce).

Electron Microscopy—Immunoelectron microscopy of ultrathin cryosections was performed essentially as described previously (26, 27). Briefly, Vero cells transfected with GFP-Rab18 were incubated overnight in the presence of 100 μ g/ml oleic acid and fixed in 2% paraformaldehyde/0.2% glutaraldehyde in 0.1 M PHEM buffer (60 mM PIPES, 25 mM HEPES, 2 mM MgCl₂, 10 mM EGTA), pH 6.9, for 1 h at room temperature. Cells were embedded in 10% gelatin, cryoprotected using PVP-sucrose, and snap frozen onto specimen holders in liquid N₂. Ultracryomicrotomy was performed by a slight modification of the Tokuyasu technique (28) as described previously (27), and sections were picked up with a 1:1 mixture of 2.3 M sucrose and 2% methyl cellulose (29). Grids were viewed using a Jeol 1010 transmission electron microscope.

To perform immunoelectron microscopy on isolated LDs, BHK cells were transfected with GFP-Rab18 or GFP and subsequently incubated in 100 μ g/ml oleic acid overnight. LDs were isolated using sucrose density gradient centrifugation as described above, and the top fractions, containing the LDs, were fixed in 4% PFA. Isolated LDs were applied to Formvar/carbon-coated copper grids and immunolabeled as described previously (25).

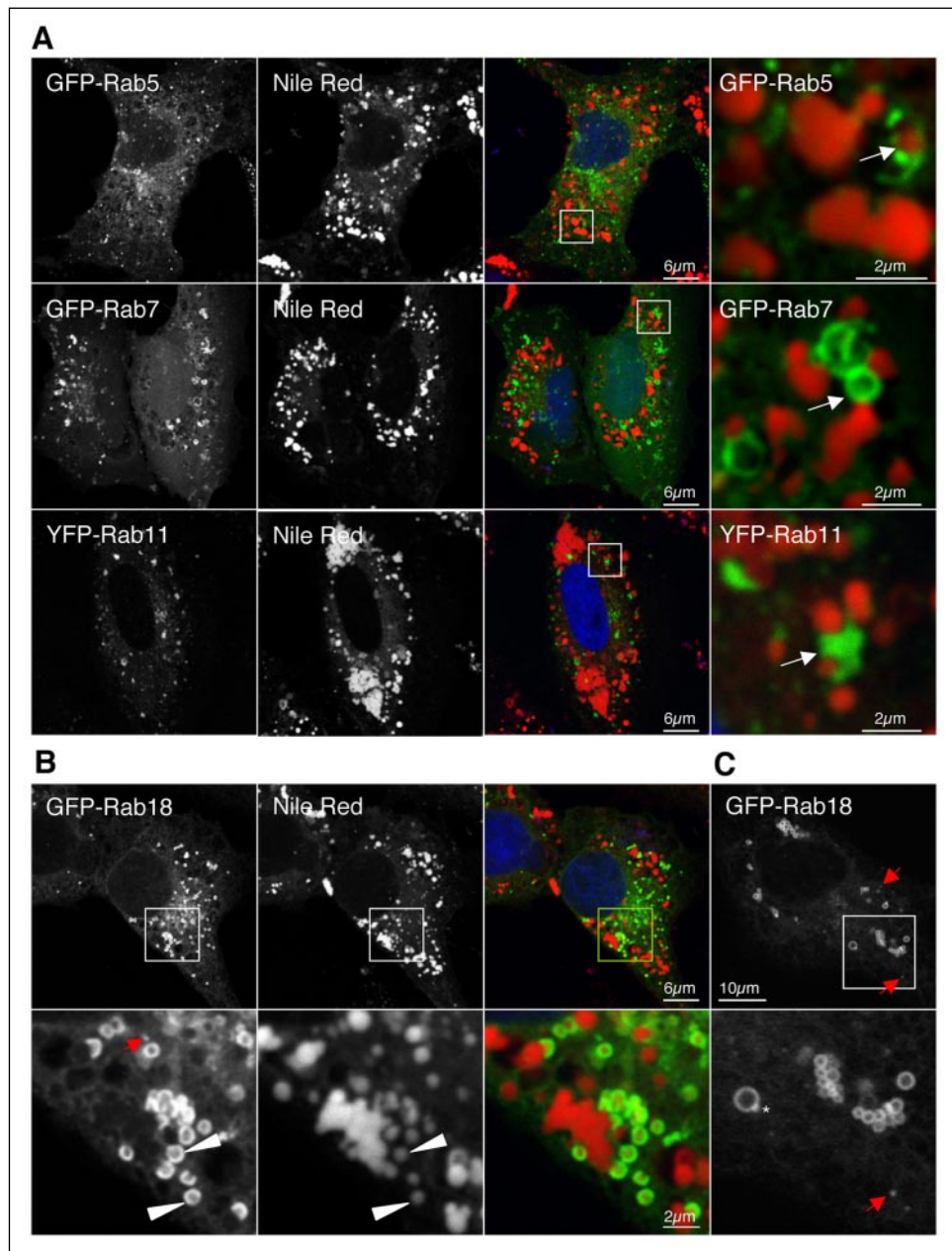


FIGURE 1. Localization of GFP-Rab proteins in oleic acid-treated Vero cells. Vero cells expressing fluorescently tagged Rab5, Rab7, Rab11, or Rab18 were incubated with 100 μ g/ml oleic acid overnight, fixed in 4% PFA, and counterstained using Nile Red to identify LDs. *A*, a proportion of GFP-Rab5-, YFP-Rab11-, and GFP-Rab7-labeled endosomes were all observed in close proximity to LDs (arrows) but did not label the surface of the LD itself. *B*, GFP-Rab18 was identified in the ER, on the surface of a subset of LDs (arrowheads), and as small puncta distributed throughout the cell (red arrows). LD labeling was often crescent-shaped in fixed cells. *C*, Vero cells expressing GFP-tagged Rab18 were incubated in oleic acid overnight and imaged in real-time in the absence of fixation. In live cells GFP-Rab18 was observed in the reticular ER, as rings surrounding a subset of LDs and as small puncta (red arrows) distributed throughout the cell. A small bright punctate dot of Rab18 labeling was occasionally observed at the periphery of the labeled LDs (asterisk).

RESULTS

Localization of GFP-Rab18 to Lipid Droplets and Apposition of Endosomal Compartments—To investigate the localization of Rab GTPases potentially involved in LD function in relation to LDs we expressed fluorescently tagged Rab5, Rab7, Rab11, and Rab18 in Vero cells. To increase LD formation, cells were incubated overnight in 100 μ g/ml oleic acid conjugated to bovine serum albumin. Fatty acid concentrations higher than physiological levels have been used previously to induce the rapid formation of LDs in cultured cells (3). Lower concentrations of oleic acid induced a similar formation over a longer period of time (results not shown). GFP-Rab5 and YFP-Rab11 were identified in punctate structures distributed throughout the cell (Fig. 1A) consistent with localization to early and recycling endosomes, respectively (20). In contrast, GFP-Rab7 was present in both small punctate vesicles and in larger endosomal vacuoles, consistent with localization to late endosomes (30). All isoforms also showed varying levels of a cytosolic pool, frequently observed when Rab proteins are over-expressed (31). When

cells were counterstained with Nile Red to identify lipid droplets, both GFP-Rab5- and YFP-Rab11-containing structures were occasionally identified in close apposition to Nile Red-positive structures, whereas GFP-Rab7-labeled endosomes were frequently observed in close apposition to LDs (Fig. 1A). However, Rab5, Rab7, and Rab11 were not observed to label the LD surface itself. In contrast, GFP-Rab18 showed specific and intense labeling of a subset of LDs (Fig. 1, *B* and *C*). In addition, GFP-Rab18 labeled the ER and small, possibly ER-associated, puncta distributed throughout the cells, as well as weak labeling in the region of the Golgi complex (Figs. 1B, 1C, and 4). In a small number of cells with very high levels of GFP-Rab18 expression there was a very strong labeling of the perinuclear region, and in these cells labeling for the Golgi marker GM130 suggested that the Golgi complex was disrupted in a similar manner to brefeldin A (results not shown). However, the predominant localization of GFP-Rab18 was to the LDs. GFP-Rab18 consistently labeled smaller sized LDs usually at the periphery of larger, unlabeled LDs, or a cluster of LDs (Fig. 1B). Intriguingly, in fixed cells

Rab18 in Lipid Droplets

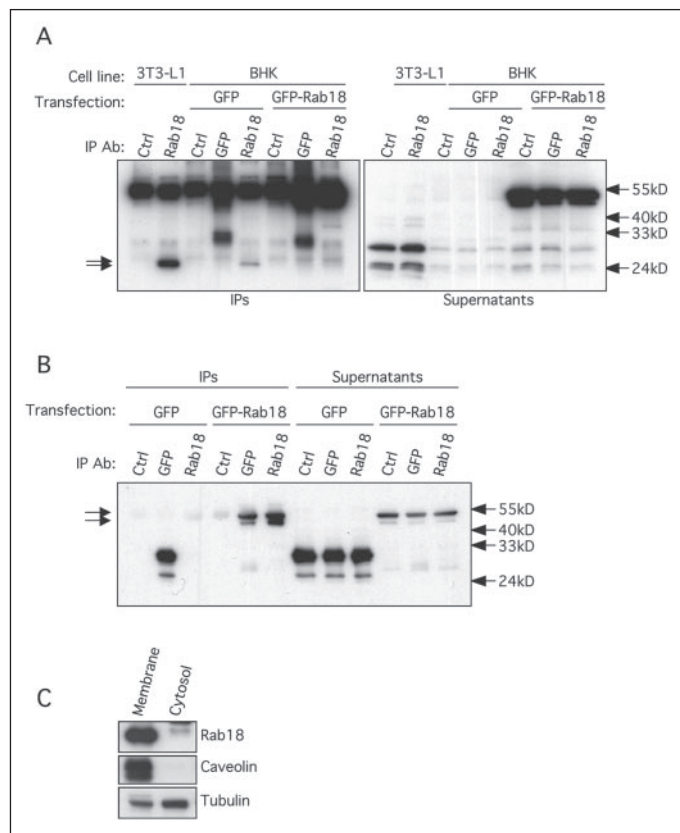


FIGURE 2. Immunoprecipitation of endogenous and expressed Rab18. *A* and *B*, immunoprecipitation of endogenous Rab18 and transfected GFP-Rab18 from 3T3-L1 adipocytes and BHK cells. Endogenous Rab18 was immunoprecipitated from solubilized 3T3-L1 adipocyte cell lysates using an antiserum raised against Rab18 or a control pre-immune rabbit serum (Ctrl). In addition, BHK cells were transfected with either GFP-Rab18 or GFP, and transfected proteins were immunoprecipitated using antisera raised against Rab18, GFP, or a pre-immune rabbit serum (Ctrl). Immunoprecipitations (IPs) and IP supernatants were analyzed by Western blotting using an anti-Rab18 antiserum (*A*) or an anti-GFP antibody (*B*). Rab18 antiserum was found to specifically immunoprecipitate a single protein of apparent molecular mass of 26 kDa from both GFP-transfected BHK cells and 3T3-L1 adipocytes, and a protein band of ~55 kDa from GFP-Rab18-transfected cells. Conversely, GFP antiserum was found to specifically immunoprecipitate GFP-Rab18, which could be detected using either the anti-GFP antiserum (*B*) or the anti-Rab18 antiserum (*A*). Both transfected Rab18 and endogenous Rab18 resolved as a doublet (*arrows*) in the supernatants. A second protein band of ~31 kDa was also consistently recognized by the Rab18 antiserum in the supernatants but was not immunoprecipitated by the antibody. *C*, endogenous Rab18 is predominantly membrane associated. 3T3-L1 adipocyte cell lysates were fractionated into membrane and cytosol by ultracentrifugation. Proteins (10 µg) were analyzed by SDS-PAGE and Western blotting for endogenous Rab18, caveolin, and α-tubulin. Rab18 and caveolin were predominantly membrane-associated, whereas tubulin displayed both membrane-associated and cytosolic pools.

GFP-Rab18 labeling was often observed to partially surround a LD, forming a crescent-shaped profile by fluorescence microscopy, suggestive of a partial enfolding of the LD surface by the Rab18 compartment (*arrowheads*, Fig. 1*B*). However, when live cells were imaged in real-time (Fig. 1*C*), the GFP-Rab18 profile was invariably ring-shaped, suggesting that PFA fixation altered the surface structure of the LDs. Differences between LD size between live and fixed, labeled cells have been described previously (4). Interestingly, an additional observation in live cells, not detectable in fixed cells, was the presence of a single persistent brighter spot of Rab18 labeling occasionally observed on the LD surface, reminiscent of GFP-Rab5 on endosomal membranes (32) (Fig. 1*C*).

Localization of Endogenous Rab18 in Fibroblasts and Adipocytes— Although expressed GFP-Rab18, but not other tested Rab proteins, was clearly localized to LDs, we next sought to investigate the localization of the endogenous Rab18 protein, both in fibroblasts and in 3T3-L1 adi-

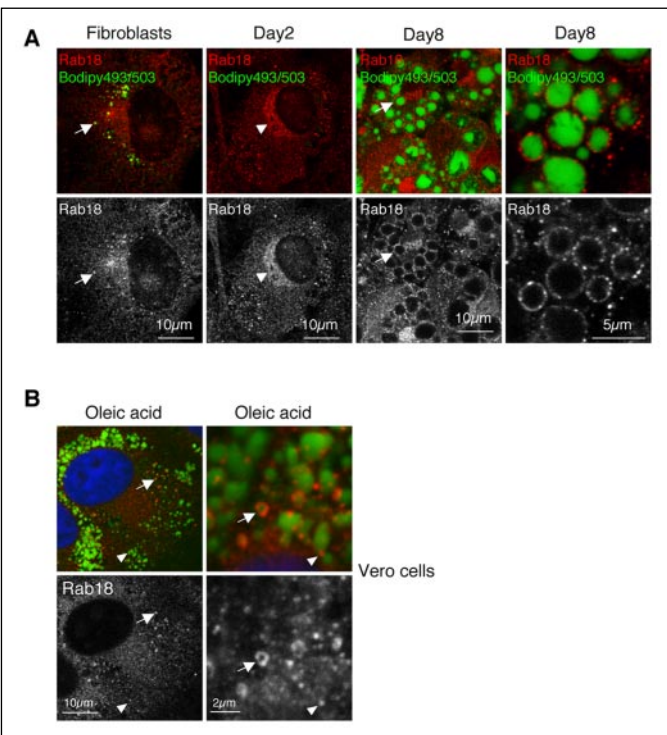


FIGURE 3. Endogenous Rab18 localizes to LDs in fibroblasts and adipocytes, but is not up-regulated during differentiation. *A*, 3T3-L1 fibroblasts were differentiated into adipocytes, fixed at various time points during the differentiation process, and labeled for Rab18. LDs were detected using Bodipy493/503. Rab18 was observed to label the surface of LDs in both fibroblasts and adipocytes (*arrows*). During the differentiation there was an increase in Golgi labeling (*arrowheads*). In fully differentiated adipocytes, Rab18 labeling was observed in distinct domains over the LD surface. *B*, Vero cells were treated overnight with 100 µg/ml oleic acid and fixed for immunofluorescence microscopy. Fixed cells were labeled for Rab18 and counterstained using Bodipy493/503 to label LDs, and 4',6-diamidino-2-phenylindole to label the nucleus. Following treatment with oleic acid Rab18 was observed to label the surface of a subset of LDs, either as a ring shape (*arrows*) or as a single punctate dot (*arrowheads*).

pocytes, cells with a large number of active lipid droplets. A rabbit antiserum raised against Rab18 (18) was found to immunoprecipitate endogenous Rab18 and heterologously expressed GFP-Rab18 (Fig. 2, *A* and *B*), and to detect heterologously expressed GFP-Rab18 by immunofluorescence microscopy (results not shown). In addition, anti-Rab18 antiserum detected GFP-Rab18 immunoprecipitated using an antiserum raised against GFP. Both endogenous Rab18 and heterologously expressed GFP-Rab18 often resolved as a doublet by Western blotting, presumably corresponding to both prenylated and non-prenylated forms. Fractionation of 3T3-L1 adipocyte cell lysates into membrane and cytosol fractions demonstrated that at steady state Rab18 was predominantly membrane associated (Fig. 2*C*).

Expression of Rab18 was found to be higher in 3T3-L1 adipocyte lysates than in BHK or Vero cells by Western blotting (results not shown). We therefore hypothesized that expression could be directly related to LD formation. However, no change in expression of Rab18 was observed during differentiation of 3T3-L1 fibroblasts into adipocytes (results not shown). We next examined the localization of endogenous Rab18 in 3T3-L1 cells during differentiation to adipocytes. In 3T3-L1 fibroblasts, Rab18 labeling was only clearly detectable in a subset of cells containing endogenous LDs, where it was observed to localize to the LD surface (Fig. 3*A*). In addition, there was a low, dispersed, punctate labeling, not observed with a nonspecific anti-serum. During the differentiation process a more pronounced perinuclear labeling was detectable consistent with Golgi localization (Fig. 3*A*). Conversion of

3T3-L1 fibroblasts to an adipocyte phenotype, characterized by the accumulation of large amounts of neutral lipid, coincided with the localization of endogenous Rab18 to the LD surface. Rab18 was observed to label LDs with a distinct, punctate labeling pattern (Fig. 3A). A similar labeling pattern was observed in oleic acid-treated Vero cells, in which a small subset of LDs were labeled heavily for Rab18, whereas a large number of LDs had a single punctate dot of Rab18 labeling associated with the surface (Fig. 3A). Thus in both adipocytes and non-adipocyte cell lines endogenous Rab18 associates with a distinct subset of LDs. Rather than a spectrum of different labeling densities on different LDs, distinct LDs are either very strongly labeled or show negligible labeling.

In conclusion, Rab18 was the only Rab protein that appeared to show specific localization to the surface of LDs as judged by light microscopy. Whether this represented *bona fide* labeling of LDs was further investigated by immunoelectron microscopy.

GFP-Rab18 Associates with the ER and Discrete Subdomains of the LD Surface—We examined the distribution of GFP-Rab18 expressed in Vero cells treated with oleic acid overnight, by immunoelectron microscopy on frozen sections. In ultrathin cryosections (~60 nm thick) in which the membrane compartments of the cell could be clearly discerned, LDs were not well preserved, appearing as irregularly shaped electron-lucent structures (Fig. 4A). However, GFP-Rab18 labeling was clearly shown to decorate the surface of LDs. In addition, and consistent with the light microscopic observations, Rab18 labeled the ER and clusters of non-clathrin-coated tubulovesicular elements (TVE) both around the LD and distributed throughout the cell (Fig. 4, A and B). The localization of GFP-Rab18 to the ER was further examined by labeling for calnexin by immunofluorescence microscopy (Fig. 4, D and E). Calnexin labeling could be seen to surround, but not co-localize with, GFP-Rab18-labeled LDs (Fig. 4E). In the peripheral ER, calnexin and GFP-Rab18 showed a similar reticular pattern, but again there was no co-localization between the two proteins suggesting that they localize to distinct domains of the ER (Fig. 4D). The small clusters of GFP-Rab18-labeled TVE were observed as dense patches of labeling throughout the sections (Fig. 4B). The nature of these compartments is not yet known, but it is possible that they correspond to the small puncta observed by IF (Fig. 1, B and C) or disrupted Golgi elements in cells with a high expression of GFP-Rab18. To improve the morphological preservation of the LD surface, thicker cryosections (~100 nm) were also prepared and labeled for GFP-Rab18 (Fig. 4C). Although most membrane compartments were only poorly discernible in these sections, preservation of the LD surface and adjacent ER was improved. GFP-Rab18 was clearly observed to strongly label the outer layer of the LD, consistent with localization to the LD surface rather than the ER. In some LDs a thin single layer of membrane could be discerned between the ER membrane and the LD core (*arrows*, Fig. 4B, *inset*). We hypothesize that this corresponds to a region of the LD monolayer.

As there was very close apposition observed between the ER membranes and the LD surface (Fig. 4, A–C), we considered the resolution of labeling in the cryosections insufficient to determine whether Rab18 was associated with the monolayer proper or with associated membranes. To maximize GFP-Rab18 expression and localization to LDs, BHK cells were transfected with GFP-Rab18 or GFP, and a subcellular fraction was enriched in LDs isolated by flotation through a sucrose density gradient (Fig. 5A). The LD fractions were fixed directly in 4% PFA and applied to an EM grid. The fractions were then immunolabeled with anti-GFP antibodies followed by protein A-gold. Labeling for GFP-Rab18 was present over the entire LD surface in a heterogeneous pattern, with areas of high concentration containing electron dense networks (Fig. 5, B–D). Labeling was also observed to associate with

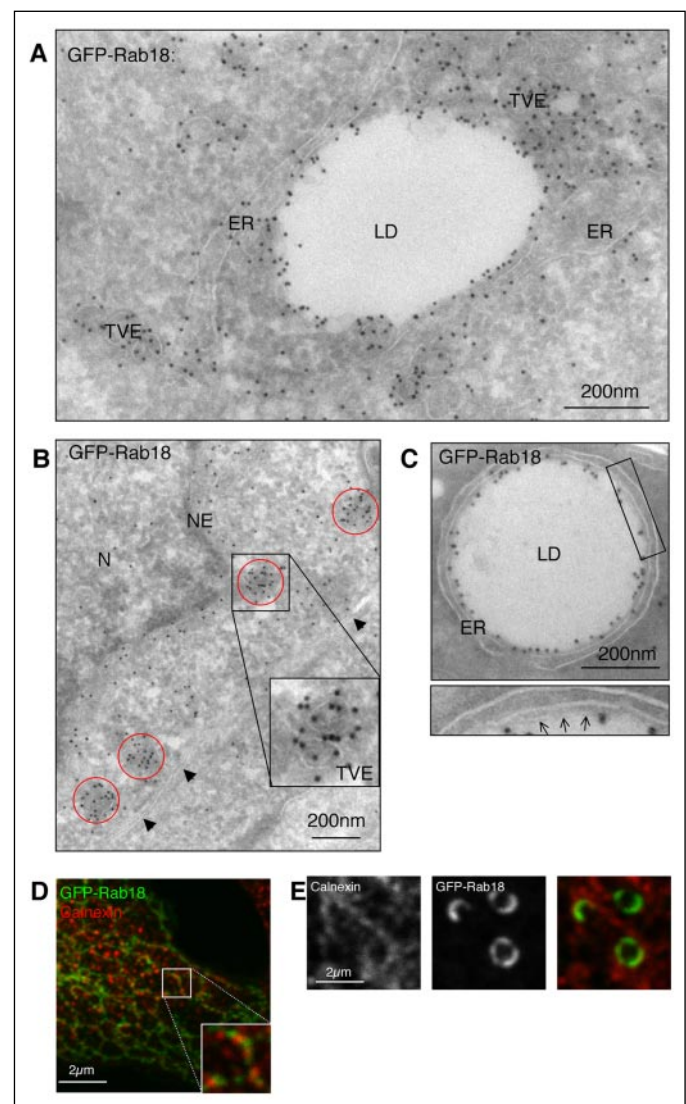
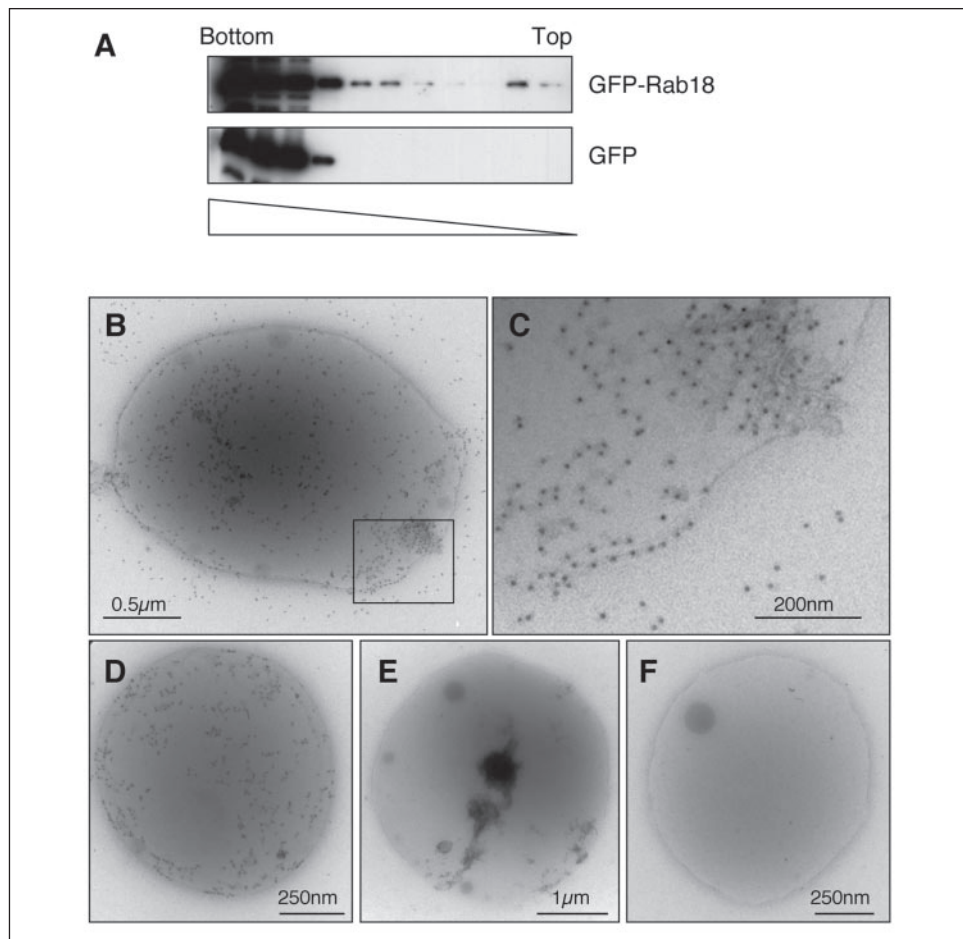


FIGURE 4. Localization of GFP-Rab18 to LDs and the ER. Vero cells expressing GFP-Rab18 were incubated with 100 μ g/ml oleic acid overnight and fixed for immunoelectron microscopy (A–C) or immunofluorescence microscopy (D and E). For immunoelectron microscopy, cryosections were labeled using anti-GFP antibodies and labeling detected using 10 nm protein A-gold. LDs were defined as large, electron-lucent structures that lacked a limiting membrane bilayer. GFP-Rab18 was highly localized to the surface of LDs (A and C), to the peripheral ER (A and D) and nuclear envelope (B), as well as groups of small, non-clathrin-coated tubulovesicular elements (TVE) adjacent to the LD surface (A) and distributed throughout the cell (B). C, in thicker cryosections Rab18 labeled a thin membrane layer adjacent to the ER, assumed to correspond to the surface of the LD itself (*arrows*). Localization of GFP-Rab18 to the ER was confirmed by immunofluorescent labeling for calnexin (D–E). Calnexin-positive structures were seen surrounding the GFP-Rab18-labeled LDs (D–E), and in a punctate reticular pattern throughout the cell, contiguous with, but not co-localizing with, a punctate reticular GFP-Rab18 labeling pattern (D). Note that as fluorescence intensity of GFP-Rab18 at the LD surface was frequently much brighter than the surrounding ER, simultaneous visualization of the two localizations was impractical. ER, endoplasmic reticulum; LD, lipid droplets; NE, nuclear envelope; N, nucleus; TVE, tubulovesicular elements; arrowheads, plasma membrane.

membranous material associated with the LDs. In other areas GFP-Rab18 labeling was completely absent. These results show that GFP-Rab18 is associated with the LD surface monolayer, as well as associated membranes, and also suggest an association with distinct cytoplasmic domains of the LD surface. Specificity of the labeling was confirmed by the absence of labeling on GFP-Rab18 containing LDs using protein A-gold in the absence of the primary anti-GFP antibody (Fig. 5E) and by labeling LDs isolated from cells expressing GFP alone (Fig. 5F).

Rab18 in Lipid Droplets



GFP-Rab18-labeled LDs and ER Compartments Are Highly Motile—Lipid droplets have been previously shown to undergo microtubule-based motility (3–5), which can be prevented by the depolymerization of microtubules (3, 4) or expression of the Cav3^{DGV} mutant (3). Inhibition of LD motility by Cav3^{DGV} suggests a role for motility in the functional regulation of LDs. To examine the motility of Rab18-labeled structures we expressed GFP-Rab18 in Vero cells that were subsequently treated with oleic acid overnight. Cells were imaged by real-time fluorescence microscopy in both the presence and absence of oleic acid to determine the motility of LDs and the ER under conditions of lipid deposition or catabolism. GFP-Rab18 was found to localize to both LDs (Fig. 6, A and B; supplementary data, videos 1 and 2) and the ER (Fig. 6, C and E; supplementary data, videos 3 and 5), as shown in Figs. 1–3, but in addition, smaller punctate and highly motile labeling was observed within the ER (Fig. 6C; supplementary data, video 4). All GFP-Rab18-labeled LDs underwent oscillatory movements and were seen to move in and out of the plane of focus within a given area of the cell (Fig. 6A (4)). However, a subset of GFP-Rab18-labeled LDs underwent rapid, saltatory movements, both in the periphery of the cell and to/from the microtubule organizing center. This was often observed to involve rapid movement in one direction, followed a few seconds later by a reverse motility back to the point of origin (Fig. 6, A and B). These linear, vectorial movements occurred over a period of 5 to 10 s and covered distances between 1 and 4 μ m. The proportion of Rab18-labeled LDs undergoing saltatory rather than oscillatory movement (~6%) was unaffected by the presence of oleic acid. In addition to the movement of the LDs, there was also clear motility of the ER membranes themselves (Fig. 6D), as well as small puncta on the ER membrane (Fig. 6C), both of

which underwent very rapidly motility in the periphery of the cells, and in close proximity to the LD membrane or to the cell surface. GFP-Rab18-labeled structures, presumed to be of ER origin, were also observed to extend away from groups of LDs (Fig. 6E). Together, these data clearly show that GFP-Rab18-labeled LDs are highly motile and display two distinct forms of motility, consistent with microtubule-based transient, vectorial movements of >1 μ m, and shorter, tethered movements around a point of origin. Additionally, GFP-Rab18 confirms the highly dynamic nature of the ER system, displaying rapid motility throughout the cell and peripherally toward the cell surface.

GFP-Rab18 and mRFP-Cav3^{DGV} Localize to Distinct LD Populations—We have previously shown that an N-terminal truncation mutant of caveolin-3, Cav3^{DGV}, localizes to LDs and the ER and inhibits both the motility and the catabolism of LDs (3, 8). We hypothesized that the inhibition of LD catabolism by Cav3^{DGV} could be a direct result of an inhibition of the recruitment of Rab18 to these organelles. To simultaneously image both Cav3^{DGV} and Rab18, we generated an N-terminal mRFP-tagged Cav3^{DGV} construct. Localization of mRFP-Cav3^{DGV} was found to be identical to previously described YFP- and GFP-tagged constructs (8). mRFP-Cav3^{DGV} was localized to LDs and the ER and, following treatment with oleic acid, induced clumping of LDs in the perinuclear area (Fig. 7A). Furthermore, expression of mRFP-Cav3^{DGV} prevented the dispersal of LDs following recovery from oleic acid as described previously for YFP-tagged Cav3^{DGV} (3) (results not shown). Co-expression of mRFP-Cav3^{DGV} and GFP-Rab18 in Vero cells demonstrated that these two proteins co-localized within the ER, but localized to distinct subsets of LDs under normal growth conditions (Fig. 7B).

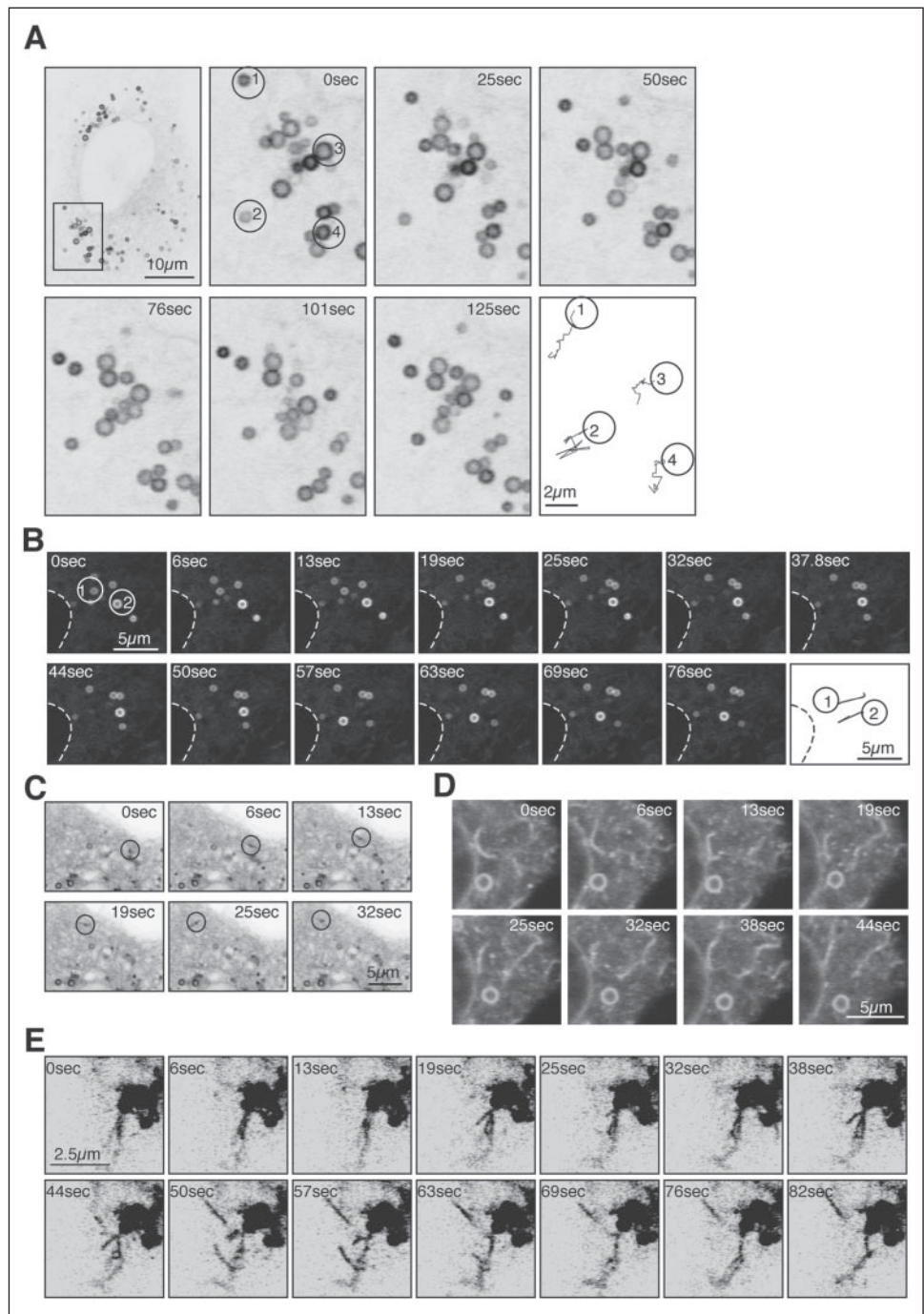


FIGURE 6. Real-time video microscopy of GFP-Rab18 in LDs and the ER. Vero cells expressing GFP-Rab18 were incubated overnight with 100 μ g/ml oleic acid then imaged in real-time in the absence of oleic acid. The motility of GFP-Rab18 was analyzed at \sim 6-s intervals for a total of 3 min. *A* and *B*, GFP-Rab18-labeled LDs were observed to oscillate, in addition to undergoing saltatory motility (see supplementary data, videos 1 and 2). Tracking the motility of individual LD particles demonstrated that, although the majority of movements were small (*A*1, *A*3, and *A*4, $<0.5 \mu$ m), around 6% of LD particles underwent longer ($>2 \mu$ m) vectorial movements (*A*2, *B*1, and *B*2). The rate of vectorial transport was estimated to be $\sim 1 \mu$ m/s. *C*, punctate foci of GFP-Rab18 labeling were observed to undergo rapid movements in the periphery of the cell (see supplementary data, video 3). *D* and *E*, GFP-Rab18 in the ER clearly demonstrated the dynamic nature of the ER membranes throughout the cell and toward the cell surface (*D*) (see supplementary data, videos 4 and 5). In addition, GFP-Rab18-labeled ER elements were seen to extend away from groups of LDs in the perinuclear region of the cell (*E*).

High expression of mRFP-Cav3^{DGV} relative to GFP-Rab18 prevented the localization of GFP-Rab18 to the LD surface and restricted it to the ER (results not shown). Following treatment of co-expressing cells with oleic acid LDs were predominantly labeled by mRFP-Cav3^{DGV}, whereas GFP-Rab18 was restricted to the ER and small puncta (Fig. 7C).

To gain further insights into the association of Rab18 with specific LD populations, we examined LD biogenesis in cells expressing GFP-Rab18 or mRFP-Cav3^{DGV}. Vero cells expressing GFP-Rab18 with or without mRFP-Cav3^{DGV} were serum-starved overnight to reduce the number of existing LDs and incubated in normal medium containing 100 μ g/ml oleic acid for 0–6 h. LDs were identified by staining neutral lipids using Nile Red (with GFP-Rab18) or using Bodipy493/503 (with mRFP-Cav3^{DGV}). Nascent LDs were first detectable within 15–30 min follow-

ing the addition of oleic acid and were clearly identifiable by 1 h. Following serum starvation, GFP-Rab18 was predominantly present in the ER and was first observed associating with LDs between 1 and 3 h after addition of oleic acid, suggesting exclusion from LDs during the earliest time points of biogenesis (Fig. 8A). In contrast, although mRFP-Cav3^{DGV} was also observed in the ER following serum starvation, it was first observed to label LDs within 15 min of initiating biogenesis (results not shown) and was clearly detectable in LDs after 1 h (Fig. 8B). Following co-expression of mRFP-Cav3^{DGV} and GFP-Rab18, the association of mRFP-Cav3^{DGV} with forming LDs was found to be identical to control conditions (Fig. 8C). However, GFP-Rab18 was unable to associate with LDs in the presence of mRFP-Cav3^{DGV} even following 6 h of formation, suggesting that the presence of mRFP-Cav3^{DGV} at the LD surface pre-

Rab18 in Lipid Droplets

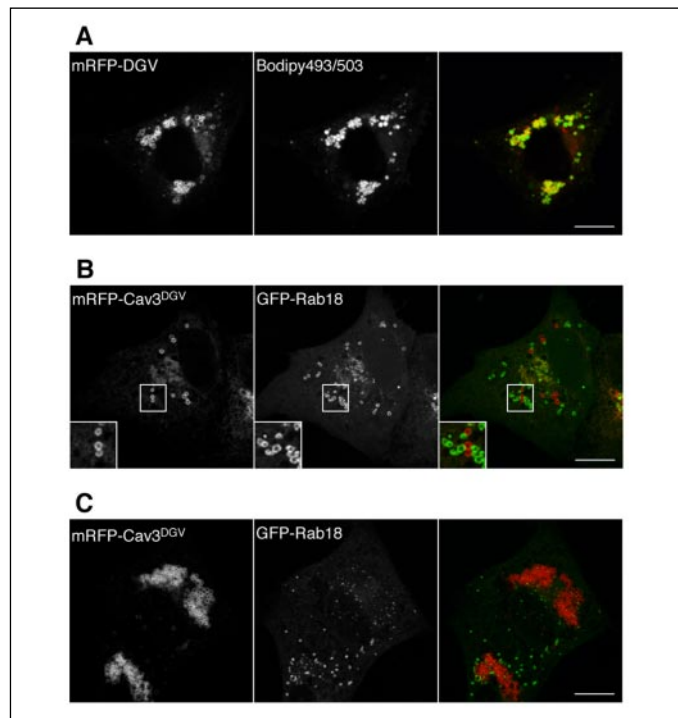


FIGURE 7. GFP-Rab18 and mRFP-Cav3^{DGIV} localize to distinct LD populations. Vero cells were transfected with mRFP-Cav3^{DGIV} in the presence or absence of GFP-Rab18 and incubated in the presence or absence of 100 μ g/ml oleic acid overnight. Cells were subsequently fixed in 4% PFA and analyzed by fluorescent microscopy. *A*, in oleic acid-treated cells mRFP-Cav3^{DGIV} was predominantly localized to large clusters of LDs in the perinuclear region, in addition to low labeling of the ER and in the Golgi area. *B*, in control cells mRFP-Cav3^{DGIV} and GFP-Rab18 were localized to distinct LD populations following co-transfection. *C*, in co-transfected cells treated with oleic acid overnight, mRFP-Cav3^{DGIV} localization was identical to that observed in the absence of GFP-Rab18. In contrast, GFP-Rab18 showed a significantly reduced LD localization and was predominantly localized to the ER, to very small LDs and to small puncta throughout the cells. Scale bars = 10 μ m.

vents the recruitment of GFP-Rab18, either directly or indirectly, and further implying that Rab18 is not required for the biogenesis of LDs.

In conclusion, we have shown that GFP-Rab18 labels a distinct population of LDs and does not associate with LDs labeled by an inhibitory caveolin mutant. Although the caveolin mutant associates with forming “early” LDs, Rab18 associates specifically with “late” LDs. In addition, we have shown that expression of the caveolin mutant prevents the association of Rab18 with the LD surface.

Stimulation of Lipolysis in Adipocytes Causes Translocation of Rab18 to the LD Surface—We hypothesized that the association of Rab18 with distinct LDs in the same cell may reflect a particular functional state of individual LDs. Proteomic analysis of LDs from basal and lipolytically active adipocytes has identified Rab18 as a candidate LD protein only under conditions of lipolysis (11). Therefore, we examined whether the localization of Rab18 was regulated by the metabolic state of the adipocyte. Stimulation of lipolysis by catecholamines occurs via a signaling cascade from the cell surface β -adrenergic receptor through G_{as} activation of adenylate cyclase, up-regulation of cAMP levels resulting in the activation of protein kinase A, and phosphorylation of two proteins involved in the regulation of lipolysis, hormone-sensitive lipase and perilipin (33). Lipolysis can be stimulated by isoproterenol activation of the β -adrenergic receptor, or by elevation of intracellular cAMP levels using forskolin to activate adenylate cyclase. In contrast, isoproterenol stimulation of lipolysis can be inhibited using propranolol, a β -adrenergic antagonist.

Following stimulation of lipolysis in 3T3-L1 adipocytes for 30 min using either 10 μ M isoproterenol or 20 μ M forskolin there was increased

labeling of Rab18 at the surface of LDs detected by immunofluorescence microscopy (Fig. 9A), concomitant with the fragmentation of perilipin-labeled LDs (Ref. 34 and results not shown). In contrast, when lipolysis was stimulated using 10 μ M isoproterenol for 30 min, followed by the addition of 200 μ M propranolol for a further 60 min, the translocation of Rab18 to the LD was completely reversed, suggesting that the association of Rab18 with the LD is tightly associated with the metabolic state of the cell. Quantification of the average pixel intensity of Rab18 immunofluorescence at the LD surface showed a ~2-fold increase in Rab18 labeling (Fig. 9B) in lipolytically active cells compared with cells in normal growth medium, or cells treated with the β -adrenergic antagonist. Three-dimensional rendering of the Rab18 labeling of LDs in lipolytically active cells demonstrated that Rab18 was present over the entire surface of the LD and was found on both large and smaller LDs (Fig. 9C).

Biochemical isolation of LDs showed that Rab18 was associated with this organelle in control cells and that this association increased by ~6-fold following activation of lipolysis (Fig. 9, D and E). Recruitment of Rab18 to the LD fraction occurred concomitant with the slowed mobility of perilipin on SDS-PAGE, consistent with its well characterized hyperphosphorylation in lipolytically active cells (Fig. 9E) (33). From these experiments we conclude that Rab18 is specifically recruited to LDs in lipolytically active cells.

DISCUSSION

Although lipid droplets have been well described in specific cell types such as adipocytes and steroidogenic cells, in recent years it has become clear that a vast variety of cell types have the capacity to synthesize neutral lipids and generate LDs in a regulated and dynamic manner (1). Despite these advances and the obvious importance of understanding the regulation of LD function for diseases such as obesity and diabetes, the molecular mechanisms underlying LD biogenesis, motility, and catabolism are still poorly understood. In the present study we have identified a member of the Rab family of small GTPases, Rab18, which shows a regulated association with the monolayer of the LD.

Rab proteins have been shown to play a leading role as membrane organizers, integrating membrane tethering and fusion with cytoskeleton-dependent motility, through their association with multiple effector proteins (15, 16). Proteomic analyses have identified over 10 different Rab proteins associated with LDs across a range of cell types (11–14). Although it is likely that a number of the Rab proteins identified in LDs are involved in the regulation of LD function, the close physical association shown in this study between LDs and both endosomal compartments and the ER suggests that, in the absence of independent evidence for a direct role, the possibility of contamination of LD preparations with membrane proteins derived from other compartments cannot be overlooked. Further independent analyses of other putative LD Rab proteins will need to be undertaken before a clear picture can emerge of the range and importance of LD interactions with other membrane compartments.

Rab18: A Lipid Droplet-associated Rab Protein—In the present study we have used light microscopy, immunoelectron microscopy, and biochemistry to localize epitope-tagged, heterologously expressed Rab18 to the LD surface. In addition, localization to LDs was confirmed using antibodies raised against the endogenous Rab18 protein. These studies clearly demonstrate that Rab18 associates with a specific subset of LDs in both the 3T3-L1 adipocyte model system and in the non-adipocyte cell lines tested. Our previous Northern blot analyses (18) showed that Rab18 has a ubiquitous expression pattern in mammalian tissues, with particularly high expression in epithelia and brain. In kidney epithelial cells, Rab18 was localized to smooth tubular membranes close to the

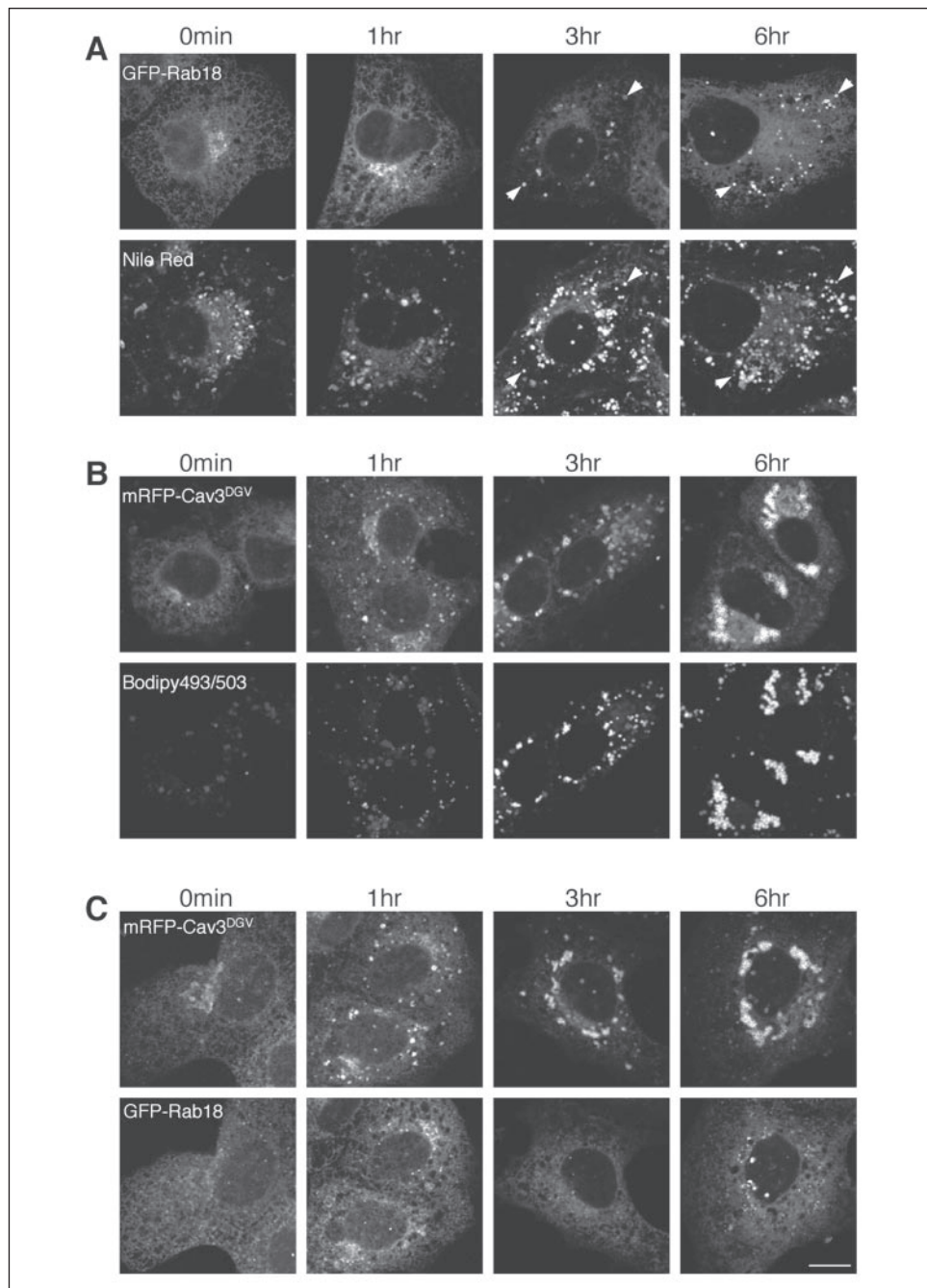


FIGURE 8. mRFP-Cav3^{DGV} localization to forming LDs precedes that of GFP-Rab18. Vero cells were transfected with GFP-Rab18 and mRFP-Cav3^{DGV} either separately or in combination, then incubated in serum-free medium overnight to reduce the number of existing LDs. Cells were subsequently incubated in 100 μ g/ml oleic acid for 0–6 h prior to fixation in 4% PFA. *A*, cells expressing GFP-Rab18 were counterstained using Nile Red to label LDs. There was no detectable labeling of forming LDs at 1 h, but significant labeling of a subset of LDs was detected at 3 h (*arrows*). *B*, cells expressing mRFP-Cav3^{DGV} were counterstained using Bodipy493/503 to label LDs. The localization of mRFP-Cav3^{DGV} to forming LDs was detectable within 1 h. *C*, in cells co-expressing both mRFP-Cav3^{DGV} and GFP-Rab18, localization of mRFP-Cav3^{DGV} to the LD surface was detected within 1 h. In contrast, GFP-Rab18 showed little LD localization during the period of the time course. Scale bar = 10 μ m.

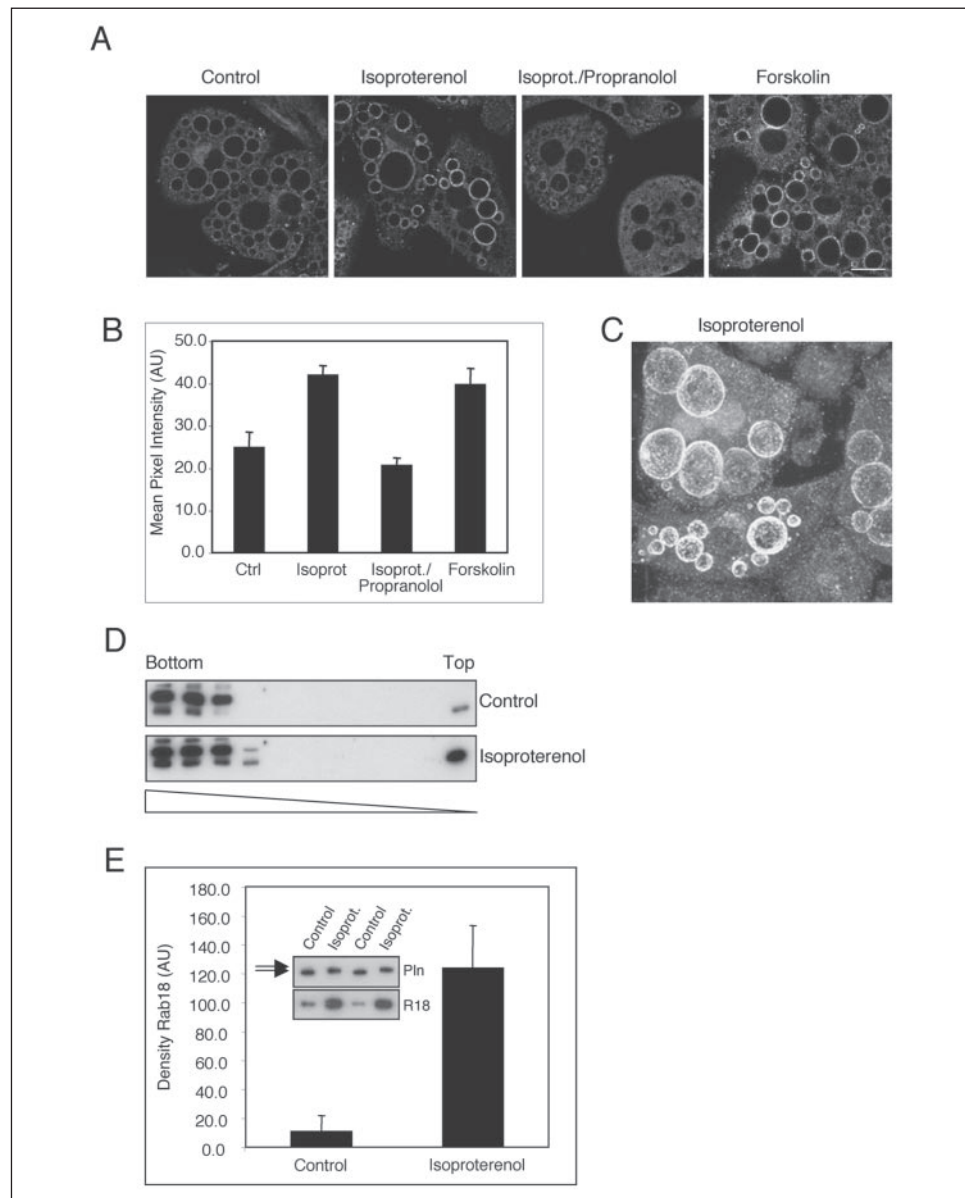
apical cell surface, proposed to be endosomal compartments based on ultrastructural analyses, and was also localized to Rab5-labeled structures upon overexpression as judged by light microscopy (18). In the present study we failed to identify GFP-Rab18 in endosomal structures by light microscopy and the punctate labeling observed for endogenous Rab18 did not coincide with expressed GFP-Rab5.³ However, as shown here, endosomal structures can closely appose (Fig. 1), and even partially enwrap,³ LDs. However, before endosomal localization is dismissed more detailed analysis of Rab18 localization in different tissues is clearly required. Localization of Rab18 to LDs and ER is at least consistent with phylogenetic analysis of mammalian Rab GTPases, in which

Rab18 is more closely related to Rab proteins involved in ER and Golgi trafficking processes, than in endosomal traffic (35).

Rab18 Localizes to the Monolayer Surface of a Subset of LDs—In the present study we have identified GFP-Rab18 at the LD surface and confirmed by electron microscopy that this represents association with the monolayer of the LD. LD localization was seen over a wide range of expression levels and was confirmed by labeling for the endogenous Rab18 protein. Intriguingly, even in cells expressing high levels of Rab18 not all LDs are labeled, and those that are labeled can have extremely high levels of Rab18. This raises interesting questions about the mechanisms involved in targeting Rab18 to the surface of these particular LDs and the molecular determinants dictating Rab18 recruitment to specific LD populations. Analysis of the effectors and other interacting proteins for some of the best understood Rabs have shown that an individual Rab

³ S. Martin and R. Parton, unpublished data.

Rab18 in Lipid Droplets



can be associated with >30 distinct proteins, either directly or indirectly (16). Furthermore, the attachment of Rab proteins to a particular membrane can be mediated not only by protein factors but also by specific phospholipids present in a domain of the membrane. To date, no interacting proteins or lipids have been identified for Rab18.

In addition to labeling of the LD monolayer, we also observed association of heterologously expressed Rab18 with the ER and with discrete clusters of tubulovesicular elements the nature of which has not yet been identified. We hypothesize that these correspond to the rapidly moving punctate structures identified by real-time microscopy. Although ER labeling was not consistently seen with antibodies against the endogenous protein, ER and TVE labeling was very specific when compared with other cellular membranes, and we assume that the lower level of Rab18 in the ER is below the detection of the antibodies. Rab18 is unusual in the Rab family in that the extreme C terminus contains a mono-cysteine prenylation motif rather than the di-cysteine prenylation motifs present in most other Rab family members. Although the reason for this difference is not known, it could be that mono-prenylation is required for Rab18 to associate with the LD monolayer. Previous

studies have shown that mutation of di-cysteine prenylation sites in endosomal Rabs to mono-cysteines results in their mis-localization to the ER (36–38), suggesting the possibility that targeting of GFP-Rab18 to the ER observed in this study could result from the default insertion of a naturally occurring mono-cysteine Rab into the ER in the absence of sufficient numbers of LDs. However, we consider this unlikely to be the case, because, under all experimental conditions used in this study, for both catabolism and LD formation, only a subset of LDs were ever labeled for Rab18 while labeling of the ER was consistently observed. The importance of Rab18 ER targeting and its relationship to lipolysis and LD function are not yet known.

Regulation of Rab18 Recruitment to LDs in Adipocytes upon Lipolysis— In this study we have directly demonstrated recruitment of a Rab protein to LDs in adipocytes in response to lipolytic stimulation. In view of the importance of understanding lipid regulation in the adipocyte to obesity this is a very significant finding. Stimulation of lipolysis in adipocytes has been well characterized (33). The mechanism of Rab18 recruitment is not yet known, but interestingly in control cells the majority of Rab18 was membrane-associated, suggesting that stimulation of lipolysis does not induce direct

recruitment of a cytosolic pool. It will be of fundamental importance to determine whether stimulation of lipolysis in an adipocyte cell line, where lipolysis is regulated through a cell type-specific mechanism, recruits a similar set of Rab18 effectors to lipolysis in non-adipocyte cell lines.

Rab18 and a Caveolin Mutant Label Distinct LD Populations, Which Differ in Metabolic State and Motility—We have previously demonstrated that a caveolin truncation mutant (Cav3^{DGV}) shows constitutive association with LDs (3), perturbs cellular cholesterol balance, inhibits signaling at the cell surface (39), causes neutral lipid accumulation due to inhibition of LD catabolism (8), and completely blocks LD motility. The primary molecular mechanisms underlying the effects of Cav3^{DGV} expression are not yet clear. A striking finding of the present study was the mutually exclusive association of Cav3^{DGV} and Rab18 with LDs. Studies of LD biogenesis illuminated clear differences in the association of Rab18 and Cav3^{DGV}. Cav3^{DGV} associates with the very earliest LDs detectable after oleic acid addition, whereas Rab18 associates with presumably fully formed LDs at much later times. This suggests that Cav3^{DGV} and Rab18 define functionally distinct LD populations. The surface properties of forming LDs are clearly different from those of later LDs. At high expression levels Cav3^{DGV} completely inhibits Rab18 recruitment to LDs. Together with our previous studies our results suggest that inhibition of LD motility by the caveolin mutant has functional consequences on LDs, both in terms of catabolism and maintenance of surface free cholesterol levels but also at the molecular level as judged by Rab18 recruitment. Although we have no evidence to suggest that the primary effect of Cav3^{DGV} is to inhibit Rab18 recruitment, we cannot rule this out.

An intriguing model is that Rab18 regulates motility required for lipid distribution to cellular membranes. LDs have been observed in apposition to many intracellular organelles, including both endosomes and the ER. It is possible that direct apposition of LDs to the limiting membranes of other organelles can facilitate the direct redistribution of lipids in response to cellular requirements. During submission of this analysis, a study describing association of Rab18 with LDs in hepatocytes was published, and a role in ER recruitment around LDs was proposed (40). In a series of experiments undertaken using both dominant-negative mutants of Rab18 and Rab18 siRNA, we have been unable to definitively identify changes in LD formation or catabolism (results not shown). We believe that this reflects the complexity of LD regulation and/or function, of which very little is currently known, as well as the fact that Rab18 associates with a distinct lipid droplet population and consequently we may not see an effect on the entire LD population. However, the characterization of a Rab protein associated with LDs provides an important new system to understand machinery involved in LD function and the role of this fascinating organelle in cellular function.

Acknowledgments—We thank Prof. John Hancock for the provision of antibodies, Prof. Roger Tsien for providing the pRSET-mRFP construct, Dr. Lucas Pelkmans for providing the pEGFP-Rab7 construct, and Dr. Richard Newton for the gift of forskolin. We also thank Annika Stark and Samantha Murphy for technical assistance, Matthew Kirkham for critical reading of the manuscript, and John Presley for discussion of his observations prior to publication.

REFERENCES

- Martin, S., and Parton, R. G. (2005) *Semin. Cell Dev. Biol.* **16**, 163–174
- Murphy, D. J. (2001) *Prog. Lipid Res.* **40**, 325–438
- Pol, A., Martin, S., Fernandez, M. A., Ferguson, C., Carozzi, A., Luetterforst, R., Enrich, C., and Parton, R. G. (2004) *Mol. Biol. Cell* **15**, 99–110
- Targett-Adams, P., Chambers, D., Gledhill, S., Hope, R. G., Coy, J. F., Girod, A., and McLauchlan, J. (2003) *J. Biol. Chem.* **278**, 15998–16007
- Valetti, C., Wetzel, D. M., Schrader, M., Hasbani, M. J., Gill, S. R., Kreis, T. E., and Schroer, T. A. (1999) *Mol. Biol. Cell* **10**, 4107–4120
- Blanchette-Mackie, E. J., Dwyer, N. K., Barber, T., Coxey, R. A., Takeda, T., Rondinone, C. M., Theodorakis, J. L., Greenberg, A. S., and Londos, C. (1995) *J. Lipid Res.* **36**, 1211–1226
- Vock, R., Hoppele, H., Claassen, H., Wu, D. X., Billeter, R., Weber, J. M., Taylor, C. R., and Weibel, E. R. (1996) *J. Exp. Biol.* **199**, 1689–1697
- Pol, A., Luetterforst, R., Lindsay, M., Heino, S., Ikonen, E., and Parton, R. G. (2001) *J. Cell Biol.* **152**, 1057–1070
- Murata, M., Peranen, J., Schreiner, R., Wieland, F., Kurzhalia, T. V., and Simons, K. (1995) *Proc. Natl. Acad. Sci. U. S. A.* **92**, 10339–10343
- Trigatti, B. L., Anderson, R. G., and Gerber, G. E. (1999) *Biochem. Biophys. Res. Commun.* **255**, 34–39
- Brasaemle, D. L., Dolios, G., Shapiro, L., and Wang, R. (2004) *J. Biol. Chem.* **279**, 46835–46842
- Liu, P., Ying, Y., Zhao, Y., Mundy, D. I., Zhu, M., and Anderson, R. G. (2004) *J. Biol. Chem.* **279**, 3787–3792
- Fujimoto, Y., Itabe, H., Sakai, J., Makita, M., Noda, J., Mori, M., Higashi, Y., Kojima, S., and Takano, T. (2004) *Biochim. Biophys. Acta* **1644**, 47–59
- Umlauf, E., Csaszar, E., Moertelmaier, M., Schuetz, G. J., Parton, R. G., and Prohaska, R. (2004) *J. Biol. Chem.* **279**, 23699–23709
- Seabra, M. C., and Wasmeier, C. (2004) *Curr. Opin. Cell Biol.* **16**, 451–457
- Zerial, M., and McBride, H. (2001) *Nat. Rev. Mol. Cell Biol.* **2**, 107–117
- Shewan, A. M., Marsh, B. J., Melvin, D. R., Martin, S., Gould, G. W., and James, D. E. (2000) *Biochem. J.* **350**, 99–107
- Lutcke, A., Parton, R. G., Murphy, C., Olkkonen, V. M., Dupree, P., Valencia, A., Simons, K., and Zerial, M. (1994) *J. Cell Sci.* **107**, 3437–3448
- Prior, I. A., Harding, A., Yan, J., Sluimer, J., Parton, R. G., and Hancock, J. F. (2001) *Nat. Cell Biol.* **3**, 368–375
- Sonnichsen, B., De Renzis, S., Nielsen, E., Rietdorf, J., and Zerial, M. (2000) *J. Cell Biol.* **149**, 901–914
- Luetterforst, R., Stang, E., Zorzi, N., Carozzi, A., Way, M., and Parton, R. G. (1999) *J. Cell Biol.* **145**, 1443–1459
- Campbell, R. E., Tour, O., Palmer, A. E., Steinbach, P. A., Baird, G. S., Zacharias, D. A., and Tsien, R. Y. (2002) *Proc. Natl. Acad. Sci. U. S. A.* **99**, 7877–7882
- Yu, W., Cassara, J., and Weller, P. F. (2000) *Blood* **95**, 1078–1085
- Morrow, I. C., Rea, S., Martin, S., Prior, I. A., Prohaska, R., Hancock, J. F., James, D. E., and Parton, R. G. (2002) *J. Biol. Chem.* **277**, 48834–48841
- Martin, S., Tellam, J., Livingstone, C., Slot, J. W., Gould, G. W., and James, D. E. (1996) *J. Cell Biol.* **134**, 625–635
- Martin, S., Ramm, G., Lytle, C. T., Meerloo, T., Stoervogel, W., and James, D. E. (2000) *Traffic* **1**, 652–660
- Martin, S., Rice, J. E., Gould, G. W., Keller, S. R., Slot, J. W., and James, D. E. (1997) *J. Cell Sci.* **110**, 2281–2291
- Tokuyasu, K. T. (1980) *Histochem. J.* **12**, 381–403
- Liou, W., Geuze, H. J., and Slot, J. W. (1996) *Histochem. Cell Biol.* **106**, 41–58
- Bucci, C., Thomsen, P., Nicoziani, P., McCarthy, J., and van Deurs, B. (2000) *Mol. Biol. Cell* **11**, 467–480
- Chavrier, P., Parton, R. G., Hauri, H. P., Simons, K., and Zerial, M. (1990) *Cell* **62**, 317–329
- Roberts, R. L., Barbieri, M. A., Pryse, K. M., Chua, M., Morisaki, J. H., and Stahl, P. D. (1999) *J. Cell Sci.* **112**, 3667–3675
- Tansey, J. T., Szaltryd, C., Hlavín, E. M., Kimmel, A. R., and Londos, C. (2004) *IUBMB Life* **56**, 379–385
- Londos, C., Brasaeimle, D. L., Schultz, C. J., Adler-Wailes, D. C., Levin, D. M., Kimmel, A. R., and Rondinone, C. M. (1999) *Ann. N. Y. Acad. Sci.* **892**, 155–168
- Pereira-Leal, J. B., and Seabra, M. C. (2000) *J. Mol. Biol.* **301**, 1077–1087
- Calero, M., Chen, C. Z., Zhu, W., Winand, N., Havas, K. A., Gilbert, P. M., Burd, C. G., and Collins, R. N. (2003) *Mol. Biol. Cell* **14**, 1852–1867
- Gomes, A. Q., Ali, B. R., Ramalho, J. S., Godfrey, R. F., Barral, D. C., Hume, A. N., and Seabra, M. C. (2003) *Mol. Biol. Cell* **14**, 1882–1899
- Overmeyer, J. H., Wilson, A. L., and Maltese, W. A. (2001) *J. Biol. Chem.* **276**, 20379–20386
- Roy, S., Luetterforst, R., Harding, A., Apolloni, A., Etheridge, M., Stang, E., Rolls, B., Hancock, J. F., and Parton, R. G. (1999) *Nat. Cell Biol.* **1**, 98–105
- Ozeki, S., Cheng, J., Tauchi-Sato, K., Hatano, N., Taniguchi, H., and Fujimoto, T. (2005) *J. Cell Sci.* **118**, 2601–2611

Regulated Localization of Rab18 to Lipid Droplets: EFFECTS OF LIPOLYTIC STIMULATION AND INHIBITION OF LIPID DROPLET CATABOLISM
Sally Martin, Kim Driessen, Susan J. Nixon, Marino Zerial and Robert G. Parton

J. Biol. Chem. 2005, 280:42325-42335.
doi: 10.1074/jbc.M506651200 originally published online October 5, 2005

Access the most updated version of this article at doi: [10.1074/jbc.M506651200](https://doi.org/10.1074/jbc.M506651200)

Alerts:

- [When this article is cited](#)
- [When a correction for this article is posted](#)

[Click here](#) to choose from all of JBC's e-mail alerts

Supplemental material:

<http://www.jbc.org/content/suppl/2005/12/19/M506651200.DC1>

This article cites 39 references, 24 of which can be accessed free at
<http://www.jbc.org/content/280/51/42325.full.html#ref-list-1>



The role of Rab GTPase in Plant development and stress

Yao Lu^a, Ke Cheng^a, Hui Tang^a, Jinyan Li^a, Chunjiao Zhang^{b, **}, Hongliang Zhu^{a,*}

^a The College of Food Science and Nutritional Engineering, China Agricultural University, Beijing, 100083, China

^b Supervision, Inspection & Testing Center of Agricultural Products Quality, Ministry of Agriculture and Rural Affairs, Beijing, 100083, China



ARTICLE INFO

Keywords:
Rab-GTPase
Membrane trafficking
Tip growth
Environmental stress
Fruit ripening

ABSTRACT

Small GTPase is a type of crucial regulator in eukaryotes. It acts as a molecular switch by binding with GTP and GDP in cytoplasm, affecting various cellular processes. Small GTPase were divided into five subfamilies based on sequence, structure and function: Ras, Rho, Rab, Arf/Sar and Ran, with Rab being the largest subfamily. Members of the Rab subfamily play an important role in regulating complex vesicle transport and microtubule system activity. Plant cells are composed of various membrane-bound organelles, and vesicle trafficking is fundamental to the existence of plants. At present, the function of some Rab members, such as RabA1a, RabD2b/c and RabF2, has been well characterized in plants. This review summarizes the role of Rab GTPase in regulating plant tip growth, morphogenesis, fruit ripening and stress response, and briefly describes the regulatory mechanisms involved. It provides a reference for further alleviating environmental stress, improving plant resistance and even improving fruit quality.

1. Introduction

Rab (Ras-like protein) is the largest subfamily of small GTPases. It can circulate between the GTP-bound active and GDP-bound inactive states in cytoplasm. These proteins are composed of approximately 200 amino acids (with 30–55% similarity) and have five conserved domains that can be divided into (1) guanine nucleotide-binding domains: G1, G3, G4 and G5; (2) effector binding domains: G2; and (3) membrane attachment domain: C-residues (Tripathy et al., 2021) (Fig. 1A) (Rutherford and Moore, 2002). In *Arabidopsis*, Rab GTPases are categorized into eight branches, namely RabD, RabB, RabF, RabH, RabG, RabE, RabA and RabC, which correspond to eight subfamilies in animals: Rab1, Rab2, Rab5, Rab6, Rab7, Rab8, Rab11 and Rab18. Among these, 26 Rabs belong to the AtRabA subclass, and the ARA6/RabF1 (Rab5) and RabA (Rab11) group possesses plant-specific features (Ebine et al., 2011). Studies have found that different Rab GTPases are localized to distinct organelles. In eukaryotes, Rab GTPases are specifically recruited to the cytosolic surface of intracellular membranes in a temporally controlled manner, and the C-terminal cysteine residues are

generally key for their association with membranes. Meanwhile, the mechanism of Rab GTPase-specific localization seems to be determined by the complex interaction of multiple factors, such as regulatory proteins, including guanine nucleotide exchange factor (GEF) and GTP enzyme activating protein (GAP) (Stenmark, 2009).

Rab GTPases function as molecular switches and are master regulators for intracellular vesicle trafficking. Plant cells are composed of many intracellular membrane structures, including Golgi apparatus, endoplasmic reticulum (ER), vacuole, trans-Golgi network/early endosome (TGN/EE) and multivesicular endosome (MVE). Vesicle transport is the fundamental system for protein, lipid and endogenous ion transport between organelles and plasma membranes. A single vesicle transport between donor and target organelle can be divided into four sequential processes: (1) vesicle formation starting from donor membrane, (2) vesicle motility, (3) vesicle binding with target membrane, and (4) vesicle tethering to acceptor membranes. Rab GTPase controls all aspects of intracellular vesicle trafficking by recruiting effector molecules in their active GTP-bound form (Fig. 2). One significant feature of Rab GTPase is the different intracellular localization patterns of the different members. For instance, AtRab5e (a member of AtRabA), located in the stroma and thylakoids (chloroplasts), participates in regulating the size, height and vesicle formation of plastid beads

* Corresponding author.

** Corresponding author.

E-mail addresses: b20213060520@cau.edu.cn (Y. Lu), bs20223060553@cau.edu.cn (K. Cheng), s20213060979@cau.edu.cn (H. Tang), sy20193061114@cau.edu.cn (J. Li), cccc15809181@163.com (C. Zhang), hlzhu@cau.edu.cn (H. Zhu).

through interaction with its effectors (Karim et al., 2014). However, its homologous protein AtRab5c locates in the new compartment of young lateral roots (named geometric edges), regulating the cell geometry in the developing lateral organs by independently interfering with growth anisotropy and cytokinesis (Kirchhelle et al., 2016). Another characteristic of Rab GTPase is its redundancy. By changing the affinity of Rab GTPase for nucleotides, conservative activated mutants that bind to GTP and dominant-negative mutants that bind to GDP were formed to further explore the molecular function of Rab (Stenmark, 2009; Cai et al., 2015).

In fact, Rab GTPase typically interacts with specific regulators to fulfill its function. Rab effectors come in many forms and range from vesicle tethers to motors, kinases, phosphatases and various adaptor proteins (Sakurai et al., 2016). During vesicle transport, Rab GTPase is activated by GEFs and then inactivated by GAPs. This process is regulated by multiple factors. Firstly, GEFs can recognize specific residues in the switch regions and facilitate GDP release (Delprato et al., 2004). The high concentration of GTP (~1 mM) in the cytoplasm causes Rab to immediately bind to GTP once dissociated from GDP, resulting in the active form of GTPases. At present, some GEFs in plants have been identified and characterized, such as SAND/MON1-CCZ1 (Cui et al., 2014), Transport Protein Particle II (Kalde et al., 2019), monensin sensitivity 1 (MON1, Cui et al., 2014), calcium caffeine zinc sensitivity 1a (Pan et al., 2021) and VPS9a (Goh et al., 2007). However, compared with animals and yeast, most GEFs in plants are unidentified. Secondly, GDP dissociation inhibitors (GDIs) give an extra level of control of Rab GTPases. The GTPase activity of Rab is inherently low, and the effective hydrolysis of GTP requires the stimulation of GAP (Rittinger et al., 1997). Once GTP is hydrolyzed, the GDP-bound form of Rab will bind to GDIs, allowing it to dissociate from the membrane and return to the cytosol. Some RabGDIs have been reported to function in abiotic stress tolerance and (SchRabGDI1, OsGDI1, RabGDI α) and fruit ripening (MiRab-GDI) processes (Liu et al., 2015). In addition, ubiquitination also can mediate Rab GTPase activation in animals. For example, the ubiquitin ligase-HACE1 can activate Rab11a by triggering ubiquitination of Rab11a-Lys145, thus promoting the recycle of the β 2-adrenergic receptor (Lachance et al., 2014). Furthermore, adenylylation and phosphocholination represent additional mechanisms for controlling Rab

activity. Research has shown that these process can modify the affinity of Rab:GDI, causing effective displacement of Rabs from GDI (Oesterlin et al., 2012). However, whether Rab GTPase in plants undergoes these modifications is worth further investigation.

Compared with animals, higher plants appear to have followed a different evolutionary pathway from animal or fungal Rabs (Minamino and Ueda, 2019). Although our knowledge of Rab GTPase functions in plants is not as rich as in mammalian cells, significant progress has been made as demonstrated in the past two years. Studies using reverse genetic methods, mostly, but not entirely, by blocking the action of Rab GTPase, have revealed the central importance of Rab GTPase in plant life, whether in highly polarized cells, such as root hairs and pollen tubes, or in fruit ripening processes. Here, we provide a comprehensive overview of the role of Rab GTPase in plants.

2. Tip growth control

2.1. Pollen tube growth

Pollen tubes and root hairs exhibit characteristic polar cell expansion, commonly referred to as tip growth. During the reproductive process of flowering plants, pollen grains form a tube that grows through female tissue in a polarized manner, ultimately fertilizing the egg cells (Rounds and Bezanilla, 2013). This process is supported by the dynamic remodeling of the actin cytoskeleton and concentrated delivery of membrane, cell wall components and lipids (Cai et al., 2015; Li et al., 2021). Several reports have unveiled the important role of Rab GTPases in plant polarization and cellular morphogenesis (Table 1).

During plant tip growth, polarized delivery of secretory vesicles is the rate-limiting step, and depends on the fine regulation of molecular motor myosin XI and endomembrane properties (Vidali et al., 2010). Excitingly, studies have shown that Rab GTPase is an important factor connecting the plant endomembrane system and cytoskeleton (Orr et al., 2021). The RabE subfamily, the homolog of Sec4/Rab8, is involvement in anterograde transport to the plasma membrane from the Golgi, and is a general requirement for plant growth and cell division (Zheng et al., 2005). It localizes to sites of polarized secretion and co-localizes with

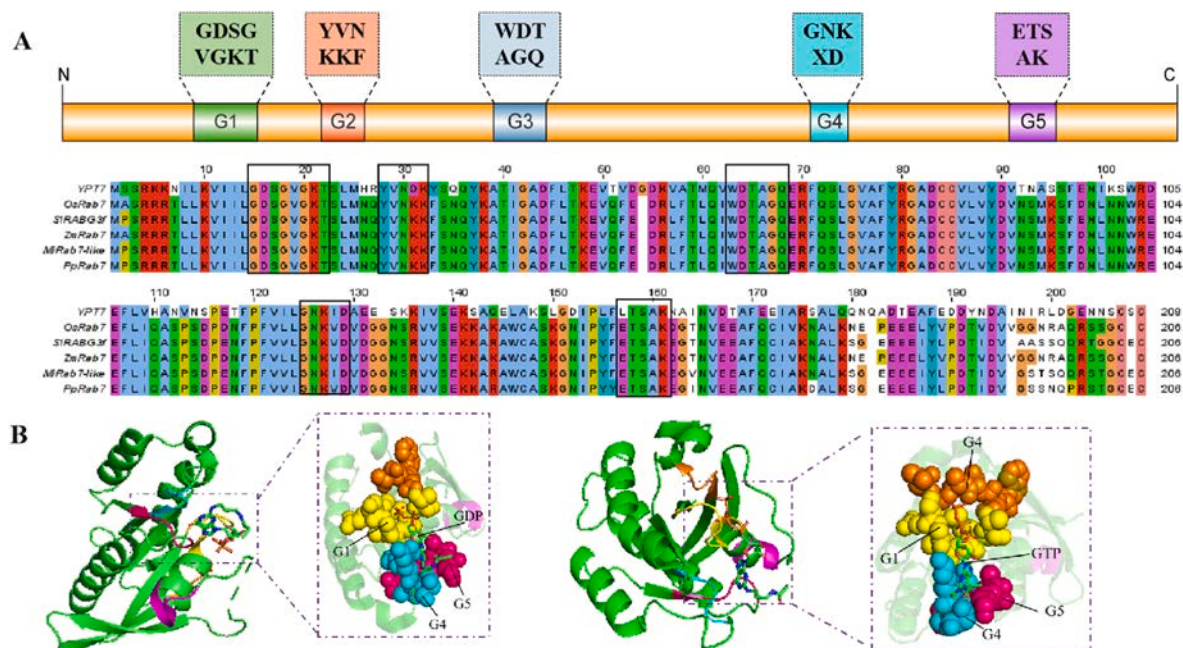


Fig. 1. Structure of Rab GTPase proteins. A: consensus amino acid sequences responsible for specific interaction with GDP/GTP and for GTPase activity. G1, G3, G4 and G5: guanine nucleotide-binding domains; G2: effector binding domains. B: spatial structure of Rab protein (from PDB database, Ypt); Left: the spatial structure of Rab combined with GDP; Right: the spatial structure of Rab combined with GTP.

myosin XI. Yeast two-hybrid assay uncovered a specific interaction between RabE and myosin XI, and the disrupt of this interaction results in a loss of polarized growth. This study provides a mechanistic link between RabE and polarized growth through an interaction with the molecular motor myosin XI (Orr et al., 2021).

Growing pollen tubes contain dynamic tubular vacuoles, and vacuolar biogenesis relies on vacuolar trafficking (Hicks et al., 2004). Hao et al. recently found that RabF/Rab5 can regulate the growth process of pollen tubes passing through the style by mediating vacuolar transport and affecting the homeostasis of the plasma membrane (Hao et al., 2023). In Arabidopsis, the genome encodes three RabF/Rab5 proteins, two canonical RHA1/RAB5F2a and ARA7/Rab5F2b, and a plant-unique ARA6/Rab5F1. Functional loss of canonical Rab5s compromises vacuolar trafficking of tonoplast proteins, vacuolar biogenesis and turgor regulation, and the functional loss of RHA1/RAB5F2a and ARA7/Rab5F2b in Arabidopsis compromises endocytic and secretory trafficking at the plasma membrane (PM), causing the enhanced deposition of cellulose or polysaccharides, cytosolic acidification and failure of pollen tubes to grow through style and thus impairing male transmission (Hao et al., 2023). RabG3f/Rab7, which localize to prevacuolar compartments (PVCs) and tonoplast, also play an important role in pollen tube growth by mediating the fusion between PVC and vacuoles (Cui et al., 2014). In Arabidopsis, the MON1-CCZ1 complex is recruited to the PVCs by active ARA7/RabF/Rab5 protein and then serves as a GEF complex activating RabG3f/Rab7. Dominant-negative RabG3f/Rab7 mutations show that its function is crucial for maintaining the tapeta programmed cell death, thereby ensuring the successful germination of pollen and the subsequent growth of pollen tubes (Brillada et al., 2018).

In addition, there are also some Rab GTPases that play important roles in pollen growth and for which the transport pathways they regulate is unknown. For example, RabA4d from Arabidopsis is the only member of RabA4 subfamily to be expressed in pollen. It interacts with PI4K β 1 to maintain the direction and rate of pollen tube growth

(Antignani et al., 2015). Loss of RabA4d function resulted in the formation of bulges in pollen tubes with a reduced rate of growth, displaying altered deposition and/or modification of pectin (Szumlanski and Nielsen, 2009), and adenosine triphosphate 3 (ALA3), the effector of RabA4d, can regulate the specific distribution of RabA4d in pollen tubes by establishing potential phospholipid signaling through the formation of phosphatidylserine. The loss of ALA3 function leads to the mislocalization of RabA4d at the top of pollen tubes, resulting in a substantial increase in pollen tube width (Zhou et al., 2020). In Arabidopsis, the RabD subfamily has four members, AtRabD1, AtRabD2a, AtRabD2b and AtRabD2c. Among them, AtRabD2b and AtRabD2c are highly expressed in pollen, and their RNA accumulation levels are negatively correlated with the process of starch synthesis (Wang et al., 2012). *Arabidopsis* double-mutant plants displayed a short siliques and have many non-fertilized ovaries phenotypes because of the collapsed pollen, shorter pollen tubes and swollen tips. However, it has not been confirmed whether AtRabD2b and AtRabD2c located in Golgi play a role in vesicular transport between the endoplasmic reticulum to the Golgi (Peng et al., 2011).

2.2. Root hair growth

Root hairs are formed by root epidermal cells. Their development is divided into four stages: cell fate specification, initiation, tip growth and maturation (Gilroy and Jones, 2000). These processes involve a balance between the directed delivery of proteins and cell wall building blocks from post-Golgi compartments to the cell apex, as well as the loosening of local cell walls and the retrieval of surplus membranes (Chin et al., 2021).

The function of Rab in root hair growth has been confirmed (Table 1). AtRabA4b shares the similarity sequence with MtRab11G and Pra3, specifically located at the tips of growing root hair cells and disappearing in mature root hair cells. Tip-localized RabA4b compartments

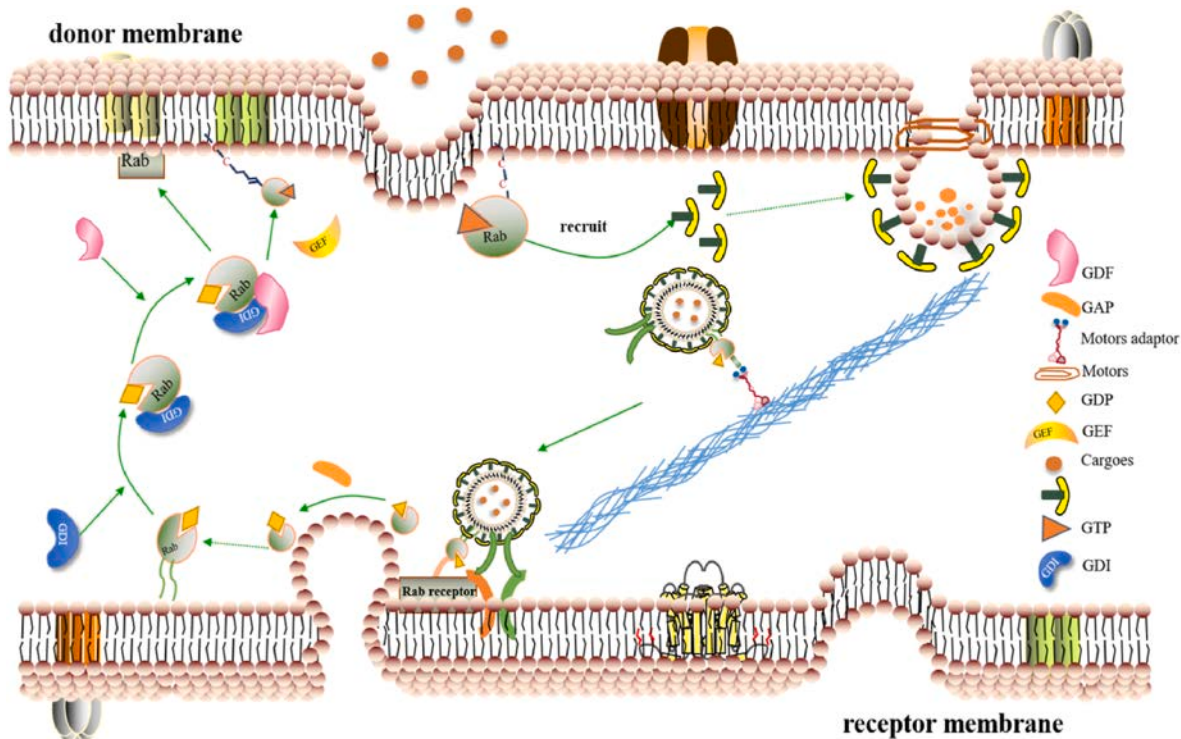


Fig. 2. Schematic representation of Rab-dependent trafficking pathways. Active GTP-bound Rab can recruit a sorting adaptor to sort a receptor into a budding vesicle, then active Rab GTPases can mediate vesicle transport along actin filaments or microtubules (collectively referred to as cytoskeletal tracts) by interaction with motors; Rab GTPases can mediate vesicle tethering by interact with tethering factors. After membrane fusion/exocytosis, GAP catalyzes the hydrolysis of GTP to GDP, and guanine nucleotide exchange factor (GEF) converts GDP-bound Rab into the GTP-bound form.

Table 1

Rab GTPase and its effectors involved in regulating various plant life activities.

	Rab GTPases	Location	Effector	Function	Species	References
Pollen tube tip growth	RabA4d	pollen tubes tips	PI4K β 1、ALA3	Changing the components of cell wall deposition	Arabidopsis	Szumlanski and Nielsen (2009); Zhou et al. (2020)
	AtRabD1	pollen tubes tips		Positively regulates autophagosome biogenesis	Arabidopsis	Wang et al. (2012); Peng et al., 2011
	AtRabD2a	pollen tubes tips		Positively regulates autophagosome biogenesis	Arabidopsis	Wang et al. (2012); Peng et al., 2011
	AtRabD2b	Golgi		Affects starch synthesis	Arabidopsis	Wang et al. (2012); Peng et al., 2011
	AtRabD2c	Golgi		Affects starch synthesis	Arabidopsis	Wang et al. (2012); Peng et al., 2011
	PpRabE14 ARA6/RabF1	sites of polarized secretion punctate organelles	pMyoXI、AtMyoXI-K VPS9a、PLANT-UNIQUE RAB5 EFFECTOR 2 (PUP2)	Support plant growth and development Maintain the endocytosis and secretion transport of the plasma membrane		Hao et al. (2023)
	ARA7/RabF2b	punctate organelles	VPS9a、CORVET、HOPS	Critical for proton homeostasis that influences the dynamic organization of actin MFs and membrane homeostasis at the PM.		Hao et al. (2023)
Root hair tip growth	RabG3f/Rab7	prevacuolar compartments (PVCs) and tonoplas vesicles appearing from TGN and this Rab GTPase	MON1-CCZ1、CORVET、HOPS	Mediate the fusion between PVC and vacuoles		Brillada et al. (2018)
	RabA4b	Root Hairs	PI4K β 1、PI4K β 2ALA3	Regulate the transport of polarized membranes in root hair cells	<i>Phaseolus vulgaris</i>	Kang et al. (2011)
	RabA2			Required for the rhizobial-activated signal transduction pathways	<i>Phaseolus vulgaris</i>	Blanco et al. (2009)
Shape of plant organs	NbRabE1	young tissues containing actively dividing cells and in stomata guard cells		Function in stomata guard cell division	<i>Nicotiana benthamiana</i>	Ahn et al. (2013)
	RabA5c	membrane vesicles lying immediately beneath the plasma membrane at cell edges		Meets a requirement to specify this cellular spatial domain during organogenesis	Arabidopsis	Kirchhelle et al. (2016)
	RabC1	young stomata	SEIPIN2、SEIPIN3	Required to regulate lipid droplet dynamics and lipid metabolism	Arabidopsis	Ge et al. (2022)
	RabE1d	Golgi apparatus and plasma membrane of mesophyll cells	PIP5K2	Play a fundamental role in the secretion of extracellular matrix molecules	Arabidopsis	Speth et al. (2009)
Biotic stress respond	RabH1b	Golgi		Maintain Golgi morphology and modulating the trafficking of cellulose synthase complexes from endosomal compartments to plasma membrane	Arabidopsis	McFarlane et al. (2014)
	PvRabA2	root nodule		Function in the biogenesis of the peribacteroid membrane		Cheon et al. (1993)
	Rab11f	in the nodules of <i>Medicago sativa</i>		Function in the biogenesis of the peribacteroid membrane	<i>Medicago sativa</i>	Schiene et al. (2004)
	RabG3b	stomatal	NETWORKED	Involved in FLS2 triggered guard cell actin reorganization	Arabidopsis	Hawkins et al. (2023)
	PagRabE1b			Positively regulates autophagosome biogenesis	Poplar	Liu et al. (2021)
	OsRabA/OsRab11	widely expressed in plants	OsGAP1、OsGDI3 和 OsOPR8	Regulate vesicular transport from the TGN to the PM or vacuole	<i>Oryza sativa</i>	Li et al. (2011); Hong et al. (2013)
	RabA4c	plasma membrane	PMR4 (callose synthase)	Regulate the biosynthesis of the callose and enhances the deposition of callose	Arabidopsis	Ellinger et al. (2014)
Abiotic stress respond	AtRabG3e	induced during programmed cell death in leaves		Increase tolerance to salt and osmotic stresses	Arabidopsis	Mazel et al. (2004)
	ARA6/RabF1 RabA1a, RabA1b, RabA1c, RabA1d AhRabG, OsRabG/ OsRab7 and OsRabA/OsRab11	endosomes		Salinity stress response Required for salinity stress tolerance	Arabidopsis	Ebine et al. (2011) Asaoka et al. (2013)
	PtRabE1b	Root		Responsive to abiotic stresses	Rice	Sui et al. (2017); Chen and Heo. (2018)
	RabA2b	plasma membrane		Maintain great root growth status under salt stress Improve drought resistance	Arabidopsis	Zhang et al. (2018)
	RabE1c	in guard cells	Pyrabactin Resistance1-like protein (PYL)	Acting as a positive regulator in ABA signaling and drought stress response	Arabidopsis	Ambastha et al. (2021)
	CaRabC	leaves		Response to salinity stresses	Chickpea	Zhao et al. (2008)
	ZmRabD1 and ZmRabD2c	Endoplasmic reticulum	Prenylated Rab Receptor 1, ZmPRA1, C1	Response to heat stress	Maize	Khassanova et al. (2019) Xie et al. (2022)

(continued on next page)

Table 1 (continued)

	Rab GTPases	Location	Effector	Function	Species	References
Fruit softening process	RabE1b	plastids		Crucial for protein translation	Arabidopsis	Li et al. (2018)
	SlRabA11a	fruit		Regulate fruits softening process	Tomato	Lu et al., 2001
	RabA3 and RabA4	fruit		Regulate fruits softening process	Mangoes	Lawson et al. (2020)
	VvRabA	fruit		Regulate fruits softening process	Vitis vinifera	Abbal et al. (2008)
	PpRABA1-, PpRABA2, PpRABD2-1, PpRABD2-2, and PpRABC2	fruit		Regulate fruits softening process	Peach	Falchi et al. (2010)

are dependent on the integrity of the F-actin cytoskeleton (Preuss et al., 2004). Further exploration found that RabA4b is localized in the vesicles appearing from TGN and that this Rab GTPase plays an important role in regulating the transport of polarized membranes in root hair cells (Kang et al., 2011). As part of this regulation, AtRabA4b exhibits the ability to recruit lipid kinases PI4K β 1 and PI4K β 2, and these proteins coordinate to regulate polarized expansion in root hairs. When the polarization position of AtRab4b changes or is absent, it can lead to deficiencies in the delivery of cell wall molecules to the cell wall, as demonstrated by the root hair development mutants *rhd1-1*, *rhd2-1* and *rhd3-1* (Preuss et al., 2004).

Similarly, RabA2 in *Phaseolus vulgaris* has also been associated with root hair development. A reverse genetic approach revealed that silencing RabA2 leads to a decrease in the number and length of root hairs, without affecting the directionality of growth (Blanco et al., 2009). RabA2 also functions in nodule organogenesis. It is required for the rhizobial-activated signal transduction pathways that lead to the induction of gene expression in the root (Blanco et al., 2009). Interestingly, the role of plant RabA family members is not limited to tip-targeted cell wall deposition, but also related to cytokinesis (Berson et al., 2014). RabA1d localizes in the trans-Golgi network and early endosomal compartments, and it accumulates on the growing cell plates during cytokinesis (Shi et al., 2023). The expansion of cell plate is largely supported by the mechanism of secretion and endocytosis. At the initial stage of cell plate formation, RabA1d forms a disc-like structure on the equatorial plane, exhibiting a steady increase in fluorescence intensity. This observation strongly suggests that RabA1d regulates the delivery of goods and membranes from early endosomes/TGN to the cell plate during cytokinesis.

Another Rab associated with root hair in *N. benthamiana* is NbRabE1 (a new RabE isoform), which mainly expresses in young tissues containing actively dividing cells and in stomata guard cells. The ectopic expression of dominant-negative NbRabE1 in Arabidopsis yields a pleiotropic phenotype, including a delayed growth rate of both shoot and root, accompanied by defective root hair formation. Dysfunction of NbRabE1 may hinder the transport and local release of polarized membrane materials and membranes, thereby interfering with the protection of cell cytoplasmic division and root hair development, leading to defects in cell plate assembly and polarized cell expansion (Ahn et al., 2013).

3. Control of the shape of plant organs

The morphogenesis of plant cells depends on the coordinated control of cell division planes and the differential growth of polyhedral cells on distinct surfaces (Uyttewaal et al., 2012). Some studies have found that cytoskeleton plays a pivotal role in cell morphogenesis, and its dynamic behavior is regulated by Rab GTPases. In mammals, Rab8 and Rab14 have a strong influence on cell morphogenesis by reorganizing actin-/microtubules, as well as regulating the process of microtubule acetylation (Peranen, 2011). However, this regulatory approach has not been reported in plants. In addition to cytoskeleton, membrane organization also plays an important role in shaping plant cells.

During the process of organogenesis in Arabidopsis, the

endomembrane system involves an important cellular spatial domain—geometric edge located directly below the plasma membrane at the cell edge, and the formation of this domain depends on RabA5c. The pattern of RabA5c accumulation at the cell edges presents in young lateral roots and young leaf primordia, and is lost in older cells. Inhibition of RabA5c activity causes radial swelling and a loss of tensile strength in growing cell walls, resulting in the gradual development of severely disordered cell shapes in the lateral roots of germinated seeds (Kirchhelle et al., 2016). RabA5c thus meets a requirement to specify this cellular spatial domain during organogenesis. In addition, recent reports also provide some insight on RabC1, the counterpart of mammalian Rab18, in the regulation of stomatal morphogenesis. RabC1 is highly expressed in young stomata and has been identified as a key regulatory factor required to regulate lipid droplet dynamics and lipid metabolism. Subcellular localization and Co-IP analyses indicate that activated RabC1 is targeted to the surface of lipid droplets, where it interacts with ER-localized SEIPIN2 and SEIPIN3, thereby regulating lipid droplet mobilization and ensuring the availability of lipids to establish functional stomata (Ge et al., 2022).

RabG/Rab7 protein in Arabidopsis also has a notable impact on vacuoles morphology. Expression of a dominant-negative RabG/Rab7 mutant induces the formation of enlarged prevacuolar compartments, disrupting vacuole morphology, inhibiting vacuolar trafficking and ultimately leading to seedling death (Cui et al., 2014). Moreover, Rabe1d localizes in the Golgi apparatus and plasma membrane of Arabidopsis mesophyll cells and plays a fundamental role in the secretion of extracellular matrix molecules. It interacts with phosphatidylinositol 1-4-phosphate 5-kinase 2 (PIP5K2) to stimulate the production of PtdIns (4,5) P2 (temporally and spatially localized) at the plasma membrane (Camacho et al., 2009). Downregulation of its expression level results in a significant alteration in leaf morphogenesis and a reduction of plant volume (Speth et al., 2009).

RabH1b is essential for maintaining Golgi morphology and modulating the trafficking of cellulose synthase complexes from endosomal compartments to plasma membrane (McFarlane et al., 2014). In plant cells, cellulose is produced through a cellulose synthase complex located in the plasma membrane, which is transported to the PM by RabH1b. The loss of RabH1b function leads to impaired exocytosis of CESA6, accumulation of vesicles around the abnormal Golgi apparatus, and an increase in the number of cisternae, thereby resulting in defects in the homeostasis of the pools, a decrease in cellulose content, and seedlings exhibiting short and fragile yellowing hypocotyls (He et al., 2018).

4. Role of rab GTPase in fruit ripening

4.1. Fruit softening

The fruit development and ripening process is a carefully designed physiological process in plants that changes fruit characteristics such as color, texture and flavor compounds, making it more attractive to seed-spreading organisms. As previously reported, fruit ripening is controlled by complex mechanisms driven by hormones, developmental factors and environmental stimuli (Herrera-Ubaldo, 2022). To improve and maintain fruit quality, researchers have established a multi-level gene

regulatory network for fruit ripening using tools such as genome editing, genomics, metabolomics and transcriptomics (Brumos, 2021; Ma et al., 2022; Deng et al., 2023). Fruit softening is a ripening-related process that is closely related to the breakdown of cell walls. It has been shown that cell-wall-modifying enzymes are the main factor affecting fruit softening. Therefore, many groups attempt to maintain cell hardness and prolong fruit shelf life by inhibiting the expression of cell wall synthesis/modification enzymes (Jiang et al., 2019). Despite the success of these technologies at the genetic level, these technologies typically produce minor phenotypical alterations in the softening process.

In the past two decades, Rab GTPase has attracted widespread attention due to its diversity and ripening-related expression in fruit. Some Rab members have been proven to play an important role in fruit ripening (Table 1), regulating the fruit softening process by secreting

and targeting enzymes that alter cell wall components (Lunn et al., 2013). As an important model system for studying fruit ripening, tomatoes contain 56 Rab GTPases, whose expression patterns are shown in Table 2. Among them, LeRab11a (Solyc07g055290) has been proven to regulate the softening process of fruits. Using antisense technology to silence tomato SlRabA11a, transgenic lines had lower levels of polygalacturonase (PG) and pectinesterase (PE) and significantly stronger fruits than untransformed lines (Lu et al., 2001). However, Lunn et al. suggest that SlRab11a reduced fruit softening by changing cell wall deposition rather than cell wall hydrolytic enzymes (Lunn et al., 2013). During fruit development, the cell wall undergoes complex compositional and structural changes. SlRab11a is highly expressed during fruit development, which is related to the period when pectin flows into the wall, and SlRab11a antisense fruit had a decreased proportion of pectin

Table 2
Rab GTPase expression levels (RPKM) in different tissues and ripening processes of tomato.

	bud	flower	leaf	root	1 cm_fruit	2 cm_fruit	3 cm_fruit	MG	Br	Br+10
Solyc01g086850	20.99	17.665	7.36	18.35	4.335	6.78	5.305	17.025	13.61	20.51
Solyc01g088560	49.395	30.785	49.355	57.62	75.665	81.355	47.985	71.57	65.4	64.93
Solyc01g090170	58.89	55	40.075	60.11	56.81	52.275	56.52	54.84	48.285	51.535
Solyc01g096220	12.54	4.995	13.81	25.68	57.5	19.36	4.655	12.28	2.465	10.48
Solyc01g103370	140.71	103.21	86.155	132.23	133.585	85.68	71.23	89.14	73.78	66.91
Solyc01g103380	22.82	17.51	15.55	18.555	29.455	28.12	14.36	31.585	19.795	20.435
Solyc01g109520	67.365	78.1	72.905	145.805	155.64	132.01	153.94	183.85	220.8	221.505
Solyc02g036450	44.365	42.36	34.24	51.43	30.34	28.875	26.725	36.465	28.52	24.805
Solyc02g069370	52.085	54.51	56.41	132.56	25.14	35.015	34.215	23.885	28.27	31.2
Solyc02g072180	33.665	10.54	14.885	35.77	52.665	32.44	14.66	12.58	4.24	1.64
Solyc02g081380	28.445	26.705	17.095	33.905	28.4	38.355	20.92	29.67	22.12	29.075
Solyc02g093530	27.33	24.49	31.795	20.865	33.795	33.215	38.215	27.1	35.88	42.035
Solyc03g064020	2.15	1.2	0.11	0.06	0.065	0	0	0.075	0	0
Solyc03g078570	77.39	64.29	73.59	66.11	87.115	63.92	91.04	60.595	47.465	43.175
Solyc03g079900	7.18	1.355	0	0	0.085	0.09	0.14	0.17	0.065	0.655
Solyc03g118820	4.925	5.165	4.535	7.13	15.62	25.55	16.945	16.64	29.14	34.89
Solyc03g120750	60.065	49.13	43.75	48.815	47.29	38.425	19.41	30.83	38.475	43.74
Solyc04g011360	62.42	65.58	41.72	79.6	66.41	62.875	70.795	75.985	69.16	85.875
Solyc04g012180	25.555	22.76	21.42	31.47	45.34	39.795	40.365	45.92	45.39	48.63
Solyc04g051700	11.53	8	10.73	10.57	13.37	11.53	8.1	10.63	8.01	9.08
Solyc04g064510	48.265	48.5	34.06	74.805	45.54	43.52	33.295	47.705	59.36	75.81
Solyc04g072060	32.84	33.925	23.63	43.3	40.19	27.835	15.9	22.225	18.2	17.225
Solyc05g045660	26.565	76.115	0.05	0.105	0	0	0.1	0.185	0.05	0
Solyc05g051570	90.21	92.855	4.96	28.495	30.015	50.14	66.015	82.51	85.96	25.655
Solyc05g052070	100.99	123.22	31.83	59.67	60.82	68.75	85.375	48.62	48.19	36.71
Solyc05g053940	95.975	86.545	74.87	116.02	103.125	100.525	69.875	86.41	100.01	87.235
Solyc05g054150	20.83	18.595	14.39	15.9	8.94	13.855	15.29	16.285	7.22	0.61
Solyc06g005350	7.195	4.52	5.42	3.515	7.19	7.335	11.71	5.695	2.635	1.705
Solyc06g005810	31.46	33.915	13.625	61.225	14.86	7.91	4.18	6.85	17.3	9.44
Solyc06g060210	0.92	0	0	0	0	0.105	0	0.105	0	0
Solyc06g076450	35.76	35.995	1.71	9.335	1.04	2.32	2.615	8.305	8.85	13.235
Solyc07g053480	27.58	9.83	11.785	28.595	67.575	33.575	19.39	14.145	2.425	2.8
Solyc07g055290	19.695	52.17	27.19	41.695	28.72	30.08	18.13	22.865	24.64	25.22
Solyc07g056150	30.255	35.895	24.655	45.605	32.825	50.4	42.525	45.91	27.92	33.75
Solyc07g064290	15.29	15.1	11.445	36.675	7.91	6.685	8.72	10.145	8.95	14.53
Solyc08g078070	73.75	95.27	40.395	117.34	28.695	32.215	16.795	69.495	119.545	136.51
Solyc09g008460	11.895	7.99	17.425	43.95	26.045	19.525	26.265	31.4	7.37	0.39
Solyc09g010370	102.52	110.865	39.65	184.29	99.235	105.23	98.78	103.39	68.685	44.555
Solyc09g056340	9.675	5.83	12.955	23.395	23.71	16.675	9.135	26.37	25.78	32
Solyc09g097900	14.115	12.14	11.125	10.45	16.125	16.55	9.02	10.77	9.015	4.445
Solyc09g098170	13.16	15.07	19.475	28.255	41.345	36.06	32.775	31.535	33.1	27.795
Solyc10g007700	30.99	30.82	32.55	70.225	44.835	47.865	50.665	52.765	59.065	20.915
Solyc10g008840	5.05	1.14	0	0.35	0	0	0.095	0.055	0.19	0.04
Solyc10g045550	34.855	21.84	29.595	37.76	65.265	51.69	19.555	33.13	22.615	23.95
Solyc10g086310	1.92	0.56	2.25	8.86	0.95	0.615	0.935	0.19	0	0.12
Solyc10g086350	75.24	60.25	61.345	97.43	55.975	49.42	68.04	79.76	67.845	73.065
Solyc11g008020	4.44	15.22	7.335	12.98	12.635	12.02	17.57	22.465	27.855	16.75
Solyc11g008430	71.195	84.005	60.465	60.19	54.73	63.86	55.205	70.235	63.62	57.47
Solyc11g010100	26.21	22.025	29.57	44.82	67.495	48.235	34.78	63.06	46.32	44.46
Solyc11g012460	74.76	52.8	14.33	27.97	13.395	25.15	49.095	30.13	20.425	10.65
Solyc11g073050	90.05	69.41	62.285	137.69	101.41	68.39	43.45	44.5	19.415	25.025
Solyc12g005840	72.285	155.715	1.94	16.16	30.58	21.955	21.325	14.84	0.055	0
Solyc12g010790	84.16	67.695	51.965	71.705	97.42	57.72	91.075	97.93	69.1	50.88
Solyc12g011130	31.74	29.83	17.125	17.065	18.735	24.16	15.825	17.645	19.25	38.66
Solyc12g014080	43.515	45.005	28.89	40.785	55.18	55.45	35.44	42.345	38.74	39.88

Data from The Tomato Genome Consortium.

in the cell wall compared with the wild type. However, during the fruit ripening process (from MG to Br+9), there are other Rab GTPase expression levels higher than those of SlRab11a, such as Solyc09g056340 (Table 2). Its role in fruit softening is worth exploring.

Recently, Lawson et al. utilized a comprehensive in silico approach to identify Rab (23 genes) in mangoes and classified them into eight subfamilies through sequence alignment and similarity tree analysis. RNA-Seq and RT-qPCR analysis showed that some members of RabA, RabC, RabD, RabE and RabF expressed differentially between the unripe (UR) and ripe (R) stages. In particular, the expression levels of most RabA genes in the UR stage were higher than those in the P stage. More noteworthy is the significant negative correlation between the expression levels of RabA3 and RabA4 genes and the fruit hardness during the immature stage of mangoes (Lawson et al., 2020). A total of 26 genes encoding Rab proteins were identified in *Vitis vinifera*, and they were expressed at all stages of fruit development. In particular, VvRabA is developmentally regulated and strongly accumulates during the ripening stage (Abbal et al., 2008). Similarly, the significant fluctuations of PpRab transcripts during fruit development and ripening also present in peach (Falchi et al., 2010). As mentioned above, accumulating evidence supports the involvement of tRab GTPases in the regulation of fruit ripening process, and they are thought to exert their functions by mediating the transport of enzymes to the cell wall.

4.2. Fruit abscission

Mature fruit abscission is another natural event related to fruit ripening. Despite there being two independent developmental and genetic processes, the former significantly affects the yield, quality and postharvest storage of fruits. The presence of a differentiation abscission zone (AZ), localized between the stem and fruit, is a prerequisite for abscission to occur (Olsson and Butenko, 2018). Only after the fruit is mature and the preformed AZ cells are activated will the fruit loosen. It will not shed until the surrounding floral organs fall off. Immature fruit do not go through abscission under normal conditions, even if AZs are formed (Briegas et al., 2020). The process of fruit ripening and abscission is the result of cell wall modification, which involves a wide range of structural proteins and hydrolytic enzymes with distinct functions in the tissues.

Many global transcriptome studies on mature fruit abscission are well documented, suggesting that, in addition to hormones and environment, vesicle formation and transport are also necessary for the changes in deposition of wall material. In melon fruit-AZ, the majority of genes displayed different expression patterns in both early and late induction of abscission, among which 22 Rab-GTPases upregulated at 38 DAP and 8 Rab11 (Raba) were expressed strongly (Corbacho et al., 2013). At the same time, Briegas et al. characterized the transcriptomes of the olive AZ. They link the wall modification process with the upregulation of Rab family members and found that in the fruit AZ Rab11, Rab18, Rab7 and ARA6 were significantly up-regulated and associated with gene-encoding members of the α -galactosidase and β -hexosaminidase, which strengthens the possibility that Rab GTPase regulated endosome transport participating in abscission signaling (Briegas et al., 2020). Thus, Rab-GTPase is thought to regulate mature fruit abscission by mediating the delivery of cell wall depolymerases (required for cell expansion and cell wall relaxation) to extracellular vesicles.

5. Role of RABs in plant biotic and abiotic stress tolerance

Environmental stressors can directly cause the change of membrane fluidity, polarizability and sodium chelating capacity in the plant cell, triggering cellular stress sensing (Zhang et al., 2022). To resist environmental pressure, plants have evolved a complex molecular mechanism that enables them to respond and adapt to the environment in a timely manner. Significantly, numerous biochemical and molecular studies have identified several Rabs as crucial regulatory factors

participating in the stress response (El-Esawi and Alayafi, 2019).

5.1. Biotic stress

Plants engage in different ecological relationships with organisms in their surroundings, including beneficial interactions (symbiosis or reciprocity) with their partners and pathogenic interactions where fungi or bacteria infect and colonize the host. A number of studies have confirmed the important role of Rab GTPase in these interactions. In leguminous plants, a mutualistic interaction is established between plants and Rhizobia, enabling legumes to obtain assimilable forms of nitrogen from bacteria in exchange for photosynthetic products. The formation of root nodule involves the growth and breakdown of cell wall. During this process, Rab GTPases are necessary for the development of functional nitrogen-fixing nodules. Previous reports have found that sRAB1 and sRAB7 influence nodule development in leguminous plants by affecting the number of bacteroids in the cytoplasm and vacuoles (Cheon et al., 1993). In addition, PvRabA2, a member of the RABA/Rab11 subgroup, plays a vital role in reorienting the polar growth of root hairs, causing them to curl around rhizobia microbiota and form infection bags (Cheon et al., 1993). Rab11f was also shown to be expressed in the nodules of *Medicago sativa* (Schiene et al., 2004).

In response to pathogens that pose a threat to plant growth and reproduction, plants employ two branches of immune system, including (1) recognizing and responding to various common microorganisms, and (2) reacting to virulence factors of pathogens directly or through their impact on host targets (Blanco et al., 2009). Multiple lines of evidence have confirmed the role of Rab GTPase in plant disease defense responses. Firstly, Rab GTPase is critical for stomatal closure induced by microbial patterns. Some pathogenic fungi specialize in using stomata as an entry route such as the rusts. It has been confirmed that many plants close their stomata when sensing microbes, which can reduce the severity of infection (Melotto et al., 2008). The dynamics of actin filaments are related to stomatal movement, forming different actin arrays within guard cells: radial orientation of open stomata and longitudinal orientation of closed stomata (Wang et al., 2017). RabG3b has been identified to be involved in FLS2-triggered guard cell actin reorganization (Hawkins et al., 2023). It interacts with NETWORKED4 (NET) as a bridge connecting actin filaments and vacuole membranes, regulating the remodeling process of actin cytoskeleton during stomatal closure. *rabg3b* mutants are unable to close stomata normally under the induction of flg22, and their phenotype is similar to that of two *net4* mutants (Hawkins et al., 2023).

RabG3b as a component of autophagy plays a positive role in autophagy and promotes hypersensitive cell death in response to avirulent bacterial pathogens in *Arabidopsis* (Kwon et al., 2013). Autophagy is vital for the direct elimination of pathogens, and its role in plant basal immunity to virulent pathogens has been determined. Apart from RabG3b, AtRabD2a and PagRabE1b positively regulate autophagosome biogenesis in *Arabidopsis* and poplar (Kwon et al., 2013; Liu et al., 2021). Rab GTPases also participate in defense signaling pathways by regulating intracellular vesicular trafficking. According to reports, OsRabA/OsRab11 along with OsGAP1 and OsGDI3 synergistically regulate vesicular transport from the TGN to the PM or vacuole in *Oryza sativa* (Li et al., 2011). They are widely expressed in plants and can be induced by jasmonic acid (JA) and elicitor treatments. Hong et al. identified OsOPR8 as one of the targets of OsRabA/OsRab11. It is a key enzyme in JA accumulation in response to environmental stress. OsRabA/OsRab11-overexpressing *Arabidopsis* transgenic plants clearly exhibited enhanced resistance to the pathogen *P. syringae* by regulating OsOPR8 and enhancing its NADPH-dependent reductase activity (Hong et al., 2013). Hence, OsRabA/OsRab11 plays an important role in JA-mediated defense signaling. When pathogens attack plants, plant cells can strengthen cell walls through the deposition of glucan polymer callose to thwart pathogen infiltration. In *Arabidopsis*, the interaction between RabA4c and its effector PMR4 (callose synthase) regulates the

biosynthesis of the callose and enhances the deposition of callose at the early stage of infection, which prevents fungal ingress into epidermal cells (Ellinger et al., 2014). In addition, some studies have found that small GTPase participates in ROS production and signaling in plant immunity, such as MtRop9, Rop6 and OsRac1 (Wang et al., 2020; Ganatra et al., 2023). The relationships between Rab GTPase and ROS in plant are poorly understood. However, there are also some Rab GTPases that negatively regulate plant disease resistance. For example, the Arabidopsis AtRABE subfamily contains five members, which are membrane proteins associated with the endomembrane system and participate in vesicle transport process (Zheng et al., 2005). Among these, AtRabE1a, AtRabE1b and AtRabE1d interact with the Arabidopsis RTNL proteins AtRTNLB1–4 and virulence protein VirB2 of *Agrobacterium tumefaciens*. The high expression levels of *rabe1a*, *rabe1b* and *rabe1d* in Arabidopsis increased the susceptibility of plants to *Pst DC3000* infection (Huang et al., 2021).

5.2. Abiotic stress

At present, various genetic, biochemical and molecular studies have identified numerous Rab GTPases as imperative components required for regulating abiotic stress tolerance across a diverse array of plant species.

5.2.1. Salt stress

Soil salinization is increasingly a problem for agriculture worldwide. The increase in salt concentration reduces the ability of plants to absorb water, and the large absorption of Na^+ and Cl^- have a negative impact on growth by damaging metabolic processes and reducing photosynthetic efficiency (Hassani et al., 2021). To resist the effects of salt stress, plants can modify the composition, localization and turnover of protein and lipid components of the plasma membrane via coordinating endocytosis, secretion and endosomal trafficking pathways (Gonzalez et al., 2022).

A recent study indicated that AtRabG3e is involved in salt stress tolerance. AtRabG3e showed a basal level expression in different Arabidopsis organs and could be induced by high but not low concentration of H_2O_2 . During salt stress, transgenic plants overexpressing AtRabG3e showed increased tolerance to salt and osmotic stresses by accelerating endocytosis, increasing sodium accumulation in the vacuole and reducing generation of ROS (Mazel et al., 2004). Plant-unique ARA6-/RabF1 also has a functional role in the salinity stress response. It regulates SNARE complex formation comprising VAMP727 and SYP121 at the plasma membrane, and participates in direct transport from the endosome to the plasma membrane. This trafficking pathway involving ARA6/RabF1 modulates the salt response, since ARA6/RabF1 loss-of-function conferred salt hypersensitivity (Ebne et al., 2011). Heterologous expression of AtARA6 in soybeans directly enhances plant salt tolerance by participating in the regulation of soybean SNARE complexes in vesicular transport pathways (Hong et al., 2022). Unlike ARA6/RabF1, members of RABA1 (RabA1a, RabA1b, RabA1c, RabA1d) are required for salinity stress tolerance, but they are not responsible for the regulation of sodium content and distribution (Asaoka et al., 2013). In *Melilotus albus*, researchers found that members of the MaRab family were widely involved in the abiotic stress response, among which MaRab1, MaRab3, MaRab5, MaRab6, MaRab11, MaRab12, MaRab17, MaRab19, MaRab22, MaRab23 and MaRab55 responded to salt stress, while the details of the regulatory mechanisms involved in the MaRab-mediated drought signal response remain an area of active investigation (Zhang et al., 2022). Furthermore, AhRabG, OsRabG/OsRab7 and OsRabA/OsRab11 are also known to be responsive to abiotic stresses, and their overexpression in transgenic peanut and rice has demonstrated elevated salinity tolerance compared with wild-type plants (Sui et al., 2017; Chen and Heo, 2018).

In the case of perennial woody plants, Rab GTPases are also crucial for development and environmental response. For instance, in poplar, a

total of 67 PtRab GTPases were identified and categorized into eight subfamilies. Among them, PtRabE1b was related to salt stress response, and the overexpression of the constitutive activated mutant form of PtRabE1b (Q74L) maintained healthy root growth status under salt stress conditions by upregulating the expression of genes related to trafficking, stress responses and developmental processes (Zhang et al., 2018).

5.2.2. Drought stress

Drought stress is another major abiotic stress that profoundly hampers the growth, development and yield of crops all over the world. Plants subjected to water stress employ various mechanisms to avert desiccation. These include the regulation of transpiration by means of stomata closure and the augmentation of cuticle thickness, optimizing water transport within the plant, enhancing succulence for water storage, bolstering cellular elasticity and accumulating protective substances, such as dehydrated proteins (Razi and Muneer, 2021). It is generally accepted that maintaining the integrity and stability of the membrane is a major component of plant drought resistance.

O'Mahony and Oliver (O'Mahony and Oliver, 1999) were the first investigators to report the relationship between Rab protein and drought stress. They found that the transcriptional level of the RabB/Rab2 gene increased during dehydration in desiccation-tolerant grass *Sporobolus stapfianus*, followed by a decrease after rehydration, which indicates that SsRab2 is involved in short-term responses and later recovers from desiccation. Since then, research has revealed associations between genes encoding Rab proteins and various stressors in numerous plant species. In Arabidopsis, RabA2b was reported to be involved in the drought resistance response. It is highly upregulated under drought stress and can be induced by osmotic stress and stress hormone ABA. Overexpression of RabA2b in Arabidopsis was strikingly drought resistant. Further investigation revealed that, under drought stress, RabA2b can alter the proteome of PM, enrich stress-coping proteins and modify cell wall/stratum corneum, thereby reducing the permeability of leaf stratum corneum and improving drought resistance in Arabidopsis (Ambastha et al., 2021). Similarly, RabE1c also is highly induced by ABA and drought stress. It has been identified as one of the abundant proteins in guard cells and has been shown to bind to ABA receptors, including Pyrabactin Resistance1-like (PYL) protein, in the plasma membrane of Arabidopsis (Zhao et al., 2008). In the loss-of-function *rabe1c*, the sensitivity of stomatal closure, endoplasmic reticulum signaling and whole plant drought stress response to ABA treatment decreased, indicating that RabE1c acts as a positive regulator in ABA signaling and drought stress (Chen et al., 2021).

Interestingly, CaRabC is also involved in response to salinity stresses. A total of 54 isoforms of CaRab genes were identified in chickpea, and all isoforms of CaRabC were strongly expressed. However, they were downregulated under the slowly developing drought, and very strongly upregulated in rapidly dehydrated leaves (Khassanova et al., 2019). They were involved in drought resistance regulation pathways different from those previously reported. In addition, PgRab7 (from *Pennisetum glaucum*), the homolog OsRab7 (from rice) and AtRab7 (from Arabidopsis) are implicated in intracellular vesicle trafficking from late endosome to the vacuole. Their overexpression has been found to enhance tolerance to mannitol and NaCl in transgenic tobacco, rice and Arabidopsis, respectively (Nahm et al., 2003; Agarwal et al., 2008). It is of interest that the transcript of PgRab7 not only increases under stress conditions but is also upregulated by auxin IAA. Consequently, it is worth further exploring whether PgRab7 has the function of balancing plant growth and stress response.

5.2.3. Temperature stress

Temperature stress (cold/heat stress) is also an important factor influencing the geographical distribution of plants and threatening food security. The perception of temperature signals and the activation of response genes are crucial for the tolerance of plants to temperature

stress (Ding and Yang, 2022). Heat stress severely disrupt intracellular protein homeostasis, leading to the accumulation of abnormally folded proteins, especially in the ER. As a receptor protein for Rab GTPase, the Prenylated Rab Receptor 1 (PRA1) domain protein is located in the endoplasmic reticulum, Golgi apparatus and endosomes/prepolar compartments, and is an important factor in regulating vesicular transport (Alvim et al., 2008). For instance, PRA1_F4 regulates protein excretion from the Golgi apparatus in *Arabidopsis* (Lee et al., 2017), while PRA1_A in tomatoes reduced the localization of pattern recognition receptors in the endosomes, effectively alleviating ER stress (Pizarro et al., 2018). In maize, ZmPRA1_C1 interacts with ZmRabD1 and ZmRabD2c and ensures their retention in the membrane of cognate organelles. ZmPRA1_C1 was not regulated by high temperature at the transcriptional level, but the soluble form of ZmPRA1_C1 rapidly decreases under heat stress conditions. Heat upregulated gene 1 (ZmHUG1) has been reported to thermally stabilize ZmPRA1_C1 and prevent its aggregation in ER. In the *zmhug* mutant, the secretion of secGFP from the ER to the apoplast was impeded and the plant experienced more severe ER stress (Xie et al., 2022).

Apart from the pivotal role in vesicle transport, Rab GTPase contributes to plant heat tolerance by regulating protein translation. RabE1b, also known as the translation elongation factor Tu (EF Tu), is a GTP-binding protein crucial for protein translation in prokaryotic, eukaryotic mitochondria and plastids (Berisio et al., 2010). Under heat stress, RabE1b is one of the most abundant aggregates in *Arabidopsis thaliana* plastids (Li et al., 2018). Knockdown of Rabe1b increased heat sensitivity, which was associated with inhibited induction of HsfA2 and its target genes under heat stress. Thus, it not only affects plastid protein translation under normal conditions/heat stress, but also affects the expression of nuclear heat response genes (Li et al., 2018). In addition, OsRab7 could improve rice tolerance to drought and heat stress conditions. Rice overexpressing OsRab7 exhibits greater tolerance to drought and heat stress effects by improving gas exchange, enhancing osmolytes and chlorophyll content, and inducing antioxidant enzyme activities under drought and heat stress (El-Esawi and Alayafi, 2019). These results provide a new molecular regulatory pathway for Rab to improve plant heat tolerance.

6. Conclusion and perspectives

At present, the importance of vesicle transport has been widely confirmed, but the molecular mechanism of this process is mostly unknown. It is now clear that Rab GTPase, as a regulatory switch, can recruit effector molecules in the active GTP-bound form, thereby controlling various aspects of vesicle transport in mammalian and yeast cells. Compared with yeast/mammals, plant Rab GTPase appears to follow different evolutionary pathways, and the diversity and specificity of plant Rabs have sparked interest in exploring its function. Accumulating evidence shows that Rab GTPases play an important role in various life activities of plants, including tip growth, plant development, biotic/abiotic stress response and fruit ripening. Our manuscript mainly summarizes the Rab GTPases that play an important role in these vital movement and the molecular pathways they may participate in.

Due to the extensive functions of Rab GTPase, the identity and function of a large number of effector molecules in plants are currently unclear. Fortunately, emerging technologies such as BioID, combined with methods such as yeast hybridization and Co-IP, will greatly expand the number of effectors. Therefore, screening the interacting proteins of functional Rab GTPase is also a focus of future work. In addition, Alphafold2 has been applied to predict protein spatial structure and predict interactions between two proteins (Tunyasuvunakool et al., 2021). The conservation of Rab-GTPase protein space provides the possibility of using structural alignment strategies to screen more Rab and its interacting proteins. Overall, numerous studies on the functional analysis of Rab GTPase have suggested that it can regulate plant morphology and fruit maturation by affecting the transport and

composition of cell -wall-modifying enzymes and cell wall polysaccharides, as well as regulating plant immunity and development by coordinating lipid transport, cell plate origin, etc. These reflect the critical requirements of Rab GTPase for plant life.

Funding

This work was supported by National Key R&D Program of China (2022YFD2100101), grants to HZ from the National Natural Science Foundation of China (32,172,639).

CRediT authorship contribution statement

Yao Lu: Writing – review & editing, Writing – original draft, Visualization. **Ke Cheng:** Writing – original draft, Conceptualization. **Hui Tang:** Software, Data curation. **Jinyan Li:** Visualization, Formal analysis. **Chunjiao Zhang:** Software, Conceptualization. **Hongliang Zhu:** Data curation, Conceptualization.

Declaration of competing interest

This manuscript has not been published or presented elsewhere in part or in entirety and is not under consideration by another journal. We have read and understood your journal's policies, and we believe that neither the manuscript nor the study violates any of these. There are no conflicts of interest to declare.

Data availability

Data will be made available on request.

References

- Abbal, P., Pradal, M., Muniz, L., Sauvage, F.X., Chatelet, P., et al., 2008. Molecular characterization and expression analysis of the Rab GTPase family in *Vitis vinifera* reveal the specific expression of a VvRabA protein. *J. Exp. Bot.* 59, 2403–2416. <https://doi.org/10.1093/jxb/ern132>.
- Agarwal, P.K., Agarwal, P., Jain, P., Jha, B., Reddy, M.K., Sopory, S.K., 2008. Constitutive overexpression of a stress-inducible small GTP-binding protein PgRab7 from *Pennisetum glaucum* enhances abiotic stress tolerance in transgenic tobacco. *Plant Cell Rep.* 27, 105–115. <https://doi.org/10.1007/s00299-007-0446-0>.
- Ahn, C.S., Han, J.A., Pai, H.S., 2013. Characterization of in vivo functions of *Nicotiana benthamiana* RabE1. *Planta* 237, 161–172. <https://doi.org/10.1007/s00425-012-1760-5>.
- Alvim, K.C., Boruc, J., Vandepoele, K., Van den Daele, H., Maes, S., Russinova, E., et al., 2008. The PRA1 gene family in *Arabidopsis*. *Plant Physiol.* 147, 1735–1749. <https://doi.org/10.1104/pp.108.122226>.
- Ambastha, V., Matityahu, I., Tidhar, D., Leshem, Y., 2021. RabA2b overexpression alters the plasma-membrane proteome and improves drought tolerance in *Arabidopsis*. *Front. Plant Sci.* 12, 738694 <https://doi.org/10.3389/fpls.2021.738694>.
- Antignani, V., Klocko, A.L., Bak, G., Chandrasekaran, S.D., Dunivin, T., Nielsen, E., 2015. Recruitment of PLANT U-BOX13 and the PI4K β 1/ β 2 phosphatidylinositol-4 kinases by the small GTPase RabA4B plays important roles during salicylic acid-mediated plant defense signaling in *Arabidopsis*. *Plant Cell* 27, 243–261. <https://doi.org/10.1105/tpc.114.134262>.
- Asaoka, R., Uemura, T., Nishida, S., Fujiwara, T., Ueda, T., Nakano, A., 2013. New insights into the role of *Arabidopsis* RABA1 GTPases in salinity stress tolerance. *Plant Signal. Behav.* 8, e25377 <https://doi.org/10.4161/psb.25377>.
- Berisio, R., Ruggiero, A., Vitagliano, L., 2010. Elongation factors EFIA and EF-tu: their role in translation and beyond. *Isr. J. Chem.* 50, 71–79. <https://doi.org/10.1002/ijch.201000005>.
- Berson, T., von Wangenheim, D., Takac, T., Samajova, O., Rosero, A., et al., 2014. Trans-Golgi network localized small GTPase RabA1d is involved in cell plate formation and oscillatory root hair growth. *BMC Plant Biol.* 14, 252. <https://doi.org/10.1186/s12870-014-0252-0>.
- Blanco, F.A., Meschini, E.P., Zanetti, M.E., Aguilar, O.M., 2009. A small GTPase of the Rab family is required for root hair formation and preinfection stages of the common bean-Rhizobium symbiotic association. *Plant Cell* 21, 2797–2810.
- Briegas, B., Corbacho, J., Parra-Lobato, M.C., Paredes, M.A., Labrador, J., Gallardo, M., et al., 2020. Transcriptome and hormone analyses revealed insights into hormonal and vesicle trafficking regulation among olea europaea fruit tissues in late development. *Int. J. Mol. Sci.* 21, 4819. <https://doi.org/10.3390/ijms21144819>.
- Brillada, C., Zheng, J., Kruger, F., Rovira-Diaz, E., Askani, J.C., Schumacher, K., et al., 2018. Phosphoinositides control the localization of HOPS subunit VPS41, which together with VPS33 mediates vacuole fusion in plants. *P NATL ACAD SCI USA* 115, E8305–E8314. <https://doi.org/10.1073/pnas.1807763115>.

The roles of endomembrane trafficking in plant abiotic stress responses^{FA}

Xiangfeng Wang^{1†*}, Min Xu^{2†}, Caiji Gao², Yonglun Zeng³, Yong Cui³, Wenjin Shen^{2*} and Liwen Jiang³

1. State Key Laboratory of Plant Physiology and Biochemistry, Department of Plant Sciences, College of Biological Sciences, China Agricultural University, Beijing 100193, China

2. Guangdong Provincial Key Laboratory of Biotechnology for Plant Development, School of Life Sciences, South China Normal University (SCNU), Guangzhou 510631, China

3. School of Life Sciences, Centre for Cell & Developmental Biology and State Key Laboratory of Agrobiotechnology, The Chinese University of Hong Kong, Shatin, Hong Kong, China

[†]These authors contributed equally to this work.

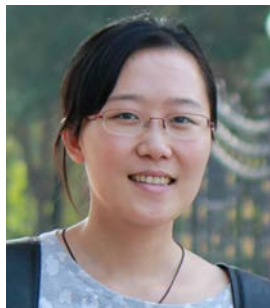
*Correspondences: Wenjin Shen (shenwenjin@m.scnu.edu.cn); Xiangfeng Wang (wangxf2017@cau.edu.cn, Dr. Wang is fully responsible for the distribution of all materials associated with this article)

doi: [10.1111/jipb.12895](https://doi.org/10.1111/jipb.12895)



Xiangfeng Wang

*Correspondences: Wenjin Shen (shenwenjin@m.scnu.edu.cn); Xiangfeng Wang (wangxf2017@cau.edu.cn, Dr. Wang is fully responsible for the distribution of all materials associated with this article)



Wenjin Shen

Abstract Endomembrane trafficking is a fundamental cellular process in all eukaryotic cells and its regulatory mechanisms have been extensively studied. In plants, the

endomembrane trafficking system needs to be constantly adjusted to adapt to the ever-changing environment. Evidence has accumulated supporting the idea that endomembrane trafficking is tightly linked to stress signaling pathways to meet the demands of rapid changes in cellular processes and to ensure the correct delivery of stress-related cargo molecules. However, the underlying mechanisms remain unknown. In this review, we summarize the recent findings on the functional roles of both secretory trafficking and endocytic trafficking in different types of abiotic stresses. We also highlight and discuss the unique properties of specific regulatory molecules beyond their conventional functions in endosomal trafficking during plant growth under stress conditions.

Edited by: ZhiZhong Gong, China Agricultural University, China

Received Oct. 30, 2019; **Accepted** Dec. 10, 2019; **Online on** Dec. 12, 2019

FA: Free Access

INTRODUCTION

Endomembrane trafficking is a fundamental cellular process conserved in eukaryotes to deliver materials between distinctive membrane-bound organelles, and performs the housekeeping functions to maintain essential cellular and developmental processes (Surpin and Raikhel 2004). The major endomembrane trafficking routes in plant cells include the secretory and endocytic pathways

(Figure 1). In the early secretory pathway of eukaryotes, newly synthesized proteins with an N-terminal signal peptide or transmembrane domains enter the conventional protein secretory (CPS) pathway starting at the endoplasmic reticulum (ER), which is also an important site for lipid synthesis, before being transported to the Golgi apparatus (Nebenfuhr and Staehelin 2001; Brandizzi and Barlowe 2013; Oikawa et al. 2013; Stefano et al. 2014). After passing through the stacks of Golgi cisternae from

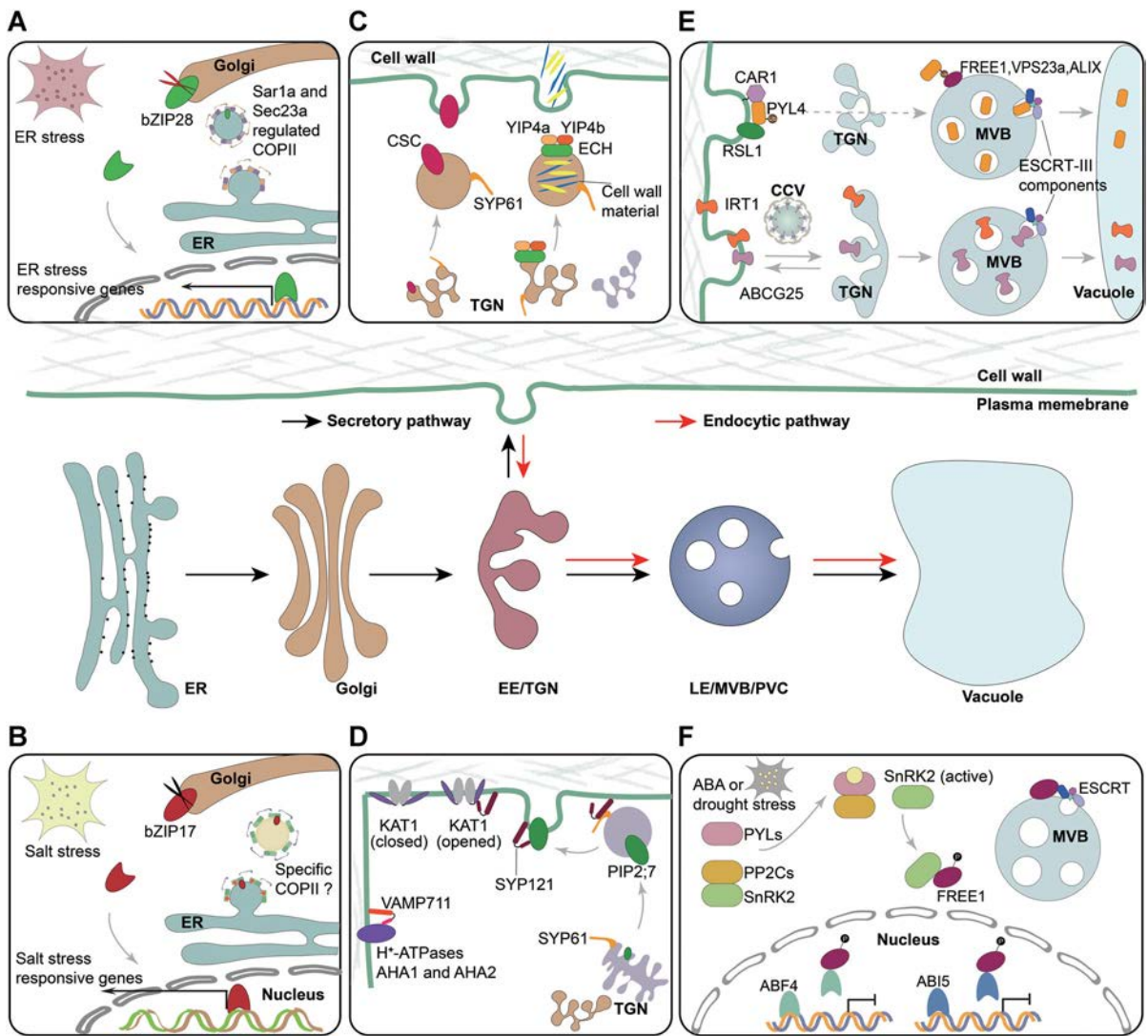


Figure 1. Endomembrane trafficking in the plant abiotic stress response

The major endomembrane trafficking routes in plant cells include the secretory and endocytic pathways, which are intensively involved in plant stress response to ensure the correct delivery of stress related cargoes. (A) Sar1a in *Arabidopsis* defines a specific population of COPII vesicles, which mediates the endoplasmic reticulum (ER) proteins export to the Golgi. Under ER stress, the COPII vesicles with Sar1a specifically mediate the ER export of transcription factor bZIP28, which could sense the ER stress and is cleaved at the Golgi. The cytosolic part of bZIP28 could be translocated into the nucleus to active the expression of downstream ER stress responsive genes. (B) Under salt stress, bZIP17 undergoes similar process with bZIP28. But whether it is mediated by a specific population of COPII vesicles is unknown. (C) SYP61 defined TGN compartments transport the cellulose synthesis complex (CSC) to the plasma membrane (PM) and deliver the cell wall materials to the apoplast with the help of ECH-YIP4a-YIP4b complex. (D) SYP61 could interact with SYP121 to facilitate the trafficking of PIP2;7 to the PM. Interestingly, SYP121 could perform its noncanonical function by interacting with the K⁺ channel KAT1 and directly regulating its activity. Likewise, VAMP711 could interact with the PM localized H⁺-ATPase AHA1 and AHA2 to inhibit their activities, regulating stomatal movement and plant sensitivity to drought stress. (E) PM localized abscisic acid (ABA) exporter ABCG25 and iron transporter IRT1 undergoes the clathrin mediated endocytosis (CME) for vacuolar degradation and recycling back to the PM. Similarly, ABA receptor PYL4, which associate with the membranes via the interaction with CAR1 protein, could be ubiquitinated by the E3 ligase RSL1 localized on the PM, and recognized by the ESCRT components FREE1, VPS23a and ALIX for vacuolar sorting and degradation. (F) Under ABA treatment or drought stress, FREE1 could be phosphorylated by SnRK2 protein kinase, and translocated into the nucleus to perform its unique function. Phosphorylated FREE1 could interact with transcription factors ABF4 and ABI5 and repress their transcriptional activities, thus attenuating the ABA response and contributing to the fine balance of plant survival and growth under stress conditions.

the *cis* side to the *trans* side, the secreted cargo molecules reach the *trans*-Golgi network (TGN) for further sorting to the plasma membrane (PM) and apoplast, or to the endosomes and vacuoles (Hwang and Robinson 2009; Robinson and Pimpl 2014). Proteins without signal peptides can also gain access to the cell exterior through unconventional protein secretion (UPS) pathways in plants either via non-vesicular secretion bypassing the Golgi or through some specific vesicles and organelles (Ding et al. 2014; Robinson et al. 2016). During the endocytic pathway, proteins are first internalized at the PM and transported to the TGN, the plant equivalent of the early endosome (EE) (Lam et al. 2007; Viotti et al. 2010). After reaching the TGN, endocytic cargos can be either recycled back to the PM, or be further transported to the vacuoles via the multivesicular body (MVB)/prevacuolar compartment (PVC), which is equivalent to the late endosome in plant cells and is formed by maturation from specific subdomains of TGN (Viotti et al. 2010; Cui et al. 2014).

In both the secretory and endocytic pathways, the movement of cargo from organelle to organelle is facilitated by vesicles, the formation of which ensures the enclosure of selective cargos and shares conserved sequential processes as well as the major molecular machineries (Valencia et al. 2016). Protein cargos are first recruited into the vesicles formed at the donor membrane via coat and adaptor proteins. These vesicles are further transported and targeted to the destination. Tethering factors help to bring the donor vesicle membrane close to the target membrane, facilitating the subsequent efficient fusion mediated by SNARE complexes. Importantly, small GTPases, for example, ARF and Sar1 GTPases, are the core governors in multiple steps in vesicle formation by recruiting coat proteins (clathrin, COPI, and COPII coatomers), and Rab GTPases in vesicle transport, vesicle tethering and endosomal maturation by selectively recruiting tethering or other specific effector proteins. The activities of small GTPases are regulated by guanine nucleotide exchange factors (GEFs) and GTPase-activating proteins (GAPs), which cycle between GTP-bound active and GDP-bound inactive forms. The retromer complex mediates the recycling of specific membrane cargos from endosomes back to the TGN/Golgi apparatus or to the PM (Robinson et al. 2012; Heucken and Ivanov 2018). Membrane cargo proteins may also be ubiquitinated and sorted into intraluminal vesicles (ILVs) inside MVBs, and are finally released into

the vacuole lumen for degradation upon the fusion between MVB and vacuole (Cui et al. 2016). Consistent with the unique morphology of ILV-containing MVBs, the biogenesis and protein sorting at the MVB are specifically regulated by an “endosomal sorting complex required for transport” (ESCRT) machinery, which consists of ESCRT-0, -I, -II, -III, and VPS4 complexes (Cai et al. 2014; Gao et al. 2017). The characterization and functions of these molecular players in plants have been extensively studied and well summarized in several recent reviews (Fan et al. 2015; Valencia et al. 2016; Gao et al. 2017).

In plants, endomembrane trafficking is indispensable for the response and adaptation to environmental stresses (Yu and Xie 2017; Rosquete and Drakakaki 2018). As sessile organisms, plants need to constantly monitor environmental changes and rapidly reprogramme their metabolism and gene-expression profiles to adapt to unfavorable conditions, such as soil salinity, drought, extreme temperatures, nutrient imbalance, and toxic metals (Zhu 2016; Yang and Guo 2018; Ding et al. 2019). In the past decades, much evidence points to plants having evolved effective and complicated response systems to cope with stress conditions, including the primary and secondary stress perception, and signaling transduction in the cells (Zhu 2016). For example, under salt stress, both the composition of the cell wall changes and PM-localized leucine-rich repeat receptor kinases (LRR-RKs) proteins sense the cell wall integrity (CWI) thereby contributing to the perception of salt signaling (Yang and Guo 2018). Moreover, it has been recently found that a PM lipid glycosyl inositol phosphorylceramide (GIPC) binds Na⁺ and controls Ca²⁺ influx channels (Jiang et al. 2019). Salt stress perceived by multiple pathways further activates the salt overly sensitive (SOS) pathway including SOS2 kinase and PM-localized SOS1 Na⁺ antiporter to export excessive Na⁺ out of the cell, facilitating plant survival, and growth (Yang and Guo 2018). The detailed mechanisms of plant responses to salt stress and other stresses have been well summarized in excellent reviews (Zhu 2016; Yu and Xie 2017; Shi et al. 2018; Yang and Guo 2018; Ding et al. 2019; Wang and Mao 2019). It is intriguing that the compartmentalization and abundance of various macromolecules, including expressed proteins, lipids, and polysaccharides, are essential and constantly regulated in plant stress responses. Since most macromolecules are produced far away from their sites of function, it is not surprising that plant stress responses frequently and

largely rely on the endomembrane trafficking to ensure the correct delivery of stress-related cargos, which are in turn dynamically regulated by the stress signals to meet the specific demands caused by adapting to the constantly changing environment. Here, we will review the recent advances and discuss the involvement of endomembrane trafficking in plant abiotic stress responses.

THE SECRETORY PATHWAY IN PLANT ABIOTIC STRESS RESPONSE

Participation of the early secretory pathway in plant environmental adaptation

The first stage of the secretory pathway is mediated by the coat protein complex II with the ensuing COPII vesicles serving as the anterograde vectors for cargo transport from the ER to the Golgi (Chung et al. 2016). The COPII machinery was first identified in yeast and is conserved in both mammals and plants. It comprises the small GTPase Sar1, the inner coat complex (Sec23-Sec24) and the outer coat complex (Sec13-Sec31) (Novick et al. 1980; Zanetti et al. 2013). One unique feature of the plant COPII machinery is the presence of multiple COPII paralogs due to gene duplication, with five Sar1, two Sec13, two Sec31, seven Sec23, and three Sec24 in *Arabidopsis*. A recent study by Zeng et al. (2015) has identified a specific pair of Sar1a and Sec23a in *Arabidopsis* with specialized functions in the ER export of specific cargos, compared to Sar1c which has a more general function in ER export (Zeng et al. 2015). Strikingly, one unique cargo of the Sar1a-regulated COPII is bZIP28, which is an ER resident protein sensing ER stress and is exported from ER to Golgi followed by cleavage and translocation of the cytosolic tail into nucleus thus functioning as a transcription factor (Figure 1A). Moreover, microarray analyses have shown that the expression of Sar1a and Sec31a is significantly upregulated under ER stress and such an increase is significantly impaired in a *bzip28bzip60* double mutant (Song et al. 2015; Chung et al. 2016). These results have demonstrated the unique role of Sar1a in ER stress and ER homeostasis in *Arabidopsis*. ER stress involves the accumulation of unfolded or misfolded proteins, which can be induced by multiple abiotic stresses (Zhu 2016). A previous study also reported a similar signaling cascade in the salt stress response that has shown that the ER localized transcription factor bZIP17 is transported to the Golgi under salt stress, whereby the cytosolic domain of

bZIP17 is cleaved followed by its translocation into the nucleus to activate the expression of downstream salt stress responsive genes (Figure 1B) (Liu et al. 2007). However, the detailed mechanism of how bZIP17 senses salt and whether bZIP17 is transported by a specific COPII machinery need to be determined. It will be interesting to get more information on the functions of specific COPII proteins in other plant stress responses. Most recently, both Hu et al. (2019) and Mitterreiter et al. (2019) reported that the component of the translocon complex Sec62 in *Arabidopsis* is involved in plant stress response in addition to its function in plant growth (Hu et al. 2019; Mitterreiter et al. 2019). *sec62* mutants show higher sensitivity to ER stress induced by dithiothreitol (DTT) or tunicamycin (TM). Moreover, the survival rate of mutant plants under high temperature stress is obviously lower than that of wild-type plants. Together with the interesting observation that Sec62 colocalizes with the autophagosome marker Atg8 upon TM treatment, it is likely that *Arabidopsis* Sec62 is involved in the autophagy-dependent clearance of excess ER proteins under stress conditions (Hu et al. 2019). Indeed, Sec62 in mammalian cells has been proved to be an autophagy receptor, though the direct evidence for this in plants is still lacking (Fumagalli et al. 2016).

Roles of TGN to PM trafficking in plant abiotic stress responses

The plant TGN is a versatile organelle with a tubular-vesicular structure and has different sub-populations including Golgi-associated TGN and free TGN (Dettmer et al. 2006; Lam et al. 2007; Kang and Staehelin 2008; Toyooka et al. 2009; Kang 2011; Gendre et al. 2015). The SNARE protein Syntaxin of Plants 61 (SYP61) defines a sub-population of TGN compartments. Zhu et al. (2002) first identified the *osm1* (for osmotic stress-sensitive mutant)/*syp61* exhibiting hypersensitivity to both salt and osmotic stresses in a large scale screening of *Arabidopsis* mutants (Zhu et al. 2002). In addition, the water loss of detached shoot from *osm1* mutant was significantly higher than in wild type plants, and abscisic acid (ABA) induced stomatal closure was impaired in the mutant. These observations point to the involvement of SYP61 in the plant response to abiotic stresses, including salt stress, osmotic stress, and drought. A subsequent proteomic study of purified SYP61 compartments provided some clues as to the specific cargos of SYP61-labeled TGN and their presumable functions in plant

abiotic stress responses (Drakakaki et al. 2012). One cargo is the cellulose synthase complex (CSC), the motile transmembrane protein complex responsible for the synthesis of cellulose microfibrils (Figure 1C). CSC has also been proved to function in salt stress, since cellulose deficient mutants show hypersensitivity to salt stress (Zhang et al. 2016). Another cargo ECHIDNA (ECH) has later been identified to form a complex with RAB GTPase interacting proteins YIP4A and YIP4B (Figure 1C) (Gendre et al. 2011, 2013). Both the ech mutant and *yip4ayip4b* double mutant showed significant defects in cell elongation and pectin mucilage secretion in the seed coat, indicating their functions in secretory trafficking of cell wall polysaccharides. Previous studies in wheat and soybean have demonstrated that there is higher level of pectin in the drought tolerant wheat cultivar and salt tolerant soybean cultivar (Konno et al. 2008; Leucci et al. 2008; Tenhaken 2014). However, direct evidence showing the function of ECH-YIP4A-YIP4B complex in plant abiotic stress responses is still lacking. Last but not least, the TGN-localized syntaxins SYP42 and SYP43 have also been identified in the proteome of the SYP61 compartment and the *syp42 syp43* double mutants were hypersensitive to salt and osmotic stress (Uemura et al. 2012), albeit the underlying molecular mechanisms are totally unknown. In summary, whether the TGN-localized syntaxins functions in stress responses through secretory trafficking of cell wall materials and whether different TGN populations performs distinctive roles in plant stress responses still need further investigation.

SYP121 is a PM-localized SNARE protein, and assembles together with other SNAREs, including TGN-localized VAM721/722 and SNAP33, to form the SNARE complex, driving the vesicle fusion at the PM and likely delivering stress-related cargos to the PM. It has been two decades since the first identification of SYP121 function in response to drought and ABA in tobacco (Leyman et al. 1999). However, Hachez et al. (2014) have recently shown that SYP121 is required for the proper trafficking of the aquaporin PIP2;7 to the PM in *Arabidopsis* (Figure 1D) (Hachez et al. 2014). Intriguingly, SYP61 was shown to interact with SYP121 to form a SNARE complex mediating the trafficking of PIP2;7 to the PM. Disruption of either SYP61 or SYP121 leads to a decrease in plant cell membrane water permeability, which is likely due to a defect in the trafficking of aquaporins to the PM (Besserer et al. 2012). However, the evidence is still lacking to show whether the physical

interaction between PIP2;7 and SNAREs can directly regulate the activity of PIP2;7. Taken together, these studies indicate that the TGN and PM localized SNAREs can directly interact with the transmembrane cargo molecules like aquaporins to mediate their secretory trafficking or recycling between the PM and TGN, thereby modulating plant adaptation to drought stress. Besides SNAREs, it has been shown that the TGN-localized RabA1 GTPase is also involved in plant salinity stress tolerance, though the underlying mechanisms remain unclear (Asaoka et al. 2013).

Unconventional functions of VSRs in plant abiotic stress response

Soluble cargo proteins like aleurain that are synthesized in the ER and transported to the vacuoles are recognized and sorted by vacuolar sorting receptors (VSRs) (Cui et al. 2016). Recently, the novel function of one *Arabidopsis* VSR homolog VSR1 in osmotic stress tolerance has been identified (Wang et al. 2015b). The mutant *vsr1/ced2* was first identified as a new regulator of ABA synthesis, which is one of the most important phytohormones involved in abiotic stress responses and many other physiological processes. Osmotic stress triggers ABA accumulation to balance growth and stress response. However, the expression of the ABA synthesis gene NCED3 and ABA levels were both reduced in the *ced2* mutant, which exhibited enhanced sensitivity to osmotic stress. Moreover, similar phenotypes were observed in plants with overexpression of dominant-negative form of VSR1 that interferes with its vacuolar sorting functions, indicating that VSR1-mediated vacuolar protein trafficking is required for stress-induced ABA synthesis and osmotic stress response.

THE ENDOCYTIC PATHWAY IN PLANT ABIOtic STRESS RESPONSE

The crucial functions of CME and recycling in plant adaption to abiotic stresses

Proteins at the PM are constantly damaged when exposed to outside environmental stresses. To ensure the normal activities of the PM in plants, it is necessary to remove damaged proteins and maintain the proper abundance and quality of functional proteins through the endocytic pathway, mainly by clathrin mediated endocytosis (CME) (Fan et al. 2015). The coat protein clathrin is

first recruited to the PM to form clathrin coated pits (CCPs), and cargo proteins are further selected into this region via an interaction with the adaptor protein 2 (AP2) complex. After the recruitment of accessory proteins and coat assembly, matured clathrin coated vesicles (CCVs) eventually detach from the PM and are transported to the EE/TGN, where the endocytosed cargo proteins are either recycled or further sorted for vacuolar degradation. Many important PM-localized proteins, such as the auxin transporters PINs, the BR receptor BRI1, and the pattern recognition receptor FLS2, are subject to the CME for protein turnover (Fan et al. 2015; Dubeaux and Vert 2017; Liu et al. 2018). Recently, the ABA exporter ABCG25 has also been reported to undergo the CME for vacuolar degradation and its spatial regulation is important for ABA homeostasis under stress conditions (Figure 1E) (Kuromori et al. 2010; Park et al. 2016; Nguyen et al. 2018). More endosomal localizations of ABCG25 were observed when treated with NaCl, indicating that salt stress enhances the endocytosis of ABCG25 to reduce the efflux of ABA and increase the ABA content inside the cells. Similar observations in mutants with defective ABA synthesis and signaling demonstrate that salt stress induced endocytosis of ABCG25 does not rely on the concentration or the signaling of ABA. Thus, the exact mechanism through which the endocytosis of ABCG25 is activated is still unclear. Interestingly, treatment with exogenous ABA increased the recycling of ABCG25 back to the PM, maintaining a high level of ABA efflux. These observations indicate that the spatial regulation of ABA transporters by CME and recycling is an effective mechanism to fine-tune the ABA level according to the environmental change. One matter we need to mention is that CME-regulated plant stress responses are definitely not specific to ABCG25, as it also functions in the internalization of other PM-localized stress regulators like receptor-like kinase ACR4, the aquaporin PIP2;1, the boric transporter BOR1, and the iron transporter IRT1 (Takano et al. 2005; Barberon et al. 2011; Ueda et al. 2016; Qin et al. 2019).

In particular, the research on trafficking of IRT1 in the past decade have demonstrated the critical roles of CME and recycling in plant nutrient homeostasis under complicated environmental conditions (Figure 1E) (Barberon et al. 2011, 2014; Shin et al. 2013; Ivanov et al. 2014; Zelazny and Vert 2015; Dubeaux et al. 2018). IRT1 is the primary determinant of iron absorption in plants, and also mediates the transport of other non-iron metals such as manganese, zinc, cobalt, and cadmium.

Although most endogenous IRT1 localized to the TGN/EE in the steady state, specific localization of IRT1 was observed at the PM upon pharmacological treatment with the CME inhibitor Tyrphostin A23 (TyrA23) or in the plants expressing the dominant-negative clathrin HUB to disrupt CME (Barberon et al. 2011, 2014). Later, another study showed that IRT1 could partially colocalize with retromer complex component SNX1 and the loss-of-function mutant of SNX1 exhibited enhanced IRT1 degradation (Ivanov et al. 2014). These results together indicate that IRT1 dynamically cycles between PM and TGN/EE through the CME-dependent internalization and the SNX1-mediated recycling. Surprisingly, the localization and dynamic of IRT1 are not regulated by iron availability, but rather by the secondary substrates like zinc and manganese (Barberon et al. 2011, 2014; Dubeaux et al. 2018). The depletion of these metals resulted in the enrichment of IRT1 at the PM, while the addition of excess metals triggered the endocytosis of IRT1 from PM to endosomes and eventually to vacuole for degradation. Interestingly, the post-translational modifications of IRT1 are critical for its dynamic and are also regulated by the availability of non-iron metals. Multi-monoubiquitination by the E3 ligase IDF1 is essential for the internalization of IRT1 from PM to TGN/EE (Barberon et al. 2011). However, when IRT1 senses the high influx of non-iron metals through direct metal binding to its histidine residues, CIPK23 kinase is recruited to phosphorylate IRT1 and enhances the interaction between IDF1 and IRT1, which in turn extends the multi-monoUb into K63-linked polyUb chains and facilitates IRT1 turnover (Dubeaux et al. 2018). Altogether, these results unraveled the elaborate regulatory mechanisms of IRT1 partition through the endomembrane system, which allows the plants to optimize the iron absorption and prevent the harmful accumulation of other metals.

Roles of MVB-mediated protein sorting and degradation in plant stress adaptation

The ubiquitinated membrane proteins for degradation are sorted into intraluminal vesicles (ILVs) inside LE/MVB governed by a multi-subunit membrane remodeling complex termed as ESCRT (Gao et al. 2017). Interestingly, recent work has highlighted a surprising role of ESCRT in cytosolic cargo proteins and in plant abiotic stress responses through engagement in plant ABA signaling (Belda-Palazon et al. 2016). The perception of ABA is

mediated by the soluble receptor pyrabactin resistance1 (PYR1)/pyr1-like (PYL)-regulatory components of aba receptors (RCAR) (Miyakawa et al. 2013). In the presence of ABA, PYR/PYLs interact with clade A protein phosphatase type 2Cs (PP2Cs), reducing the phosphatase activities of PP2Cs and releasing the ABA-activated sucrose non-fermenting 1-related protein kinase (SnRK2s). SnRK2s phosphorylate downstream ABA-responsive transcription factors and other proteins regulating cellular activities (Umezawa et al. 2013; Wang et al. 2013). Although PYR/PYL receptors are soluble proteins without a transmembrane domain, they can partially associate with the PM via an interaction with CAR1 protein containing a lipid binding C2 domain (Rodriguez et al. 2014). The receptors are further ubiquitinated by the PM-localized E3 ligase RSL1, allowing the membrane associated PYL receptors to be recognized by the ESCRT components and to be sorted into an endosomal compartment (Figure 1E). FYVE DOMAIN PROTEIN REQUIRED FOR ENDOSOMAL SORTING 1 (FREE1) is a plant specific ESCRT component which binds to ubiquitin and phosphatidylinositol 3-phosphate (PI3P), and interacts with multiple ESCRT proteins including VPS23 in ESCRT-I, SNF7 in ESCRT-III and AtBRO1/ALIX in accessory protein complex (Gao et al. 2014; Gao et al. 2015; Belda-Palazon et al. 2016). It was recently reported that the N terminus of FREE1 directly interacts with the ABA receptor PYL4 and mediates the vacuolar degradation of ubiquitinated PYL4 (Belda-Palazon et al. 2016). A *free1/fyve1* heterozygous mutant with reduced expression of FREE1 displayed enhanced sensitivity to ABA treatment, because of the accumulation of functional PYL4 in the mutant. In addition, other plant ESCRT components including VPS23 and ALIX have also been shown to use a similar mechanism to recognize a subfraction of ubiquitinated ABA receptors and to regulate their vacuolar sorting and degradation, thereby negatively modulating plant ABA signaling and drought stress response (Yu et al. 2016; Garcia-Leon et al. 2019).

In another study, however, the ESCRT accessory protein LIP5 was demonstrated to play a positive role in ABA signaling as the *lip5* mutant was insensitive to ABA treatment and more sensitive to drought stress, although the underlying mechanism is unknown (Xia et al. 2016). Besides the drought stress response, LIP5 was also shown to play a critical role in plant responses to salt and heat stresses presumably by regulating the vacuolar degradation of ubiquitinated aggregated proteins under stress conditions (Wang

et al. 2015a). Consistent with the critical role of ESCRT in plant stress adaption, the expression levels of several ESCRT-related genes, such as *LIP5* and *SKD1*, were upregulated upon salt stress; as a consequence plants with reduced expression of *SKD1* displayed an imbalanced Na^+/K^+ homeostasis and a reduced salinity tolerance (Ho et al. 2010). Another ESCRT accessory protein ALIX was also proved to regulate the vacuolar degradation of high-affinity phosphate transporters PHT1 and maintain the phosphate homeostasis in *Arabidopsis* (Cardona-Lopez et al. 2015). Besides the ESCRT complex, MVB and vacuole localized Rab small GTPases are also involved in plant abiotic stress responses. For example, overexpression of the tonoplast-localized RabG3e gene in *Arabidopsis* leads to an increase in tolerance to salt and osmotic stresses and reduced accumulation of reactive oxygen species (Mazel et al. 2004), while overexpression of a constitutively active mutant of the plant unique Rab5 protein ARA6(Q93L) enhanced tolerance to salt stress (Ebine et al. 2011). Future work will be to characterize the stress-induced cargos that are sorted by MVB-mediated transport using a combination of omics approaches and to figure out the link between stress signaling and vacuolar sorting pathway.

THE ROLES OF UNIQUE SNARE AND ESCRT: BEYOND TRAFFICKING IN PLANT ABIOTIC STRESS RESPONSES

Non-endosomal function of SNAREs in plant stress responses

SYP121 and SYP122 shares 76% amino acid similarity, similar expression patterns with no tissue specificity and have a similar ability to form SNARE complexes at the PM. What is more, growth is greatly repressed in only *syp121syp122* double mutants but not single mutants, indicating their redundancy in plant growth (Assaad et al. 2004). However, it is intriguing to note that stomatal reopening was only delayed in the *syp121* mutant but not in the *syp122* mutant, showing the unique function of SYP121 in stomatal movement and abiotic response (Eisenach et al. 2012). More strikingly, Honsbein et al. (2009) showed that SYP121, but not SYP122, directly interacts with the regulatory K^+ channel KC1 on the PM to form a tripartite complex with KC1 and the K^+ channel AKT1, thus regulating

channel activity to promote K⁺ uptake. The mutant *syp121*, but not *syp122*, showed a similar phenotype with *kc1* and *akt1* mutants in the low K⁺ condition with the presence of NH4⁺. Subsequent studies have demonstrated a direct interaction between SYP121 and another K⁺ channel KAT1, and have shown that the addition of SYP121 could enhance the whole cell current when coexpressed with KAT1 in *Xenopus* oocytes. Studies with temporal kinetics of the channel gating showed that expression of SYP121 significantly alters the lifetime of KAT1 in both open and close states (Figure 1D) (Lefoulon et al. 2018). These findings confirmed the unique function of SYP121 in the direct regulation of K⁺ channel activities. Likewise, in a more recent study, the R-SNARE protein VAMP711 was shown to directly interact with the *Arabidopsis* PM H⁺-ATPases AHA1 and AHA2 to inhibit their activities (Figure 1D). Deletion of VAMP711 in *Arabidopsis* results in a higher PM H⁺-ATPase activity and slower stomatal closure in response to ABA, thereby making the mutant plants more sensitive to drought treatments (Xue et al. 2018). Together, these studies demonstrate the unique roles of SNAREs in directly modulating the activity of their transmembrane cargos, which function as transporters or channels, besides their conserved function as vesicle fusion modulators in mediating the endosomal trafficking and targeting of cargo proteins.

Non-endosomal function of plant unique ESCRT component FREE1 in plant environmental adaptation
 Besides the canonical function of ESCRT in endosomal trafficking of stress-response cargo molecules as discussed above, a more recent study has also demonstrated a non-endosomal function of ESCRT subunit FREE1 as a transcriptional regulator in plant responses to ABA signaling (Figure 1F). FREE1 was previously shown to interact with both ESCRT components and autophagy regulators like SH3P2 and the PI3K complex (Gao et al. 2015). Consistent with these diverse interaction partners, FREE1 performs dual functions in both endosomal trafficking and autophagic pathways. Loss of function mutant *free1* is seedling lethal, showing abnormal MVBs, defective vacuolar transport and accumulation of autophagosomes (Gao et al. 2014, 2015). Interestingly, the newly generated *free1* weak allele using CRISPR-Cas9 makes it possible to uncover the novel function of FREE1 (Li et al. 2019). The mutant named as *free1-ctmut* is

hypersensitive to ABA treatment without obvious defects in MVB biogenesis and vacuolar degradation. Moreover, both the full length FREE1 and FREE1(FYVE) with deletion of the PI3P-binding FYVE domain complemented the ABA hypersensitive phenotype, while the FREE1-CTmut could not, indicating the importance of the C terminal coiled-coil domain in the involvement of FREE1 in ABA signaling independent of its conventional functions in endosomal trafficking. Further detailed analysis revealed that exogenous ABA treatment significantly increased nucleus localized FREE1, relying on the phosphorylating residues residing in the C-terminal coiled-coil region of FREE1 by SnRK2 protein kinase. And in turn, FREE1 in the nucleus could interact with transcriptional factor ABF4 and ABI5 to repress their DNA binding ability and transcriptional activities, thus attenuating the ABA response and releasing the inhibitory effect on plant growth. This study, together with the previously mentioned ESCRT mediated ABA receptor turnover, providing an interesting demonstration of the elegant coordination of endosomal trafficking and unique protein function in the balance of plant survival and growth under stress conditions.

CONCLUDING REMARKS

In this review, we have discussed recent studies supporting the involvement of endomembrane trafficking in plant abiotic stresses and revealing their potential underlying mechanisms (Figure 1; Table 1). However, we are still far away from the finalized picture as to how the plant integrates numerous environmental signals and flexibly adjusts its endomembrane trafficking and growth. In addition to stress-related protein cargos, other macromolecules are also delivered through the endomembrane system and play essential roles in plant stress responses, including polysaccharides, lipids and small RNAs. In combination with bioinformatic analysis, the developing techniques of plant proteomics, glycomics, and metabonomics could help to provide more information on putative stress related trafficking regulators. In addition, it will be necessary to pay more attention to the cellular responses to the crosstalk of multiple stresses, and to the crosstalk between environmental stresses and internal growth signals. It is because of this that plants might need to respond to different stresses at

Table 1. Endomembrane trafficking proteins in plant abiotic stress responses

Proteins		Functions in endomembrane trafficking	Participation in abiotic stresses	Mechanisms	References
Coat and adaptor proteins	Sec31a	Outer coat protein of COPII vesicles	ER stress	Unknown	Song et al. 2015; Chung et al. 2016
	Sec23a	Inner coat protein of COPII vesicles	ER stress	Forming a specific pair with Sar1a, and regulating the ER export of ER stress related transcription factor bZIP28	Zeng et al. 2015; Chung et al. 2016
	ECA4	Adaptor in CCV	Salt stress	Mediating the recycling of ABA transporter ABCG25 back to the PM	Nguyen et al. 2018
SNAREs	SYP61	TGN localized SNARE protein driving membrane fusion	Salt stress; osmotic stress; drought stress	Mediating the secretory trafficking of multiple cargoes related to stress responses	Zhu et al. 2002; Konno et al. 2008; Leucci et al. 2008; Drakakaki et al. 2012; Tenhaken 2014; Zhang et al. 2016
	SYP121	PM localized SNARE protein driving membrane fusion	Drought stress; K ⁺ stress	1. Delivering stress related cargoes to the PM such as aquaporin PIP2;7; 2. Interacting with K ⁺ channels and regulating the channel activity to promote K ⁺ uptake	Leyman et al. 1999; Honsbein et al. 2009; Besserer et al. 2012; Eisenach et al. 2012; Hachez et al. 2014; Lefoulon et al. 2018
	SYP42/SYP43	TGN localized SNAREs driving membrane fusion	Osmotic stress; salt stress	Unknown	Uemura et al. 2012
VAMP711		TGN localized SNAREs driving membrane fusion	Drought stress	Interacting with PM localized H ⁺ -ATPases and inhibiting their activities, thus	Xue et al. 2018

(Continued)

Table 1. Continued

Proteins		Functions in endomembrane trafficking	Participation in abiotic stresses	Mechanisms	References
Small GTPases	Sar1a	Mediating the COPII vesicle formation	ER stress	regulating stomatal movement in drought stress Forming a specific pair with Sec23a, and regulating the ER export of ER stress related transcription factor bZIP28	Song et al. 2015; Zeng et al. 2015; Chung et al. 2016
	RABA1s	Regulating the vesicle trafficking between the TGN and the PM	Salt stress	Unknown	Asaoka et al. 2013
	RABF1/ARA6	Plant unique RAB5 protein localized on both endosomes and the PM, regulating endosomal trafficking	Salt stress	Regulating the specific SNARE complex formation on the PM and involved in salt stress response with a yet unclear mechanism	Ebine et al. 2011
	RabG3e	Tonoplast localized small GTPase functioning in vacuolar transport	Salt stress; osmotic stress	Unknown	Mazel et al. 2004
ESCRT complex	FREE1	Plant unique ESCRT-I component performing multiple functions in MVB biogenesis, endosomal sorting and autophagic pathways	Drought stress	1. Interacting with ABA receptor PYLs and mediating their vacuolar sorting and degradation; 2. Regulating the polarized PM localization of IRT1 with a yet unclear mechanism 3. Translocating into	Barberon et al. 2014; Belda-Palazon et al. 2016; Li et al. 2019

(Continued)

Table 1. Continued

Proteins	Functions in endomembrane trafficking	Participation in abiotic stresses	Mechanisms	References
VPS23a	Plant ESCRT-I component mediating the MVB biogenesis and endosomal sorting	Drought stress	the nucleus after being phosphorylated by SnRK2s and repressing the transcriptional activities of ABF4 and ABI5	Interacting with ABA receptor PYLs and mediating their vacuolar sorting and degradation Yu et al. 2016
ALIX	Accessory protein mediating the MVB biogenesis and endosomal sorting	Drought stress	1. Interacting with ABA receptor PYLs and mediating their vacuolar sorting and degradation 2. Regulating the vacuolar degradation of high-affinity phosphate transporters PHT1 and maintaining the phosphate homeostasis in <i>Arabidopsis</i>	Cardona-Lopez et al. 2015; Garcia-Leon et al. 2019
LIP5	Accessory protein mediating the MVB biogenesis and endosomal sorting	Drought stress; heat stress; salt stress	1. Functioning as a positive regulator in ABA signaling with a yet-unknown mechanism; 2. Regulating the vacuolar degradation of ubiquitinylated	Wang et al. 2015a; Xia et al. 2016

(Continued)

Table 1. Continued

Proteins	Functions in endomembrane trafficking	Participation in abiotic stresses	Mechanisms	References
VPS4/SKD1	AAA-type ATPase mediating the MVB biogenesis and endosomal sorting	Salt stress	Maintaining the Na^+/K^+ homeostasis and salt tolerance with a yet-unknown mechanism	Ho et al. 2010
Vacuole sorting receptors	VSR1 Recognizing the soluble vacuolar cargo proteins and mediating the vacuolar transport	Osmotic stress	Affecting the expression of ABA synthesis gene and ABA level with a yet-unknown mechanism	Wang et al. 2015b

the same time in nature, with the coexistence of insects, bacteria, and pathogens, and need to fine-tune the balance between stress-related cargo delivery and housekeeping trafficking to maintain cell integrity and plant survival.

ACKNOWLEDGEMENTS

We apologize to those colleagues whose works were not cited due to space limitations. This work was supported by grants from the National Natural Science Foundation of China (31872644) to X.W., the National Natural Science Foundation of China (31701246) to W.S., the National Natural Science Foundation of China (31671467, 31870171) to C.G. L.J. is supported by Research Grants Council of Hong Kong (AoE/M-05/12 and C4002-17G).

AUTHOR CONTRIBUTIONS

X.W., M.X., and W.S. wrote the manuscript. Y.Z., Y.C., C.G., and L.J. edited the manuscript. All authors read and approved the paper.

REFERENCES

- Asaoka R, Uemura T, Ito J, Fujimoto M, Ito E, Ueda T, Nakanishi A (2013) Arabidopsis RABA1 GTPases are involved in transport between the trans-Golgi network and the plasma membrane, and are required for salinity stress tolerance. *Plant J* 73: 240–249
- Assaad FF, Qiu JL, Youngs H, Ehrhardt D, Zimmerli L, Kalde M, Wanner G, Peck SC, Edwards H, Ramonell K, Somerville CR, Thordal-Christensen H (2004) The PEN1 syntaxin defines a novel cellular compartment upon fungal attack and is required for the timely assembly of papillae. *Mol Biol Cell* 15: 5118–5129
- Barberon M, Zelazny E, Robert S, Conejero G, Curie C, Friml J, Vert G (2011) Monoubiquitin-dependent endocytosis of the iron-regulated transporter 1 (IRT1) transporter controls iron uptake in plants. *Proc Natl Acad Sci USA* 108: E450–458
- Barberon M, Dubeaux G, Kolb C, Isono E, Zelazny E, Vert G (2014) Polarization of IRON-REGULATED TRANSPORTER 1 (IRT1) to the plant-soil interface plays crucial role in metal homeostasis. *Proc Natl Acad Sci USA* 111: 8293–8298
- Belda-Palazon B, Rodriguez L, Fernandez MA, Castillo MC, Anderson EM, Gao C, Gonzalez-Guzman M, Peirats-Llobet M, Zhao Q, De Winne N, Gevaert K, De Jaeger G, Jiang L, Leon J, Mullen RT, Rodriguez PL (2016) FYVE1/FREE1 interacts with the PYL4 ABA receptor and mediates its delivery to the vacuolar degradation pathway. *Plant Cell* 28: 2291–2311
- Besserer A, Burnette E, Bienert GP, Chevalier AS, Errachid A, Grefen C, Blatt MR, Chaumont F (2012) Selective regulation